A Study of Factorization and a Measurement of CP Violation

Bryan Dahmes

UNIVERSITY OF CALIFORNIA
Santa Barbara

A Study of Factorization and a Measurement of CP Violation

A Dissertation submitted in partial satisfaction
of the requirements for the degree of

Doctor of Philosophy

in

Physics

by

Bryan Dahmes

Committee in Charge:

> Professor C. Campagnari, Chair
>
> Professor D. Berenstein
>
> Professor D. Stuart

December 2006

The Dissertation of
Bryan Dahmes is approved:

_____

Professor D. Berenstein

_____

Professor D. Stuart

_____

Professor C. Campagnari, Committee Chairperson

September 2006

A Study of Factorization and a Measurement of CP Violation

Acknowledgements

I would like to thank my advisor, Claudio Campagnari, for his efforts during my graduate student career. When I was a bright-eyed graduate student, I remember our talks at the Oasis in Menlo Park, where he helped me understand what could be accomplished at $B\!A\!B\!A\!R$, and what was so fun about particle physics. As I matured, he taught me how to be a physicist. Graduating now, I realize that his guidance has prepared me for the next stage in my career.

I would also like to thank Jeff Richman, Pat Burchat, and Bill Dunwoodie for several conversations, mostly relating to physics, that I have shared with each of them over the years. I owe at least a small part of my growth to each of them.

I would like to thank several of my $B\!A\!B\!A\!R$ friends for making these years enjoyable: Jeff Berryhill, Adam Cunha, Steve Levy, Chris Roat, Stephanie Majewski, and Virginia Azzolini. My time with them was often focused on physics, but there was also plenty of time for sports, games, and life in general. I would especially like to thank Michael Mazur for all the lunch conversations, and the cribbage games he let me win.

I am extremely grateful to eveyone that I have met as a result of becoming a SLAC tour guide. With rare exception, every tour I gave was an extreme pleasure. My enjoyment of physics increased with every tour that I gave. Thanks to Emily Ball for getting me started, and to Maura Chatwell for chatting with me so often,

and being one of the friendliest bosses I've ever had. Thanks to Barbara Hoddy and Melinda Lee. You have both been great friends. Knowing that you had my paycheck was all the excuse I ever needed (as if I needed an excuse) to come and visit. Finally, I would like to thank Ellie Lwin, and of course Pief, for being great friends to me.

I've had a very enjoyable life outside of SLAC, and I owe most of this to folks in the Stanford Tae Kwon Do club. Coach Ghormley has had a strong influence on my life, and I am grateful for the time I spent with the competitive team under the direction of Coach Kim. My TKD friends have been my California family. To thank each person in this group would take too long, and will ignore somebody important, but I'll try anyway. Thanks to Ron, Ernest, Greg, Filip, Paul, Parilee, Alby, Julie, Randall, Pat, Bob, Jacky, Grace, Pablo and Mariana, and Becca. Thanks to Richard O'Grady for being a great friend. Thanks to Ian Sas and Khoua Vang, who have opened up their home and their lives to me, and for making me an "uncle" to Caelyn. Thanks to my sister, Audrey Yap. I wish I had the words.

Thank you Sharon. I liked you from the moment I met you, and to have you in my life has been a blessing beyond any expectations. You are smart, kind, patient, beautiful, loving, and so much more. Thank you so much. I love you. xo.

Thank you to my family. Mom and Dad, Brittney (and Dan and Tate), and Andy. It's been tough for me to be away from you for so long, and I know it's been tough on you. Thank you for your love and continued support. I am who I am because of each of you.

Thanks to my Lord and Savior, Jesus Christ. May I always serve Him first.

Curriculum Vitæ

Bryan Dahmes

Education

1998	Bachelor of Science in Physics and Mathematics, with High Distinction in both Physics and Mathematics, University of Minnesota, Minneapolis.

Experience

1998 – 2006	Graduate Student Researcher, University of California, Santa Barbara.

Selected Publications

Measurement of branching fractions for exclusive B decays to charmonium final states

B. Aubert *et al.* (BaBar Collaboration), Phys. Rev. **D65**, 032001 (2002).

Measurement of the CP Asymmetry Amplitude $\sin 2\beta$

B. Aubert *et. al.* (BaBar Collaboration), Phys. Rev. Lett. **89**, 201802 (2002).

Study of the Decay $\bar{B}^0 \to D^{*+} \omega \pi^-$

B. Aubert *et. al.* (BaBar Collaboration), Phys. Rev. **D74**, 012001 (2006).

Abstract

A Study of Factorization and a Measurement of CP Violation

Bryan Dahmes

We report on a study of the decay $\bar{B}^0 \to D^{*+}\omega\pi^-$ with the BABAR detector at the PEP-II B-factory at the Stanford Linear Accelerator Center. Based on a sample of 232 million $B^0\bar{B}^0$ decays collected between 1999 and 2004, we measure the branching fraction $\mathcal{B}(\bar{B}^0 \to D^{*+}\omega\pi^-) = (2.88\pm0.21(\text{stat.})\pm0.31(\text{syst.}))\times10^{-3}$. We study the invariant mass spectrum of the $\omega\pi^-$ system in this decay. This spectrum is in good agreement with expectations based on factorization and the measured spectrum in $\tau^- \to \omega\pi^-\nu_\tau$. We also measure the polarization of the D^{*+} as a function of the $\omega\pi^-$ mass. In the mass region 1.1 to 1.9 GeV we measure the fraction of longitudinal polarization of the D^{*+} to be $\Gamma_L/\Gamma = 0.654\pm0.042(\text{stat.})\pm 0.016(\text{syst.})$. This is in agreement with the expectations from heavy-quark effective theory and factorization assuming that the decay proceeds as $\bar{B}^0 \to D^{*+}\rho(1450)^-$, $\rho(1450)^- \to \omega\pi^-$.

Furthermore, we present the results on the time-dependent CP asymmetry in neutral B meson decays to the CP eigenstate $J/\psi K_L$. The measurements use a data sample of about 88 million $\Upsilon(4S) \to B\bar{B}$ decays collected between 1999 and

2002 with the BABAR detector. We study events in which one neutral B meson is fully reconstructed in the $J/\psi K_L$ final state and the other B meson is determined to be either a B^0 or a $\bar{B}^0$ from its decay products. The amplitude of the CP asymmetry, which in the Standard Model is proportional to $\sin 2\beta$, is derived from the decay-time distributions in such events. We measure $\sin 2\beta = 0.723 \pm 0.158(\text{stat.}) \pm 0.086(\text{syst.})$, which is consistent with Standard Model expectations.

Professor C. Campagnari

Dissertation Committee Chair

Contents

List of Figures

xvi

List of Tables

Chapter 1

Introduction to the Standard Model

Our understanding of particle physics, obtained from several decades of research, has been collected into what is commonly referred to as The Standard Model of particle physics. Up to this point, the Standard Model has been very successful in describing the behavior of matter in our universe. The electromagnetic and weak interactions of matter have been satisfactorily described by Glashow, Salam, and Weinberg [1], and the origin of mass can be explained by the Higgs mechanism [2]. Quantum Chromodynamics (QCD) summarizes the strong interactions between quarks. Only gravity escapes understanding within the context of this model. Standard Model predictions have repeatedly been verified by experimental data without any significant inconsistencies.

Although extensive in its treatment of matter, the Standard Model is not without its shortcomings. For example, there are several parameters that are not

predicted by the Standard Model and must therefore be determined by experiment. They include

- The masses of the six quarks (u, d, c, s, t, b) and three leptons (e, μ, τ). Neutrino masses, recently determined to be non-zero [3], must also be determined by experiment.

- The coupling strengths of the strong and electroweak interactions.

- The parameters associated with the Higgs mechanism.

- The four parameters of the CKM matrix (which will be discussed more fully in Section 6). There are also four parameters needed to describe the neutrino mixing matrix.

There are also several features of the Standard Model that are currently unexplained. We list some of these questions below:

- Why are there only three quark generations, and why is there such a large variation in the quark and lepton masses?

- Why does the weak interaction prefer left-handed particles?

- The CP violation seen in the interaction of quarks is not enough to explain the dominance of matter in the universe [4]. What accounts for this discrepancy?

- What is the nature of neutrinos? Are they majorana particles?

In addition, it is likely that physics at the next energy scale (beyond 1 TeV) will produce new results that are not consistent with our current understanding. Particle masses originate due to interactions with the Higgs field, but the realization of this field in Nature is not understood. The Standard Model prediction of a single scalar Higgs boson is unsatisfying, as it introduces the need to adjust model parameters precisely in order to agree with observations. Without any mechanism for this fine-tuning, several questions are left unanswered. Consequently, it is possible that the Higgs boson(s), when (and if) found, will not coincide with the Standard Model.

Existing data suggest that the Standard Model accurately describes physical phenomena observable today, and yet we anticipate there will be a breakdown of our understanding in the near future. As a result, there are two primary tasks to accomplish:

1. Precision tests of Standard Model predictions. If the Standard Model is incomplete, at some point physical data will disagree with expectations.

2. Improve the predictive power of the Standard Model. By increasing theoretical understanding of physical processes, comparisons with experimental data will be more meaningful.

In this thesis, I will address each of these tasks with two separate analyses. In Chapters 2-3 and 5, I will summarize my study of $\bar{B}^0 \to D^{*+} \omega \pi^-$ decay. This study provides a good laboratory to test factorization in B meson decay. In Chapters 6-8, I study $B^0 \to J/\psi\, K_L$ decay in order to obtain the CP Violating parameter $\sin 2\beta$. Each of these analyses were performed on data obtained from the BABAR detector located at the Stanford Linear Accelerator Center. I briefly describe this experiment, and the BABAR detector, in Chapter 4.

1.1 The Electroweak Interaction

The theory of the electroweak interaction merges the electromagnetic and weak forces on matter. This feat is made possible by the introduction of massive force carriers, $W^\pm$ and Z^0, for the weak force in the same fashion that the photon mediates the electromagnetic interaction. In this sense, the coupling strength of the weak interaction is similar to the electromagnetic interaction, but its effectiveness is reduced at low energies ($E \ll m_{W,Z}$) because of the large mass of the $W^\pm$ and Z bosons.

The existence of the charged W boson allows flavor-changing currents within the weak interaction. This behavior is responsible for nuclear β decay, in which a neutron ($n = udd$) decays into a proton ($p = uud$) when $d \to uW^*$, followed

by $W^* \rightarrow e^- \bar{\nu}_e$. The long lifetime of the neutron ($\tau_n \sim 15$ minutes) is due in part to the energy scale of the interaction: as $m_n - m_p \ll M_W$, the interaction is suppressed.

The weak interaction is also responsible for the (relatively) long lifetimes for other particles. If we consider the lightest meson, the pion, we see that the lifetime of the charged $\pi^\pm$ is $\sim 10^{-8}$ seconds, while $\pi^0 \rightarrow \gamma\gamma$ in about 10^{-16} seconds. While the neutral pion may decay electromagnetically to two photons, in order to conserve charge the charged pion must decay weakly.

One of the interesting aspects of the weak force is that it acts on a mixture of quark states. As a result, as long as the process is kinematically allowed, an up-type quark may interact with any down-type quark. At BABAR, this means that while the decay of B mesons proceed primarily through $b \rightarrow cW^*$, $b \rightarrow uW^*$ transitions also occur (at less than 1% of the $b \rightarrow cW^*$ rate). As $m_t \gg m_b$, the (favored) weak interaction between b and t quarks can only occur in off-shell (virtual) loop processes, such as $b \rightarrow t^* \rightarrow s$. The strength of these transitions are described by the CKM matrix in the Standard Model, which will be discussed in Section 6.2.

1.2 The Strong Interaction

Quantum Chromodynamics (QCD), which describes the interactions between quarks, is a local gauge theory whose formulation was motivated by the success of Quantum Electrodynamics (QED). Before the discovery of quarks, it was known that there must exist some "strong" force that is capable of binding protons and neutrons within the nucleus of an atom. As it became evident that the supposedly fundamental nucleons were composite particles made up of quarks, the forces governing quarks needed to be understood.

Quarks have an electric charge, and quarks can also interact weakly with other quarks. In this sense, they are similar to more familiar particles, such as the electron. However, unlike the electron, quarks possess an additional charge, known as color, which subjects them to the effects of the strong force.

The strong force was only "discovered" recently due to the following reasons:

- All leptons are colorless and are therefore "blind" to the effects of the strong interaction.

- Hadrons, which are formed from either a quark-antiquark pair $(q\bar{q}')$ or a quark/antiquark triplet $(qq'q''$ or $\bar{q}\bar{q}'\bar{q}'')$, are colorless objects.

- Ignoring top, strong interactions between quarks keep them confined within hadrons [5].

As quarks are never found in a "free" state, it was difficult to predict their behavior before they were observed.

Quarks were first discovered in scattering experiments at SLAC [6], This work led to the realization that the proton and neutron are composed of three quarks:

$$p = uud \quad \text{and} \quad n = udd,$$

where the u (up) quark has electric charge $+\frac{2}{3}e$, and the d (down) quark has charge $-\frac{1}{3}e$, where e is the magnitude of the electron charge. Further research led to the discovery of four more quarks. The results are summarized in Figure 1.1.
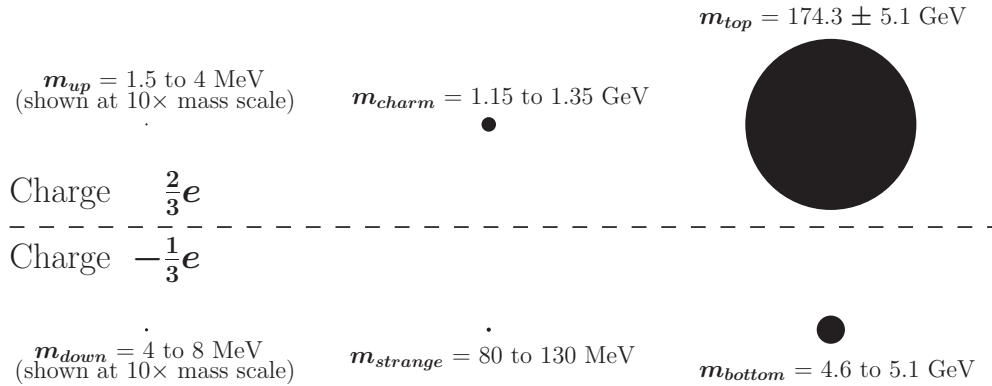
Figure 1.1: The quarks of the Standard Model, where the relative sizes shown indicate the relative mass of each quark. The up and down quarks are shown at 10× scale.

All hadrons are composed of some combination of quarks and anti-quarks. In this thesis, I will study some of the properties of the B^0 meson ($\bar{b}d$), but this work

also involves charm ($D^{(*)} = c\bar{d}$ or $c\bar{u}$, $J/\psi = c\bar{c}$), strange ($K = s\bar{u}$ or $s\bar{d}$), or light (π and ω, composed of u and d and their antiparticles) mesons.

By observing the production rate of $e^+e^- \rightarrow$ hadrons, we concluded that the color charge is a triplet charge. As a result, we refer to the color charge of quarks as either red, green, or blue. Colored quarks combine to form color-neutral baryons (such as p, n, Λ, etc.); mesons are formed from a color/anti-color combination of a quark and an anti-quark (such as a blue u + anti-blue $\bar{d} = \pi^+$).

Within a hadron, complicated strong interactions are taking place between quarks. These interactions are responsible for holding the hadron together. Within the proton, the two up quarks (both with charge $+\frac{2}{3}e$) would be electromagneti-cally repelled from each other if not for the strong interaction between them. The force due to the color charge of the quarks overrides the electromagnetic force and keeps the proton stable.

1.2.1 Strong force computations

Although we know the strong interaction plays a vital role in the natural world, our ability to understand this force is currently limited. The tremendous success of QED, which accurately describes electromagnetic interactions, led to hopes that a similar model could be used to parametrize the strong interaction.

In QED, electromagnetic interactions arise as the result of an exchange of (virtual) photons between charged objects. As the photon is massless, the range of the electromagnetic force is infinite. The coupling strength of the photon to charges is small compared to unity, $\alpha \sim 1/137$. Accurate theoretical predictions of electromagnetic interactions can be calculated perturbatively by expanding the calculations in powers of the coupling constant.

As an example of the success of this method, consider the anomalous magnetic moment of the electron. According to the Dirac equation, the magnetic moment of the electron is given by

$$\mu = -g\frac{e}{2m}\, S \tag{1.1}$$

where e and m represent the charge and mass of the electron, respectively. The spin of the electron is described by S. The Dirac equation predicts $g = 2$ for a fundamental particle. Experimentally, the value of g exceeds two by a small amount, and it turns out that this difference can be perturbatively accounted for in QED. Expanding in powers of the coupling strength α, we find

$$\begin{aligned}
\frac{g-2}{2} &= \frac{1}{2}\left(\frac{\alpha}{\pi}\right) \;-\; 0.32848\left(\frac{\alpha}{\pi}\right)^2 \;+\; 1.19\left(\frac{\alpha}{\pi}\right)^3 \;+\; \cdots \\
&= (11596524 \pm 4)\times 10^{-10},
\end{aligned}$$

up to $\mathcal{O}(\alpha^3)$ [7]. This prediction is in excellent agreement with the experimental value of $(11596521.9 \pm 0.04) \times 10^{-10}$ [8]. By exploiting the strength of the electromagnetic coupling, QED predictions can be tested to extraordinary accuracy.

Our natural aim is now to apply this approach to strong interactions in the hopes that this method will prove successful when dealing with colored particles. In QCD, the photon is replaced by a collection of messenger particles known as gluons. These gluons are massless, like the photon. However, while the photon is electrically neutral (and therefore cannot carry charge), the gluons are colored objects. A natural consequence of this trait is that gluons interact with each other. As our goal was to perturbatively expand QCD calculations in powers of the coupling strength, the self-interacting gluons present an interesting twist with respect to our work in QED.

Serious problems develop when we consider the coupling strength of the strong interaction, α_s. In QED, the small size of α allowed electromagnetic interactions to be calculated perturbatively. In the strong interaction, the coupling strength is often comparable to unity, as can be seen in Figure 1.2. At high energies, when the quark is essentially free, α_s is small compared to unity, and QCD calculations can proceed perturbatively. However, at low energies, when quarks are bound within hadrons, α_s is large. This makes perturbative calculations impossible, as higher order terms would actually dominate over the simplest ones.
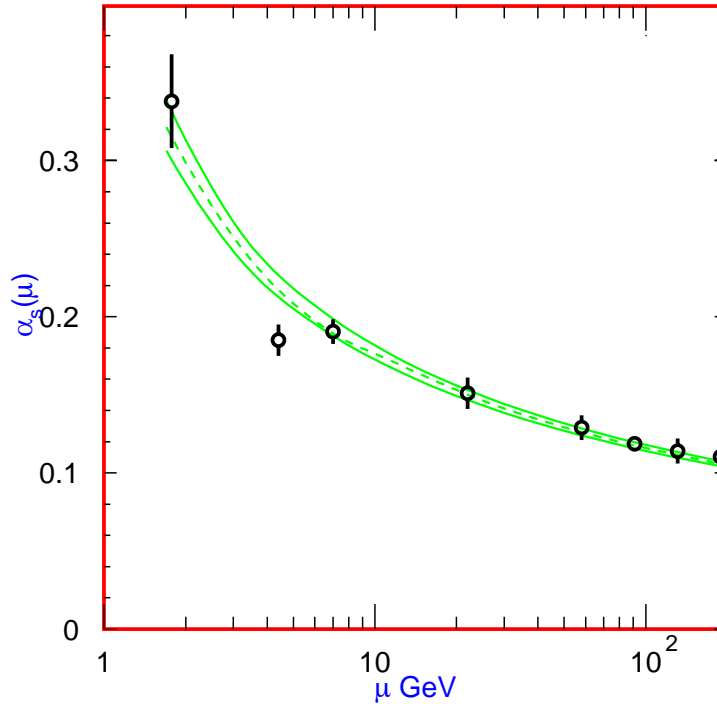
Figure 1.2: Summary of the values of α_S as a function of measurement energy. Figure taken from [8].

As a result, our hopes to exploit the success of QED in order to develop and manipulate a theory of the strong interaction are left unfulfilled. Although QCD allows us to understand the nature of the strong interaction, it is difficult to accurately predict the behavior of quarks with this theory, especially at low energies. Significant progress in this area has been made using lattice QCD [9], but we still hope to discover ways to reasonably simplify QCD interactions in order to gain insight into strong phenomena.

Chapter 2

Weak decays of the B meson

Theoretical calculations involving the strong interaction are naturally quite complicated. Perturbative calculations of QCD are not useful at low energies when quarks are bound within hadrons. As a result, it is advantageous to consider interactions when strong force effects can be minimized.

2.1 Leptonic Decay

All hadrons, with the exception of the proton, are observed to have finite lifetimes. By studying the decay of various hadrons, we can gain insight into the interactions between quarks.

Let us first consider the simplest case of the leptonic decay of a meson, where the initial state quarks annihilate in the decay and produce only leptons in the final state. As a result, all the complications associated with strong interactions are limited to the initial state.
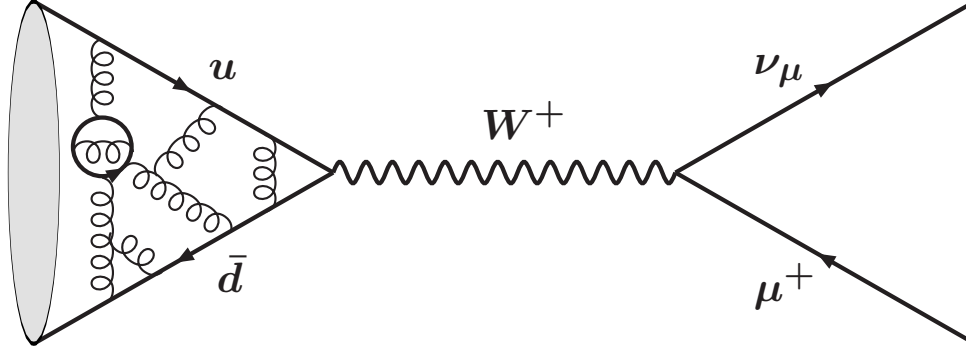
Figure 2.1: Sample leptonic decay $\pi^+ \to \mu^+ \nu_\mu$.

Let us consider the specific case of $\pi^+ \to \mu^+ \nu_\mu$ decay, which is shown in Figure 2.1. In this case, the pion (with momentum q) is comprised of a $u\bar{d}$ pair which eventually meet at a point. When this happens, these quarks annihilate via a virtual W^*, followed by $W^* \to \mu^+ \nu_\mu$. Because the μ and ν_μ have no color charge, they do not interact strongly with each other or with the initial quarks. This simplifies our calculation of the amplitude for this decay, as the matrix element can be expressed as the product of hadronic and leptonic currents:

$$\mathcal{M} = \frac{G}{\sqrt{2}} V_{ud} \langle 0 | J_\mu | \pi^+ \rangle \cdot \bar{u}(p) \gamma^\mu (1 - \gamma_5) v(k), \tag{2.1}$$

where $p(k)$ is the 4-momentum of the $\mu(\nu_\mu)$, and $q = p + k$. G is the Fermi coupling constant, and V_{ud} is the relevant CKM element. As the π^+ has no spin, the only 4-vector that can be used to construct the current J_μ is the initial pion

4-momentum (q_μ). Consequently, we can express the hadronic current as

$$\langle 0|J_\mu|\pi^+\rangle = -iq_\mu f(q^2) \equiv -iq_\mu f_\pi, \qquad (2.2)$$

where f is a function of the Lorentz scalar q^2. As q is the 4-momentum of the

pion, we have $q^2 = m_\pi^2$, and so $f(m_\pi^2) \equiv f_\pi$ is a constant.

At this point, we are able to calculate the leptonic decay rate of the pion. We

obtain

$$\Gamma(\pi^+ \to \mu^+\nu_\mu) = \frac{G^2}{8\pi} f_\pi^2 \, m_\pi m_\mu^2 (1 - \left(\frac{m_\mu}{m_\pi}\right)^2)^2. \qquad (2.3)$$

In this fashion, our understanding of QCD processes may be tested by comparing

theoretical predictions of decay constants to experimental values.

It is also possible to remove the effects of the strong interaction entirely in

some calculations. If we consider the decay $\pi^+ \to e^+\nu_e$, we expect

$$\frac{\Gamma(\pi^+ \to \mu^+\nu_\mu)}{\Gamma(\pi^+ \to e^+\nu_e)} = \left(\frac{m_e}{m_\mu}\right)^2 \left(\frac{m_\pi^2 - m_e^2}{m_\pi^2 - m_\mu^2}\right)^2 = 1.2 \times 10^{-4}. \qquad (2.4)$$

This value is in good agreement with experimental results.

2.1.1 Hadronic τ decay

We may extend our treatment of leptonic decay to include hadronic decays of

the μ and τ leptons. In this case, the $\tau \to W^*\nu_\tau$ transition is understood, and

the hadronization of the $W^* \to q\bar{q}'$ system can be parametrized as above. If we
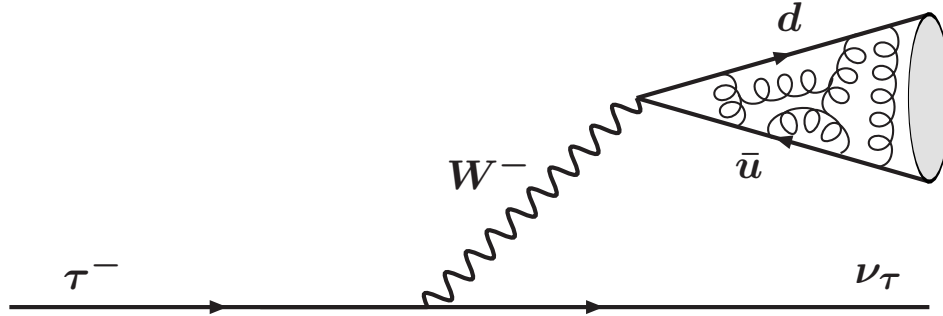
Figure 2.2: Sample hadronic decay $\tau^- \to \pi^- \nu_\tau$.

consider the decay $\tau^+ \to \pi^+ \nu_\tau$ (see Figure 2.2), we obtain

$$\Gamma(\tau^+ \to \pi^+ \nu_\tau) = \frac{G^2}{16\pi} f_\pi^2 V_{ud}^2 m_\tau^3 \left(1 - \frac{m_\pi^2}{m_\tau^2}\right)^2. \tag{2.5}$$

We may also generalize our results, by considering the decay $\tau \to X \nu_\tau$, where X is some hadronic system. In this case, we find [10]

$$\frac{d\Gamma}{dm_X^2} = \frac{G^2 |V_{qq'}|^2}{32\pi^2 m_\tau^3} (m_\tau^2 - m_X^2)^2 (m_\tau^2 + 2m_X^2) v_X(m_X^2), \tag{2.6}$$

where $V_{qq'}$ describes the relevant CKM element. The function v_X characterizes the physics involved in the formation of the hadronic system X, and must be determined from experiment. The CLEO collaboration has measured $v_X(m_X^2)$ in the case where X is a system of two to four pions [11, 12].

In each of these cases, the effects of the strong interaction are limited to functions which depend on the square of invariant mass of the hadronic system (recall
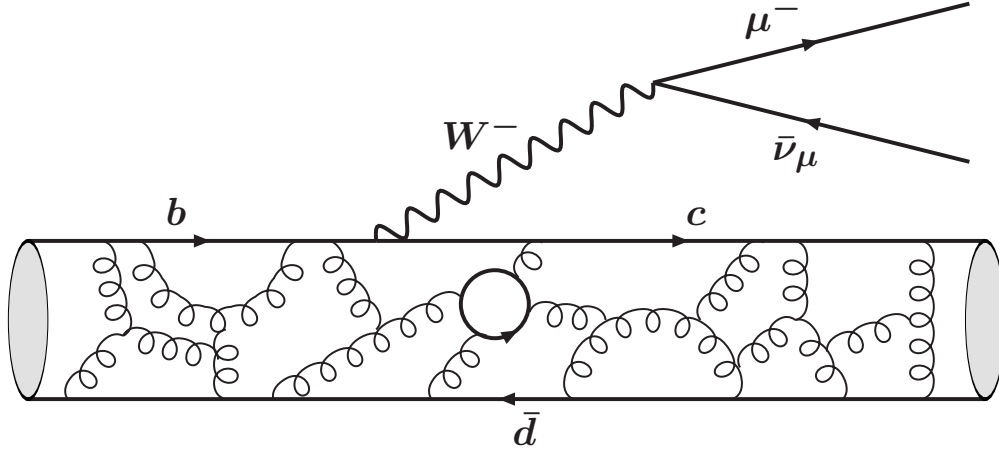
Figure 2.3: Sample semileptonic decay $\bar{B}^0 \rightarrow D^{*+}\mu^-\bar{\nu}_\mu$.

that $f_\pi = f(m_\pi^2)$). These functions can be determined from experiment, and can be used to verify QCD predictions obtained from various theoretical models.

2.2   Semileptonic Decay

In the previous Section, we discussed the leptonic decay of mesons, where the complications due to the strong interaction are absent in the final state. This simplifies the theoretical treatment of these decays, allowing for meaningful calculations to be performed for leptonic decays. In this Section, we will discuss decays that include both leptons and hadrons in the final state. Semileptonic decays, as shown in Figure 2.3, allow us to determine the effects of the strong interaction on the weak decay of quarks.

As leptons are not affected by color forces, the effects of the strong interaction are limited to the hadronic current. As a result, the complicated QCD interactions between initial and final state quarks can be parametrized in terms of form factors. These form factors are functions of q^2, the square of the mass of the virtual W. By reducing the treatment of the hadronic current to a number of form factors which depend on q^2, theoretical estimates of semileptonic processes become more robust.

Another simplification of semileptonic decays occurs if the process involves heavy quarks. For $b \to c\ell\nu_\ell$ decays, reliable predictions can be made using Heavy Quark Effective Theory (HQET). This theory explores the behavior of QCD in the limit of infinite quark mass, as b and c quark masses are large compared to the light quarks u, d, and s. In the infinite mass limit, the heavy quark is isolated from the treatment of the light quarks in a hadronic system. This allows $b \to c$ transitions, such as $B \to D^{(*)}X$ decay, to be expressed in terms of a universal form factor $\xi(v \cdot v')$, known as the Isgur-Wise function [13]. This form factor depends on the four-velocities (not momenta, as the mass of the heavy quarks is dropped) of the initial (v) and final-state (v') heavy quarks. At present, this function must be determined experimentally, such as through a measurement of the $B \to D^*\ell\nu_\ell$ rate as a function of q^2.

Corrections to HQET due to non-infinite quark masses are typically small for $b \rightarrow c$ transitions. In Figure 2.4 we present the extreme kinematic conditions for the semileptonic decay of a B meson. At maximum q^2, the $D^{(*)}$ is produced at rest in the frame of the parent B meson, and the mass of the $\ell \nu_\ell$ system is greatest. In this situation, the $B \rightarrow D^{(*)}$ form factors are largest. If q^2 is minimized, the hadronic system containing the c quark has its largest possible momentum in the B rest frame. In this case, the $B \rightarrow D^{(*)}$ rate is expected to be minimized. From Table 2.1, we see that the change in the recoil energy of the hadronic system is small. As the assumptions of HQET mimic the actual physics in this case, HQET provides a good theoretical framework for reliable calculations of the hadronic system in semileptonic B decay.

q^2 (GeV^2)	γ_{D^*}
$q^2_{min} \approx 0$	1.50
m^2_π	1.50
m^2_K	1.49
m^2_D	1.34
$m^2_{D^*}$	1.31
$q^2_{max} \approx 10.7$	1.00

Table 2.1: Relativistic boost factor $\gamma = (M^2_B + m^2_{D^*} - q^2)/(2M_B \cdot m_{D*})$ of the D^*, computed in the B rest frame, for $B \rightarrow D^* \ell \bar{\nu}_\ell$ transitions as a function of q^2.
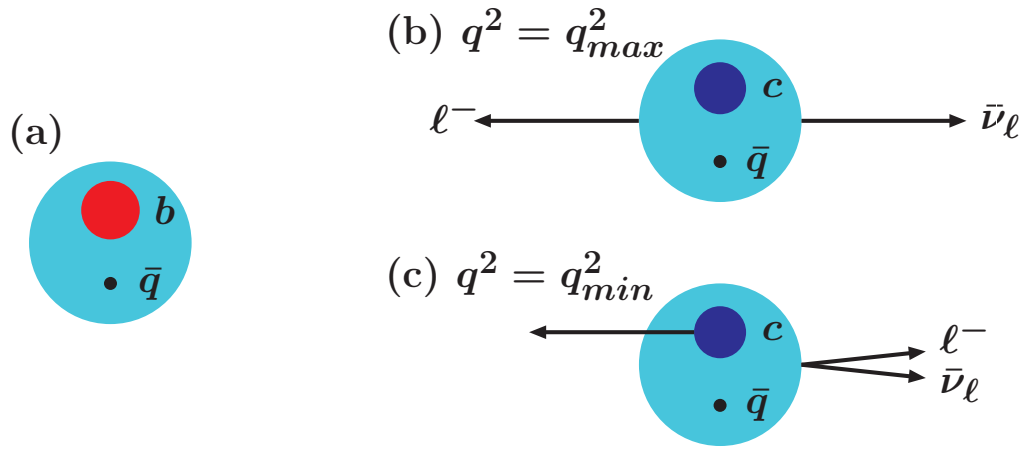
Figure 2.4: Kinematic extremes for $b \to c\ell^-\bar{\nu}_\ell$ decay (Figure taken from Reference [14]). In (a), the b quark in the $(b\bar{q})$ meson decays in its rest frame. In (b), the c quark is produced at rest relative to the parent b, and the $\ell\bar{\nu}_\ell$ pair are emitted back to back. This maximizes q^2. In (c), which depicts the minimum q^2 configuration, the c quark is produced with maximum momentum, and $\ell\bar{\nu}_\ell$ are nearly collinear in the b rest frame.

2.3   Hadronic Decay

If we consider the decay of the B meson, the strong interactions between quarks must be handled with some care. We have seen that in the case of leptonic decay, such as $B^+ \to \tau \nu_\tau$, QCD effects can be summarized by a decay constant. In the case of semileptonic decays of the B meson, such as $B^0 \to X \ell^+ \nu_\ell$, complicated effects from strong interactions can be parameterized by form factors, which are functions of the square of the mass of the $\ell \nu_\ell$ system. Assuming the hadronic system X contains a heavy c quark further simplifies calculations, paving the way for meaningful studies of these decays. However, the vast majority of B decays proceed without producing a lepton in the final state. We must boldly confront the complexities of the strong interaction in these decays in order to gain the most insight out of B physics.

Hadronic (or non-leptonic) decays of the B still involve the weak decay of the b quark ($b \to cW^*$), but in this case the virtual W creates a quark-antiquark pair. Consequently, the final state of these B decays is composed entirely of quarks. In this case, all of the final state particles interact strongly with each other, and it is very difficult to isolate and understand QCD effects. See, for example, Figure 2.5.
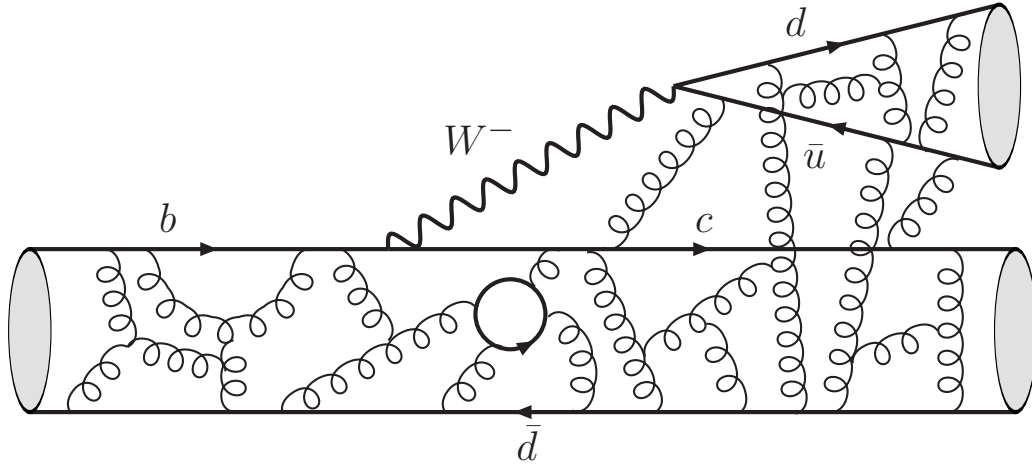
Figure 2.5: Sample hadronic decay $\bar{B}^0 \to D^+\pi^-$. Note that in this process, all final state quarks can interact with each other.

As it is difficult to make meaningful theoretical predictions which involve the strong interaction, it might be tempting to ignore these processes. It is therefore useful to include some benefits associated with hadronic decay processes. First, hadronic decays can be fully reconstructed with relative ease, as all daughter particles leave a detectable signature. In the previous classes of B decay, the neutrino escapes detection, and so part of the event is missing in reconstruction. Although this is not a fatal problem, the ability to reconstruct a B meson can increase the precision of a measurement. Second, hadronic decays account for roughly three-fourths of all B meson decays. The sum total of hadronic decays are a combination of multiple distinctive processes. This provides a laboratory to test many interesting physics processes (one such example, CP violation, will be discussed later). One other obvious reason is that our goal as physicists is to

test the Standard Model of particle physics. The effects of non-Standard Model physical processes might be missed if we do not have a good understanding of the strong interaction. For this reason, we should be thankful that there are many hadronic B decays!

Although there are several advantages to studying hadronic decays, there are some significant complications that must be addressed. In the previous Sections, we were able to break the decay of the B into parts: a leptonic current and a hadronic process that could be described using form factors or decay constants. For hadronic decays, the quarks produced from the virtual W interact with each other, but they also "see" the strong charge of the remaining quarks from B decay. If any meaningful conclusions can be drawn from these decays, we need to circumvent these complications or find a way to deal with them.

In this thesis, I study two hadronic decay modes of the B^0 meson, $\bar{B}^0 \to D^{*+}\omega\pi^-$ and $B^0 \to J/\psi \, K_L$. My analysis of $\bar{B}^0 \to D^{*+}\omega\pi^-$ decay provides a good laboratory to test the factorization hypothesis, which simplifies the complexities of QCD interactions. These conclusions help strengthen a model that is used to make predictions involving many different hadronic decays. Following this work, I will focus on the study of CP violation in the $B^0 \to J/\psi \, K_L$ system, which manages to bypass many of the complications of the strong interaction.

Chapter 3

Factorization

Within the framework of the Standard Model, hadronic weak decays of the B meson are dominated by the $b \to cW^*$ transition, where quarks are produced in the decay of the virtual W (see Figure 2.5). QCD interactions between final state quarks can be separated into two categories:

1. Short distance effects due to hard (high-momentum) gluon exchange between quarks. These effects can be accounted for, down to a cutoff scale μ typical for the interaction, using perturbative methods and renormalization group techniques [15].

2. Long range effects due to soft gluon exchange below the scale μ. These exchanges account for the binding of quarks into hadrons.

We assume that the two scales can be separated [16]. This leads to the effective Hamiltonian [17] (where we neglect penguin contributions)

$$H_{eff}(b \to c\bar{u}d) = \frac{G}{\sqrt{2}} V_{cb} V_{ud}^* \left[c_1(\mu)(\bar{d}u)(\bar{c}b) + c_2(\mu)(\bar{c}u)(\bar{d}b) \right] \tag{3.1}$$

for $b \to cW^*$, with $W^* \to \bar{u}d$, where the Wilson coefficients $c_1(\mu)$ and $c_2(\mu)$ account for the hard-gluon effects in the interaction down to a scale $\mu = m_b$, and $(\bar{u}d)$ represents the $V - A$ color-singlet current $\bar{u}\gamma_\nu(1-\gamma_5)d$. The long range QCD effects, described by form factors and decay constants, need to be related in some way to the four-quark operators $(\bar{d}u)(\bar{c}b)$ and $(\bar{c}u)(\bar{d}b)$.

It has been proposed that the long range QCD effects can be factorized for selected hadronic decays, which dramatically simplifies theoretical calculations. In this Chapter, I will present an overview of this hypothesis.

3.1 Naïve Factorization

The motivation for factorization was originally presented by Bjorken [18]. As an example, let us consider $\bar{B}^0 \to D^+\pi^-$ decay. The $\bar{u}d$ pair which forms the π^- is produced as a color singlet state from the virtual W. In the rest frame of the parent $\bar{B}^0$, the $\bar{u}d \to \pi^-$ system is moving rapidly with respect to the remaining $c\bar{d}$ system (the $\bar{d}$ is the spectator antiquark from the $\bar{B}^0$). If the motion of the $\bar{u}d$ pair is "fast enough", these quarks could escape the interaction region without

influencing the hadronic system formed by the $c\bar{d}$ pair. Although this cannot be a valid description of the decay, as it ignores long range QCD interactions between quarks, it may be close enough to allow theoretical predictions to be reasonably accurate.

In the case of $\bar{B}^0 \to D^+\pi^-$, which proceeds primarily through the color-favored spectator diagram (Figure 2.5), the decay amplitude can be factorized into a product of two hadronic currents [19]:

$$A(B^0 \to D^+\pi^-) = \frac{G}{\sqrt{2}}V_{cb}V_{ud}^* \cdot a_1 \langle \pi^-|(\bar{d}u)|0\rangle \langle D^+|(\bar{c}b)|\bar{B}^0\rangle. \qquad (3.2)$$

The $B \to D$ matrix element is identical to that encountered in semileptonic decay, and therefore this component can be expressed in terms of the $B \to D$ form factor. The creation of a pion from vacuum can be described in terms of the pion decay constant f_π (see Equation 2.2). The coefficient a_1 describes the physics necessary to make Equation 3.2 exact. It is worth noting that in the absence of QCD effects, $a_1 = 1$. QCD corrections modify the value of a_1, which we will discuss below.

Let us take a moment to examine the behavior of the $W^* \to \bar{u}d \to \pi^-$ transition. In the rest frame of the parent B, the fast moving $\bar{u}d$ pair, created at a point from the virtual W decay, is composed of quarks moving with nearly equal velocities. These quarks will hadronize in the typical hadronization time $\tau_h \sim 1$ fm/c, multiplied by the boost factor $\gamma \sim 16.6$. As a result, the pion hadronization occurs at a distance far removed from the remaining quarks. Near the interaction

region, the $\bar{u}d$ pair behaves as a colorless point-like particle, and therefore should minimally interact with the $c\bar{d}$ system. In this case the assumptions made by factorization are very reasonable, and thus we would expect the $B^0 \rightarrow D^+\pi^-$ decay process to be dominated by factorizable contributions.

If we examine the effective Hamiltonian in Equation 3.1, we can separate weak hadronic B decays into three classes [20]:

1. Class I decays dominated by an external spectator Feynman diagram. These decays, such as $B^0 \rightarrow D^+\pi^-$, are color favored. In this case, the QCD coefficient a_1 can be expressed as

$$a_1 = c_1(\mu_f) + \zeta c_2(\mu_f) \tag{3.3}$$

where $\zeta \sim 1/N_c$ (N_c is the number of quark colors), and μ_f is the factorization point. At $\mu_f \sim m_b$, the calculated values for the Wilson coefficients are $c_1(m_b) = 1.12$ and $c_2(m_b) = -0.29$ [15], so we expect $a_1 \approx c_1$ for these decays.

2. Class II decays dominated by an internal spectator diagram. These decays are color suppressed, and the spectator antiquark hadronizes with a quark produced from virtual W decay. In decays such as $\bar{B}^0 \rightarrow D^0\pi^0$, the relevant QCD contribution is given by

$$a_2 = c_2(\mu_f) + \zeta c_1(\mu_f). \tag{3.4}$$

The suppression of c_1 relative to c_2 in this case makes factorization highly dependent on the value of μ_f and ζ.

3. Class III decays are the result of an interference between a_1 and a_2 amplitudes, such as in $B^- \to D^0 K^-$ decay.

We see that the naïve factorization model only applies in the case of Class I decays, as it requires quarks produced from the virtual W to be ignored by the remaining quarks. In Class II or III decays, this assumption does not hold. In these cases, factorization may still be on relatively stable theoretical footing provided the decay products of the B are sufficiently energetic. In any case, the simple motivation for factorization is expected to fail as the mass of the virtual W system increases. If we can no longer assume that the quarks from the W decay are fast moving relative to the remaining decay products, we would expect significant QCD interactions to be present.

3.1.1 Tests of naïve factorization

Obviously, if we are meant to take the factorization hypothesis seriously, some useful results must be obtained from experiment. In this Section, we will consider some tests of the naïve factorization hypothesis.

Our naïve factorization model is best suited for interactions with high momentum transfer (see Figure 2.4(c), and replace the $\ell\nu_\ell$ pair with $q\bar{q}'$) based on the idea of color transparency. As there is no clear boundary for this motivation, we can test predictions based on factorization as the mass of the virtual W decay products increases. One such test uses the ratios of various hadronic B decays.

If we return to the equation for the decay amplitude for $B^0 \to D^+\pi^-$, where we have assumed that factorization holds (Equation 3.2), we find that

$$
\begin{aligned}
A(B^0(p) \to D^+(p')\pi^-(q)) &= \frac{G}{\sqrt{2}}V_{cb}V_{ud}^* \cdot a_1\langle\pi^-(q)|(\bar{d}u)|0\rangle\langle D^+(p')|(\bar{c}b)|\bar{B}^0(p)\rangle \\
&= \frac{G}{\sqrt{2}}V_{cb}V_{ud}^* \cdot a_1(-if_\pi q_\mu) \\
&\quad \times (F_1(q^2)\left[(p+p')^\mu - \frac{m_B^2 - m_D^2}{q^2}q^\mu\right] \\
&\quad + F_0(q^2)\frac{m_B^2 - m_D^2}{q^2}q^\mu),
\end{aligned}
\tag{3.5}
$$

where the four-momentum of the pion $q = p+p'$. When we evaluate Equation 3.5 further, we find that the term proportional to $F_1(q^2)$ vanishes:

$$
A(B^0(p) \to D^+(p')\pi^-(q)) = -i\frac{G}{\sqrt{2}}V_{cb}V_{ud}^*a_1f_\pi(m_B^2 - m_D^2)F_0(m_\pi^2).
\tag{3.6}
$$

Semileptonic B decays give almost no information about the form factor $F_0(q^2)$, but fortunately we may determine $F_0(q^2)$ in the limit that the mass of the b and c quarks are infinite. We may express the form factor F_0 in terms of the Isgur-Wise function $\xi(v \cdot v')$ using HQET [21]. This method may be extended to other hadronic B decays, as the traditional form factors are all related to the Isgur-Wise

function in the infinite quark mass limit. As a result, by taking the ratio of various hadronic B decays, the QCD parameter a_1 in Equation 3.6 cancels and we are able to make several predictions.

Some predictions for Class I decays using the model discussed in Reference [22] include:

$$\frac{BF(\bar{B}^0 \to D^+\pi^-)}{BF(\bar{B}^0 \to D^{*+}\pi^-)} = 1.04 \quad [1.00 \pm 0.12]$$

$$\frac{BF(\bar{B}^0 \to D^+\rho^-)}{BF(\bar{B}^0 \to D^{*+}\rho^-)} = 0.88 \quad [1.13 \pm 0.24],$$

where the experimental values [8] are given in parentheses. Similarly, we may make predictions for decays where the meson produced by the virtual W differs in the two decay modes:

$$\frac{BF(\bar{B}^0 \to D^{*+}\pi^-)}{BF(\bar{B}^0 \to D^{*+}\rho^-)} = 0.88 \left(\frac{f_\pi}{f_\rho}\right)^2 = 0.34 \quad [0.40 \pm 0.07],$$

where the predictions are again in agreement with experimental results. In this case, we have taken the decay constants of the charged π and ρ mesons

$$f_\pi = 130.7 \pm 0.4 \text{ MeV} \quad \text{and} \quad f_\rho = 210 \pm 1 \text{ MeV},$$

where f_π is obtained from $\pi \to \mu^+ \nu_\mu$ decay, and f_ρ is calculated from $\tau^- \to \rho^- \nu_\tau$ decay [8]. Extending our treatment further, we find

$$
\begin{aligned}
\frac{BF(\bar{B}^0 \to D^{*+} a_1^-)}{BF(\bar{B}^0 \to D^{*+} \rho^-)} &= 1.20 \left(\frac{f_{a_1}}{f_\rho} \right)^2 \\
\frac{BF(\bar{B}^0 \to D^+ D_s^-)}{BF(\bar{B}^0 \to D^+ \pi^-)} &= 1.02 \left(\frac{f_{D_s}}{f_\pi} \right)^2 .
\end{aligned}
$$

If we combine these predictions with the experimentally-determined branching fractions found in Reference [8], we find

$$
f_{a_1} = (1.26 \pm 0.19) \cdot f_\rho = 260 \pm 40 \text{ MeV}
$$

$$
f_{D_s} = (1.69 \pm 0.33) \cdot f_\pi = 220 \pm 40 \text{ MeV},
$$

which agree with experimental results. This result is perhaps a bit of a surprise, as the D_s can no longer be considered "light" (it contains a heavy c quark), and so the assumption of color transparency breaks down. Nevertheless, we see that these predictions based on the naïve factorization model have been verified by experiment at the 10-20% level.

3.1.2 Factorization predictions for D^* polarization

For $B \to D^* X_V$ decay, where X_V is a vector meson, the factorization hypothesis implies the vector meson should be equivalent to the $\ell\nu$ pair from semileptonic

decay. Consequently, the polarization of the D^* produced in hadronic $B \to D^* X_V$ decay should be equal to the D^* polarization in semileptonic decay at $q^2 = m_{X_V}^2$. We can therefore use a precise measurement of the D^* polarization in hadronic $B \to D^* X_V$ decays to test the factorization hypothesis [23].

The polarization of the D^* is a measure of the fraction of longitudinally polarized D^* mesons produced in B meson decay,

$$\frac{\Gamma_L}{\Gamma} = \frac{|H_0|^2}{|H_0|^2 + |H_+|^2 + |H_-|^2}, \qquad (3.7)$$

where $H_{0,\pm}(q^2)$ represent the amplitudes for helicity $0, \pm1$. These amplitudes can be expressed in terms of the $B \to D^*$ form factors, and evaluated in the limit of infinite b quark mass using HQET. Longitudinal polarization is expected to dominate at low q^2 as the high-momentum D^* is recoiling against a nearly collinear $\ell\nu$ system. At maximal q^2 the D^* is produced at rest, making all polarization states equally likely.

In Figure 3.1 we present D^* polarization measurements for various $B^0 \to D^* X_V$ decays made by CLEO [24, 25], Belle [26] and BABAR [27], and compare them to predictions based on factorization and HQET, extrapolated from $\bar{B}^0 \to D^{*+} \ell^- \bar{\nu}$ form factor results [28]. We can see that, even as q^2 increases, there is good experimental agreement with theoretical expectations.
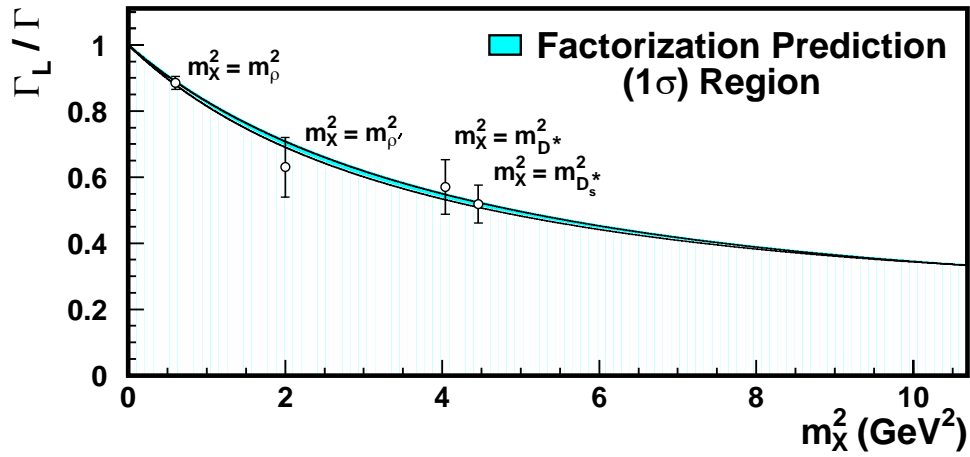
Figure 3.1: The fraction of longitudinal polarization as a function of m_X^2, where X is a vector meson. We show measurements (indicated by open circles) of $\bar{B}^0 \rightarrow D^{*+}\rho^-$ [24], $\bar{B}^0 \rightarrow D^{*+}\rho'^-(1450)$ [25], $\bar{B}^0 \rightarrow D^{*+}D^{*-}$ [26], and $\bar{B}^0 \rightarrow D^{*+}D_s^{*-}$ [27]. The shaded region represents the prediction ($\pm$ one standard deviation) based on factorization and HQET, extrapolated from the semileptonic $\bar{B}^0 \rightarrow D^{*+}\ell^-\bar{\nu}$ form factor results [28].

3.2 Test of Factorization using $\bar{B}^0 \to D^{*+}\omega\pi^-$

The factorization model is a theoretical "shortcut" that provides a means to determine the behavior of energetic weak hadronic decays of B and D mesons. This approach is reasonably successful for Class I decays of the B meson, as discussed in Sections 3.1.1 and 3.1.2. In these tests, we see that the primary motivation of color transparency seems to work very well in two-body $B \to D^{(*)}X$ decays, where X is a light meson.

However, it is known that factorization cannot truthfully describe strong interaction effects in weak decay because it ignores the long range interactions between quarks due to the exchange of low-momentum (soft) gluons. If we include factorization-violating terms in the effective Hamiltonian, we may rewrite Equation 3.2 in the following way:

$$
\begin{aligned}
\langle D\pi|H_{eff}|B\rangle &= \frac{G}{\sqrt{2}}V_{cb}V_{ud}^*(c_1(m_b) + \zeta c_2(m_b)) \\
&\times \langle \pi^-|\bar{d}\gamma^\mu(1-\gamma_5)u|0\rangle\langle D^+|\bar{c}\gamma_\mu(1-\gamma_5)b|\bar{B}^0\rangle + \cdots, \quad (3.8)
\end{aligned}
$$

where $\zeta \sim 1/3$. The $B \to D^{(*)}$ matrix element is determined from semileptonic decay and the formation of the pion can be described using hadronic τ decay, as mentioned in Section 2.1.1:

$$
\frac{d\Gamma(\tau \to \pi\nu_\tau)}{dm_X^2} = \frac{G^2|V_{ud}|^2}{32\pi^2 m_\tau^3}(m_\tau^2 - m_\pi^2)^2(m_\tau^2 + 2m_\pi^2)v_\pi(m_\pi^2). \quad (3.9)
$$

In Equation 3.8, the Wilson coefficients c_1 and c_2 are evaluated at the factorization scale $\mu = m_b$. In order for factorization to work as a viable theory, the scale dependence of the effective Hamiltonian must be eliminated. In order to cancel this scale dependence, we need to introduce "non-factorizable" contributions to the decay amplitude, which are represented by the ellipsis in Equation 3.8.

It is important to estimate (or even better, to explicitly determine) the effect of contributions beyond the naïve factorization approach. The experimental tests listed in Sections 3.1.1 and 3.1.2 are designed to search for a breakdown of factorization at different values of $q^2 = m_X^2$ by evaluating several two-body B decays.

If we examine hadronic τ decay in order to determine the behavior of the $W^* \to X$ system, the $v_X(m_X^2)$ term in Equation 3.9 (where $X = \pi$) holds even if X is composed of more than one final state particle. As a result, we may take X to be a multi-body final state. The benefit of this approach is that the factorization hypothesis can be tested over a broad q^2 range, rather than at discrete points determined by meson masses. In this case, the factorization prediction becomes [29]

$$\frac{d\Gamma(B \to D^{(*)}X)/dm_X^2}{d\Gamma(B \to D^{(*)}\ell\bar{\nu}_\ell)/dm_X^2} = 3\pi \left(c_1(m_b) + \zeta c_2(m_b)\right) v_X(m_X^2)(1 + \delta_{NF}) \qquad (3.10)$$

for $B \to D^{(*)}X$ decays. Non-factorizable contributions are contained in the parameter δ_{NF}. Before proceeding further, it is useful to spend some time discussing the expected behavior of δ_{NF}.

3.2.1 δ_{NF} in the $1/N_c$ expansion

As factorization ignores the color of the quarks produced by the virtual W, it is instructive to rewrite the Hamiltonian in a way that restores this dependence. In this case, the QCD coefficients a_1 and a_2 for the decay amplitude from naïve factorization are replaced as follows:

$$
\begin{aligned}
a_1 \to a_1^{eff} &= \left(c_1(\mu) + \frac{c_2(\mu)}{N_c} \right) [1 + \epsilon_1(\mu)] + c_2(\mu)\epsilon_8(\mu) \\
a_2 \to a_2^{eff} &= \left(c_2(\mu) + \frac{c_1(\mu)}{N_c} \right) [1 + \epsilon_1(\mu)] + c_1(\mu)\epsilon_8(\mu).
\end{aligned}
\tag{3.11}
$$

The hadronic parameters $\epsilon_i(\mu)$ parametrize the non-factorizable contributions to the hadronic matrix elements. The subscript refers to the color structure of the operators in the hadronic matrix elements. These functions depend on the particles involved, and hence their nature is process dependent. Without loss of generality, we may define the $\epsilon_i(\mu)$ functions such that the scale dependence of a_i^{eff} is removed. As a result,

$$
A(\bar{B} \to D^{(*)}X) = \frac{G}{\sqrt{2}} V_{cb}V_{ij}^* \cdot a_1^{eff} \langle X|(\bar{q}_i q_j)|0\rangle \langle D^{(*)}|(\bar{c}b)|\bar{B}\rangle.
\tag{3.12}
$$

becomes an exact expression for the amplitude of Class I $\bar{B} \to D^{(*)+}X$ decay, where a_1^{eff} must be determined from experiment.

In order to place factorization on a more stable theoretical foundation, it is useful to determine the nature of the hadronic parameters $\epsilon_i(\mu)$, and hence the coefficients a_i^{eff}. One approach has been to expand the functions $\epsilon_i(\mu)$ in powers of $1/N_c$, where N_c is the number of colors. Physically, $N_c = 3$, and so higher order terms are not strongly suppressed, but it is useful to examine the behavior of the factorization model when we set $N_c \to \infty$.

If we consider the large-N_c limit in QCD [30], we discover that [31]

$$\epsilon_1 = O(1/N_c^2) \quad \text{and} \quad \epsilon_8 = O(1/N_c), \tag{3.13}$$

independent of the scale μ where factorization is assumed to hold. As a result, $|\epsilon_1|$ contributions vanish, while terms that include ϵ_8 can be more significant.

Similarly, we may determine the behavior of the Wilson coefficients at the factorization scale. For $\mu = m_b$, we find

$$c_1(m_b) = 1 + O(1/N_c^2) \quad \text{and} \quad c_2(m_b) = O(1/N_c). \tag{3.14}$$

To lowest order, this implies $a_1^{eff} \approx 1$ and $a_2^{eff} \approx c_2(m_b) + \zeta c_1(m_b)$ in B decays, where $\zeta \equiv 1/N_c + \epsilon_8(m_b)$. As $\epsilon_8(m_b) = O(1/N_c)$, in principle the value of ζ should be considered as an unknown parameter. However, the success of factorization for $B \to D\pi$ transitions implies that $\zeta \approx 1/3$, and it is believed that the process

dependence of ζ is small: $\Delta\zeta \sim \Delta E/m_b$, where ΔE is the difference in the energy release in different B decay channels (and is smaller than 1 GeV for $W^* \to$ light meson) [31].

At the lowest order in the $1/N_c$ expansion, the results are in good agreement with naïve factorization, with $a_1 = c_1 + c_2/N_c$ replaced by $a_1^{eff} \approx 1$, and $a_2 = c_2 + c_1/N_c$ replaced by $a_2^{eff} \approx c_2 + \zeta c_1$, with $\zeta \approx 1/N_c$. Higher order terms in the $1/N_c$ expansion account for corrections to naïve factorization. As the corrections to factorization can be summarized by the variation in ζ for different B decays, the $1/N_c$ expansion predicts that corrections to factorization should remain small as the mass of the light meson system increases [31, 32].

3.2.2 δ_{NF} in perturbative QCD

In the previous Section, we saw that factorization is justified in the limit of a large number of colors. Unfortunately, this approach oversimplifies QCD, as $N_c \to \infty$ is a far cry from $N_c = 3$ in the physical world. Additionally, as factorization assumes that no gluons are exchanged below $\mu \sim m_b$, final state interactions are forbidden in the naïve framework.

It would be nice if factorization could be strengthened with more rigorous treatment of hadronic B decay. In this fashion, we can take advantage of the heavy mass of the b quark and treat the interaction perturbatively [33]. Let us
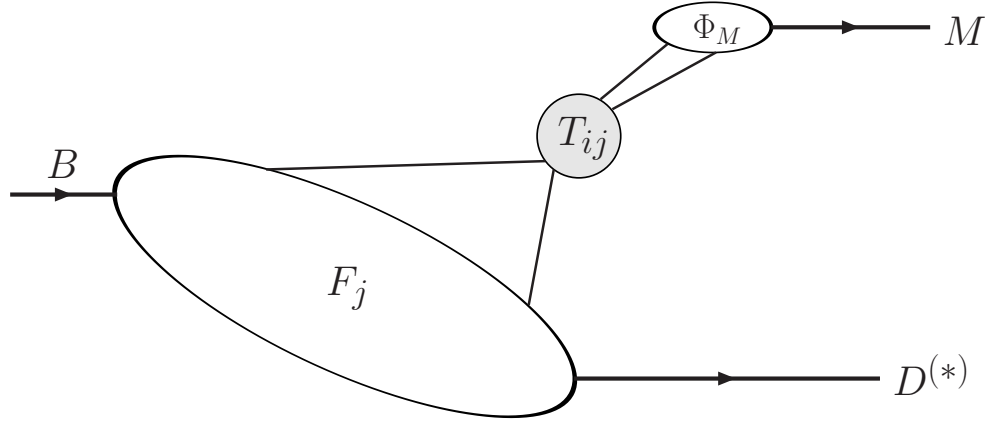
Figure 3.2: Graphical representation of Equation 3.15. Figure taken from Reference [33].

consider the weak decay $B \to D^{(*)}X$, where X is a "light" meson taken to have mass near the QCD scale, $\Lambda_{QCD} \ll m_b$. At the lowest order in Λ_{QCD}/m_b, we may express the transition matrix element of an operator $\mathcal{O}_i$ in the weak Hamiltonian as follows:

$$\langle D^{(*)}X|\mathcal{O}_i|\bar{B}\rangle = \Sigma_j F_j(m_X^2) \int_0^1 du T_{ij}(u)\Phi_X(u), \qquad (3.15)$$

where $F_j(m_X^2)$ denotes the $B \to D^{(*)}$ form factors, and $\Phi_X(u)$ describes the behavior of the quark-antiquark state forming the final-state X meson with momentum fraction u. These quantities summarize the non-perturbative contributions to the interaction, while the hard-scattering function $T_{ij}(u)$ can be calculated perturbatively. Equation 3.15 is represented graphically in Figure 3.2.

Any hard gluon exchange is accompanied by one power of α_s. The α_s^0-order contribution to $T_{ij}(u)$ is independent of u and as a result Equation 3.15 reproduces naïve factorization at leading order. Corrections to factorization are introduced through gluon interactions. Single-gluon exchange diagrams are shown in Figures 3.3 and 3.4. The diagrams in Figure 3.3 do not need to be calculated, as they are already contained in the calculation of the $B \to D^{(*)}$ form factors and the X decay constant. The diagrams in Figure 3.4 describe the "non-factorizable" contributions to $B \to D^{(*)}X$ decay. These diagrams are contained in $T_{ij}(u)$ and contribute at order α_s. Each diagram in Figure 3.4 violates factorization if the gluons exchanged are soft. Complicating matters further, we find that each diagram is also infrared divergent. Fortunately, the divergences cancel in the sum of the diagrams. This is seen as a technical manifestation of Bjorken's argument for color transparency [18]. Hard gluons that interact with the quarks formed from the virtual W^* will affect the formation of the escaping meson. These "non-factorizable" contributions depend on the involved mesons.

This cancellation of soft gluon effects is only possible if the quark-antiquark pair is nearly collinear. If the quarks from the W^* are produced in a very asymmetric configuration, where one of the quarks carries most of the momentum of the X system, the argument for color transparency breaks down. The probability
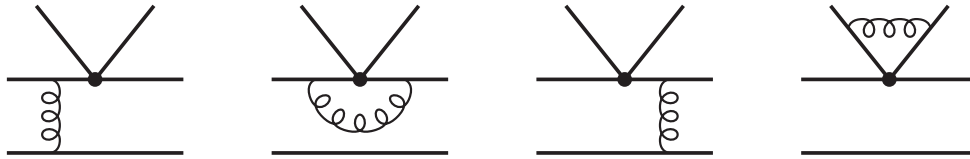
Figure 3.3: Single-gluon exchange diagrams that do not violate factorization. The weak decay of the b quark is represented by the black circle. Figure taken from Reference [33].
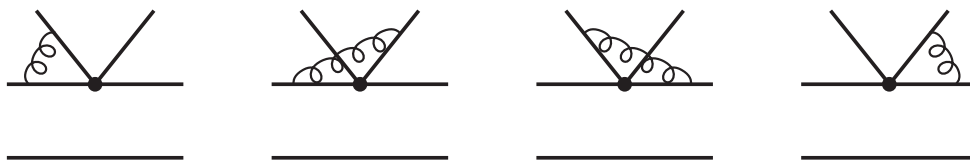
Figure 3.4: Lowest order factorization-violating diagrams. The weak decay of the b quark is represented by the black circle. Figure taken from Reference [33].

for a single X meson, such as a pion, to form in this manner is suppressed by factor of roughly $(\Lambda_{QCD}/m_b)^2$.

We note that gluon exchange diagrams involving the spectator quark, which contribute to the hard scattering term in Figure 3.2, will also violate factorization. However, if the gluon exchanged is hard, the large momentum transfered to the spectator quark is not consistent with the formation of the $D^{(*)}$ meson. In the event that the gluon is soft, the non-factorizable contributions to the decay amplitude are suppressed by a factor of (Λ_{QCD}/m_b) relative to the factorizable contribution.

The perturbative QCD approach reproduces factorization in the decay $B \to D^{(*)}X$ in the event that the quark-antiquark system hadronizes into an energetic X state. In this case, the quarks are tightly packed, and carry similar momenta. If these conditions are not met, the perturbative justification for factorization breaks down. Factorization-violating soft gluon exchanges between quarks become significant if the X system is asymmetric. This effect is suppressed in the formation of a light X meson, but as the mass of the X system (assumed to be of order Λ_{QCD}) becomes comparable to m_b, non-factorizable contributions are expected to increase. If the X system is no longer light relative to the b quark mass, the quarks from the W^* will be produced in an asymmetric state. In this case, soft

gluon effects are expected to become significant, and factorization will begin to break down.

3.2.3   Probing δ_{NF} with $\bar{B}^0 \rightarrow D^{*+}\omega\pi^-$ decay

In Equation 3.10 we introduced the parameter δ_{NF}, which describes all non-factorizable contributions to $B \rightarrow D^{(*)}X$ decay. In Sections 3.2.1 and 3.2.2 we found that the naïve factorization picture of weak B decays can be justified in different ways:

- The perturbative QCD picture of factorization expands the B decay amplitude in powers of $m_X/m_b \sim \Lambda_{QCD}/m_b$. As the b quark is heavy, non-factorizable contributions are suppressed for a light X system. As the mass of the X system increases, non-factorizable contributions to the decay amplitude become significant. For this reason, we expect corrections to factorization to grow with m_X/E_X, where E_X is the energy of the X system [29].

- Factorization in the large-N_c limit does not depend on the mass of the escaping X system. Expanding the B decay amplitude about the number of colors, we find that non-factorizable contributions are suppressed as we take $N_c \rightarrow \infty$. In this picture, we do not expect the accuracy of factorization predictions to decrease as m_X increases.

Factorization has already been tested on a variety of two-body $B \to D^{(*)}X$ decays. Some of these results have been accumulated in Sections 3.1.1 and 3.1.2. We see that the current experimental data agrees with factorization predictions at the 10-20% level.

Rather than testing factorization at discrete points in kinematic space, namely at $q^2 = m_\pi^2, m_\rho^2$, etc., we can use Equation 3.10 to test factorization over a broad kinematic range using a final state system X containing two or more light hadrons [29]. If we can assure ourselves that the decay of the virtual W is entirely responsible for the light meson system in the final state, then we can test factorization over a broad kinematic range. From Equation 3.9, we see that the differential decay rate for $B \to D^*(n\pi)$ can be anticipated using τ decay. CLEO has measured $v_X(m_X^2)$ for two- to four-pion final states [11, 12]. As the ρ dominates two-pion final states, it is useful to examine the three- or four-pion final states, which are not dominated by a single narrow resonance, in order to test factorization throughout the region accessible in τ decay.

By comparing results for $B \to D^*(n\pi)$ decay to predictions derived from factorization, we may be able to extract the nature of the non-factorizable corrections. As $m_X/E_X = 0.24$ at $m_X = m_{3\pi\pi^0}$ and increases to 0.70 at $m_x = m_\tau$, order m_X/E_X corrections should change significantly over the region made available

by τ decay. This would help determine the role that perturbative QCD plays in factorization.

In this thesis, I will examine the decay mode $\bar{B}^0 \to D^{*+}\omega\pi^-$, as suggested by Ligeti, Luke, and Wise [29]. These results will be compared to predictions using τ decay data, and will therefore be able to test factorization up to $m_{\omega\pi} = m_\tau$. This mode provides an excellent laboratory to test factorization:

- The $X = \omega\pi$ final state is not dominated by any narrow resonance. Consequently, there is no sharp falloff in the differential decay rate from $m_X = m_\omega + m_\pi$ through $m_X = m_\tau$. This serves as a good probe of order m_X/E_X corrections to factorization.

- $\bar{B}^0 \to D^{*+}\omega\pi^-$ decay is not expected to have large non-factorizable backgrounds. If factorization holds, this decay is expected to proceed as indicated in the Feynman diagram in Figure 3.5. As the ω has no charge, the pion must be a product of the virtual W decay. In order for the heavy ω ($m_\omega = 782.6$ MeV) to be produced along with the D^*, the $D^*\omega$ state must originate from the decay of a higher mass charm state, $C_{D^*\omega} \to D^*\omega$, produced in B decay. We can estimate the $B \to C_{D^*\omega}\pi$ decay rate by searching for $B \to C_{D^*\omega}\ell\nu_\ell$ and assuming factorization. This decay has not been seen, and the rate is expected to be small in most models [34]. Consequently,

we expect the decay to proceed as indicated in Figure 3.5 with minimal contamination from non-factorizable diagrams.

- The presence of the ω simplifies experimental complications associated with the reconstruction of $\bar{B}^0 \to D^{*+} \omega \pi^-$ decay. Many charged particles and photon signatures must be successfully reconstructed within the BABAR detector [35] in order to obtain a clear picture of the event. The large multiplicity associated with this decay raises the likelihood that random combinations of particles may be mistaken for a true signal ($\bar{B}^0 \to D^{*+} \omega \pi^-$) event. This possibility is reduced if we require a $\pi^+ \pi^- \pi^0$ combination to be consistent with the experimentally-determined ω mass.

- The branching fraction for $\bar{B}^0 \to D^{*+} \omega \pi^-$ is about 0.3%, which is quite large for B meson decay. The large number of $\tau \to \omega \pi \nu_\tau$ decays available result in a precise factorization prediction (see Figure 3.6), and so the ability to reconstruct a large number of $\bar{B}^0 \to D^{*+} \omega \pi^-$ decays will increase the precision of a test of factorization.

The $\bar{B}^0 \to D^{*+} \omega \pi^-$ decay was first studied by the CLEO collaboration using 9.7 million $B\bar{B}$ pairs produced at the $\Upsilon(4S)$ resonance at the Cornell Electron Storage Ring. They found $BF(\bar{B}^0 \to D^{*+} \omega \pi^-) = (0.29 \pm 0.03$ (stat) ± 0.04 (syst))% [25]. The plot of the differential decay rate is shown in Figure 3.6 using
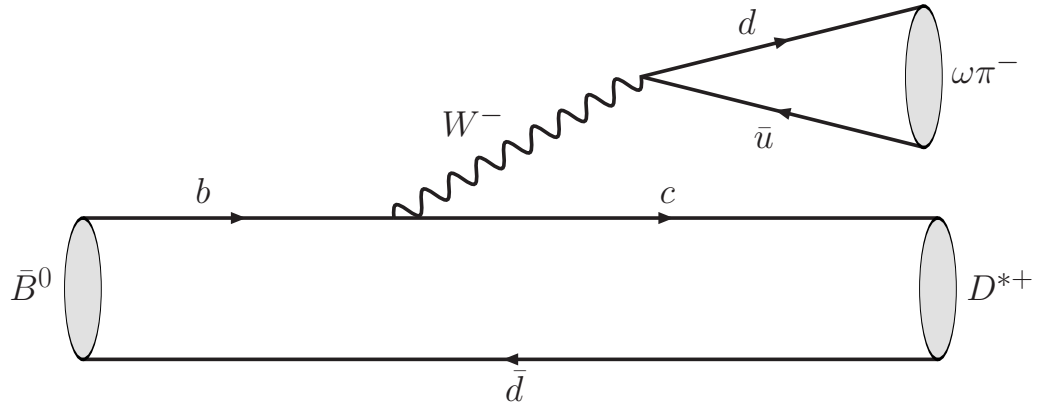
Figure 3.5: Feynman diagram for $\bar{B}^0 \rightarrow D^{*+}\omega\pi^-$ decay, according to the factorization hypothesis.

the CLEO data. Within experimental sensitivity, experimental results agree with

factorization predictions using $\tau \rightarrow \omega\pi\nu_\tau$ decay data.
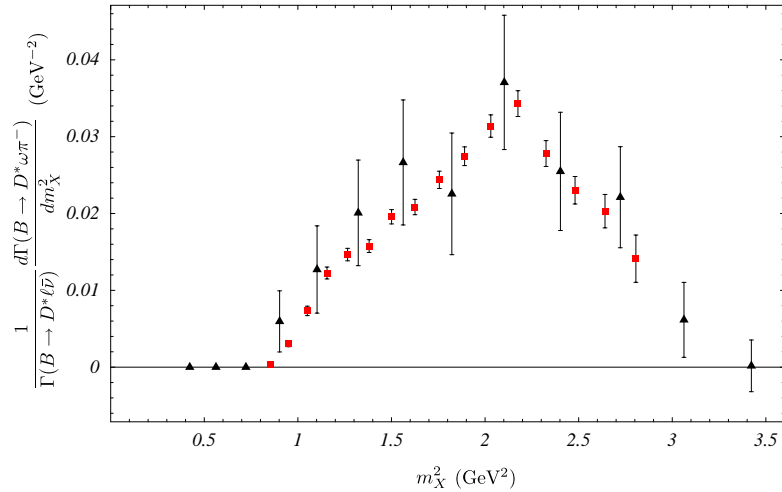
Figure 3.6: Spectrum of the invariant mass squared of the $\omega\pi$ system (m_X^2) in $\bar{B}^0 \rightarrow D^{*+}\omega\pi^-$. The black triangles are from CLEO data [25], and the red squares are theoretical predictions based on τ-decay data [12]. There is an additional 9% uncertainty in the B decay data from the overall normalization. Figure taken from Reference [29].

CLEO also studied the decay $\bar{B}^0 \to D^+ \omega \pi^-$ in Reference [25]. By measuring the polarization of the ω, they were able to determine that $\bar{B}^0 \to D^+ \omega \pi^-$ decay is dominated by $\bar{B}^0 \to D^+ \rho'(1450)^-$, followed by $\rho'(1450)^- \to \omega \pi^-$. Due to the presence of the vector D^*, it was not possible to verify that this is also the case for $\bar{B}^0 \to D^{*+} \omega \pi^-$ decay. However, if we assume that the $\rho'(1450)$ also dominates the $D^* \omega \pi$ final state, we may use factorization to predict the polarization of the D^*, as described in Section 3.1.2. For $\omega \pi$ masses consistent with the $\rho'(1450)$ (1.1 $\leq m_{\omega \pi} < 1.9$ GeV), CLEO measured found that $(63 \pm 9)\%$ of all D^* produced in $\bar{B}^0 \to D^{*+} \omega \pi^-$ decay were longitudinally polarized. This is consistent with expectations from factorization and HQET (see Figure 3.1).

The BABAR experiment has accumulated more than twenty times the number of $B\bar{B}$ mesons used in the initial CLEO experiment. We can therefore substantially improve the precision of the initial measurements. The increase in statistical precision is especially useful for large $\omega \pi$ mass, where perturbative QCD factorization predictions may be tested.

As a final note, we must not forget that in addition to the Feynman diagram presented in Figure 3.5, $\bar{B}^0 \to D^{*+} \omega \pi^-$ decay can also proceed as shown in Figure 3.7. In this case, the $D^* \omega \pi$ final state is produced through the color-suppressed decay $\bar{B}^0 \to D^{**0} \omega$, followed by $D^{**0} \to D^{*+} \pi^-$. As Figure 3.5 interprets $\bar{B}^0 \to D^{*+} \omega \pi^-$ as a Class I decay, factorization is well-motivated. If this
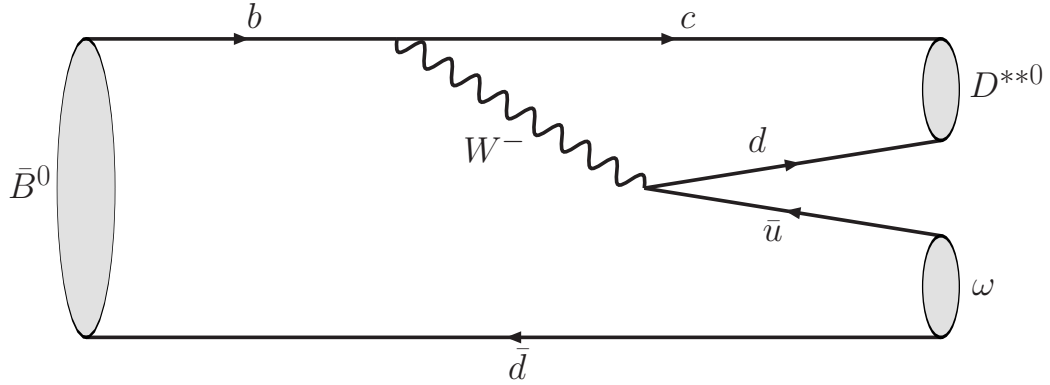
Figure 3.7: Feynman diagram for the color-suppressed $\bar{B}^0 \to D^{**0}\omega$, $D^{**0} \to D^{*+}\pi^-$ decay.

decay proceeds via Class II decay (Figure 3.7) at a significant rate, the factorization interpretation for the decay becomes less clear.

During the course of the analysis, we discovered an enhancement of events for $D^*\pi$ mass in the region of 2.5 GeV. These events could be the result of resonant $D^{**} \to D^*\pi$ decay. Although the impact on our final result is small (as would be expected for color-suppressed decay), it is important to keep this enhancement in mind.

Chapter 4

The BaBar Experiment

The primary focus of the BABAR experiment [36, 37] is to measure CP-violating asymmetries in the B meson system. This experiment makes use of the PEP-II asymmetric e^+e^- storage ring located at the Stanford Linear Accelerator Center (SLAC). A center of mass (CM) energy of 10.58 GeV is obtained by colliding electron and positron beams with lab energies equal to 9 and 3.1 GeV, respectively. The CM energy is equal to the mass of the $\Upsilon(4S)$ resonance, which decays almost exclusively into $B\bar{B}$ pairs. The asymmetric beam energies introduce a relative velocity along the beam direction (z) between the lab and CM frames, described by $\beta\gamma = 0.56$. This boost gives us the chance to determine the relative distance between the decay positions of B and $\bar{B}$ mesons. As the relative distance is related to the difference in decay time, $\Delta z \approx \gamma\beta c\Delta t$, we can extract time-dependent CP violating asymmetries from B decay data.

The BABAR and BELLE experiments [38] have been referred to as B factories due to the large volume of $\Upsilon(4S) \to B\bar{B}$ events produced by each experiment. At design luminosity, $\mathcal{L} = 3 \times 10^{33}$ cm^{-2} sec^{-1}, the BABAR experiment produces over 30 million $B\bar{B}$ pairs every 10^7 seconds[1]. The experiment has consistently run above design luminosity, resulting in 232 million $\Upsilon(4S) \to B\bar{B}$ decays collected between 1999 and 2004.

In this Chapter I will describe the BABAR detector and datasets used in physics analysis for this thesis. The detector is described in detail elsewhere [35], but it is useful to give a brief overview here, highlighting the features which facilitate the analysis of the $\bar{B}^0 \to D^{*+}\omega\pi^-$ and $B^0 \to J/\psi\ K_L$ decay modes. I will also briefly discuss the simulated data used by these analyses.

4.1   The BaBar Detector

Branching fractions for B meson decays are typically quite small. For example, the branching fraction for $\bar{B}^0 \to D^{*+}\omega\pi^-$, which is relatively large, is about 0.3%. This implies that the BABAR detector must be able to fully reconstruct a relatively small number of signal B decays in order to separate desired events from background. For a time-dependent analysis such as $B^0 \to J/\psi\ K_L$, it is also

---

[1]Experience teaches us that this is the typical operating period for an accelerator each year, where a year is 3×10^7 seconds.

necessary to determine the flavor of the other B in the event. These requirements place several strict demands on the detector:

- A large, uniform acceptance. This is especially important in the forward direction, as the CM frame is boosted relative to the lab frame.

- Excellent reconstruction efficiency for charged particles and photons down to low momentum.

- Very good position, momentum and energy resolution throughout the detector.

- Efficient particle identification, with a low rate of misidentification.

- Low levels of detector noise.

- Ability to operate reliably in a high radiation environment. This requires the detector components to be able to withstand significant doses of radiation as well as perform design tasks in high-background conditions.

In the following sections I will describe the various components of the BABAR detector, shown in Figures 4.1 (cross section along the beam axis) and 4.2 (cross section perpendicular to the beam axis). The description of each subsystem will be motivated by the detector demands listed above. Most of the detector falls within a 1.5 T magnetic field, which causes the charged particles to travel in
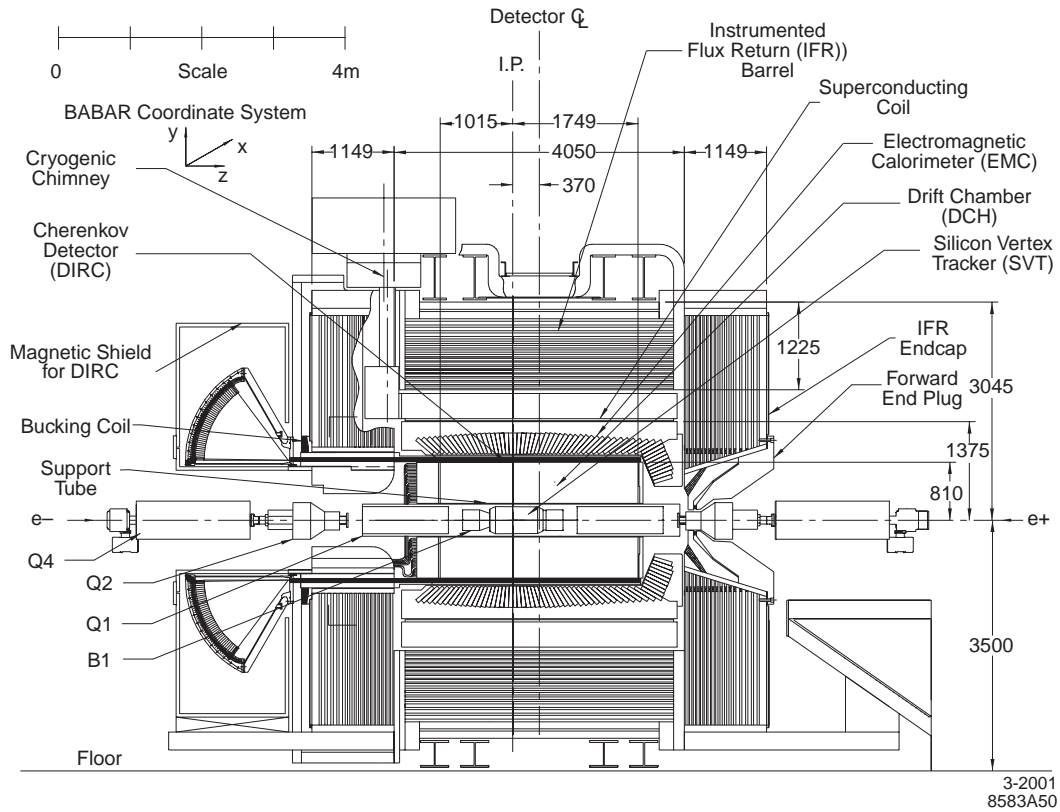
Figure 4.1: A cross section of the BABAR detector viewed parallel to the beam axis. Figure obtained from Reference [35].

curved paths within the detector volume. As a result, the tracking system is able to reconstruct the momentum of charged particles with good resolution.

4.1.1 The Silicon Vertex Tracker

The Silicon Vertex Tracker (SVT) is essential for measurements involving time-dependent observables. Located as close as possible to the interaction region, it provides excellent position resolution on the decay vertex of B mesons. In addi-
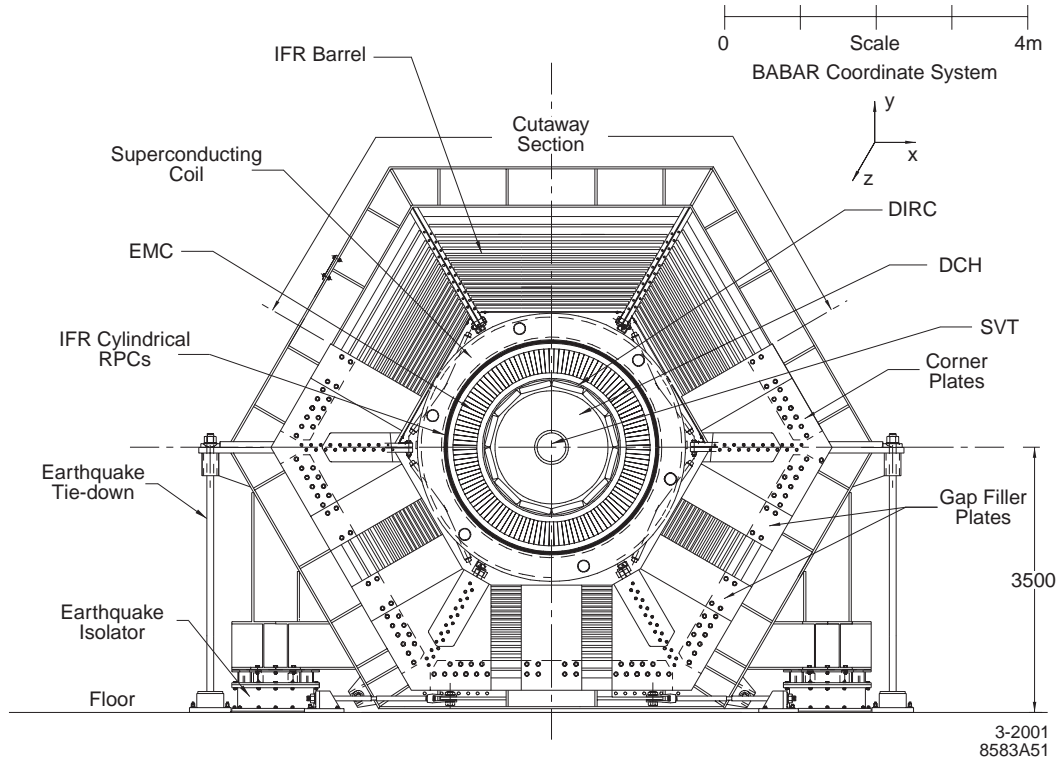
Figure 4.2: A cross section of the BABAR detector viewed perpendicular to the beam axis. Figure obtained from Reference [35].

tion, the SVT and Drift Chamber (DCH) make up the charged particle tracking system. In most cases, the SVT supplements the DCH measurements, but in the event that a charged particle does not have enough momentum to reach the DCH, its trajectory can still be determined using the information from the SVT.

The SVT is composed of five double-sided layers of reverse-biased silicon strip detectors. On one side the strips run parallel to the beam direction, and the strips on the other side of each sensor are perpendicular to the beam axis. Energy is deposited by a charged particle as it traverses the silicon which produces electron-

hole pairs in the silicon. These charges separate, due to the applied electric potential, and collect at electrodes. The resulting signal provides excellent spatial resolution, since the strip pitch varies from 50-110 μm in the inner three layers to 100-210 μm in layers 4 and 5. The spatial resolution for perpendicular tracks is 10-15 μm in the inner three layers, and about 40 μm in the outer layers.

In Figure 4.3 we present a cross section of the SVT perpendicular to the beam direction. The inner three layers, located as close as possible to the interaction region (32 to 54 mm from the beam axis), are essential for vertex measurements. The outer layers, due to their distance from the interaction region (91-144 mm from the beam axis), are better suited for pattern recognition and reconstruction of low momentum charged particles. Along the beam axis, the SVT allows the B decay vertex to be determined with a resolution of typically 40-80 μm, depending on the decay mode. This resolution is sufficient for the time dependent analysis of decays such as $B^0 \rightarrow J/\psi\ K_L$.

As the SVT is the innermost detector, its acceptance must be as large as possible without resulting in excess material near the interaction region. The active portion of the SVT extends to within $20(30)°$ of the beam axis in the lab frame in the forward (backward) direction, which amounts to a geometric acceptance of 90% of the solid angle in the CM system. In order to reduce the amount of material traversed by traveling particles, the SVT electronics are pushed
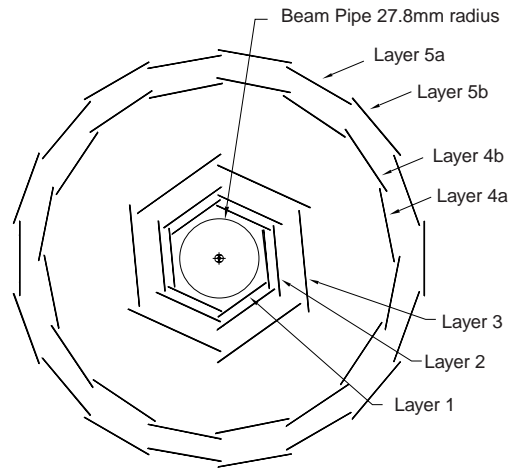
Figure 4.3: A cross section of the *BaBar* SVT viewed perpendicular to the beam axis. Layers 4 and 5 are divided into sublayers and placed at slightly different radii. Figure obtained from Reference [35].

to the ends of the silicon sensors. As a result, the SVT material impeding particles traversing the silicon is only a few percent of a radiation length.

4.1.2   The Drift Chamber

The *BaBar* Drift Chamber is the primary detector used to reconstruct charged particles with momenta above 120 MeV. The DCH is composed of 40 layers of small hexagonal cells filled with an 80:20 helium:isobutane mixture. Gold plated wires run the 3 m length of each cell. As the gas is primarily helium, the material in the path of the traveling particles is kept to a minimum. The wires and gas of the DCH comprise less than 0.2% of a radiation length, and the entire DCH

is made up of about 1% of a radiation length of material. This reduces multiple scattering within the detector and improves momentum resolution measurements.

As a charged particle travels through the DCH, it ionizes the gas within the relevant cells. The electrons released collect on high voltage sense wires in each chamber after a small "drift" time of about a few hundred nsec. In 24 of the 40 layers, the wires are placed at small angles (40-80 mrad) relative to the beam axis in order to obtain longitudinal position information. The position resolution for a given DCH layer is typically better than about 0.2 mm.

Position and angle measurements near the interaction point are primarily determined by the SVT, but the DCH dominates the measurement of transverse momentum (p_T). The typical resolution is about

$$\sigma_{p_T}/p_T \sim 0.0013 \cdot p_T + 0.0045,$$

where the transverse momentum is measured in GeV.

For low momentum charged particles, particle identification can be performed in the DCH and SVT by measuring the energy lost as particles travel through the detector volume. The mean rate of energy loss over distance ($\mathrm{d}E/\mathrm{d}x$) is a function of the speed of the charged particle ($\beta = v/c$) and the properties of the traversed material. In Figure 4.4 we present $\mathrm{d}E/\mathrm{d}x$ in the DCH as a function of charged particle momentum. For particles with enough transverse momentum

to completely traverse the DCH, the DIRC (the Detector of Internally Reflected

Cherenkov light) provides vital information regarding particle identity.
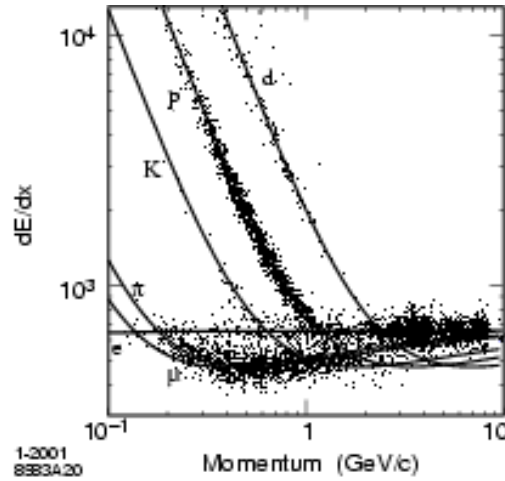
Figure 4.4: Measurement of $\mathrm{d}E/\mathrm{d}x$ in the DCH as a function of charged particle momentum. The curves show the Bethe-Bloch predictions for particles of different masses. Figure obtained from Reference [35].

4.1.3   The DIRC

In most cases, particle identity can be determined for low momentum particles

using $\mathrm{d}E/\mathrm{d}x$ information from the DCH (and SVT). However, as momentum

increases, it becomes increasingly difficult to properly identify some particles.

The BABAR DIRC uses Cherenkov radiation to identify charged particles. The

DIRC is composed of 144 synthetic silica bars (17 mm $\times$ 35 mm $\times$ 4900 mm) that

run parallel to the beam axis at a distance of 80 cm from the interaction point.

Particles that escape the DCH (p_T greater than about 250 MeV) will encounter

the DIRC before reaching the calorimeter. If the charged particle speed exceeds

the speed of light in the silica bars, the particle will emit Cherenkov radiation.

This radiation will be released in a cone around the traveling particle, described

by

$$\cos \theta_c = \frac{1}{n\beta}, \tag{4.1}$$

where $n = 1.474$ is the index of refraction of the DIRC bars. The Cherenkov

threshold for various charged particles is given in Table 4.1. We see from this Table

that the Cherenkov threshold for kaons is well below where $\mathrm{d}E/\mathrm{d}x$ measurements

in the DCH begin to have difficulty separating kaons from pions (about 700 MeV,

see Figure 4.4).

Particle	mass (MeV)	p_C (MeV)
μ	105.66	97.6
π	139.57	128.9
K	493.68	455.9
p	938.27	866.4

Table 4.1: Momentum threshold (p_C) for producing Cherenkov light for various charged particles found at BABAR.

After Cherenkov radiation is emitted, at least some of the photons are inter-

nally reflected by the DIRC bars. As a result, the Cherenkov light travels down

the length of the bars to an array of nearly 12,000 photomultiplier tubes (PMTs)

fixed to a standoff box located in the backward region of the BABAR detector. The

DIRC assembly is shown in Figure 4.5. As the photons reach the end of the silica,

they enter the standoff box which is filled with about 6000 l of purified water $(n \approx 1.346)$. As the Cherenkov angle θ_C is preserved by reflection within the bars, and a majority of the photons successfully traverse the silica-water barrier, the ring of photons observed by the PMTs can be used to identify the charged particle. In this way, the DIRC provides excellent $(\sim 4\sigma)$ π/K separation from the pion Cherenkov threshold up to particle momenta of about 4 GeV. This is extremely useful at BABAR, as pions and kaons dominate the final states for B and D meson decays.
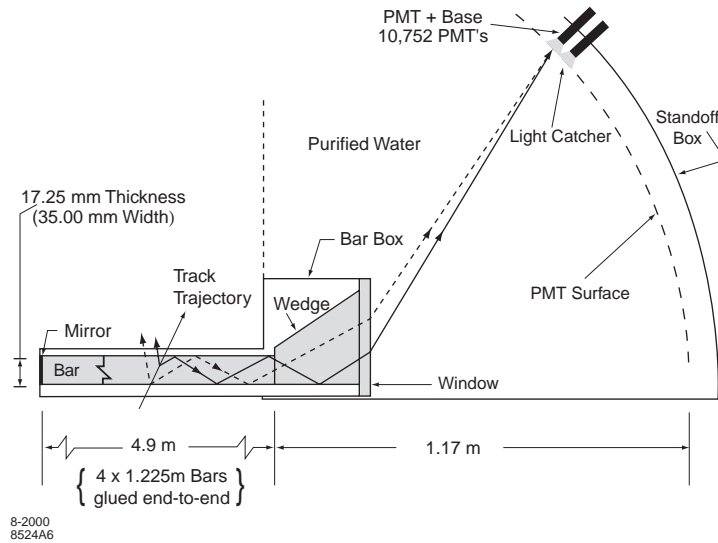
Figure 4.5: Diagram of the DIRC silica radiator bar and imaging region. Figure obtained from Reference [35].

4.1.4   The Electromagnetic Calorimeter

The Electromagnetic Calorimeter (EMC) measures electromagnetic showers with excellent energy and angular resolution from about 30 MeV to about 9 GeV. The measurement efficiency over this energy range is also excellent. (Energy leakage in the EMC reduces the precision of the measured cluster energy at the high energy limit by a few percent). The need to reconstruct $\pi^0 \to \gamma\gamma$ at energy scales appropriate for B decay drives the energy resolution requirements of the EMC. For particle energies common to *BABAR*, where the π^0 typically has energy below 2 GeV, π^0 mass resolution is dominated by the EMC energy resolution.

In order to meet the standards imposed by reconstruction demands at the $\Upsilon(4S)$, the EMC was built as a collection of 6580 thallium-doped cesium iodide crystals. These crystals have a high light yield, small Molière radius, and short radiation length. This allows for excellent energy and angular resolution while simultaneously containing electromagnetic showers in a compact volume. The energy and angular resolution for the *BABAR* EMC is given by

$$\frac{\sigma_E}{E} = \frac{2.32\%}{\sqrt[4]{E(\text{GeV})}} \oplus 1.85\%, \quad \text{and} \quad \sigma_\theta = \sigma_\phi = \frac{3.87}{\sqrt{E(\text{GeV})}} \text{ mrad.}$$

This results in a π^0 mass resolution of about 6.5 MeV for π^0 energies below 1 GeV.

The polar angle coverage in the lab extends from 15.8° from the beam axis in the forward end to 38° from the beam axis in the backward end. This amounts to a solid angle coverage of 90% in the CM system.

4.1.5 The Instrumented Flux Return

Each of the detector subsystems described above are located within a 1.5 T magnetic field. This field is necessary in order to accurately determine the momenta of charged particles as they move through the detector. The Instrumented Flux Return (IFR) uses the steel flux return of the magnet to identify muons and detect neutral hadrons (such as K_L).

The IFR is a set of layers of steel plates interspersed with instrumentation. The steel plates increase in thickness from 2 cm (in the innermost plates) to 10 cm for the outermost plates. This provides position resolution as good as a few mm in the inner region of the IFR, with increased stopping power as the plate thickness increases.

In Figure 4.6 we present an overview of the IFR. Until recently, the IFR instrumentation was made up of resistive plate chambers (RPCs), which detect particles via capacitive readout strips. Muon identification was made possible by matching a signal in the IFR with a charged particle track in the DCH (and SVT), and comparing the IFR material traversed by the candidate muon to expectations.

Neutral hadrons, such as K_L, were identified by clusters in the IFR not associated with any charged track.
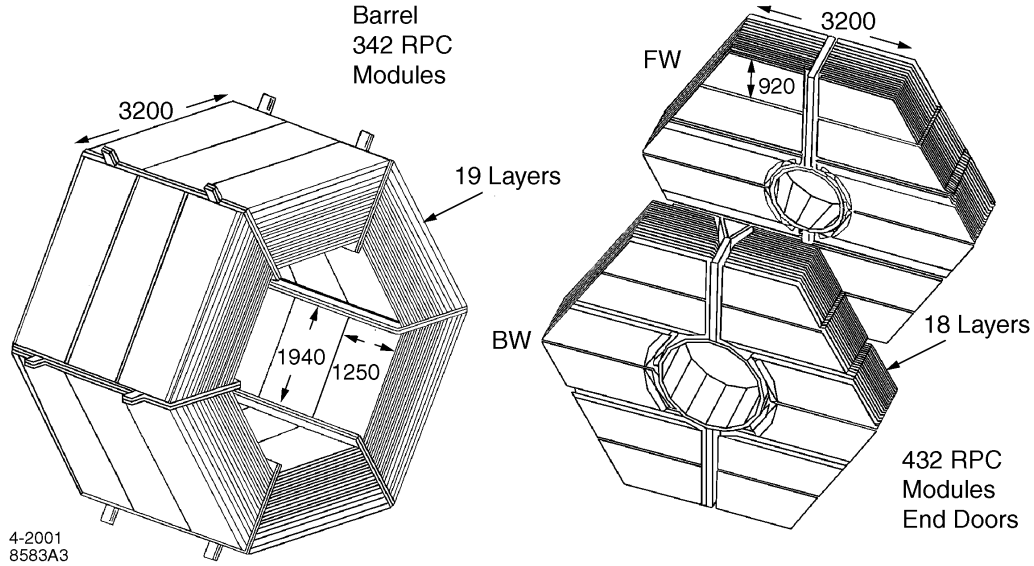
Figure 4.6: Overview of the IFR, including the barrel section as well as the forward (FW) and backward (BW) end doors. The dimensions on the Figure are given in mm. Figure obtained from Reference [35].

Over time, the quality of IFR measurements began to deteriorate as RPCs developed efficiency problems. This eventually led to the replacement of the RPCs in the IFR more than a year after the $B^0 \to J/\psi \; K_L$ analysis (as documented here) was completed. As the $\bar{B}^0 \to D^{*+}\omega\pi^-$ analysis does not require measurements from the IFR, neither analysis was significantly affected by detector modifications.

4.1.6 Monte Carlo event simulation

At B*A*B*AR*, Monte Carlo $B\bar{B}$ events are generated using `EvtGen` [39], and continuum $q\bar{q}$ (where $q = u$, d, s, or c) events are generated using `JetSet` [40]. The response of the B*A*B*AR* detector is simulated using the GEANT4 [41] program. In each of the analyses covered here, event reconstruction efficiency is determined from simulated Monte Carlo events. The event selection criteria is also optimized using simulated signal and background events.

Whenever possible, the response of the Monte Carlo events is checked against actual data. At times, it is necessary to make small corrections to results obtained from Monte Carlo event samples in order to account for differences between data and Monte Carlo. These include, but are not limited to, the following:

- The reconstruction of charged particles. Monte Carlo performance relative to data is checked using a variety of control samples.

- The reconstruction efficiency of photons and $\pi^0 \rightarrow \gamma\gamma$ events is studied using a control sample of π^0 events obtained from τ decay.

- Particle Identification efficiency differences between Monte Carlo and data, specifically focusing on the ability to separate kaons from pions, are determined using a control sample of $D^{*+} \rightarrow D^0\pi^+$, $D^0 \rightarrow K^-\pi^+$ events.

- Event selection efficiency. At times, data and Monte Carlo events respond differently to the event selection criteria. These differences vary as a function of the applied cut and the analysis in question.

In all cases, Monte Carlo event behavior is found to be very similar to data. Corrections are applied when necessary, and we assign a systematic uncertainty in order to account for our understanding of any discrepancies.

Chapter 5

Analysis of $\bar{B}^0 \to D^{*+}\omega\pi^-$ Decay

The analysis of $\bar{B}^0 \to D^{*+}\omega\pi^-$ events was performed using 232 million $\Upsilon(4S) \to$ $B\bar{B}$ decays accumulated between 1999 and 2004 with the BABAR detector located at SLAC, and has been published in Reference [42]. The documentation of this analysis proceeds as follows:

1. We first develop a set of event selection criteria in Section 5.1.

2. We discuss the observed signal yield and m_X^2 distribution in Section 5.2. In this Section, we also introduce a background subtraction using the mass sidebands of the ω. Kinematic distributions of interest, such as m_X^2 (where $X = \omega\pi$), are obtained using this subtraction.

3. We discuss our treatment of the $\bar{B}^0 \to D^{*+}\omega\pi^-$ reconstruction efficiency in Section 5.3.

4. Our results, and their associated systematic uncertainties, can be found in Section 5.4, and concluding remarks can be found in Section 5.5.

5.1 Event Selection

The criteria for selecting $\bar{B}^0 \to D^{*+}\omega\pi^-$ events were optimized based on studies of off-resonance data and simulated $B\bar{B}$ and continuum events. Whenever we impose constraints on the event selection, the cut value chosen maximizes $S^2/(S+B)$, where S represents the number of reconstructed signal $\bar{B}^0 \to D^{*+}\omega\pi^-$ events and B describes the expected number of background events.

5.1.1 Charged particle and π^0 selection

We form charged particle candidates from signatures in the SVT and DCH. We place the following requirements on these candidates:

- Charged particle candidates must have lab momentum below 10 GeV, and transverse momentum (p_T) above 100 MeV.

- The charged particle candidate must come from the interaction region. In order to be assured that this happens, we require that the reconstructed track passes within 1.5 cm of the interaction point in the plane perpendicular to the beam axis, and within 10 cm along the beam axis.

- The charged particle candidate is required to leave a signature in at least 12 DCH layers.

- We relax these requirements in the case of the pion from $D^{*\pm} \to D^0\pi^\pm$ decay. At B$_A$B$_{AR}$ energies, this pion often has very low momentum (typically below a few hundred MeV in the lab frame). In order to improve reconstruction efficiency, we drop the minimal p_T and DCH hit requirements for the soft pion.

Energy deposits measured by the EMC that are not associated with any charged particle track are considered photon candidates provided they have lab energies of at least 30 MeV, and their signature in the EMC is consistent with that of a photon. These candidate photons are used to form $\pi^0 \to \gamma\gamma$ candidates. We require the lab energy of the two-photon system to be at least 200 MeV, and $115 \leq m_{\gamma\gamma} \leq 150$ MeV. We determine the mass of the candidate π^0 by assuming the photons originate from the primary vertex. We then constrain the mass of the π^0 candidate to the nominal value (135 MeV) [8].

For each event, we take charged particle and π^0 candidates and attempt to build the desired $\bar{B}^0 \to D^{*+}\omega\pi^-$ decay. We enumerate the reconstruction requirements below, which include requirements on the B and intermediate $D^{(*)}$ and ω

meson reconstruction, as well as additional criteria to reject backgrounds from continuum $q\bar{q}$ (where $q = u$, d, s, or c) events.

5.1.2 ω reconstruction

We reconstruct $\omega \to \pi\pi\pi^0$ candidates from a pair of oppositely charged tracks, assumed to be a $\pi^+\pi^-$ pair, and a π^0 candidate. The invariant mass of the $\pi^+\pi^-\pi^0$ system is required to fall within 70 MeV of the nominal ω mass (782.6 MeV) [8]. This requirement is quite loose, as the natural width of the ω is $\Gamma = 8.5$ MeV, and the experimental resolution is 5.6 MeV. The choice of a wide mass window for the omega will become useful later, as the ω mass sidebands will be used extensively in this analysis. Throughout this analysis, we label events as "signal" provided the 3π mass lies within 20 MeV of the nominal ω mass. Events in which the ω candidate satisfies $35 \le |m_{\pi\pi\pi^0} - m_\omega^{PDG}| < 70$ MeV, where m_ω^{PDG} is the nominal ω mass, are referred to as "sideband".

In order to reduce the number of false ω candidates formed from random combinations of pions, we impose one additional requirement on ω reconstruction that is motivated by ω decay dynamics. We first define Dalitz plot [43] coordinate axes

$$X = \frac{3T_0}{Q} - 1, \quad \text{and} \quad Y = \sqrt{3}\left(\frac{T_+ - T_-}{Q}\right),$$

where $T_{\pm,0}$ are the kinetic energies of the pions in the ω rest frame, and $Q \equiv T_+ + T_- + T_0$. We then define the normalized distance from the center of the Dalitz plot,

$$R \equiv \sqrt{\frac{X^2 + Y^2}{X_b^2 + Y_b^2}}, \tag{5.1}$$

where X_b and Y_b are the location of the intersection between the line passing through $(0,0)$ and (X, Y) and the kinematic boundary of the Dalitz plot. Since the Dalitz plot density peaks at $R = 0$ [44], we require $R < 0.85$. This requirement is 93% efficient for signal $\bar{B}^0 \to D^{*+}\omega\pi^-$ events, and rejects 25% of the combinatoric background.

5.1.3 $D^{(*)}$ reconstruction

We reconstruct $D^{*+} \to D^0 \pi^+$ decay, where the D^0 decays into one of the following final states: $K^-\pi^+$, $K^-\pi^+\pi^0$, or $K^-\pi^+\pi^-\pi^+$. Charge conjugate modes are implied here and throughout this analysis.

We require the kaon candidate track used to reconstruct the D^0 meson to satisfy a set of particle identification criteria. Kaons are identified at BABAR using ionization energy loss $(\mathrm{d}E/\mathrm{d}x)$ measurements from the SVT and DCH and the observed pattern of Cherenkov radiation in the DIRC. The kaon identification efficiency depends on particle momentum and polar angle in the detector, and is

typically 93%. These requirements provide a rejection factor of order 10 against pions.

After identifying the kaon, we require the invariant mass of the $D^0 \rightarrow K^-\pi^+$, $K^-\pi^+\pi^-\pi^+$ candidates to fall within 15 MeV of the nominal D^0 mass (1865 MeV) [8], where the experimental resolution is about 6 MeV. In $D^0 \rightarrow K^-\pi^+\pi^0$ decay, we require the D^0 candidate mass to be within 25 MeV of the nominal value, as the presence of the π^0 degrades the resolution to about 10 MeV.

For $D^0 \rightarrow K^-\pi^+\pi^0$ candidates, we also exploit the known properties of this decay [45] to further reduce background. We calculate the square of the decay amplitude ($|A|^2$), and retain candidates if $|A|^2$ is greater than 2% of its maximum possible value. The signal efficiency of this requirement is 91%, and it rejects 20% of the $D^0 \rightarrow K^-\pi^+\pi^0$ combinatorial background. We construct $D^{*+} \rightarrow D^0\pi^+$ candidates by combining the D^0 candidate with an additional charged particle track that we assume is a pion. We require the measured mass difference $\Delta m \equiv m(D^{*+}) - m(D^0)$ to be between 143.4 and 147.4 MeV, where the resolution on this quantity is 0.3 MeV with some non-Gaussian behavior due to the reconstruction of the low momentum pion.

5.1.4 $\bar{B}^0$ reconstruction

We reconstruct $\bar{B}^0 \to D^{*+}\omega\pi^-$ candidates by combining ω and D^* candidates with an additional pion track. We impose the following requirements on the reconstruction of the B meson:

- We compute the energy-substituted mass for each $\bar{B}^0$ candidate:

$$m_{ES} \equiv \sqrt{E^{*2}_{\text{beam}} - \vec{p}^{*\,2}_{B}}, \qquad (5.2)$$

  where E^*_{beam} is the beam energy and $\vec{p}^{*\,2}_{B}$ represents the momentum of the $\bar{B}^0$ in the CM frame. This quantity peaks at m_{B^0} for signal events, with an experimental resolution of around 3 MeV. We retain candidates with m_{ES} above 5.2 GeV, where $m_{ES} > 5.27$ GeV defines the signal region. The m_{ES} sideband, where $5.2 < m_{ES} < 5.25$ GeV, is a useful sample for studies of background events.

- We also compute ΔE, defined as

$$\Delta E \equiv E^*_{\text{beam}} - E^*_B, \qquad (5.3)$$

  where E^*_B represents the energy of the $\bar{B}^0$ in the CM frame. This quantity peaks at zero for signal events. We select $D^0 \to K^-\pi^+, K^-\pi^+\pi^-\pi^+$ events with $-50 < \Delta E < 35$ MeV, and $D^0 \to K^-\pi^+\pi^0$ events with $-70 < \Delta E < 40$ MeV. The experimental resolution is about 25 MeV for $D^0 \to K^-\pi^+\pi^0$

events (20 MeV for the other modes), with non-Gaussian tails at negative

values due to energy leakage in the calorimeter.

We improve the quality of the B meson reconstruction by refitting the momenta of the daughters of the B, taking into account geometric constraints. We apply these constraints with the knowledge that the decay products of the B (as well as the D^*, D^0 and ω) must originate from a common point in space. The entire decay tree is fit simultaneously in order to account for any correlations between particles.

5.1.5 Continuum rejection criteria

We apply additional criteria to reject background from continuum events:

- The ratio of the 0th and 2nd Fox-Wolfram moments [46], R_2, is required to be below 0.5.

- We require $|\cos\theta_B| < 0.9$, where θ_B is the angle of the B with respect to the e^- beam in the CM frame. Signal $B\bar{B}$ events follow a $1 - x^2$ distribution, where $x = \cos\theta_B$, while background from continuum events tends to be flat in this variable.

- We also construct a Fisher discriminant using the quantities $\mathcal{L}_0 = \sum_i p_i^*$ and $\mathcal{L}_2 = \sum_i p_i^* \cos^2 \alpha_i^*$, where the sum is taken over all tracks and clusters not

used to reconstruct the B candidate, p_i^* is the magnitude of the momentum of particle i, and α_i^* is the angle between its momentum and the thrust axis of the B candidate in the CM frame. We calculate

$$\mathcal{F} = 0.5319 - 0.1790 \cdot \mathcal{L}_0 + 0.8465 \cdot \mathcal{L}_2 \tag{5.4}$$

and require $\mathcal{F} < 1.35$. The requirements on $\cos\theta_B$ and $\mathcal{F}$ are 95% efficient for signal and reject nearly 40% of the continuum background.

5.1.6 Cut-based corrections to the Monte Carlo

Each of the above selection requirements rejects some fraction of signal events in addition to background. Signal event loss is often minimal, but we must take care to ensure that this loss is well understood, as it influences the event reconstruction efficiency.

In order to adjust the Monte Carlo event sample to account for any discrepancies found relative to data, we compare the response of data with respect to Monte Carlo for each selection requirement. We then determine the relative difference between data and Monte Carlo, and assign a correction factor to the Monte Carlo:

$$\epsilon_{\text{Corr}} = \frac{\epsilon_{\text{Data}}}{\epsilon_{\text{MC}}}. \tag{5.5}$$

We summarize the individual corrections to the Monte Carlo in Table 5.1. We apply a correction factor to signal Monte Carlo events (ϵ_{Corr}) equal to 0.948 for $D^0 \to K\pi$, 0.922 for $D^0 \to K\pi\pi^0$, and 0.994 for $D^0 \to K3\pi$.

Variable	Correction ($\epsilon_{\text{Data}}/\epsilon_{\text{MC}}$)	Uncertainty (%)
m_ω	1.032	1.0
R	none	2.1
m_{D^0}	none	1.0
Rel. wgt.	0.927 ($K\pi\pi^0$)	3.3 ($K\pi\pi^0$)
Δm	none	none
$\theta_B + \mathcal{F}$	0.945	1.9
m_{ES}	none	none
ΔE	0.972 ($K\pi$), 1.020 ($K\pi\pi^0$), 1.019 ($K3\pi$)	2.0

Table 5.1: Summary of the cut-based corrections applied to the Monte Carlo. Unless otherwise specified, the correction applies to all D^0 decay modes.

5.1.7 Arbitration

Each of the criteria discussed above were applied in order to help preferentially select reconstructible $\bar{B}^0 \to D^{*+}\omega\pi^-$ decays instead of background. However, even after all our cuts are applied, we still expect that random combinations of charged and neutral particles will sneak into our event sample. On average, 1.7 signal candidates are present after all cuts in $\bar{B}^0 \to D^{*+}\omega\pi^-$ Monte Carlo events where at least one reconstructed event passes all of our analysis requirements.

In an attempt to reduce the impact these multiple candidates could have on our final event sample, we impose a χ^2 selector to choose a "best" candidate, based

on the difference between the measured and known values, and the experimental

resolution, of the D^0 mass and the mass difference Δm:

$$\chi^2 \equiv \left(\frac{m_{D^0} - m_{D^0}^{PDG}}{\sigma_{D^0}}\right)^2 + \left(\frac{\Delta(m_{D^0\pi} - m_{D^0}) - \Delta m_{D^*-D^0}^{PDG}}{\sigma_{\delta m}}\right)^2. \qquad (5.6)$$

We then select the candidate with the lowest χ^2. The mass of the ω is not included

in this calculation in order to avoid introducing a bias in the ω mass distribution,

as this distribution will be used extensively in later studies.

5.2 Observed Events

In the previous Section we outlined our event selection criteria. In this Section, we will elaborate on the m_{ES} and omega mass (m_ω) requirements and introduce a background subtraction using the mass sidebands of the ω.

5.2.1 m_{ES} distribution

In Figure 5.1, we present the m_{ES} distribution for reconstructed $\bar{B}^0 \to D^{*+}\omega\pi^-$ candidates in data. The m_{ES} distribution for candidates in the m_ω signal region are fit to the sum of a threshold background function [47] and a Gaussian centered at the B^0 mass. The 2.8 MeV Gaussian width is determined from studies of Monte Carlo simulated decays. We find 2461 ± 69 signal events in the Gaussian peak above $m_{ES} = 5.27$ GeV.

It is clear from the results of Figure 5.1 that we must view this yield with some degree of skepticism. The m_{ES} distribution for the m_ω sideband region demonstrates that there is a background component, which peaks at the B^0 mass, that is not well described by the threshold background function. Monte Carlo studies indicate that roughly one-third of this background is composed of signal $\bar{B}^0 \to D^{*+}\omega\pi^-$ decays where the $\omega \to \pi\pi\pi^0$ decay is misreconstructed, such as when one of the pions from the ω is lost, and a pion from the other B decay is
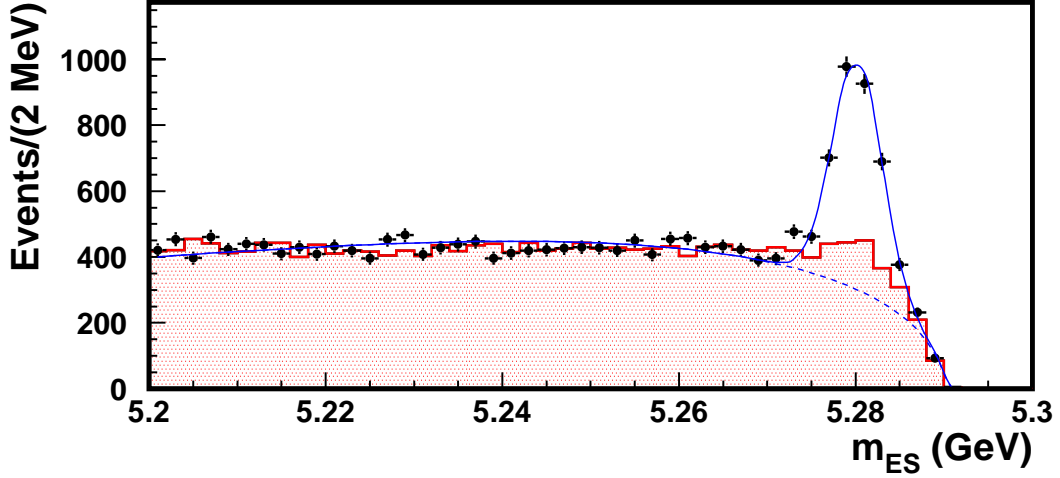
Figure 5.1: m_{ES} distributions for candidates with reconstructed ω mass in the signal (points) and sideband (shaded histogram) regions. The distribution for events in the sideband region has been rescaled to match the expected background in the m_ω signal region. The fitted function is described in the text.

substituted in reconstruction. The remaining background is from $\bar{B}^0 \to D^{*+}(4\pi)^-$ decays, where no $\omega \to \pi\pi\pi^0$ decay is present.

5.2.2 m_ω distribution

We present the m_ω distribution for $\bar{B}^0 \to D^{*+}\omega\pi^-$ candidates in data, with $m_{ES} > 5.27$ GeV, in Figure 5.2. The data is modelled by the sum of a linear background and a Voigtian function, where a Voigtian function is the convolution of a Breit-Wigner function with a Gaussian. The width of the Breit-Wigner is fixed to the nominal ω width ($\Gamma = 8.5$ MeV), and the remaining terms are allowed

to float in the fit. We find 1799 ± 87 events in the Voigtian in the m_ω signal region, compared to 2461 ± 69 events obtained from the m_{ES} fit in Figure 5.1.
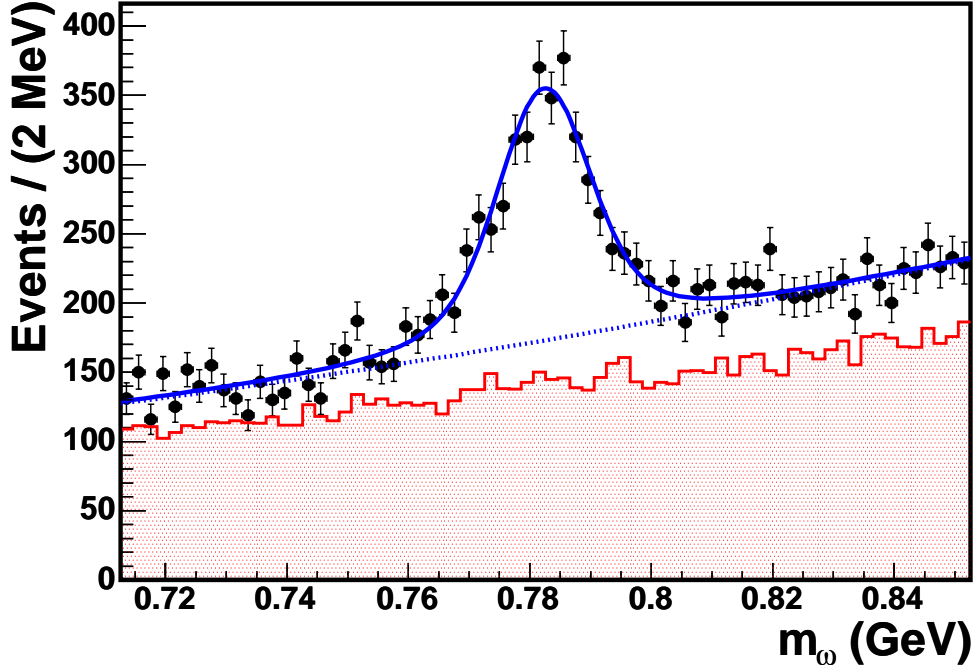
Figure 5.2: Distribution of reconstructed m_ω for events with $m_{ES} > 5.27$ GeV (points) and events in the m_{ES} sideband ($5.20 < m_{ES} < 5.25$ GeV, indicated by the shaded histogram). The superimposed fit is described in the text. The events from the m_{ES} sideband have been scaled to the expected background from an m_{ES} fit to events with $|m_\omega - m_\omega^{PDG}| < 70$ MeV (*i.e.*, the range shown in this figure).

The apparent "drop" in the yield is due the removal of background events which mimic the m_{ES} behavior of well-reconstructed signal decays. In Figure 5.2, we include the m_ω distribution for events in the m_{ES} sideband ($5.20 < m_{ES} < 5.25$ GeV). This background distribution is scaled to the expected number of

background events above $m_{ES} = 5.27$ GeV in a fit to the m_{ES} distribution where we require $|m_\omega - m_\omega^{PDG}| < 70$ MeV. The difference between the number of events seen in data away from the m_ω peak and the predicted background from the m_{ES} sideband is due to background events that peak in m_{ES}.

The signal yield from the m_ω distribution is only valid if it turns out that the background is indeed linear in m_ω. This requires that there are no background sources that include real $\omega \to \pi\pi\pi^0$ decays. From the results of Figure 5.2, we can see that there is not a significant source of real ω decays in the background, but it would be useful to be more thorough. We examined and fit the m_ω distribution for m_{ES} sideband events in data as well as Monte Carlo simulations of $B\bar{B}$ background events, and we find that the m_ω distributions for each of the background samples are well modelled by linear functions. There is no evidence that real ω decays are present in the background, and we estimate that this component can affect the signal yield, extracted from the fit in Figure 5.2, by (at most) a few percent.

5.2.3 m_ω sideband subtraction

Although well-reconstructed $\bar{B}^0 \to D^{*+} \omega \pi^-$ decays populate the (m_{ES},m_ω) signal window, backgrounds from poorly reconstructed signal decay, $\bar{B}^0 \to D^{*+}(4\pi)^-$ events, and random combinations of particles still populate the signal region. In this analysis, we are interested in studying several distributions for $\bar{B}^0 \to D^{*+} \omega \pi^-$,

such as the square of the invariant mass of the $\omega\pi$ system (m_X^2). Measurements of these distributions must account for the presence of background in our event sample.

In Section 5.2.2 we learned that selecting real ω decays in our sample is equivalent to selecting well-reconstructed $\bar{B}^0 \to D^{*+}\omega\pi^-$ decays. With this information, we use events reconstructed in the m_ω sidebands to remove the effects of the background in the m_ω signal region on a statistical basis. As the background is modelled by a linear function, we find the number of observed signal events is given by

$$N_{\rm rec}(m_X^2) = S_{\rm rec}(m_X^2) - \left(\frac{4}{7}\beta\right) \cdot B_{\rm rec}(m_X^2), \qquad (5.7)$$

where $S_{\rm rec}$ and $B_{\rm rec}$ represent the number of events reconstructed in the m_ω signal and sideband regions, respectively. The fraction $\frac{4}{7}$ is used to normalize the m_ω sideband region to the signal area. This fraction assumes a linear model for the background distribution, and hence the quantity β is introduced to correct for any possible bias introduced by this assumption. Ideally, β is equal to one.

5.2.4   Testing sideband subtraction

In Figure 5.3 we examine the impact of the m_ω sideband subtraction on signal Monte Carlo events. We see that the events in the sideband account for $\bar{B}^0 \to D^{*+}\omega\pi^-$ decays that are poorly reconstructed in the signal region. By ap-

plying an m_ω sideband subtraction, the effects of this background are statistically

removed, leaving only well-reconstructed signal events.
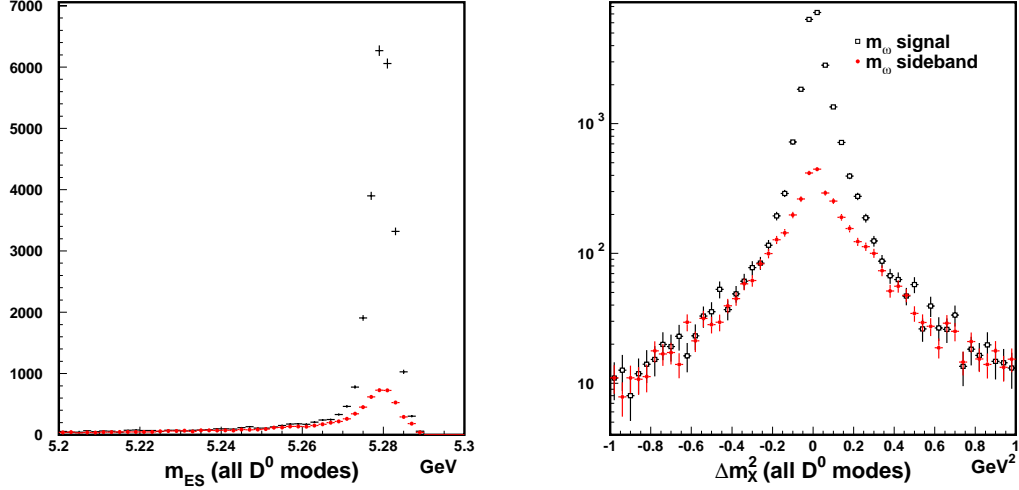
Figure 5.3: m_{ES} and Δm_X^2 distributions for signal Monte Carlo, where Δm_X^2 is the difference between generated and reconstructed m_X^2 values in simulated $\bar{B}^0 \to D^{*+}\omega\pi^-$ events, provided $m_{ES} > 5.27$ GeV. The events from the m_ω sideband region (solid red) have been scaled to match the expected background in the m_ω signal region (black), where we assume $\beta = 1$. All D^0 decay modes are combined in these plots.

Our next aim is to test the behavior of the sideband subtraction for m_X^2 using

various background samples in Monte Carlo as well as the m_{ES} and ΔE sidebands

in data:

- $-100 \leq \Delta E < -80$ MeV, $70 \leq \Delta E < 100$ MeV for $D^0 \to K\pi\pi^0$;

- $-100 \leq \Delta E < -70$ MeV, $60 \leq \Delta E < 100$ MeV for $D^0 \to K\pi$, $K3\pi$.

As real ω decays should be absent from each background sample, the post-subtraction m_X^2 distribution is expected to be featureless and statistically consistent with zero events. These tests were grouped according to the decay mode of the D^0. The results of each test were in agreement with expectations. As an example, we present the results of the m_ω sideband subtraction for the m_{ES} sideband sample, with all D^0 decays combined, in Figure 5.4. We conclude from these results that we can successfully remove the effects of all backgrounds from events reconstructed in the m_ω signal region using events reconstructed in the ω mass sidebands.

5.2.5   Kinematic corrections

The range of invariant mass for the $\pi^+\pi^-\pi^0$ system differs in the m_ω signal and sideband regions. Consequently, the m_ω sidebands have slightly different kinematic limits for the energy of the ω candidate. This effect can bias our results at kinematic extremes, as illustrated in Figure 5.5. In this Figure, we examine the energy of the $\pi\pi\pi^0$ ("ω") system in the B rest frame using $B^\pm$ Monte Carlo events. The difference between the high and low m_ω sidebands and the m_ω signal region are noticeable.

To correct for this effect, we linearly rescale the ω energy, m_X^2, etc., in the ω mass sidebands so that their kinematic limits match those in the m_ω signal region.
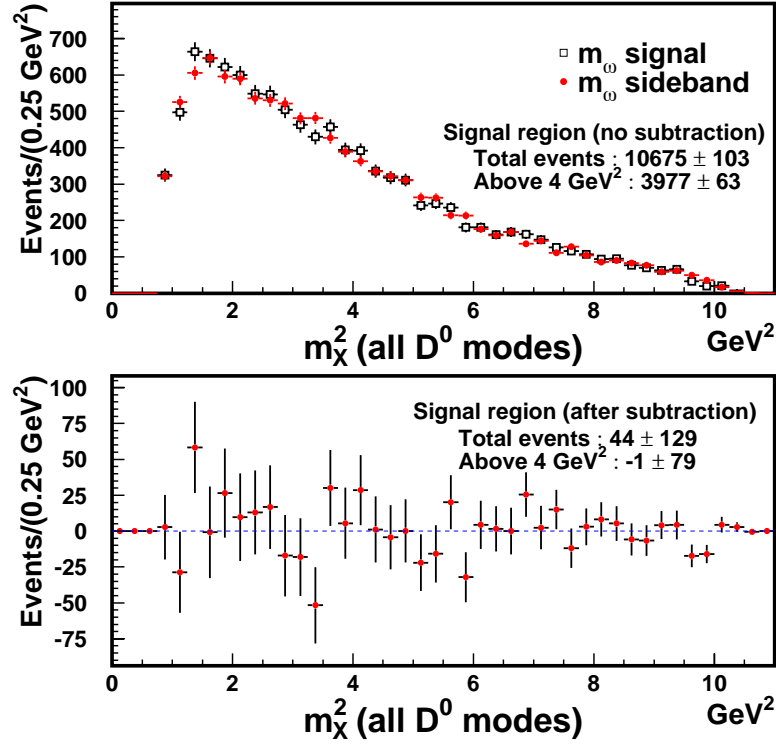
Figure 5.4: m_X^2 distributions for the m_{ES} sideband data sample. All D^0 decay modes have been combined in this Figure. The top plot gives the m_X^2 distribution for the m_ω signal (open squares) and sideband (red circles) regions. The m_ω sideband has been scaled to match the expected background in the signal region. The bottom plot shows the results of the sideband subtraction. We correct the m_X^2 distribution in the m_ω sidebands as described in Section 5.2.5, and we assume β from Equation 5.7 is equal to one.

This correction eliminates the structure in E_ω^B near the kinematic limit, as shown in Figure 5.6, without changing the shape of the distribution. The impact of this correction is less dramatic for the m_X^2 distribution (also shown in Figure 5.6), as $m_X^2(E_\omega^B)$ does not vary significantly near the kinematic limit.
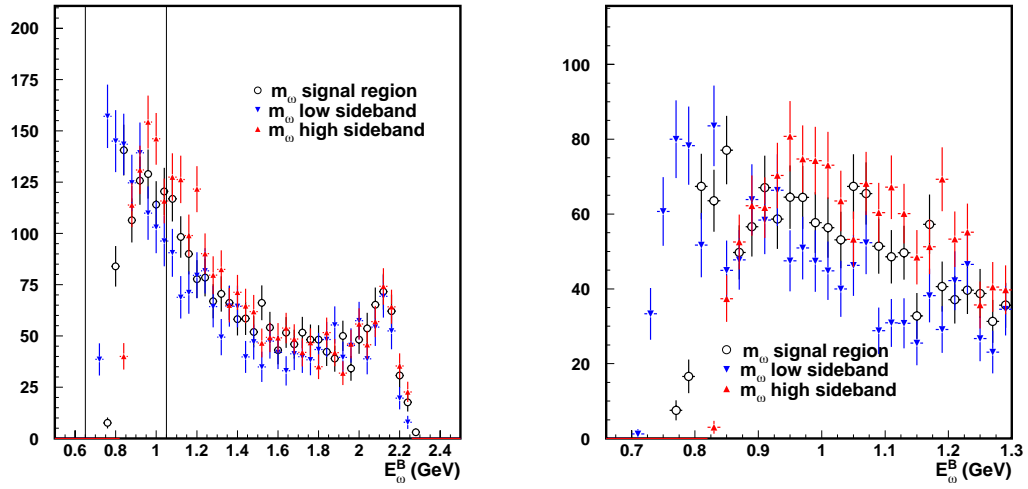
Figure 5.5: E_ω^B distributions for different m_ω regions, using $B^\pm$ Monte Carlo. All D^0 decay modes have been combined in these plots, and the m_ω sideband distributions have been normalized to the number of events in the signal region. The E_ω^B region between the lines on the left plot is examined in more detail at right.
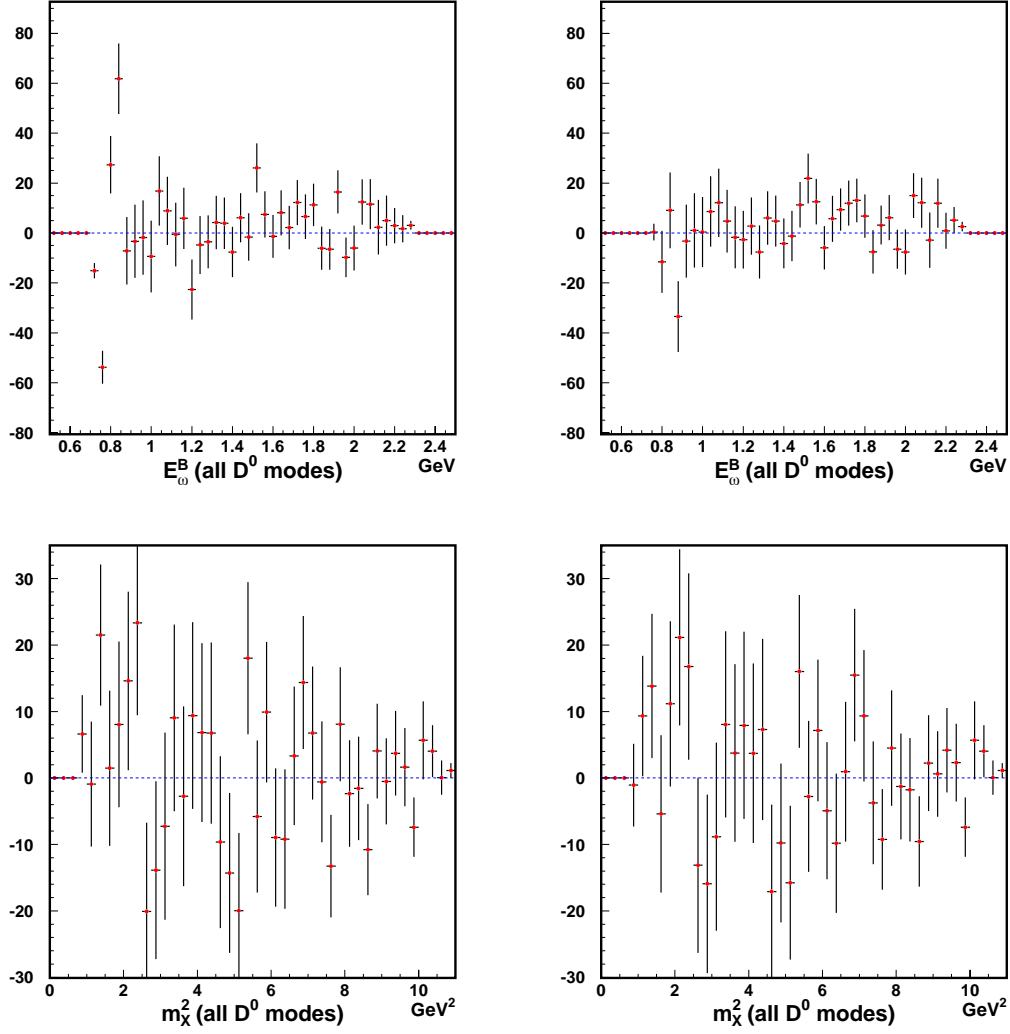
Figure 5.6: m_ω sideband-subtracted E_ω^B (top) and m_X^2 (bottom) distributions using $B^\pm$ Monte Carlo, where we assume β from Equation 5.7 is equal to one. All D^0 decay modes have been combined in these plots. At left the results are shown with no correction applied to account for problems near the kinematic limit. Kinematic corrections have been applied in the right plot. The vertical scale is identical for each set of plots.

5.2.6   Observed m_X^2 distribution

In Figure 5.7 we present the observed m_X^2 distribution before and after we apply the background subtraction using the mass sidebands of the ω. The events seen above $m_X^2 = 4$ GeV^2 were not seen when $\bar{B}^0 \to D^{*+}\omega\pi^-$ decays were first observed by CLEO, as they did not have a sufficient number of $B\bar{B}$ decays to find these events. Despite the success of the sideband subtraction in various control samples, it is useful to verify that the events seen at various m_X^2 values correspond to real $\omega \to \pi\pi\pi^0$ decays. To do this, for events which pass all cuts (excluding m_ω), we fit the m_ω distribution in bins of m_X^2. We then compare the results of the m_ω fits to those obtained from the m_X^2 distribution after performing the sideband subtraction.

In Figure 5.8, the $m_{\pi\pi\pi^0}$ distribution is examined (for events with m_{ES} above 5.27 GeV) in different regions of m_X^2. No sideband subtraction was performed. The fitted $\omega \to \pi\pi\pi^0$ yield within 20 MeV of the nominal ω mass is compared to results obtained from the m_X^2 distributions after sideband subtraction, and these results are shown in Tables 5.2 and 5.3. From this information we conclude that the number of reconstructed $\bar{B}^0 \to D^{*+}\omega\pi^-$ events present after the m_ω sideband subtraction are correlated with real ω decays. This confirms our assumption that the background subtraction keeps well-reconstructed signal decays while removing the effects of all backgrounds.
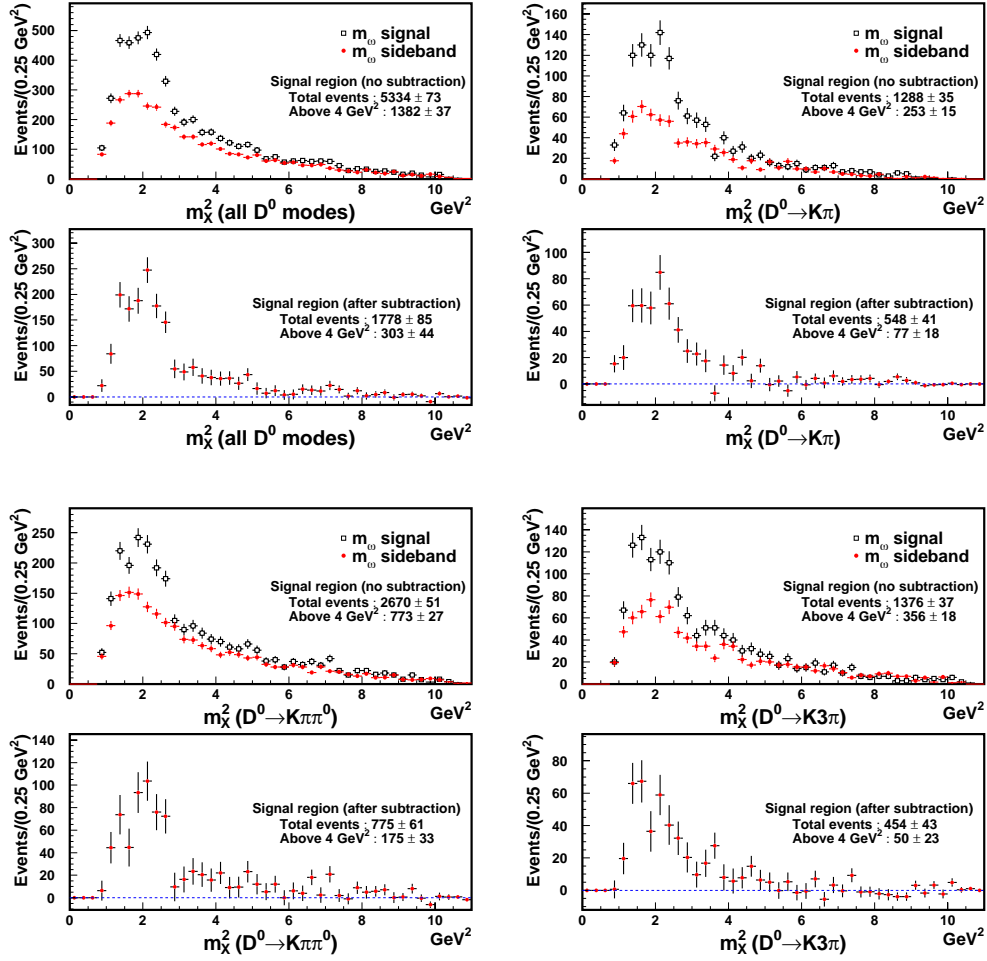
Figure 5.7: m_X^2 distributions for data events with $m_{ES} > 5.27$ GeV, and m($\pi\pi\pi^0$) within 20 MeV of the nominal ω mass. Results are grouped according to D^0 decay mode. For each D^0 mode, the top plot presents the m_X^2 distribution for the m_ω signal (open squares) and sideband (red circles) regions. The m_ω sideband has been scaled to match the expected background in the signal region, and we set β from Equation 5.7 equal to one. The bottom plot gives the results of the sideband subtraction.
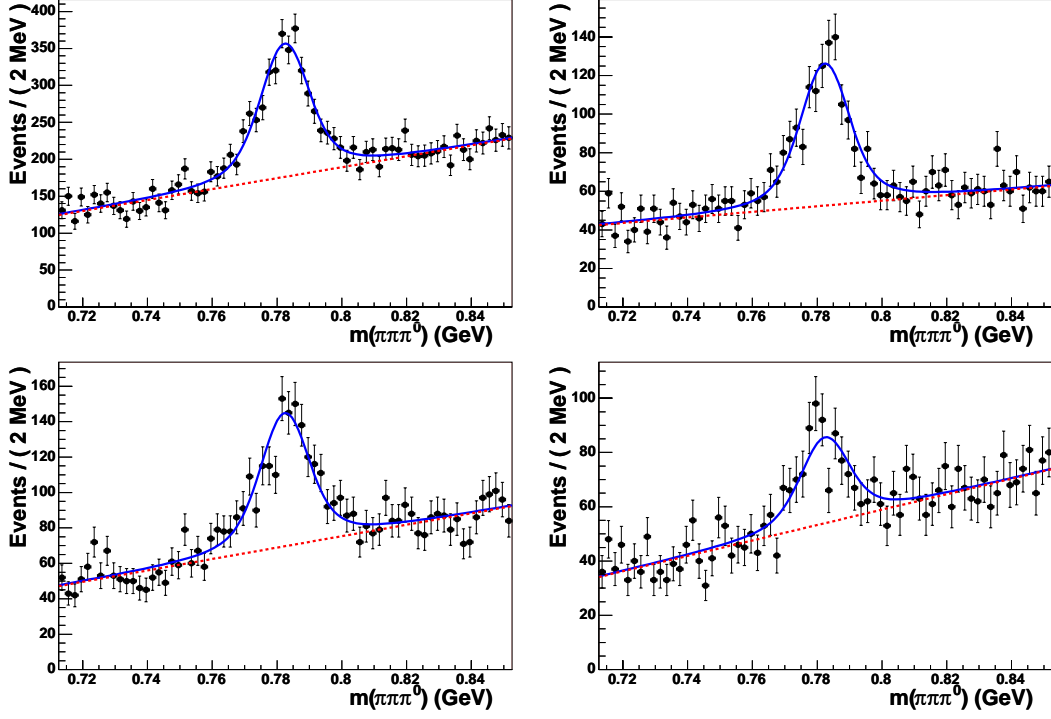
Figure 5.8: $m_{\pi\pi\pi^0}$ distributions for data events with $m_{ES} \geq 5.27$ GeV. All D^0 modes are combined in these plots. (Top left) All m_X^2 values, (Top right) $0 \leq m_X^2 < 2$ GeV^2, (Bottom left) $2 \leq m_X^2 < 4$ GeV^2, and (Bottom right) $m_X^2 \geq 4$ GeV^2. The signal is fit to a Voigtian, and the background is assumed to be described by a first order polynomial.

D^0 Decay Mode	m_X^2 Range (GeV^2)			
	$0 \leq m_X^2 < 2$	$2 \leq m_X^2 < 4$	$4 \leq m_X^2$	All
$D^0 \to K\pi$	212 ± 25	259 ± 27	77 ± 19	549 ± 41
$D^0 \to K\pi\pi^0$	262 ± 34	337 ± 38	175 ± 33	775 ± 61
$D^0 \to K3\pi$	190 ± 25	214 ± 28	51 ± 23	454 ± 44
All D^0 decays	664 ± 49	810 ± 54	303 ± 45	1778 ± 86

Table 5.2: m_X^2 results for data events in the m_ω signal region obtained after m_ω sideband subtraction, where the parameter β from Equation 5.7 has been set to one. These results are also shown in Figure 5.7.

D^0 Decay Mode	m_X^2 Range (GeV^2)			
	$0 \leq m_X^2 < 2$	$2 \leq m_X^2 < 4$	$4 \leq m_X^2$	All
$D^0 \to K\pi$	216 ± 22	272 ± 25	86 ± 16	559 ± 37
$D^0 \to K\pi\pi^0$	300 ± 30	277 ± 32	179 ± 28	766 ± 53
$D^0 \to K3\pi$	210 ± 22	200 ± 24	68 ± 19	482 ± 38
All D^0 decays	728 ± 44	745 ± 47	312 ± 38	1799 ± 87

Table 5.3: Results of the fit to the $m_{\pi\pi\pi^0}$ in data for events with $m_{ES} > 5.27$ GeV. The fits are shown in Figure 5.8.

5.3   Efficiency Parameterization

In order to extract useful results from our sample of reconstructed events, we must correct for the signal reconstruction efficiency, which is determined from $\bar{B}^0 \rightarrow D^{*+}\omega\pi^-$ Monte Carlo events. In this Section, we will define our efficiency $\epsilon(\vec{x})$, where $\vec{x}$ describes the set of quantities that specify the kinematics of a given $\bar{B}^0 \rightarrow D^{*+}\omega\pi^-$ event.

In the absence of background, the number of events corrected for efficiency in a given bin of m_X^2 is equal to

$$N(m_X^2) = \sum_{\text{signal}} \frac{1}{\epsilon(\vec{x}_i)} \tag{5.8}$$

where the sum is over all signal events in a given m_X^2 bin and $\vec{x}_i$ is the set of kinematic quantities for the ith event in the sum.

We have demonstrated that we must perform a background subtraction using the m_ω sideband. Thus, Equation 5.8 is modified as follows:

$$N(m_X^2) = \sum_{\text{signal}} \frac{1}{\epsilon(\vec{x}_i)} - \left(\frac{4}{7}\beta\right) \sum_{\text{sideband}} \frac{1}{\epsilon(\vec{x}_j)} \tag{5.9}$$

where the first sum is unchanged, while the second sum is taken over all m_ω sideband events in the given bin of m_X^2, and $\vec{x}_j$ represents the set of kinematic quantities for the jth event in the sum. Note that we apply the efficiency calculated for signal events (namely, $\epsilon(\vec{x})$) to events in the m_ω sideband. The factor of $\frac{4}{7}$ is

necessary to adjust for the relative size of the ω signal and sideband regions, and the quantity β is again included to correct for any possible bias in the background subtraction procedure. As before, β is ideally equal to one.

$\bar{B}^0 \to D^{*+}\omega\pi^-$ is a three-body decay with two vectors in the final state, so in principle we should parametrize the efficiency in terms of the following seven variables:

1. E_ω^B, the energy of the ω in the $\bar{B}^0$ rest frame;

2. $E_{D^*}^B$, the energy of the D^* in the $\bar{B}^0$ rest frame;

3. $\cos\theta_{D^*}$, where the decay angle θ_{D^*} is the angle between the D^0 and direction opposite the flight of the $\bar{B}^0$ in the D^* rest frame;

4. $\cos\theta_\omega$, where the decay angle θ_ω is defined (in the ω rest frame) as the angle between the vector normal to the ω decay plane and the direction opposite the flight of the $\bar{B}^0$;

5. The two azimuthal angles (ϕ_{D^*} and ϕ_ω) that describe the orientation of the decay planes of the D^* and the ω with respect to the $\bar{B}^0$ decay plane, as shown in Figure 5.9;

6. d, an index that indicates the D^0 decay mode ($K\pi$, $K\pi\pi^0$, or $K3\pi$).

The angles that describe $\bar{B}^0 \to D^{*+}\omega\pi^-$ decay are shown in Figure 5.9. From studies of signal Monte Carlo events, we have concluded that signal reconstruction efficiency does not depend on the azimuthal angles ϕ_{D^*} or ϕ_ω. As a result, we set

$$\epsilon(\vec{x}) \equiv \epsilon(E_\omega^B, E_{D^*}^B, \cos\theta_{D^*}, \cos\theta_\omega, d). \tag{5.10}$$

The first two variables, E_ω^B and $E_{D^*}^B$, are the usual Dalitz plot variables for a three-body decay. (Note that these two variables are entirely equivalent to the square of the $D^*\pi$ and $\omega\pi$ masses as a result of energy-momentum conservation.) The two angular variables, θ_{D^*} and θ_ω, are necessary to account for the possible polarization of the D^* and the ω. Finally, we must also consider any potential efficiency dependence on d, the decay mode of the D^0. To simplify matters, we express the efficiency as the product of three terms:

$$\epsilon(E_\omega^B, E_{D^*}^B, \cos\theta_{D^*}, \cos\theta_\omega, d) = \epsilon'(E_\omega^B, E_{D^*}^B, d) \times c_1(E_\omega^B, \cos\theta_\omega) \times c_2(E_{D^*}^B, \cos\theta_{D^*}, d)$$

$$\tag{5.11}$$

This parameterization is motivated by the assumption that the D^* and ω efficiencies should factorize. The first term (ϵ') describes the efficiency as a function of the two Dalitz plot variables, averaged over the D^* and ω polarizations. The functions c_1 and c_2 represent corrections to the unpolarized efficiency due to possible
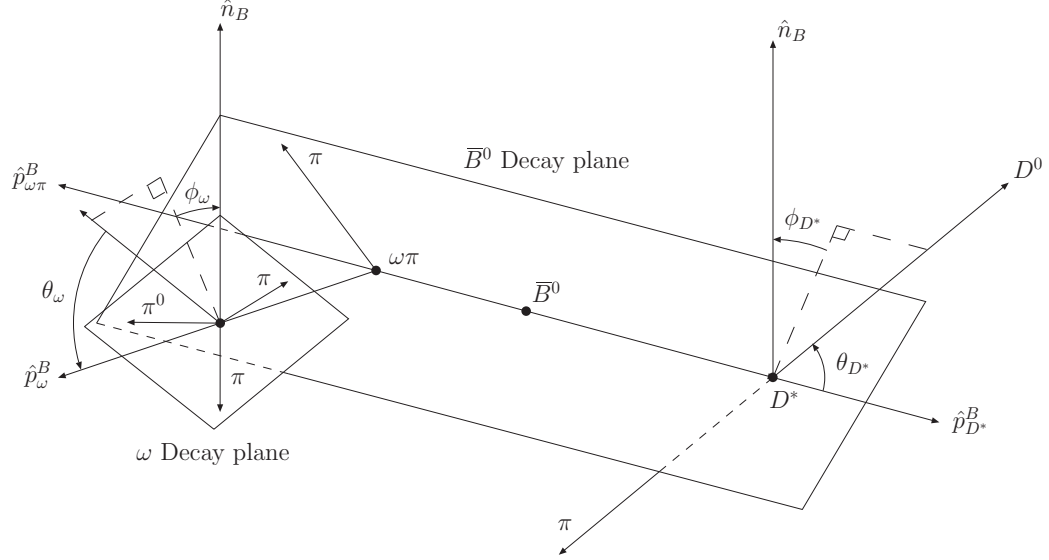
Figure 5.9: Graphical depiction of the angles needed to describe the kinematics of $\bar{B}^0 \to D^{*+}\omega\pi^-$ decay. The polar angles, θ_{D^*} and θ_ω, are measured relative to $\hat{p}^B_{D^*}$ and $\hat{p}^B_\omega$, respectively. These vectors describe the flight directions of the D^* and ω in the rest frame of the B^0. The azimuthal angles, ϕ_{D^*} and ϕ_ω, measured in the plane perpendicular to the D^* (ω) flight directions, describe the orientation of the decay of the D^* (ω) relative to the B decay plane.

polarization effects. These functions are defined such that

$$\int_{-1}^{1} c_1(E^B_\omega, \cos\theta_\omega) \ \mathrm{d}(\cos\theta_\omega) = 2, \tag{5.12}$$

$$\int_{-1}^{1} c_2(E_{D^*}, \cos\theta_{D^*}, \mathrm{mode}) \ \mathrm{d}(\cos\theta_{\mathrm{D}^*}) = 2. \tag{5.13}$$

To understand the chosen normalization, consider that if the efficiency was independent of either θ_ω or θ_{D^*}, the associated c_1 or c_2 corrections would be identically equal to one.

The functions ϵ', c_1, and c_2 are extracted from Monte Carlo and stored as two-dimensional histograms for further use. Consequently, our results depend on the number of simulated Monte Carlo decays that are reconstructed in each efficiency bin. We will discuss the effect of a finite Monte Carlo sample size in Section 5.4.1.

In order to extract each efficiency component, we perform a sideband subtraction using the mass sidebands of the ω. This subtraction removes the effects of poorly reconstructed $\bar{B}^0 \to D^{*+}\omega\pi^-$ decays. We define the efficiency in terms of the number of reconstructed signal events remaining after background subtraction.

5.3.1 Efficiency component $\epsilon'(E_\omega^B, E_{D^*}^B, d)$

In order to obtain $\epsilon'(E_\omega^B, E_{D^*}^B, d)$, we need to understand the reconstruction efficiency for signal events at each point $(E_\omega^B, E_{D^*}^B)$ in the $\bar{B}^0$ Dalitz plot. Taking signal Monte Carlo events reconstructed in the (m_{ES}, m_ω) signal region, we populate the Dalitz plot according to the generated (true) energies of the D^* and ω in the $\bar{B}^0$ rest frame. The m_ω sideband subtraction is then performed in order to remove background from poorly reconstructed signal events. Once the reconstructed $(E_\omega^B, E_{D^*}^B)$ distribution has been obtained for each D^0 decay mode, we take the ratio of the reconstructed and generated distributions (separated by D^0 decay, with each distribution compiled from generated energies) to obtain ϵ'. For convenience later, we construct the $E_{D^*}^B$ bins to match the binning of the m_X^2

distribution used in Section 5.2. In the rest frame of the $\bar{B}^0$,

$$E^B_{D^*} = \frac{M_B^2 - m_X^2 + m_{D^*}^2}{2M_B} \qquad (5.14)$$

implies that the nominal $\Delta m_X^2 = 0.25$ GeV^2 spacing (see Figure 5.7) would correspond to a bin width of 23.7 MeV in $E^B_{D^*}$. As there are no similar restrictions on the binning in E^B_ω, we choose a bin width of 55 MeV.

The $D^0 \to K\pi, K\pi\pi^0, K3\pi$ decays are not expected to have the same reconstruction efficiency. Multiple effects, such as track multiplicity and π^0 reconstruction, are expected to change the relative population of the Dalitz plot at a given $E^B_{D^*}$ for each D^0 decay. As a result, we split the unpolarized efficiency according to the reconstructed D^0 decay mode.

In Figures 5.10-5.12 we show $\epsilon'(E^B_\omega, E^B_{D^*}, d)$ obtained from simulated Monte Carlo signal events, separated by the decay of the D^0. These Figures clearly demonstrate the efficiency variation throughout the available phase space.

Monte Carlo statistics are significant in the data-like (low-m_X^2, or high $E^B_{D^*}$) region, but regions of small D^* energy (high m_X^2) tend to suffer from statistical effects brought about by low reconstruction efficiency. Because we compute a binned efficiency correction, finite Monte Carlo sample size can diminish the accuracy and precision of our results. This is especially true in regions where the reconstruction efficiency is small. In order to minimize the impact of low statis-
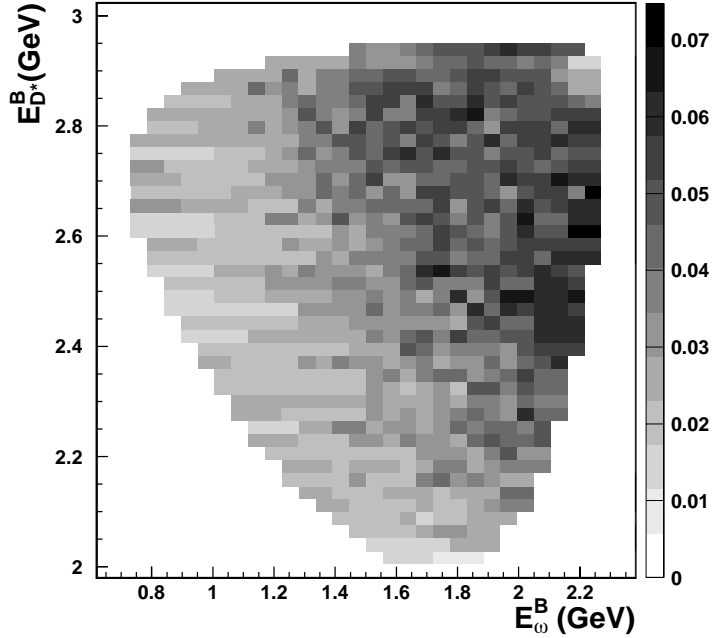
Figure 5.10: The $\epsilon'(E_\omega^B, E_{D^*}^B, D^0 \rightarrow K\pi)$ distribution for $\bar{B}^0 \rightarrow D^{*+}\omega\pi^-$ Monte Carlo events.

tics, we merge the contents of several nearby bins in order to compute an average efficiency in this region. This is done with the following requirements in mind:

- As all events in a given $E_{D^*}^B$ bin can be found in one m_X^2 bin (by construction), most merging occurs across E_ω^B bins.

- We combine bins until the error on the efficiency drops below 30% of the value. This forces a minimum of at least 10-15 events in each (merged) bin after background subtraction. This allows us to treat the uncertainty on each value of $\epsilon'(\vec{x}_i)$ as Gaussian.
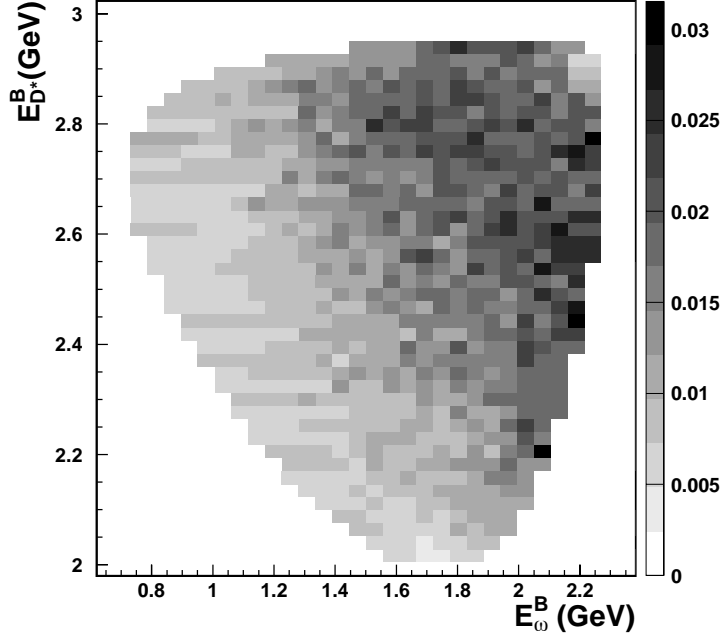
Figure 5.11: The $\epsilon(E_\omega^B, E_{D^*}^B, D^0 \to K\pi\pi^0)$ distribution for $\bar{B}^0 \to D^{*+}\omega\pi^-$ Monte Carlo events.

If it is necessary to merge nearby bins, the relevant bins in the generated and reconstructed histograms are combined, and an efficiency is calculated for the merged region of ϵ' space. As the binned efficiency varies slowly over the entire $(E_\omega^B, E_{D^*}^B)$ space, this technique reduces the impact of low-statistics bins without diminishing the accuracy of the final result.
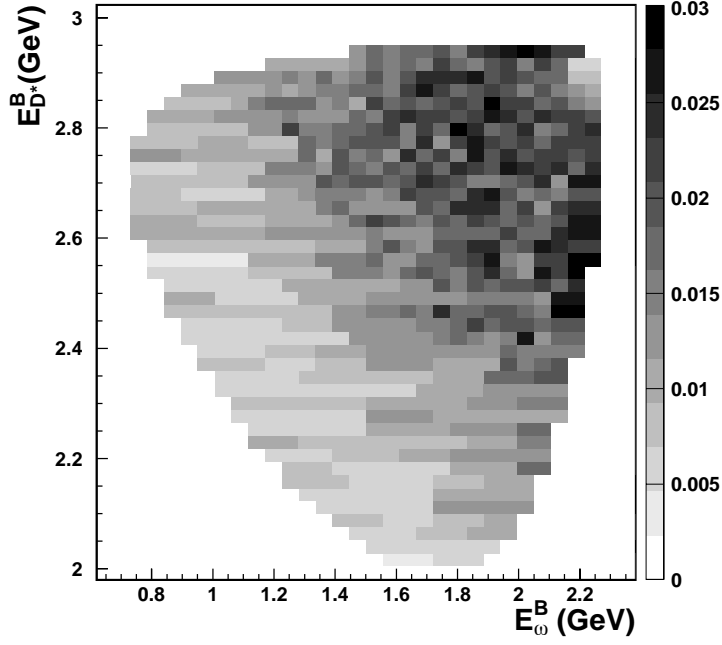
Figure 5.12: The $\epsilon(E_\omega^B, E_{D^*}^B, D^0 \to K3\pi)$ distribution for $\bar{B}^0 \to D^{*+}\omega\pi^-$ Monte Carlo events.

5.3.2   Efficiency correction: $c_1(E_\omega^B, \cos\theta_\omega)$

The $(E_\omega^B, E_{D^*}^B)$ efficiency calculated in the Section 5.3.1 makes no assumptions about the decay of the ω and D^* produced in $\bar{B}^0$ decay. We need to include corrections to ϵ' in order to account for any reconstruction dependence on the polarization of the vector mesons. In this section we will address the correction due to the decay of the ω, and our treatment of the D^* follows in Section 5.3.3.

The polarization of the ω determines the orientation of the ω decay plane with respect to its flight direction [48]. In the rest frame of the ω, we define the normal

to the decay plane as

$$\hat{n}_\omega \equiv \hat{p}_{\pi^+} \times \hat{p}_{\pi^-}, \tag{5.15}$$

where $\hat{p}_{\pi^\pm}$ describes the momentum direction of the $\pi^\pm$ daughter in the ω rest frame. The decay angle θ_ω (see Figure 5.9) describes the angle between $\hat{n}_\omega$ and the direction opposite the flight of the $\bar{B}^0$ in the ω rest frame.

When we examine Monte Carlo $\bar{B}^0 \to D^{*+}\omega\pi^-$ events, we notice a significant dip in reconstruction efficiency when the decay plane of the ω is nearly coincident with its flight direction (near $\cos\theta_\omega = 0$), as shown in Figure 5.13. Signal re-
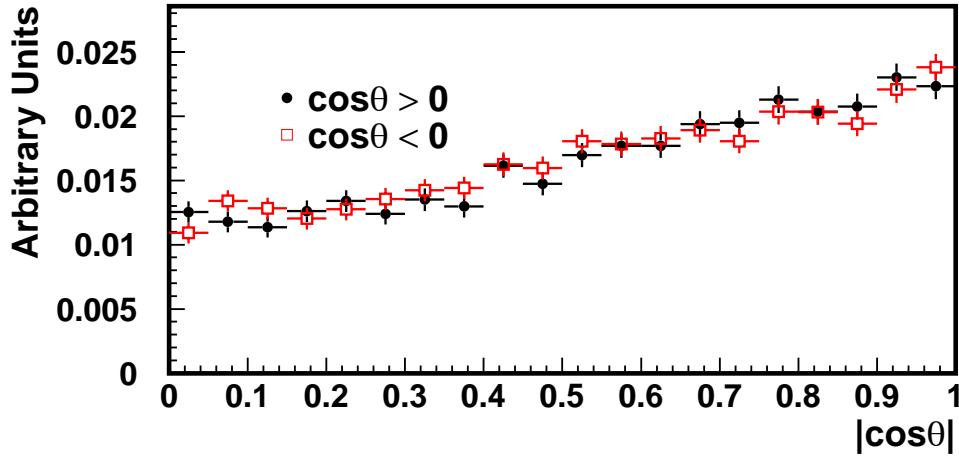
Figure 5.13: Efficiency of $\bar{B}^0 \to D^{*+}\omega\pi^-$ reconstruction using signal Monte Carlo as a function of the ω decay angle. For this efficiency projection plot, the signal events were generated with a phase space model, and the D^* and ω are unpolarized. The vertical scale is arbitrary, as the distributions are normalized to equal area.

construction efficiency clearly depends on the orientation of the $\omega \to \pi\pi\pi^0$ decay plane. We address this dependence using the correction

$$c_1(E_\omega^B, \cos\theta_\omega) \to c_1(E_\omega^B, |\cos\theta_\omega|), \tag{5.16}$$

where we have taken advantage of the symmetry in $\cos\theta_\omega$ (Figure 5.13) in order to reduce the statistical uncertainty in c_1.

Following the procedure outlined in Section 5.3.1, we obtain a distribution for generated and reconstructed signal $\bar{B}^0 \to D^{*+}\omega\pi^-$ decays in $(E_\omega^B, |\cos\theta_\omega|)$ space. The efficiency correction is given by

$$c_1(E_\omega^B, |\cos\theta_\omega|) = \frac{N(\bar{B}^0 \to D^{*+}\omega\pi^-) \text{ reconstructed with } (E_\omega^B, |\cos\theta_\omega|)}{N(\bar{B}^0 \to D^{*+}\omega\pi^-) \text{ generated with } (E_\omega^B, |\cos\theta_\omega|)} \tag{5.17}$$

for each bin of $(E_\omega^B, |\cos\theta_\omega|)$ space. As before, it is useful to merge bins in order to reduce the impact of the finite Monte Carlo sample size on our results. Taking advantage of the increased statistics available in all c_1 bins (as D^0 decay modes are merged), we lower the maximum bin error to 15%.

Finally, we normalize $c_1(E_\omega^B, \cos\theta_\omega)$ so that the correction for any fixed value of E_ω^B is unity:

$$\sum_{|\cos\theta_\omega|} c_1(E_\omega^B, \cos\theta_\omega) \equiv 1, \tag{5.18}$$

We present the normalized correction factor, c_1, in Figure 5.14.
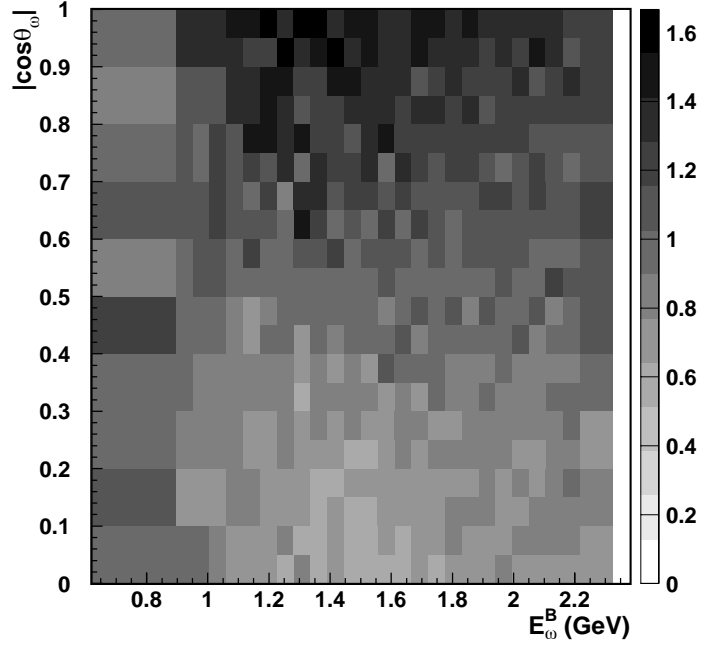
Figure 5.14: The $c_1(E_\omega^B, |\cos\theta_\omega|)$ correction for $\bar{B}^0 \to D^{*+}\omega\pi^-$ Monte Carlo events.

5.3.3 Efficiency correction: $c_2(E_{D^*}^B, \cos\theta_{D^*}, d)$

In the D^* rest frame, the pion is produced with very low momentum (less than 40 MeV). In the event that this pion is produced against the D^* boost, the chance of finding the soft π in our detector would most likely drop. These expectations are confirmed in Figure 5.15, where we see that efficiency drops significantly as $\cos\theta_{D^*} \to 1$. In contrast to our treatment of the ω decay, the efficiency is not symmetric as a function of $\cos\theta_{D^*}$.
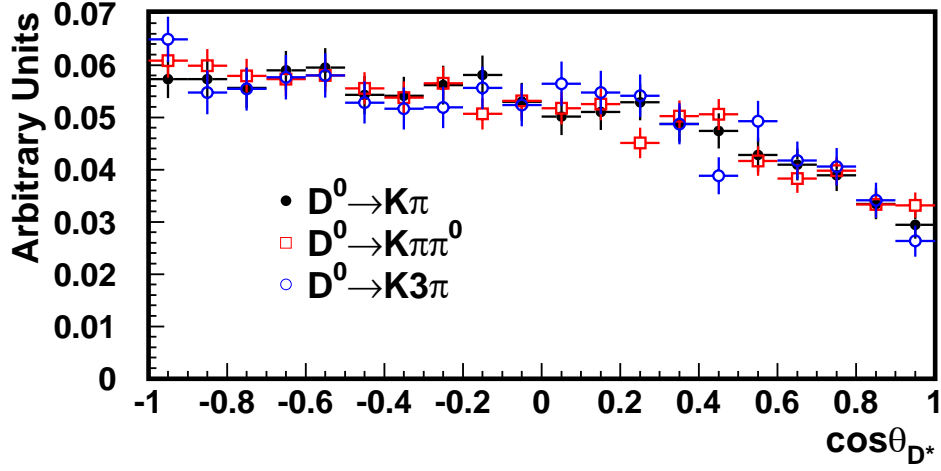
Figure 5.15: $\bar{B}^0 \to D^{*+}\omega\pi^-$ reconstruction efficiency as a function of the D^* decay angle θ_{D^*}. For this efficiency projection plot, the signal events were generated with a phase space model, and the D^* and ω are unpolarized. Each D^0 distribution has been normalized to equal area (i.e. the vertical scale is arbitrary).

We determine $c_2(E^B_{D^*}, \cos\theta_{D^*}, d)$ in a manner similar to our work with the c_1 correction, and we present the results in Figures 5.16-5.18. We notice that the drop in c_2 is most pronounced at low D^* energies, where the daughter π (produced anti-parallel to $\hat{p}^B_{D^*}$, see Figure 5.9) has very little momentum in the laboratory frame. As the D^* energy increases, this effect becomes less pronounced. As the c_2 correction varies rapidly in a small section of $(E^B_{D^*}, \cos\theta_{D^*})$ space, we restrict ourselves to the region of phase space where the efficiency variation is less extreme. The ignored region is indicated on each plot. Events in the ignored region of c_2 are not considered for the efficiency correction. This has no impact on our test of
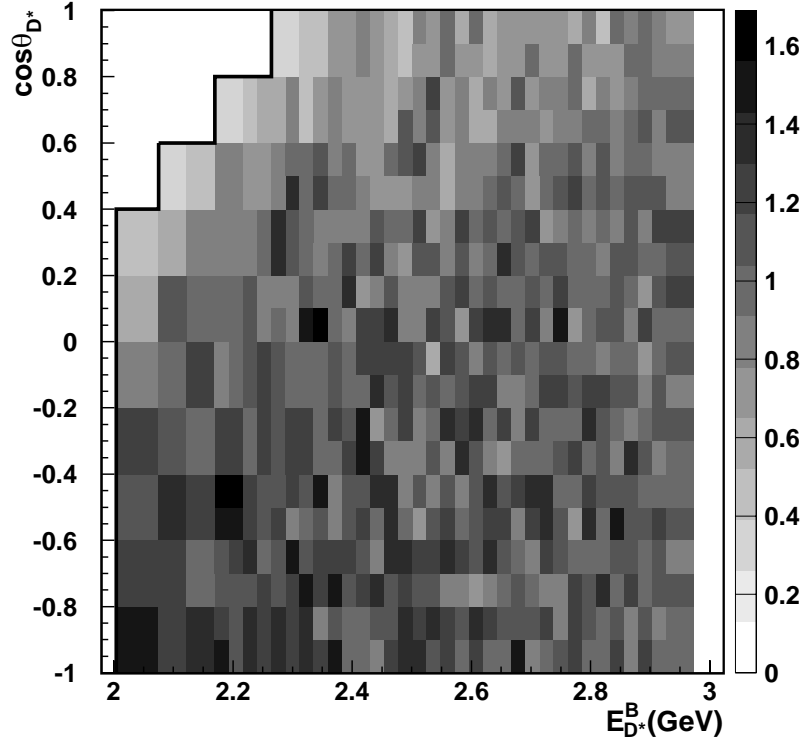
Figure 5.16: The $c_2(E_{D^*}^B, \cos\theta_{D^*}, D^0 \rightarrow K\pi)$ correction for signal $\bar{B}^0 \rightarrow D^{*+}\omega\pi^-$ Monte Carlo events. We ignore events reconstructed outside the solid black boundary lines.

factorization, as the ignored events have low D^* energy (high m_X^2), and therefore lie outside the region that can be tested using τ data. We address the impact of this exclusion in Section 5.4.1.
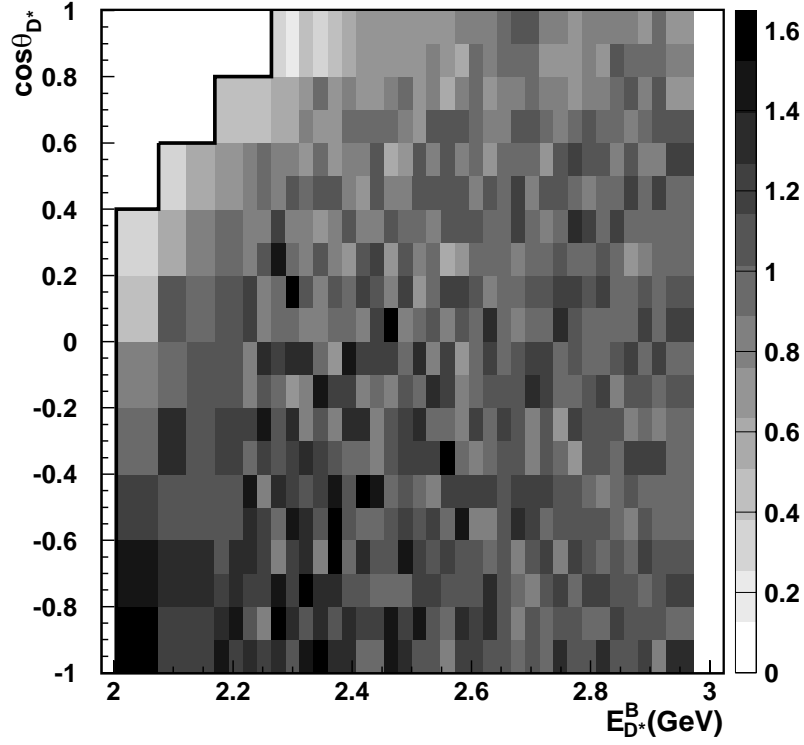
Figure 5.17: The $c_2(E^B_{D^*}, \cos\theta_{D^*}, D^0 \to K\pi\pi^0)$ correction for signal $\bar{B}^0 \to D^{*+}\omega\pi^-$ Monte Carlo events. We ignore events reconstructed outside the solid black boundary lines.

5.3.4 Validating the efficiency parameterization

In Section 5.2 we demonstrated that the m_ω sideband subtraction successfully removes all but well-reconstructed $\bar{B}^0 \to D^{*+}\omega\pi^-$ decays for the observed m_X^2 distribution. Within statistical precision, the observed m_X^2 distributions for various background samples were consistent with zero signal events (as can be seen for events in m_{ES} sideband in data in Figure 5.4).
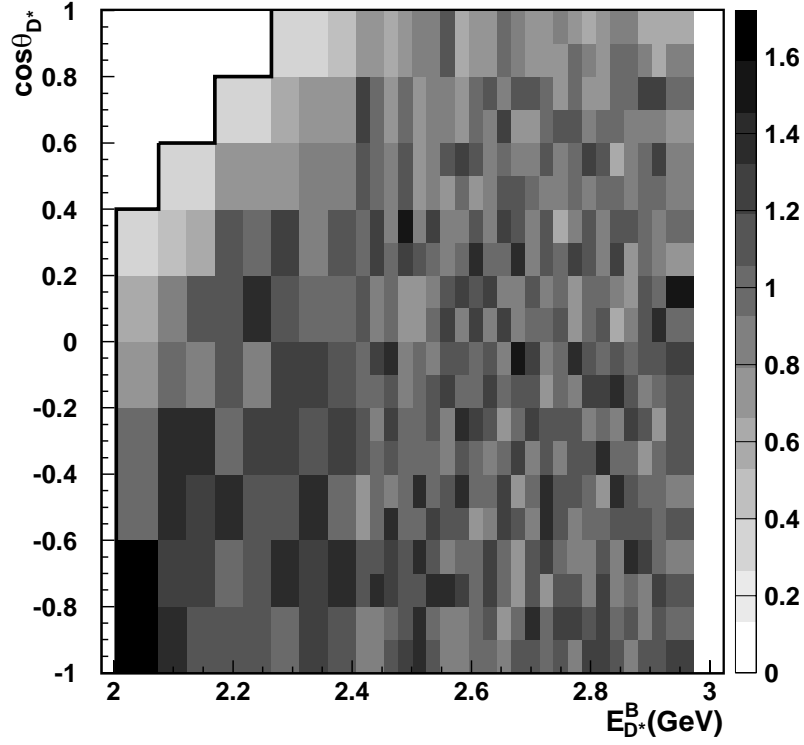
Figure 5.18: The $c_2(E^B_{D^*}, \cos\theta_{D^*}, D^0 \rightarrow K3\pi)$ correction for signal $\bar{B}^0 \rightarrow D^{*+}\omega\pi^-$ Monte Carlo events. We ignore events reconstructed outside the solid black boundary lines.

In this Section, we again address the m^2_X distribution produced from various background samples. In our observations of the raw distributions in Section 5.2, we saw no evidence for bias in the m_ω sideband subtraction. Returning to Equation 5.9, we need to assign a value for the correction factor β. In the event that the m_ω sideband subtraction is unbiased after correcting for reconstruction efficiency, we can set $\beta = 1$.

As an example, we present the m_X^2 distributions for data events reconstructed in the m_{ES} sideband, after correcting for reconstruction efficiency, in Figure 5.19. We expect that the m_ω sideband subtraction will eliminate all non-ω events in each of the background samples, leaving us with a flat distribution consistent with zero events. We discovered that the m_ω sideband-subtracted m_X^2 distributions for Monte Carlo and data background samples show no significant structure, but there is a small bias in the background-subtracted yields if we assume $\beta = 1$. It turns out that if $\beta = 1$, on average the m_ω sidebands overestimate the signal yield by 2.5%. Consequently, we set $\beta = 0.975$, with an estimated uncertainty of ± 0.010.

At this point, we need to test the efficiency parametrization (and background subtraction) using samples of Monte Carlo signal events. These samples are generated with a variety of ad-hoc kinematic properties:

1. The shape of the m_X^2 distribution is modified to more closely resemble data. Our signal Monte Carlo does not account for the $B^0 \to D^*\rho'$, $\rho' \to \omega\pi$ decay, which is expected (from work by CLEO) to dominate our results for $m_X^2 < 4 \text{ GeV}^2$.

2. We consider different polarizations for the D^* and the ω. This change is not meant to anticipate any specific behavior in data. Instead, we wish to test
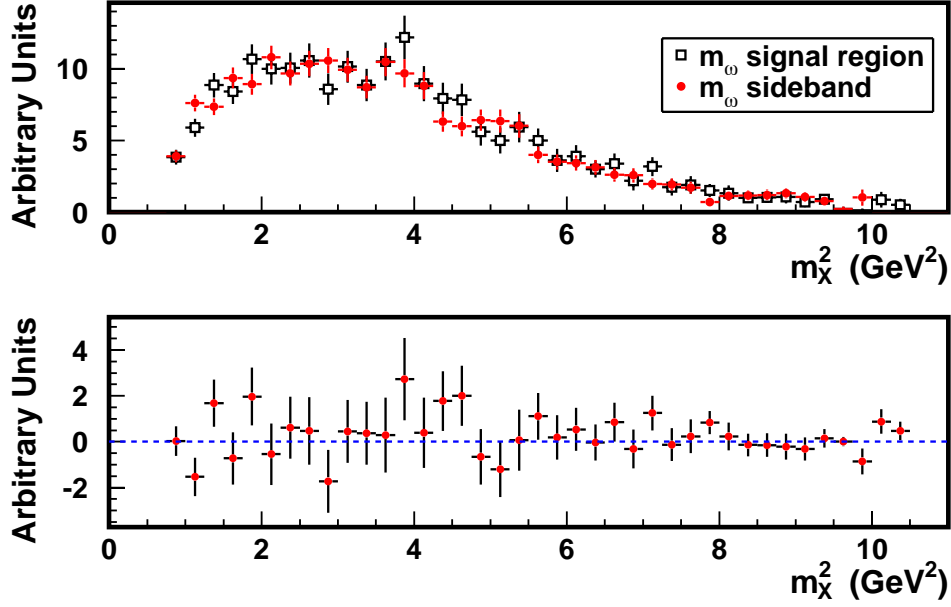
Figure 5.19: Efficiency-corrected m_X^2 distributions for $\bar{B}^0 \rightarrow D^{*+}\omega\pi^-$ events with $D^0 \rightarrow K\pi$ from the m_{ES} sideband in data. In the top plot, we give the m_X^2 distributions for events with reconstructed m_ω in the signal and sideband regions. The distribution for events in the m_ω sideband region has been scaled by a factor of $\frac{4}{7}$. The bottom plot gives the results of the sideband subtraction, assuming $\beta = 1$. The vertical scale is given in arbitrary units.

our ability to recognize and reconstruct potential decay angle distributions

as they might appear in data.

As an example, we present results for longitudinally polarized D^* decay in Figure 5.20. We find that we are able to successfully reproduce the shape of the parent distribution in all cases. Close examination of our results points to a small bias introduced by the efficiency correction. This bias is caused by the large, but finite, amount of simulated Monte Carlo $\bar{B}^0 \rightarrow D^{*+}\omega\pi^-$ decays used to determine

our reconstruction efficiency. Even though the uncertainty on $\epsilon(\vec{x})$ is Gaussian, distributions such as $d\Gamma/dm_X^2$ are obtained by dividing the observed distribution by the efficiency (recall Equation 5.9):

$$N(m_X^2) = \sum_{\text{signal}} \frac{1}{\epsilon(\vec{x}_i)} \quad - \quad \left(\frac{4}{7}\beta\right) \sum_{\text{sideband}} \frac{1}{\epsilon(\vec{x}_j)}, \qquad (5.19)$$

and the factor of $1/\epsilon(\vec{x})$ does not obey Gaussian statistics.

Fortunately, this bias is bounded by the measurement uncertainty for the reconstruction efficiency. Our deviation from the true efficiency is characterized by the statistical uncertainty on the binned efficiency. Our decision to merge groups of low-statistics bins in our determination of the reconstruction efficiency was motivated in part by the desire to minimize the size of this bias. In the limit of infinite Monte Carlo sample size, the bias due to this effect would vanish.

In order to quantify the bias on the nominal result due to the finite amount of signal Monte Carlo events available, we first generate a set of 400 new ϵ', c_1'. and c_2' templates based on the nominal efficiency templates. If the measured efficiency in a given bin of the nominal template is $\mu \pm \sigma$, the corresponding efficiencies in the new templates are drawn from a Gaussian distribution of mean μ and standard deviation σ. We then determine the mean number of reconstructed signal events in data ($N(m_X^2)$, see Equation 5.19) for each of the 400 new efficiency templates. As expected, this mean overshoots the nominal result by a few percent (δ).

We then repeat this procedure using signal Monte Carlo. One sample is desig-nated as the "efficiency" sample, and is used to calculate the nominal "efficiency" as well as the 400 new "efficiency" templates. These templates are then used on a second sample of signal Monte Carlo which acts as "data". In this fashion, we are able to describe the bias in terms of the quantity δ. From these signal Monte Carlo studies, we find that after applying the efficiency correction and subtract-ing the m_ω sideband, the total number of events reconstructed using signal Monte Carlo exceeds the true value by $(0.6 \pm 0.4) \cdot \delta$. We correct our final results by this amount, which is on the order of a few percent.
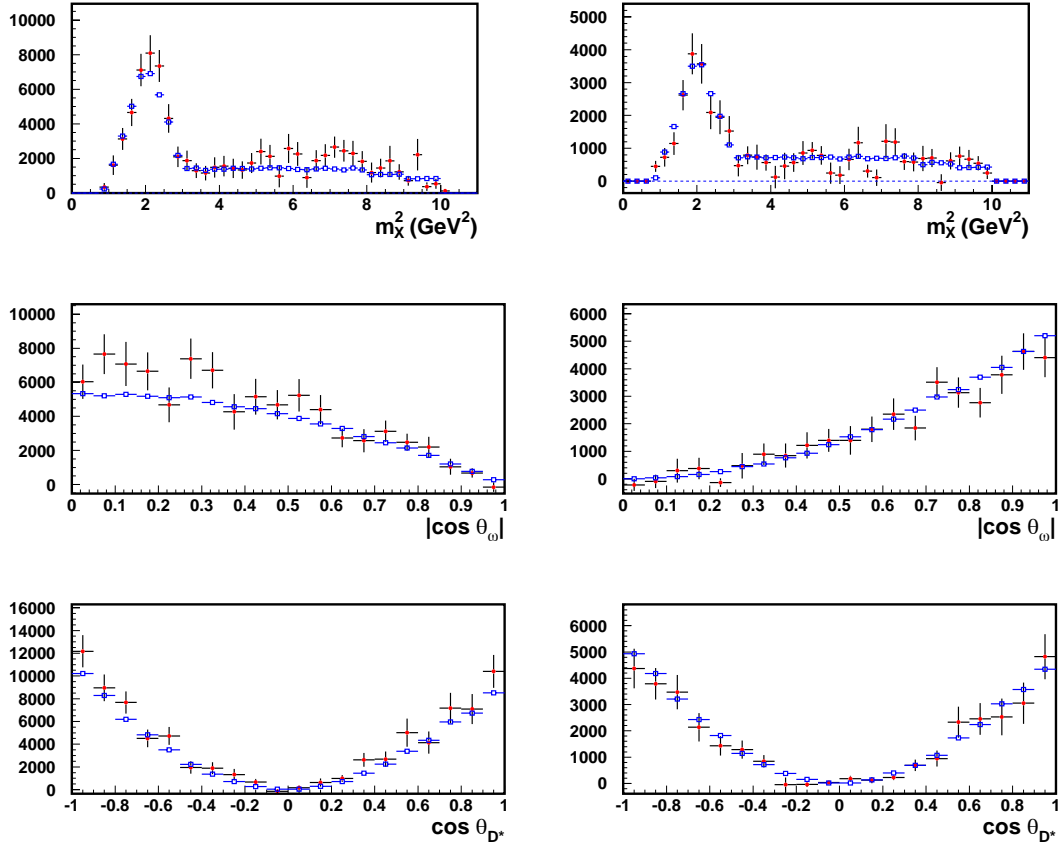
Figure 5.20: Efficiency-corrected and m_ω sideband subtracted distributions for modified $\bar{B}^0 \to D^{*+}\omega\pi^-$ Monte Carlo events (described in the text). (Top row) m_X^2 distribution; (Middle row) $\cos\theta_\omega$ distribution; (Bottom row) $\cos\theta_{D^*}$ distribution. In these plots, the D^* is longitudinally polarized, and each column represents a different forced behavior for the ω: (Left) transverse and (Right) longitudinal polarization. After correcting for reconstruction efficiency and applying the m_ω sideband subtraction, we compare our results (red points) to the generated distribution (open blue squares) in each plot. We correct the reconstructed m_X^2 values for m_ω sideband events as described according to Equation 5.19, where we set $\beta = 0.975$.

5.4   Results and Systematics

After correcting for reconstruction efficiency and applying the background subtraction using the m_ω sidebands, we are able to determine the branching fraction, the m_X^2 distribution, the Dalitz plot (E_ω^B, $E_{D^*}^B$) distribution, the $m_{D^*\pi}$ distribution, and the polarization of the D^* as a function of m_X for $\bar{B}^0 \to D^{*+}\omega\pi^-$ decay.

We first consider the branching fraction for $\bar{B}^0 \to D^{*+}\omega\pi^-$ decay, which is determined as follows:

$$\mathcal{B}(\bar{B}^0 \to D^{*+}\omega\pi^-) \equiv \frac{\sum_{m_X^2} N(m_X^2)}{N_{B\bar{B}} \times \epsilon_{\text{Corr}} \times \Pi_{BF} \times \Delta m_X^2}, \tag{5.20}$$

where $\sum_{m_X^2} N(m_X^2)$ describes the efficiency-corrected number of events remaining after m_ω sideband subtraction (see Equation 5.19), $N_{B\bar{B}}$ describes the number of $\Upsilon(4S) \to B\bar{B}$ decays present in the BABAR dataset, and

$$\Pi_{BF} \equiv BF(\omega \to \pi\pi\pi^0) \times BF(D^* \to D^0\,\pi) \times BF(D^0 \to K\pi, K\pi\pi^0, K3\pi) \tag{5.21}$$

represents the product of the relevant branching fractions for reconstructed events. The quantity ϵ_{Corr} summarizes the cut-based corrections to the reconstructed efficiency determined from simulated Monte Carlo decays as discussed in Section 5.1.6.

Before we extract the branching fraction, and other results, from reconstructed $\bar{B}^0 \to D^{*+}\omega\pi^-$ events, it is useful to discuss the systematic uncertainties associated with our analysis.

5.4.1 Systematic uncertainties

Evaluating the systematic uncertainties that are present in measurements of $\bar{B}^0 \to D^{*+}\omega\pi^-$ events is fairly straightforward. We may group our uncertainties into two categories:

1. **Bin-by-bin uncertainties**, which vary as a function of m_X^2;

2. **Global uncertainties**, which do not depend on the value of m_X^2.

We summarize these uncertainties below.

Recall from Section 5.3 that the $\bar{B}^0 \to D^{*+}\omega\pi^-$ reconstruction efficiency is stored as a set of two-dimensional histograms. This allows us to determine the reconstruction efficiency in a model-independent way, as we evaluate the efficiency at each point (bin) in the kinematically allowed region. Unfortunately, we are still sensitive to effects introduced from using a finite sample of Monte Carlo events. In Section 5.3.4 we investigated the nature of this bias. Creating 400 new efficiency templates, we were able to express this bias in terms of the quantity

$$\delta = \sum_{m_X^2} N(m_X^2) - \frac{1}{400} \sum_{i=1}^{400} \left(\sum_{m_X^2} N_i(m_X^2) \right), \tag{5.22}$$

where $N_i(m_X^2)$ represents the number of events reconstructed in a given bin of m_X^2 after correcting for the efficiency using the ith (of 400) efficiency template and performing the m_ω sideband subtraction.

Studies of this effect using signal Monte Carlo events imply that we need to correct our nominal yield by $(0.6\pm0.4)\cdot\delta$. In Table 5.4 we summarize the correction to $\sum_{m_X^2} N(m_X^2)$ as a function of the D^0 decay mode. This correction modifies the results obtained for the $\bar{B}^0 \to D^{*+}\omega\pi^-$ branching fraction, m_X^2 distribution, Dalitz plot distribution, and $m_{D*\pi}$ distribution by a few percent (The D^* polarization measurement is not affected as we compute a ratio of reconstructed events). Notice that the correction varies according to the decay of the D^0, as we do not expect δ to be constant across all D^0 modes. In addition, we examine the $N(m_X^2)$ distribution

D^0 Decay Mode	Bias Correction $\pm$ Systematic (%)
$D^0 \to K\pi$	-4.0 $\pm$ 2.7
$D^0 \to K\pi\pi^0$	-3.5 $\pm$ 2.4
$D^0 \to K3\pi$	-4.9 $\pm$ 3.3

Table 5.4: Bias (in %) due to finite signal Monte Carlo sample size, separated by D^0 decay mode.

in each bin of m_X^2 in order to determine the bin-by-bin measurement uncertainty. We take the RMS of the $N_i(m_X^2)$ distribution (in each bin of m_X^2) as the systematic uncertainty for the given bin. We present the results of this study in Figure 5.21. Overall, this systematic uncertainty is small when compared to the statistical error in each bin of m_X^2.

As mentioned in Section 5.3.3, we ignore a small region of $(E_{D*}^B, \cos\theta_{D*})$ phase space due to low acceptance. As a result, we miss some fraction of events beyond

$m_X^2 = 8.0$ GeV^2. The fraction of events lost depends on the polarization of the

D^* in this region and reaches nearly 50% as $\Gamma_L/\Gamma \to 1$ above $m_X^2 = 10$ GeV^2.

We rescale the number of events reconstructed at high values of m_X^2 in order

to account for lost events. We first calculate the scale factor needed in the case
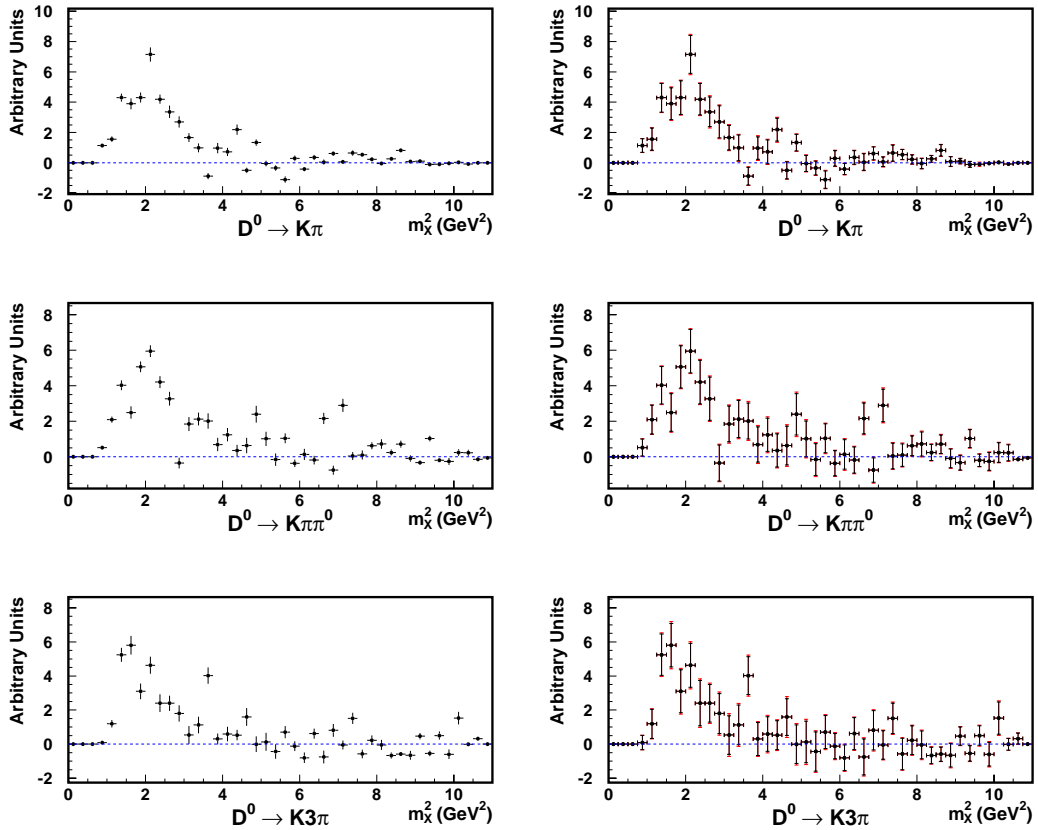
Figure 5.21: Bin-by-bin uncertainties for the m_X^2 distribution due to finite Monte Carlo sample size. At left, the uncertainty on each bin represents the uncertainty due to finite signal Monte Carlo sample size. At right, this uncertainty is combined in quadrature with the statistical error for each bin (black). The contribution from the Monte Carlo statistical uncertainty can be seen as the (red) extension on the nominal statistical uncertainty. The scale of the vertical axis is arbitrary.

of fully longitudinally or transversely polarized D^* mesons. We take the average of these values as our correction factor and assign an uncertainty large enough to cover both polarization extremes. For example, for $8.0 \leq m_X^2 < 9.0$ GeV^2, we obtain a scale factor of 1.32 for full longitudinal polarization (to account for a loss of 24.4% of the events) and 1.03 if $\Gamma_L = 0$ (2.8% of the events lost). We then assign a correction factor of 1.18 ± 0.15, which increases the total signal yield by $(18 \pm 13)\%$ for $8.0 \leq m_X^2 < 9.0$ GeV^2. These results are summarized in Table 5.5. This correction has a very small impact on both our nominal results and the total systematic uncertainty, as there are very few events in the data found at high values of m_X^2.

m_X^2 Range (GeV^2)	$\Gamma_L = \Gamma$	$\Gamma_L = 0$	Correction Factor
8.0 - 9.0	24.4	2.8	1.18 ± 0.15
9.0 - 10.0	39.2	10.4	1.38 ± 0.26
10.0 - 11.0	46.8	21.6	1.58 ± 0.30

Table 5.5: Corrections to the event yield at high m_X^2. The fraction of events lost (in %) in bins of m_X^2 are given assuming fully longitudinally ($\Gamma_L = \Gamma$) or transversely ($\Gamma_L = 0$) polarized D^* mesons. From these results, we compute a correction factor for the signal yield in this region. The correction factor is given in the far right column.

Several of the systematic uncertainties for the analysis of $\bar{B}^0 \rightarrow D^{*+}\omega\pi^-$ events are independent of m_X^2. We list these global uncertainties below, and summarize our findings in Table 5.7.

- At *BABAR*, it is estimated that the uncertainty on the reconstruction efficiency of neutral pions is 3% per π^0. This amounts to a 6% systematic uncertainty on our results for events reconstructed with $D^0 \to K\pi\pi^0$, and 3% for the other modes. Combining D^0 decay modes, we assign a systematic uncertainty of 4.3% from this source.

- The uncertainty associated with the reconstruction of charged particles at *BABAR* depends on the transverse momentum of the reconstructed track. Using a variety of control samples, we estimate a 0.6% (0.8%) uncertainty for each track with transverse momentum above (below) 200 MeV in the lab frame. Low momentum charged pions produced in D^* decay carry an additional uncertainty. Neglecting the soft pion (from the D^*) for the moment, we assign a systematic uncertainty of 3.1% for $D^0 \to K\pi, K\pi\pi^0$ decays and 4.3% for $D^0 \to K3\pi$ decays. This yields a partial tracking systematic uncertainty of 3.4% for all D^0 modes. After we include the additional systematic uncertainty associated with the reconstruction of the soft pion, we obtain a total tracking systematic uncertainty of 5.3%.

- The uncertainty associated with particle identification at *BABAR* is calibrated using a sample of $D^* \to D^0 \pi, D^0 \to K\pi$ decays. We assign a systematic uncertainty of 2% for the kaon from the D^0 decay.

- In Section 5.1.6, we found small differences in the selection efficiency between Monte Carlo and data. We adjust the Monte Carlo efficiency to account for this discrepancy, and assign a systematic uncertainty to our results due to this correction. We summarized our findings in Table 5.1, which we repeat here (Table 5.6) for convenience. The systematic uncertainty associated with the event selection criteria are 3.7% for $D^0 \rightarrow K\pi, K3\pi$, and 5.0% for $D^0 \rightarrow K\pi\pi^0$.

Variable	Correction	Uncertainty (%)
m_ω	1.032	1.0
R_{CLEO}	none	2.1
m_{D^0}	none	1.0
Rel. wgt.	0.927 ($K\pi\pi^0$)	3.3 ($K\pi\pi^0$)
δm	none	none
$\theta_B + \mathcal{F}$	0.945	1.9
m_{ES}	none	none
ΔE	0.972 ($K\pi$), 1.020 ($K\pi\pi^0$), 1.019 ($K3\pi$)	2.0

Table 5.6: Summary of the cut-based corrections applied to the Monte Carlo. Unless otherwise specified, the correction applies to all D^0 decay modes.

- The uncertainties associated with the world average D^*, D^0, and ω branching fractions [8] contribute 5% to our systematic uncertainty.

- There is a 1.1% uncertainty on the number of $\Upsilon(4S) \rightarrow B\bar{B}$ events in the BABAR event sample. The procedure used to determine this value is discussed in Reference [49].

- Using signal Monte Carlo $\bar{B}^0 \to D^{*+}\omega\pi^-$ events, we examined the effect of reconstruction resolution on the overall normalization of the m_X^2 distribution. Instead of using detector-derived values (m_X^2, E_ω^B, $E_{D^*}^B$, etc.) for each reconstructed $\bar{B}^0 \to D^{*+}\omega\pi^-$ decay, we took the true (generated) values for these quantities. By repeating our analysis using reconstructed values, we are able to quantify the effects of reconstruction on our results. We found that no bias is introduced by reconstruction resolution, and we assign a 1% systematic uncertainty to account for this effect.

- The 1% uncertainty on the quantity β in Equation 5.9 introduces an uncertainty on $\sum_{m_X^2} N(m_X^2)$ of 2.6%. We add this uncertainty to the total systematic uncertainty.

	$K\pi$	$K\pi\pi^0$	$K3\pi$	All D^0
Signal MC sample size (Bias)	2.7	2.4	3.3	2.8
π^0 reconstruction	3.0	6.0	3.0	4.3
Track reconstruction	5.0	5.0	6.1	5.3
Kaon identification	2.0	2.0	2.0	2.0
Event selection	3.7	5.0	3.7	4.3
$BF(D^*, D^0, \omega)$	2.3	6.8	4.7	5.0
$N(B\bar{B})$	1.1	1.1	1.1	1.1
Reconstruction resolution	1.0	1.0	1.0	1.0
m_ω sideband (β)	1.6	3.1	3.2	2.6
Total	8.4	12.4	10.5	10.5

Table 5.7: Global Systematic errors (in %) for $\bar{B}^0 \to D^{*+}\omega\pi^-$ reconstruction as a function of D^0 decay mode.

5.4.2 $\bar{B}^0 \to D^{*+}\omega\pi^-$ branching fraction

We correct our event yield $(\sum_{m_X^2} N(m_X^2)$ in Equation 5.20) to account for the bias introduced by the efficiency correction and to replace the events lost due to low acceptance. Combining all D^0 decay modes, we find

$$BF(\bar{B}^0 \to D^{*+}\omega\pi^-) = (2.88 \pm 0.21(\text{stat.}) \pm 0.31(\text{syst.})) \times 10^{-3},$$

where the total systematic uncertainty of 10.8% is the sum (in quadrature) of the 10.5% global systematic uncertainty (see Table 5.7) and the systematic uncertainties that vary as a function of m_X^2:

- The correction due to the removal of events in $(E_{D^*}^B, \cos\theta_{D^*})$ space: 0.3%.

- The bin-by-bin measurement uncertainty due to Monte Carlo sample size, estimated to be 2.4% for all D^0 modes.

These results are in good agreement with previous results from CLEO, $(2.9 \pm 0.3(\text{stat.}) \pm 0.4(\text{syst.})) \times 10^{-3}$ [25].

5.4.3 $d\Gamma/dm_X^2$ distribution

The differential decay rate, normalized to the semileptonic width $\Gamma(B^0 \to D^*\ell\nu)$, is presented in Figure 5.22. A common scale uncertainty of 11.3% is not shown. This uncertainty combines a 4.2% uncertainty in $\Gamma(B^0 \to D^*\ell\nu)$ with

the 10.5% uncertainty from the sources listed in Table 5.7. The bulk of the data is concentrated in a broad peak around $m_X^2 \approx 2$ GeV^2, in the region of $\rho(1450) \rightarrow \omega\pi$.

We compare our results to previous results from CLEO, and factorization predictions using $\tau^- \rightarrow \omega\pi^-\nu_\tau$ decay data, in the bottom half of Figure 5.22. We see no evidence for a breakdown in factorization up to the τ mass.
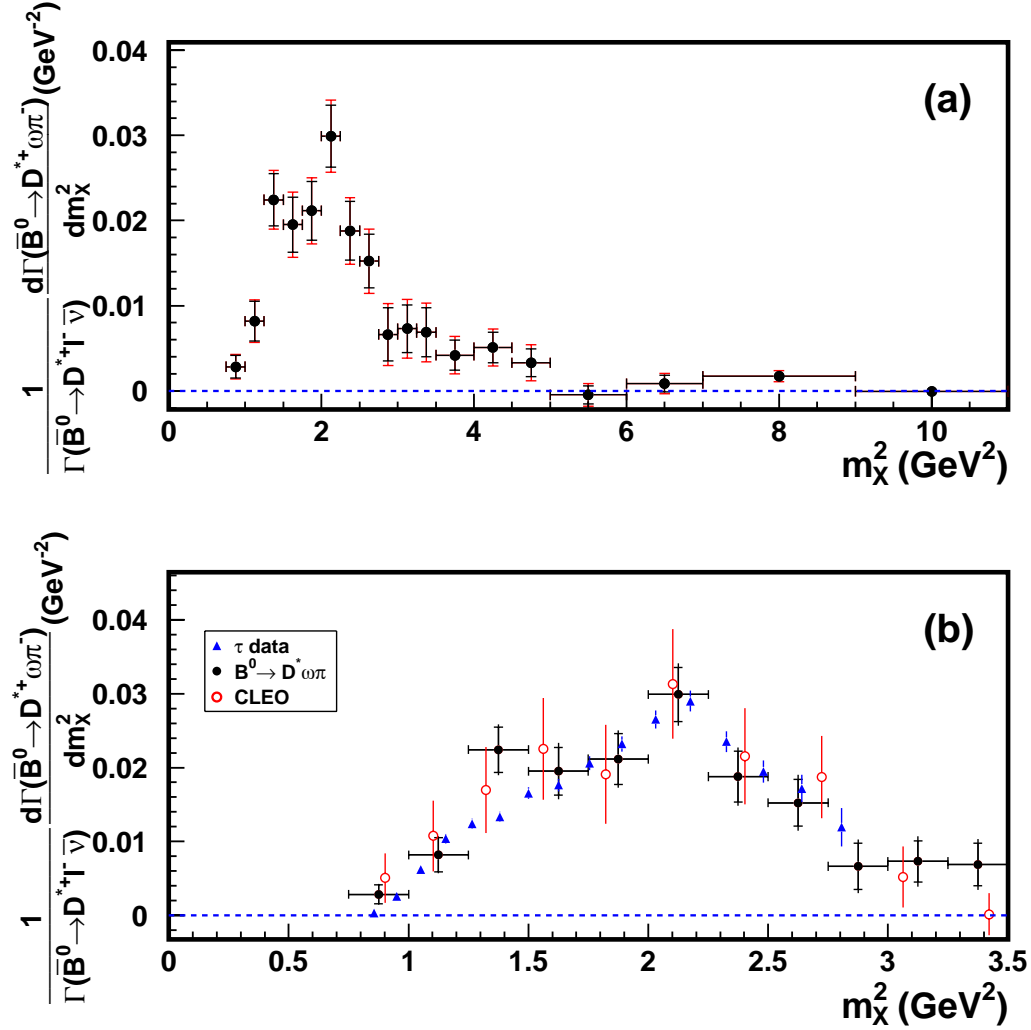
Figure 5.22: (a) Data m_X^2 (where $X = \omega\pi$) distribution normalized to the semileptonic width $\Gamma(B \to D^*\ell\nu)$. The inner error bars reflect the statistical uncertainties on the data. The total error bars include the m_X^2-dependent systematic uncertainties. A common 11.3% scale systematic uncertainty is not shown. (b) Same as (a) but zoomed-in on the low m_X^2 region, where comparisons based on factorization and τ data can be made. Also shown here are the results from the CLEO analysis [25].

5.4.4 $\bar{B}^0 \to D^{*+}\omega\pi^-$ **Dalitz plot**

With the large number of $B\bar{B}$ decays available at BABAR, it is possible to determine the Dalitz plot distribution for $\bar{B}^0 \to D^{*+}\omega\pi^-$ decay. We present the background-subtracted and efficiency-corrected Dalitz plot for all D^0 decay modes in Figure 5.23. We can clearly see an enhancement around $m_X^2 \approx 2$ GeV^2 indicating the presence of $\rho(1450) \to \omega\pi$ as seen in Figure 5.22 and expected from previous work by the CLEO collaboration [25]. One other notable feature of the decay distribution is the enhancement seen for $D^*\pi$ masses around 2.5 GeV ($m_{D^*\pi}^2 \sim 6.3$ GeV^2). This enhancement could be the result of the color-suppressed decay $B^0 \to \bar{D}^{**0}\omega$, $\bar{D}^{**0} \to D^{*-}\pi^+$.

5.4.5 $m_{D^*\pi}$ **distribution**

The spectroscopy of D^{**} states is shown in Figure 5.24. Four D^{**} states are expected, three of which can decay into $D^*\pi$ and thus contribute to our signal through $B^0 \to \bar{D}^{**0}\omega$ decay, followed by $\bar{D}^{**0} \to D^{*-}\pi^+$. The states that decay through a D-wave are expected to be narrow. These states are well established [8]:

- $D_1(2420)$:   mass = 2422 ± 2 MeV, $\Gamma = 19 \pm 4$ MeV

- $D_2^*(2460)$:   mass = 2459 ± 2 MeV, $\Gamma = 23 \pm 5$ MeV.
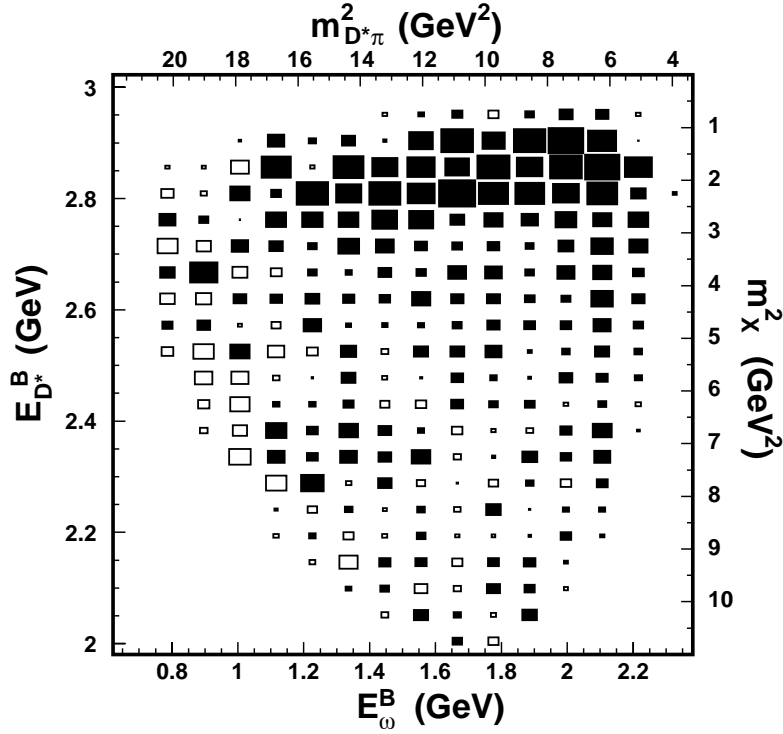
Figure 5.23: Background-subtracted and efficiency-corrected Dalitz plot for $\bar{B}^0 \to D^{*+}\omega\pi^-$. The relative box sizes indicate the population of the bins. Black boxes indicate positive values, white boxes indicate negative values, which can occur because of statistical fluctuations in the subtraction procedure.

The broad $D_1' \to D^*\pi$ state was first observed by the Belle collaboration in $B \to D_1'\pi$ decays, with $m_{D_1'} = 2427 \pm 36$ MeV, $\Gamma = 384^{+130}_{-105}$ MeV [50]. They measured $BF(B^- \to D_1'\pi^-) \times BF(D_1' \to D^{*+}\pi^-) = (5.0 \pm 1.1) \times 10^{-4}$. For comparison, $B^- \to D^{*0}\pi^-$ is about one order of magnitude larger.

According to HQET, if the broad enhancement seen in Figure 5.23 is the result of the $D_1' \to D^*\pi^-$, the decay is expected to proceed only via S-wave.
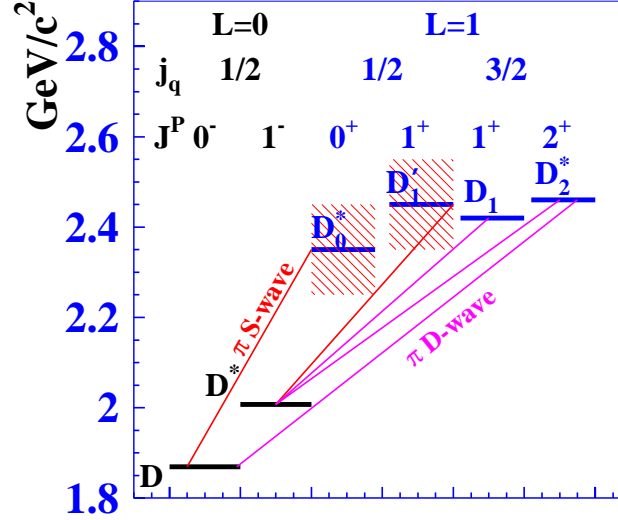
Figure 5.24: The expected spectroscopy of excited charmed mesons. Figure taken from Reference [50].

Consequently, we expect the population of efficiency-corrected and background-subtracted events should be uniform with respect to $\cos\theta_{**}$, where θ_{**} is defined in the $D^*\pi$ rest frame as the angle between the D^* and the direction opposite the flight of the $\bar{B}^0$. We present a plot of the efficiency-corrected and background-subtracted $m_{D^*\pi}$ vs. $\cos\theta_{**}$ distribution in Figure 5.25. If we omit the region dominated by $\rho(1450) \to \omega\pi$ decay $(\cos\theta_{**} < 0.5)$, we see that the $m_{D^*\pi} \sim 2.5$ GeV enhancement appears to be relatively uniform as a function of $\cos\theta_{**}$. This is consistent with expectations for S-wave $D_1' \to D^*\pi^-$ decay.
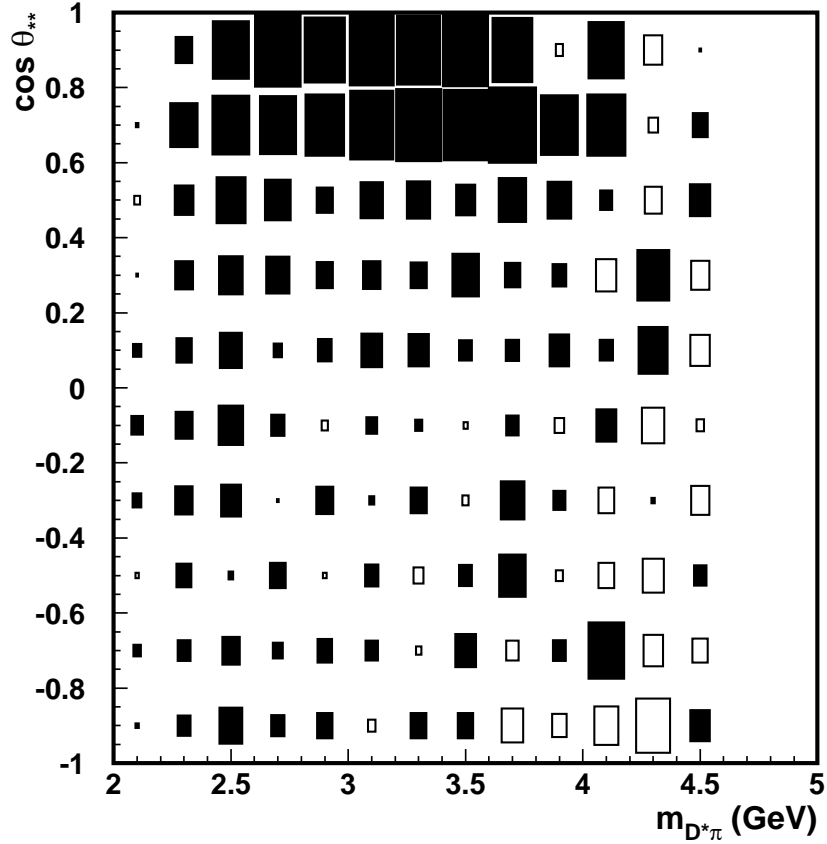
Figure 5.25: Plot of the $D^*\pi$ mass vs. $\cos\theta_{**}$ for reconstructed events in data after efficiency correction and m_ω sideband subtraction. All D^0 modes have been combined in this plot. The size of the boxes in the plot indicate the absolute deviation from zero events. Solid boxes indicate positive values, and negative values appear as open boxes.

In Figure 5.26 we present the efficiency-corrected and background-subtracted $m_{D^*\pi}$ distribution for events with $\cos\theta_{**} < 0.5$. The distribution is fit to the sum of a relativistic Breit-Wigner and a 4th order polynomial. The fitted mass and width of the Breit-Wigner in Figure 5.26 are m $= 2477\pm28$ MeV and $\Gamma = 266\pm97$

MeV, respectively. These values are consistent with the parameters of the broad D_1' measured by the Belle collaboration. We repeated this fit in bins of $\cos\theta_{**}$
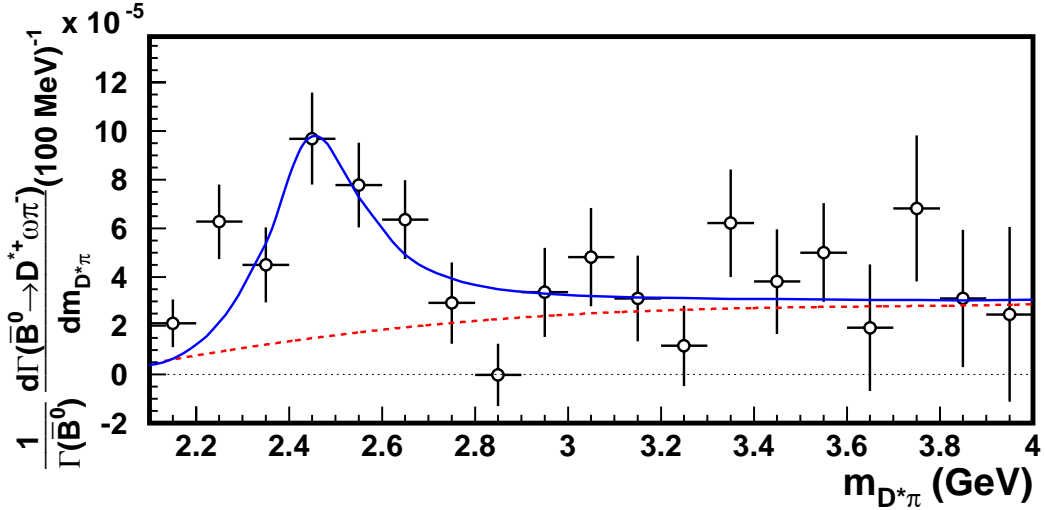
Figure 5.26: Background-subtracted and efficiency-corrected $D^*\pi$ mass distribution with $\cos\theta_{D^*} < 0.5$. The superimposed fit is described in the text.

in order to test the D_1' S-wave decay hypothesis, and the results are summarized in Table 5.8. Within statistical uncertainties, we find that the amplitude of the Breit-Wigner is consistent with expectations for S-wave $D_1' \to D^{*+}\pi^-$ decay. If we assume that the $m_{D^*\pi} \sim 2.5$ GeV enhancement is due to the color-suppressed $\bar{B}^0 \to D_1'\omega$, with S-wave $D_1' \to D^{*+}\pi^-$ decay, we may use our results to extract the branching fraction. The branching fraction is obtained using the fit for events with $\cos\theta_{**} < 0.5$, and scaling our result up by a factor of $\frac{4}{3}$ in order to cover the entire range of $\cos\theta_{**}$. This procedure neglects interference effects between

$\cos\theta_{**}$	mean (MeV)	width (MeV)	Yield
$-1.0 \to -0.5$	2463 ± 57	331 ± 200	14391 ± 7631
$-0.5 \to 0$	2377 ± 126	484 ± 208	14414 ± 4688
$0 \to 0.5$	2482 ± 42	296 ± 227	23943 ± 8397
$-1.0 \to 0.5$	2477 ± 28	266 ± 97	42826 ± 12707

Table 5.8: Results for BW+P_4 fit to the $m_{D^*\pi}$ distribution for efficiency corrected, background subtracted events in data. All D^0 modes have been combined for these fits. The yields are in arbitrary units.

$\bar{B}^0 \to D_1'\omega$ and $\bar{B}^0 \to D^{*+}\omega\pi^-$. We find

$$BF(\bar{B}^0 \to D_1'\omega) \times BF(D_1' \to D^{*+}\pi^-) = (4.1 \pm 1.2 \pm 0.4 \pm 1.0) \times 10^{-4}. \quad (5.23)$$

In this measurement, the first uncertainty is statistical and the second uncertainty (10.8%) is due to uncertainties in common with the $BF(\bar{B}^0 \to D^{*+}\omega\pi^-)$ measurement. The final uncertainty arises from the following sources:

- The uncertainty on the shape of the background in Figure 5.26. We assume different shapes for the background and observe the change in the yield of the Breit-Wigner. From this study, we estimate the uncertainty due to this effect is 10%.

- The uncertainties associated with the parameters of the D_1' resonance measured by Belle. We fit the $m_{D^*\pi}$ distribution assuming the Belle values for the mean and width of the Breit-Wigner and vary these numbers within their quoted uncertainties. We take the maximum deviation from our nominal yield (22%) as the systematic uncertainty.

The branching fraction in Equation 5.23 is comparable to the branching fractions for $\bar{B}^0 \to D^{(*)0}\omega$ [8]. We see no evidence for decays into the two narrow D^{**} resonances at 2420 and 2460 MeV. This is in contrast to the color-favored $B^- \to D^{**0}\pi^-$ decays, where the three D^{**} modes contribute with comparable strengths, and where the $B^- \to D_1'\pi^-$ branching fraction is one order of magnitude smaller than that of $B^- \to D^{(*)0}\pi^-$.

The presence of $\bar{B}^0 \to D_1'\omega$ would affect the comparison of the data with the theoretical predictions of Fig. 5.22. As can be seen in Fig. 5.23, $\bar{B}^0 \to D_1'\omega$ would mostly contribute at high m_X^2 values, while the factorization test can be carried out only where the τ data is available; *i.e.*, for $m_X^2 < 3$ GeV^2. Based on the estimated branching fraction of $\bar{B}^0 \to D_1'\omega$, and neglecting interference effects, the contribution of $\bar{B}^0 \to D_1'\omega$ to the m_X^2 distribution for values below 3 GeV^2 would be less than 5%.

5.4.6 D^* polarization

If the decay $\bar{B}^0 \to D^{*+}\omega\pi^-$ proceeds dominantly through $\bar{B}^0 \to D^{*+}\rho(1450)^-$, with $\rho(1450)^- \to \omega\pi^-$, a measurement of the polarization of the D^* can provide a further test of factorization and HQET [51]. The angular distribution in the $D^{*+} \to D^0\pi^+$ decay can be written as a function of three complex amplitudes H_0

(longitudinal), and H_+ and H_- (transverse), as

$$\frac{d\Gamma}{d\cos\theta_{D^*}} \propto 4|H_0|^2\cos^2\theta_{D^*} + (|H_+|^2 + |H_-|^2)\sin^2\theta_{D^*}, \qquad (5.24)$$

where θ_{D^*} is the decay angle of the D^* defined earlier. The longitudinal polarization fraction

$$\frac{\Gamma_L}{\Gamma} = \frac{|H_0|^2}{|H_0|^2 + |H_+|^2 + |H_-|^2}, \qquad (5.25)$$

can then be extracted using Equation 5.24 from a fit to the angular distribution in the decay of the D^*.

We divide our dataset in ranges of m_X^2, and perform binned chi-squared fits to the efficiency-corrected, background-subtracted, D^*-decay angular distributions. In Figure 5.27, we present the results of the fit for events in the range specified by the initial CLEO analysis: $1.1 < m_X < 1.9$ GeV. In these measurements, nearly all of the systematic uncertainties discussed in Section 5.4.1 cancel. As a result, the m_X^2-dependent uncertainty due to the finite Monte Carlo sample size is the dominant systematic uncertainty, and typically results in an uncertainty on Γ_L/Γ at the few percent level. We also include a systematic uncertainty due to the parameter β in Equation 5.9. This uncertainty is about one order of magnitude smaller.

The measured longitudinal polarization fractions as a function of m_X are presented in Table 5.9. Near the mean of the $\rho(1450)$ resonance ($1.1 < m_X < 1.9$

GeV), we find $\Gamma_L/\Gamma = 0.654 \pm 0.042(\text{stat.}) \pm 0.016(\text{syst.})$. This result is in agreement with the previous result in the same mass range from the CLEO collaboration, $\Gamma_L/\Gamma = 0.63 \pm 0.09$ [25]. It is also in agreement with predictions based on HQET, factorization, and the measurement of semileptonic B-decay
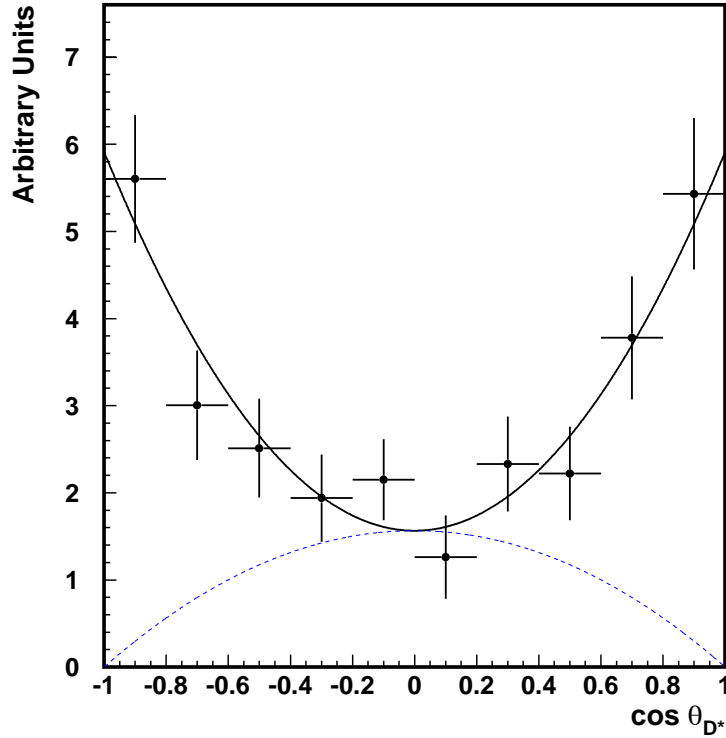
Figure 5.27: The $\cos\theta_{D^*}$ distribution for efficiency-corrected and background-subtracted events in data with $1.1 \leq m_X < 1.9$ GeV. All D^0 modes have been combined in this Figure. The full fit (adding the longitudinal and transverse components) is represented by the solid black line. The longitudinal component of the fit is taken as the difference between the full fit and the transverse component (dashed blue). The scale of the vertical axis is arbitrary.

form factors, $\Gamma_L/\Gamma = 0.684 \pm 0.009$ [28], assuming that the decay proceeds via

$\bar{B}^0 \to D^{*+}\rho(1450)^-$, $\rho(1450)^- \to \omega\pi^-$. These results are shown in Fig. 5.28.

m_X range (GeV)	Γ_L/Γ
below 1.1	$0.46 \pm 0.19 \pm 0.06$
1.1 - 1.35	$0.78 \pm 0.06 \pm 0.02$
1.35 - 1.55	$0.73 \pm 0.07 \pm 0.02$
1.55 - 1.9	$0.44 \pm 0.10 \pm 0.04$
1.9 - 2.83	$0.66 \pm 0.18 \pm 0.08$

Table 5.9: Results of the D^* polarization measurement in bins of m_X. The first uncertainty is statistical and the second is systematic.

As m_X^2 increases, we see from Table 5.9 that the D^* polarization measurement falls off from HQET and factorization predictions for $B \to D^* X_V$ decay, where X_V is a vector meson. In the m_X^2 region dominated by $\rho(1450) \to \omega\pi$, we may assume the decay of the $\bar{B}^0$ is well-described by $\bar{B}^0 \to D^{*+}\rho(1450)^-$, and it is useful to test factorization in this region. Away from the $\rho(1450)$, we would not expect the D^* polarization results to agree with predictions that assume a two-body vector-vector decay of the B.
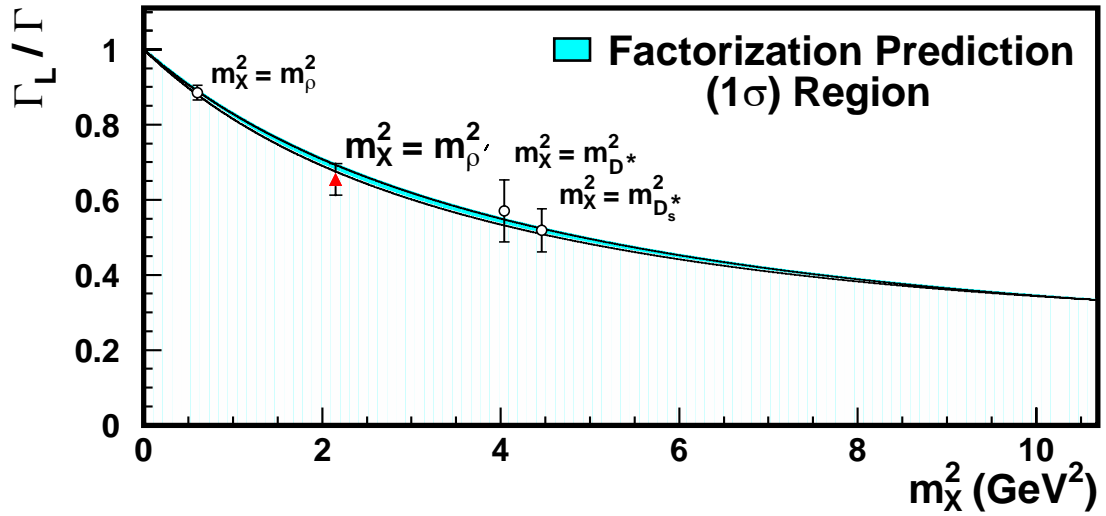
Figure 5.28: The fraction of longitudinal polarization as a function of m_X^2, where X is a vector meson. Shown (as a triangle) is the $\bar{B}^0 \to D^{*+}\omega\pi^-$ polarization measurement for events with $1.1 < m_X < 1.9$ GeV ($m_X^2 = m_{\rho'}^2$, where $\rho' \equiv \rho(1450)$), as well as earlier measurements (indicated by open circles) of $\bar{B}^0 \to D^{*+}\rho^-$ [24], $\bar{B}^0 \to D^{*+}D^{*-}$ [26], and $\bar{B}^0 \to D^{*+}D_s^{*-}$ [27]. The shaded region represents the prediction ($\pm$ one standard deviation) based on factorization and HQET, extrapolated from the semileptonic $\bar{B}^0 \to D^{*+}\ell^-\bar{\nu}$ form factor results [28].

5.5 Conclusions

We have studied the decay $\bar{B}^0 \to D^{*+}\omega\pi^-$ with a data sample that is approximately 20 times than what was previously available. The results reported here have been published in Reference [42].

We measure the branching fraction

$$BF(\bar{B}^0 \to D^{*+}\omega\pi^-) = (2.88 \pm 0.21(\text{stat.}) \pm 0.31(\text{syst.})) \times 10^{-3}, \qquad (5.26)$$

and the invariant mass spectrum of the $\omega\pi$ system is found to be in agreement with theoretical expectations based on factorization and τ decay data. The Dalitz plot for this mode is very non-uniform, with most of the rate at low $\omega\pi$ mass. We also find an enhancement for $D^*\pi$ masses broadly distributed around 2.5 GeV. This enhancement could be due to color-suppressed decays into the broad D'_1 resonance, $\bar{B}^0 \to D'_1\omega$, followed by $D'_1 \to D^{*+}\pi^-$, with a branching fraction comparable to $\bar{B}^0 \to D^{(*)0}\omega$.

We also measure the fraction of D^* longitudinal polarization in this decay. In the region of $\omega\pi$ mass between 1.1 and 1.9 GeV, where one expects contributions from $\bar{B}^0 \to D^{*+}\rho(1450)^-$, $\rho(1450)^- \to \omega\pi^-$, we find $\Gamma_L/\Gamma = 0.654 \pm 0.042(\text{stat.}) \pm 0.016(\text{syst.})$, in agreement with predictions based on HQET, factorization, and the measurement of semileptonic B-decay form factors.

5.5.1 Future prospects

The current B$_A$B$_{AR}$ data sample, accumulated through August 2006, contains close to double the number of $B\bar{B}$ events used in this analysis. The factorization comparison using the m_X^2 distribution still requires more data between 2 to 3 GeV^2 in order to effectively probe the role of perturbative QCD in factorization. Continued analysis of this decay mode could reduce statistical uncertainties to a point where more rigorous comparisons could be made. Additionally, the broad enhancement seen at $m_{D^*\pi} \approx 2.5$ GeV could be explored in more detail, which could lead to more information regarding excited charm mesons.

Chapter 6

Introduction to CP Violation

A funny thing happened in 1964. At the Alternating Gradient Synchrotron in Brookhaven, the group of Christenson, Cronin, Fitch, and Turlay observed the decay $K_L \to \pi^+\pi^-$ [52], which was expected to be forbidden. Awarded the Nobel Prize for this work in 1980, Fitch notes in his Nobel lecture that

> ...Professor Cronin and I are being honored for a purely experimental discovery, a discovery for which there were no precursive indications, either theoretical or experimental. It is a discovery for which after more than 16 years there is no satisfactory accounting. But...it touches on our understanding of nature at its deepest level [53].

This discovery of CP violation in the kaon system, although unexpected, has been a great benefit to physicists. This feature of Nature is needed to help explain the dominance of matter in the universe [54], although it is worth noting that the Standard Model mechanism for CP violation in the quark sector cannot account for the matter-antimatter imbalance we see in the universe today [4].

We may test the Standard Model of particle interactions by measuring the effects of CP violation in the B meson system and comparing experimental results to Standard Model predictions. In this Chapter, I will introduce the Standard Model picture of CP violation and discuss the first observation of this phenomena in the K system. I will then discuss the CP observable $\sin 2\beta$ and the benefits of the B meson system. In preparing this introduction, I found the review by Richman [14] to be particularly useful.

6.1 Terminology and First Observation of CP Violation

Symmetries of a given physical system are of great interest in physics. As an example, the equations of motion in a system that is spherically symmetric lead to angular momentum conservation. In particle physics, we focus our attention on three discrete transformations that are potential symmetries of a field theory Lagrangian [55]:

- Charge conjugation, represented by the unitary operator C, which converts a particle to its antiparticle;

- Parity inversion, represented by the unitary operator P, inverts the spatial coordinates of the system: $(t, \vec{x}) \rightarrow (t, -\vec{x})$;

- Time inversion, which reverses the flow of time in the interaction. Represented by the operator T, it sends $(t, \vec{x}) \rightarrow (-t, \vec{x})$.

All observations to date indicate that the operation CPT is a perfect symmetry of Nature. All forces, with the exception of the weak interaction, are symmetric with respect to each of the C, P, and T transformations individually. C and P are violated by the weak interaction, but before 1964 there was no evidence that CP was not conserved.

If we consider a particle M with four-momentum $(E, \vec{p})$ and helicity λ, then under parity inversion

$$P|M(E, \vec{p}, \lambda)\rangle = \eta_P |M(E, -\vec{p}, -\lambda)\rangle. \tag{6.1}$$

As the parity transformation reverses the momentum direction without affecting spin, the helicity $\lambda = \vec{s} \cdot \hat{p}$ reverses sign under parity. We require P to satisfy the conditions $P^2 = 1$ and $P = P^{-1} = P^\dagger$, which forces $\eta_P = \pm 1$.

Parity violation in the weak interaction was first observed in the β-decay of cobalt nuclei:

$$^{60}\text{Co} \rightarrow {}^{60}\text{Ni} + e^- + \bar{\nu}_e.$$

The nuclear spins in the ^{60}Co sample were aligned using an external magnetic field, and an asymmetry was observed in the direction of the emitted electrons [56]. This indicates that the electrons have a preferred emission direction, which violates parity conservation.

Under charge conjugation, we find

$$C|M(E,\vec{p},\lambda)\rangle = \eta_C|\bar{M}(E,\vec{p},\lambda)\rangle, \tag{6.2}$$

where $\bar{M}$ is the antiparticle of M, and the momentum and helicity are unchanged in the operation. Paralleling our treatment of P, $C^2 = 1$ and $C = C^{-1} = C^\dagger$ implies

$$|M\rangle = C^2|M\rangle = \eta_C(M)|\bar{M}\rangle = \eta_C(M)\eta_C(\bar{M})|M\rangle \tag{6.3}$$

so that $\eta_C(M)\eta_C(\bar{M}) = 1$, leaving $\eta_C(M) = e^{i\theta_C}$, or $\eta_C(M) = \eta_C(\bar{M}) = \pm 1$ if M is an eigenstate of C.

It is easy to see that the weak interaction violates both parity and charge conjugation invariance when we examine interactions involving a neutrino. Experimental evidence indicates that only left-handed neutrinos ν_L (or right-handed anti-neutrinos $\bar{\nu}_R$) participate in the weak interaction. Consequently,

$$\Gamma(\pi^+ \to \mu^+\nu_L) \neq \Gamma(\pi^+ \to \mu^+\nu_R) = 0 \qquad \text{violates } P$$

$$\Gamma(\pi^+ \to \mu^+\nu_L) \neq \Gamma(\pi^- \to \mu^-\bar{\nu}_L) = 0 \qquad \text{violates } C,$$

where in this case ν is a muon neutrino. This result is a feature of the $V - A$ structure of the charged weak current, which suppresses final states with the "wrong" helicity configuration. Parity inversion and charge conjugation convert a left-handed neutrino into a right-handed neutrino or a left-handed anti-neutrino, respectively. Both of these final states are forbidden, in the limit of zero neutrino mass, by the weak interaction. However, the combined transformation CP

$$CP|M(E, \vec{p}, \lambda)\rangle = \eta_{CP}|\bar{M}(E, -\vec{p}, \lambda)\rangle, \tag{6.4}$$

where $\eta_{CP} = \eta_C \cdot \eta_P$, results in the allowed configuration $\nu_L \to \bar{\nu}_R$ for the outgoing neutrino.

In order to see that CP is not conserved by the weak interaction, let us consider the kaon system, where CP violation was first observed. This system has a neutral pseudoscalar meson ($K^0 = \bar{s}d$) which is distinct from its antiparticle ($\bar{K}^0 = s\bar{d}$). Both particles may decay to a two-pion final state ($\pi^+\pi^-$ or $\pi^0\pi^0$). The 2π system is in an eigenstate of CP with eigenvalue

$$\eta_{CP}(\pi\pi) = (-1)^\ell (\eta_P)^2 \eta_C \eta_C^* = 1, \tag{6.5}$$

where $\ell = 0$ is the orbital angular momentum of the system. Neither the K^0 nor the $\bar{K}^0$ mesons are eigenstates of CP:

$$CP|K^0\rangle = e^{2i\theta_{CP}}|\bar{K}^0\rangle \qquad CP|\bar{K}^0\rangle = e^{-2i\theta_{CP}}|K^0\rangle. \tag{6.6}$$

If we assume that CP is conserved by the weak interaction, we can construct two orthogonal CP eigenstates with eigenvalues $\eta_{CP} = \pm 1$:

$$
\begin{aligned}
K_S \equiv |K_{(CP+)}\rangle &= \frac{1}{\sqrt{2}}(|K^0\rangle + e^{2i\theta_{CP}}|\bar{K}^0\rangle) \\
K_L \equiv |K_{(CP-)}\rangle &= \frac{1}{\sqrt{2}}(|\bar{K}^0\rangle - e^{2i\theta_{CP}}|K^0\rangle)
\end{aligned} \tag{6.7}
$$

If CP is conserved in K^0 decays, then the amplitude for $K^0 \to \pi\pi$ decay can be described as follows:

$$
A_{2\pi} \equiv \langle 2\pi|H|K^0\rangle = e^{2i\theta_{CP}}\langle 2\pi|H|\bar{K}^0\rangle \equiv e^{2i\theta_{CP}}\bar{A}_{2\pi}, \tag{6.8}
$$

where we have taken advantage of the fact that $(CP)(CP)^\dagger = 1$ by definition, and the that the operator for a conserved quantity commutes with the Hamiltonian. It follows that

$$
\begin{aligned}
A_{2\pi}^\pm &= \langle 2\pi|H|K_{(CP\pm)}\rangle \\
&= \frac{1}{\sqrt{2}}(\langle 2\pi|H|K^0\rangle \pm e^{2i\theta_{CP}}\langle 2\pi|H|\bar{K}^0\rangle) \\
&= \frac{1}{\sqrt{2}}(A_{2\pi} \pm e^{2i\theta_{CP}}\bar{A}_{2\pi}) \\
&= \frac{1}{\sqrt{2}}(A_{2\pi} \pm e^{2i\theta_{CP}}e^{-2i\theta_{CP}}A_{2\pi}) \\
&= \frac{1}{\sqrt{2}}A_{2\pi}(1 \pm 1),
\end{aligned}
$$

which implies that the $\eta_{CP} = -1$ eigenstate (K_L) cannot decay into two pions. In reality, the long-lived K_L decays into a two pion final state with branching ratios

$$BF(K_L \to \pi^+\pi^-) = (20.90 \pm 0.25) \times 10^{-4}$$

$$BF(K_L \to \pi^0\pi^0) = (9.32 \pm 0.12) \times 10^{-4} \ [8],$$

which was the first evidence that the weak interaction violates CP conservation.

6.2 CP Violation and the CKM matrix

In the Standard Model, the charged weak current operator $\mathcal{J}^\mu$ couples the W boson to quarks:

$$\mathcal{J}^\mu \equiv \sum_{i,j} \bar{u}_i \gamma^\mu \frac{1 - \gamma_5}{2} V_{ij} d_j. \tag{6.9}$$

The indices i, j run over the three quark generations, and the operators $u_i(d_i)$ annihilate up(down)-type quarks or create their antiparticles. The constants V_{ij} are elements of the Cabibbo-Kobayashi-Maskawa (CKM) matrix [57, 58].

The CKM matrix is a unitary matrix that represents a "rotation" from the mass eigenstates (d, s, b) to a new set of weak eigenstates (d', s', b'):

$$\begin{pmatrix} d' \\ s' \\ b' \end{pmatrix} = \begin{pmatrix} V_{ud} & V_{us} & V_{ub} \\ V_{cd} & V_{cs} & V_{cb} \\ V_{td} & V_{ts} & V_{tb} \end{pmatrix} \begin{pmatrix} d \\ s \\ b \end{pmatrix} \tag{6.10}$$

The charged weak current then couples to the "rotated" quark states

$$\begin{pmatrix} u \\ d' \end{pmatrix} \quad \begin{pmatrix} c \\ s' \end{pmatrix} \quad \begin{pmatrix} t \\ b' \end{pmatrix}.$$

To a good approximation, the CKM matrix is diagonal, so that the transitions $d \to u$, $c \to s$, and $t \to b$ are dominant. However, none of the off-diagonal elements are exactly zero. This leads to weak transitions that span quark generations and, as it turns out, produce CP violation in the quark sector.

The CKM elements, and the fermion mass terms, appear in the Standard Model as couplings of fermions to the Higgs field [59]. These Yukawa terms in the Lagrangian are not required to preserve quark flavor:

$$\mathcal{L}_{Yukawa} = \sum_{i,j} \left[Y_{ij}(\bar{u}_L^i \ \ \bar{d}_L^i)\phi^\dagger u_R^j + Y'_{ij}(\bar{u}_L^i \ \ \bar{d}_L^i)\phi d_R^j + \text{herm. conj.} \right], \qquad (6.11)$$

where the indices i, j run over the quark generations, L and R represent the left- and right-handed components of the quark fields, and the Yukawa couplings are given by the terms Y_{ij} and Y'_{ij}.

In the Standard Model, the complex Higgs field ϕ acquires a vacuum expectation value from spontaneous breaking of $SU(2)$ symmetry,

$$\phi(x) \equiv \begin{pmatrix} \phi^+ \\ \phi^0 \end{pmatrix} \to \frac{1}{\sqrt{2}} \begin{pmatrix} 0 \\ v + H(x) \end{pmatrix}, \qquad (6.12)$$

where v is the Higgs vacuum expectation value and the field $H(x)$ corresponds to the Higgs boson. After spontaneous symmetry breaking of the Higgs field, the

Lagrangian is modified:

$$\mathcal{L}_{Yukawa} = \sum_{i,j} \left[Y_{ij} \bar{u}_L^i u_R^j + Y'_{ij} \bar{d}_L^i d_R^j + \text{herm. conj.} \right] \cdot \frac{1}{\sqrt{2}} \left(v + H(x) \right). \qquad (6.13)$$

The terms proportional to v couple to the left- and right-handed components of the quark fields, thereby introducing mass terms to the Lagrangian

$$m_{ij} = -\frac{v}{\sqrt{2}} Y_{ij} \quad \text{and} \quad m'_{ij} = -\frac{v}{\sqrt{2}} Y'_{ij}.$$

We may determine the mass of the quarks by diagonalizing the quark mass matrices m_{ij} and m'_{ij}. This feat may be accomplished using a set of unitary matrices. The CKM matrix is a product of these matrices, and is unitary by construction. By convention, we define the CKM matrix to act on the down-type quarks.

At present, the values of the CKM matrix elements can only be determined by experiment. They must be taken as inputs to the Standard Model, as we mentioned in Chapter 1. We might guess from Equation 6.10 that we need to experimentally determine the values of all nine CKM elements, but these elements can be completely determined in terms of only four real, independent parameters in the Standard Model:

- An arbitrary $n \times n$ unitary matrix has $2n^2$ real parameters, but not all of these parameters are independent. There are n constraints due to the normalization of each column, and $n(n-1)$ constraints from orthogonality

relations between each pair of columns. This leaves a total of n^2 independent real parameters.

- As physical interactions are not affected if we attach a phase factor to each of the quark operators ($u \rightarrow u e^{i\theta_u}$), not all of the n^2 parameters are physically significant. In fact, $2n - 1$ phases, where n is the number of quark generations, can be absorbed by our ability to select phases for the quark fields. As a result, there are $n^2 - (2n-1) = (n-1)^2$ independent physical parameters in the CKM matrix for n quark generations. As $n = 3$ in the Standard Model, this implies the nine CKM elements can be expressed in terms of four independent physical (real) parameters.

The standard parameterization of the CKM matrix in the Standard Model expresses the nine CKM elements in terms of three rotation angles (θ_{12}, θ_{13}, and θ_{23}) and one phase δ [60]:

$$
V_{ij} = \begin{pmatrix} c_{12}c_{13} & s_{12}c_{13} & s_{13}e^{-i\delta} \\ -s_{12}c_{23} - c_{12}s_{23}s_{13}e^{i\delta} & c_{12}c_{23} - s_{12}s_{23}s_{13}e^{i\delta} & s_{23}c_{13} \\ s_{12}s_{23} - c_{12}c_{23}s_{13}e^{i\delta} & -c_{12}s_{23} - s_{12}c_{23}s_{13}e^{i\delta} & c_{23}c_{13} \end{pmatrix} \tag{6.14}
$$

where $c_{ij} \equiv \cos\theta_{ij}$ and $s_{ij} \equiv \sin\theta_{ij}$.

In the Standard Model, CP violation in the quark sector originates from the phase factor δ in Equation 6.14. If $\delta = 0$, then all nine CKM elements would

be real and CP would be conserved. In addition, with fewer than three quark generations, the phase factor vanishes. It turns out that the Standard Model only provides a mechanism for CP violation in the event that we have at least six quarks.

In order to demonstrate the importance of three quark generations with regards to CP violation, let us return briefly to $K^0/\bar{K}^0 \to \pi^+\pi^-$ decay. If there were only two quark generations, then the two-generation quark mixing matrix is entirely real and can be expressed in terms of a single rotation angle θ_C:

$$\begin{pmatrix} d' \\ s' \end{pmatrix} = \begin{pmatrix} V_{ud} & V_{us} \\ V_{cd} & V_{cs} \end{pmatrix} \begin{pmatrix} d \\ s \end{pmatrix} = \begin{pmatrix} \cos\theta_C & \sin\theta_C \\ -\sin\theta_C & \cos\theta_C \end{pmatrix} \begin{pmatrix} d \\ s \end{pmatrix}. \tag{6.15}$$

θ_C is known as the Cabibbo angle, and $\sin\theta_C \approx 0.22$ [57]. Ignoring penguin decay, the interference between K mixing and direct decay (See Feynman diagrams for $\bar{K}^0 \to \pi^+\pi^-$ decay in Figure 6.1) yields decay amplitudes that are of the form

$$A_{2\pi} \equiv A(K^0 \to \pi^+\pi^-) = c_1 \cdot V_{us}^* V_{ud} + c_2 \cdot \left(\frac{V_{cs}^* V_{cd}}{V_{cs} V_{cd}^*}\right) V_{us} V_{ud}^*$$

$$\bar{A}_{2\pi} \equiv A(\bar{K}^0 \to \pi^+\pi^-) = c_1 \cdot V_{us} V_{ud}^* + c_2 \cdot \left(\frac{V_{cs} V_{cd}^*}{V_{cs}^* V_{cd}}\right) V_{us}^* V_{ud} \tag{6.16}$$

where the coefficients $c_1 \equiv |c_1|e^{i\delta_1}$ and $c_2 \equiv |c_2|e^{i\delta_2}$ (δ_1 and δ_2 are commonly called strong phases) describe various QCD effects. The strong phases (and by extension, c_1 and c_2) do not change sign under CP.

Consequently, the difference in the decay rates is proportional to

$$|\bar{A}_{2\pi}|^2 - |A_{2\pi}|^2 = 4 \cdot \text{Im}(c_1 c_2^*) \cdot \text{Im}\left[(V_{us}^* V_{ud})^2 \frac{V_{cs} V_{cd}^*}{V_{cs}^* V_{cd}}\right]. \tag{6.17}$$

The unitarity of the CKM matrix requires $V_{us}^* V_{ud} + V_{cs}^* V_{cd} = 0$, and so there can be no CP asymmetry in this decay.
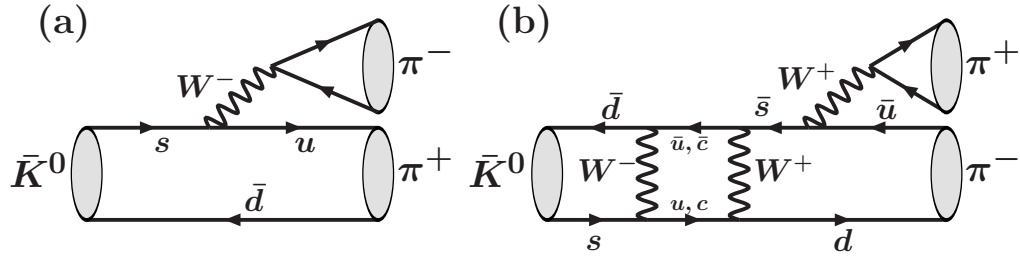
Figure 6.1: Tree and Mixing Feynman diagrams for $\bar{K}^0 \to \pi^+ \pi^-$ decay. In (a), the $\bar{K}^0$ decays to $\pi^+ \pi^-$ directly. In (b), the initial $\bar{K}^0$ mixes, and the resulting K^0 decays to the $\pi^+ \pi^-$ final state. Note that only one mixing diagram is shown as an example.

6.3   The Wolfenstein Parameterization

Before we continue, it is useful to introduce a common representation of the CKM matrix, proposed by Wolfenstein [61], that takes advantage of the experimental revelation that there is a hierarchy in the rotation angles:

$$\sin \theta_{12} \gg \sin \theta_{23} \gg \sin \theta_{13}. \tag{6.18}$$

Expanding in terms of $\lambda \equiv \sin\theta_{12} = \sin\theta_C$, we obtain

$$
\begin{aligned}
V_{CKM} &\equiv
\begin{pmatrix}
V_{ud} & V_{us} & V_{ub} \\[1em]
V_{cd} & V_{cs} & V_{cb} \\[1em]
V_{td} & V_{ts} & V_{tb}
\end{pmatrix} \\[2em]
&=
\begin{pmatrix}
1 - \tfrac{1}{2}\lambda^2 & \lambda & A\lambda^3(\rho - i\eta) \\[1em]
-\lambda & 1 - \tfrac{1}{2}\lambda^2 & A\lambda^2 \\[1em]
A\lambda^3(1 - \rho - i\eta) & -A\lambda^2 & 1
\end{pmatrix}
+ \mathcal{O}(\lambda^4), \quad (6.19)
\end{aligned}
$$

where the terms A, ρ, and η are real numbers that are of order unity.

The unitarity of the CKM matrix produces useful relations between the various CKM elements. One such relation is of particular interest, where all the terms in the sum are of order λ^3:

$$
V_{ud}V_{ub}^* + V_{cd}V_{cb}^* + V_{td}V_{tb}^* = 0. \tag{6.20}
$$

This relation may be represented as a triangle in the complex plane, as shown in Figure 6.2. In the Wolfenstein parameterization, the vertices of this "Unitarity Triangle" are (0,0), (1,0), and (ρ,η).

The terms that produce CP violation in the Standard Model are proportional to the quantity [59]

$$
J_{CP} = |\text{Im}(V_{ij}V_{il}^*V_{kj}^*V_{kl})|, \qquad \text{where } i \neq k, \ j \neq l. \tag{6.21}
$$
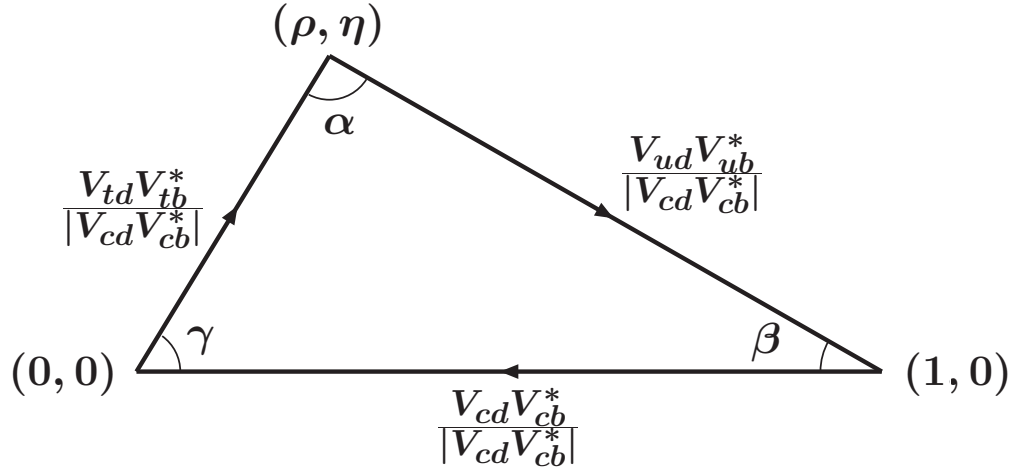
Figure 6.2: Representation in the complex plane of the triangle formed by $V_{ud}V_{ub}^* + V_{cd}V_{cb}^* + V_{td}V_{tb}^* = 0$ in the Wolfenstein parameterization.

If we define the quantities $z_1 = V_{ij}V_{il}^*$ and $z_2 = V_{kj}V_{kl}^*$, then $\text{Im}(z_1 z_2^*)$ is proportional to the area of a triangle with sides z_1 and z_2. In the Wolfenstein parametrization, this implies

$$J_{CP} \approx A^2 \eta \lambda^6, \tag{6.22}$$

and so CP violation in the Standard Model requires η to be nonzero.

There are five other triangles, besides the one already mentioned, that are determined from the unitarity relations between the various rows and columns of the CKM matrix. In fact, we may conclude from Equation 6.21 that all six unitarity triangles have the same area. The Unitarity Triangle in Figure 6.2 receives special attention as it is the only triangle where all three sides are of

equal order of magnitude, and as a result it should be easier to notice CP-violating

effects.

6.4 CP **Violation in** $B^0 \rightarrow J/\psi \ K_L$ **decays**

In order to test the Standard Model picture of CP violation, we need to

measure the various elements of the CKM matrix, as well as the angles α, β, and

γ of the Unitarity Triangle, with good precision. Any experimental results that

contradict Standard Model predictions will point to some new breed of physics.

In the Standard Model, CP violation naturally manifests itself if any of the

elements of the CKM matrix are complex. For a given decay, CP violation may

appear in one (or more) of the following forms [14]:

- CP Violation in decay, where the rate for a given decay process differs from

  the rate for its CP-conjugate process;

- CP Violation in mixing, where the magnitude for a $P^0 \rightarrow \bar{P}^0$ transition

  differs from the magnitude for the conjugate $\bar{P}^0 \rightarrow P^0$ transition.

- CP Violation in the interference between mixing and decay.

CP violation can only occur if more than one amplitude for a given process

is present, where the amplitudes must interfere in order to produce CP-violating

effects. This situation is readily available in the neutral B system, provided there exists a final state X_f that can be reached directly by B^0 and $\bar{B}^0$ decay. In this case, the amplitude for direct decay $B^0 \to X_f$ interferes with the amplitude for $B^0/\bar{B}^0$ mixing followed by $\bar{B}^0 \to X_f$ decay. Consequently, the 3rd form of CP violation listed above is a powerful probe of the Standard Model due to the favorable rate of $B^0/\bar{B}^0$ mixing (nearly 20% of the time, a produced B^0 decays as a $\bar{B}^0$ [8]), so that the interfering amplitudes are of comparable size. This is a tremendous benefit, as the associated asymmetries can be very large.

6.4.1 $B^0/\bar{B}^0$ mixing

The phenomenon of mixing, when a particle oscillates into its own antiparticle, can readily occur in Nature as a consequence of the weak interaction. The dominant mixing diagrams for the B^0 system are shown in Figure 6.3.
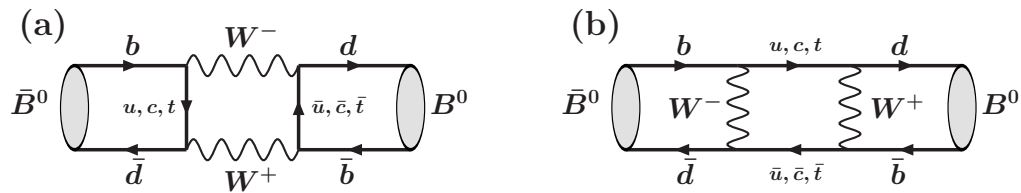
Figure 6.3: Dominant Feynman diagrams responsible for $B^0 - \bar{B}^0$ mixing. Due to its large mass, the top quark is the major contributor to the loop.

Let us begin with a generic linear combination of the flavor eigenstates,

$$\psi(t) = a(t)|B^0\rangle + b(t)|\bar{B}^0\rangle,$$ (6.23)

which satisfies the time-dependent Schrödinger equation

$$H\begin{pmatrix} a(t) \\ b(t) \end{pmatrix} = \begin{pmatrix} H_{11} & H_{12} \\ H_{21} & H_{22} \end{pmatrix} \begin{pmatrix} a(t) \\ b(t) \end{pmatrix} = i\frac{\partial}{\partial t}\begin{pmatrix} a(t) \\ b(t) \end{pmatrix}.$$ (6.24)

The Hamiltonian (H) is not Hermitian, as we have ignored the final state particles produced in the decay of the $B^0/\bar{B}^0$ mesons. We may express the Hamiltonian as the sum of two Hermitian matrices, as follows:

$$H \equiv \begin{pmatrix} H_{11} & H_{12} \\ H_{21} & H_{22} \end{pmatrix} = \begin{pmatrix} M & M_{12} \\ M_{12}^* & M \end{pmatrix} - \frac{1}{2}\begin{pmatrix} \Gamma & \Gamma_{12} \\ \Gamma_{12}^* & \Gamma \end{pmatrix}$$

$$= M - \frac{i}{2}\Gamma.$$ (6.25)

The matrices M and Γ are referred to as the mass and decay matrices, respectively. $H_{11} = H_{22}$ is required by CPT invariance [62], but there are no requirements placed on H_{12} and H_{21}. The off-diagonal elements of the mass and decay matrices are due to $B^0 \leftrightarrow \bar{B}^0$ transitions via off-shell (virtual) or on-shell intermediate states, respectively. $B^0\bar{B}^0$ mixing in the Standard Model is dominated by the virtual top quark in box diagrams (Figure 6.3), which implies that $|M_{12}| \gg |\Gamma_{12}|$ and thus $H_{12} = M_{12}$ to a good approximation.

The eigenstates of the Hamiltonian are of the form

$$|B_\pm^0\rangle = \frac{1}{\sqrt{|p|^2 + |q|^2}}(p|B^0\rangle \pm q|\bar{B}^0\rangle), \tag{6.26}$$

and solving for the eigenvalues of the Hamiltonian in Equation 6.24, we find

$$\left(\frac{q}{p}\right)^2 = \frac{H_{21}}{H_{12}} = \frac{M_{12}^* - \frac{i}{2}\Gamma_{12}^*}{M_{12} - \frac{i}{2}\Gamma_{12}},$$

$$\mu_\pm = H_{11} \pm \sqrt{H_{12}H_{21}} \equiv M_\pm - \frac{i}{2}\Gamma_\pm. \tag{6.27}$$

where $M_\pm = M \pm \mathrm{Re}\,\sqrt{H_{12}H_{21}}$ and $\Gamma_\pm = \Gamma \mp \mathrm{Im}\,\sqrt{H_{12}H_{21}}$ are both real.

The time evolution of the states that are produced as either a pure B^0 ($|B^0(t)\rangle$) or $\bar{B}^0$ ($|\bar{B}^0(t)\rangle$) is given by

$$|B^0(t)\rangle = f_+(t)|B^0\rangle + \left(\frac{q}{p}\right)f_-(t)|\bar{B}^0\rangle$$

$$|\bar{B}^0(t)\rangle = \left(\frac{p}{q}\right)f_-(t)|B^0\rangle + f_+(t)|\bar{B}^0\rangle, \tag{6.28}$$

where

$$f_\pm(t) = \frac{1}{2}(e^{-iM_+t}e^{-\Gamma_+t/2} \pm e^{-iM_-t}e^{-\Gamma_-t/2}). \tag{6.29}$$

As time passes, particle and antiparticle states mix, so that the physical states are neither a pure $|B^0\rangle$ nor a pure $|\bar{B}^0\rangle$ according to Equation 6.28.

In the neutral B system, we may safely set the lifetime difference $\Delta\Gamma = \Gamma_- - \Gamma_+$ to zero. This allows us to express the functions $f_\pm(t)$ in terms of the mass difference $\Delta m_d = M_- - M_+$ (which is greater than zero by choosing M_- to be the

heavier state) and $M = (M_+ + M_-)/2$:

$$
\begin{aligned}
f_+(t) &= e^{-iMt}e^{-\Gamma t/2}\cos\frac{\Delta m_d t}{2} \\
f_-(t) &= ie^{-iMt}e^{-\Gamma t/2}\sin\frac{\Delta m_d t}{2}.
\end{aligned}
\tag{6.30}
$$

The evolution of an initially pure B^0 or $\bar{B}^0$ state over time is then given by

$$
\begin{aligned}
|B^0(t)\rangle &= e^{-iMt}e^{-\Gamma t/2}\left[\cos\left(\frac{\Delta m_d t}{2}\right)|B^0\rangle + i\,\frac{q}{p}\,\sin\left(\frac{\Delta m_d t}{2}\right)|\bar{B}^0\rangle\right] \\
|\bar{B}^0(t)\rangle &= e^{-iMt}e^{-\Gamma t/2}\left[i\,\frac{p}{q}\,\sin\left(\frac{\Delta m_d t}{2}\right)|B^0\rangle + \cos\left(\frac{\Delta m_d t}{2}\right)|\bar{B}^0\rangle\right].
\end{aligned}
\tag{6.31}
$$

We see from Equation 6.31 that the frequency of $B^0 - \bar{B}^0$ oscillations is described by $\Delta m_d \cdot t = (\Delta m_d/\Gamma) \cdot (t/\tau_B)$, where τ_B is the lifetime of the B^0. As the ratio $\Delta m_d/\Gamma$ is near unity, the $B^0 - \bar{B}^0$ mixing rate is roughly equivalent to the B^0 lifetime. As a result, it is likely that a $B^0/\bar{B}^0$ will change into its antiparticle before decaying.

6.4.2 CP **Violation in mixing and decay**

If we consider the decay of the physical $B^0/\bar{B}^0$ states to a common final state (that we take to be an eigenstate of CP, with eigenvalue $\eta_{CP} = \pm 1$), we obtain the decay amplitudes

$$
\begin{aligned}
A(B^0(t) \to f_{CP}) &\equiv \langle f_{CP}|H|B^0(t)\rangle \\
&= e^{-iMt}e^{-\Gamma t/2} \\
&\times \left[\langle f_{CP}|H|B^0\rangle \cos\left(\frac{\Delta m_d t}{2}\right) + \right. \\
&\quad \left. i\,\frac{q}{p}\,\langle f_{CP}|H|\bar{B}^0\rangle \sin\left(\frac{\Delta m_d t}{2}\right)\right] \\
A(\bar{B}^0(t) \to f_{CP}) &\equiv \langle f_{CP}|H|\bar{B}^0(t)\rangle \\
&= e^{-iMt}e^{-\Gamma t/2} \\
&\times \left[i\,\frac{p}{q}\,\langle f_{CP}|H|B^0\rangle \sin\left(\frac{\Delta m_d t}{2}\right) + \right. \\
&\quad \left. \langle f_{CP}|H|\bar{B}^0\rangle \cos\left(\frac{\Delta m_d t}{2}\right)\right].
\end{aligned}
\tag{6.32}
$$

In Equation 6.32 we see two contributing amplitudes whose interference can produce a CP asymmetry, which we can express in terms of the difference between the $B^0/\bar{B}^0 \to f_{CP}$ decay rates. If we rewrite these equations in terms of the ratio of amplitudes

$$
\lambda = \left(\frac{q}{p}\right) \cdot \frac{\langle f_{CP}|H|\bar{B}^0\rangle}{\langle f_{CP}|H|B^0\rangle},
\tag{6.33}
$$

then we may express the probability for an initially pure B^0 state to decay to f_{CP} in the following way:

$$
\begin{aligned}
|\langle f_{CP}|H|B^0(t)\rangle|^2 &= e^{-\Gamma t}|\langle f_{CP}|H|B^0\rangle|^2 \\
&\times \left[\cos^2\left(\frac{\Delta m_d t}{2}\right) + |\lambda|^2 \sin^2\left(\frac{\Delta m_d t}{2}\right) - \right. \\
&\quad \left. 2\,\mathrm{Im}\,\lambda \cdot \cos\left(\frac{\Delta m_d t}{2}\right)\sin\left(\frac{\Delta m_d t}{2}\right)\right] \\
&= e^{-\Gamma t}|\langle f_{CP}|H|B^0\rangle|^2 \times [\frac{1}{2}(1+|\lambda|^2) + \\
&\quad \frac{1}{2}(1-|\lambda|^2)\cos\left(\Delta m_d t\right) - \mathrm{Im}\,\lambda \cdot \sin\left(\Delta m_d t\right)]. \quad (6.34)
\end{aligned}
$$

In a similar fashion, the probability for an initially pure $\bar{B}^0$ state to decay to the final state f_{CP} is given by

$$
\begin{aligned}
|\langle f_{CP}|H|\bar{B}^0(t)\rangle|^2 &= \left|\frac{p}{q}\right|^2 e^{-\Gamma t}|\langle f_{CP}|H|B^0\rangle|^2 \times [\frac{1}{2}(1+|\lambda|^2) - \\
&\quad \frac{1}{2}(1-|\lambda|^2)\cos\left(\Delta m_d t\right) + \mathrm{Im}\,\lambda \cdot \sin\left(\Delta m_d t\right)]. \quad (6.35)
\end{aligned}
$$

We can use Equations 6.34 and 6.35 to calculate the time-dependent CP asymmetry. As $\Gamma_{12} \ll M_{12}$, we may simplify the results of Equation 6.27:

$$
\frac{q}{p} \equiv \left(\frac{M_{12}^* - \frac{i}{2}\Gamma_{12}^*}{M_{12} - \frac{i}{2}\Gamma_{12}}\right)^{\frac{1}{2}} \rightarrow \sqrt{\frac{M_{12}^*}{M_{12}}}, \quad (6.36)
$$

which implies that, to a good approximation, $|\frac{q}{p}| = 1$. This fact simplifies our calculation of the time-dependent CP asymmetry considerably:

$$
\begin{aligned}
\mathcal{A}_{CP} &\equiv \frac{|\langle f_{CP}|H|B^0(t)\rangle|^2 - |\langle f_{CP}|H|\bar{B}^0(t)\rangle|^2}{|\langle f_{CP}|H|B^0(t)\rangle|^2 + |\langle f_{CP}|H|\bar{B}^0(t)\rangle|^2} \\
&= \frac{(1-|\lambda|^2)\cos\left(\Delta m_d t\right) - 2\,\mathrm{Im}\,\lambda \cdot \sin\left(\Delta m_d t\right)}{1+|\lambda|^2}. \quad (6.37)
\end{aligned}
$$

6.4.3 $B^0 \rightarrow J/\psi \ K_L$ **decay**

In order to calculate the time-dependent CP asymmetry as given in Equation 6.37, we need to determine the value of λ (see Equation 6.33), which depends on the final state f_{CP}. For $B^0 \rightarrow J/\psi K^0$ decay, the tree diagram (Figure 6.4) is expected to dominate the direct decay to the $J/\psi K^0$ final state[1]. This simplifies matters, as we may write

$$
\begin{aligned}
\langle f_{CP}|H|B^0\rangle &= |A| \cdot e^{i(\delta_S+\phi_W)} \\
\langle f_{CP}|H|\bar{B}^0\rangle &= \langle f_{CP}|(CP)^\dagger(CP)H(CP)^\dagger(CP)|\bar{B}^0\rangle \\
&= \eta_{CP}(f_{CP})e^{-2i\theta_{CP}}\langle f_{CP}|(CP)H(CP)^\dagger|B^0\rangle \\
&= \eta_{CP}(f_{CP})|A| \cdot e^{-2i\theta_{CP}}e^{i(\delta_S-\phi_W)} \quad (6.38)
\end{aligned}
$$

where $\eta_{CP}(f_{CP})$ is the CP eigenvalue for the final state f_{CP}, δ_S is a (CP conserving) phase that describes strong interaction effects, and ϕ_W is the (potentially CP-violating) weak phase associated with the dominant decay amplitude. This phase changes sign for $B^0/\bar{B}^0$ decay. Essentially, the amplitudes for B^0 and $\bar{B}^0$ decay to the final state f_{CP} are identical, differing by a phase that is a combination of the weak phase ϕ_W (that we want to extract from the measurement) and a convention-dependent phase θ_{CP}. Standard Model calculations for the mass

[1]In addition, the dominant penguin diagram has the same weak phase in the Standard Model.
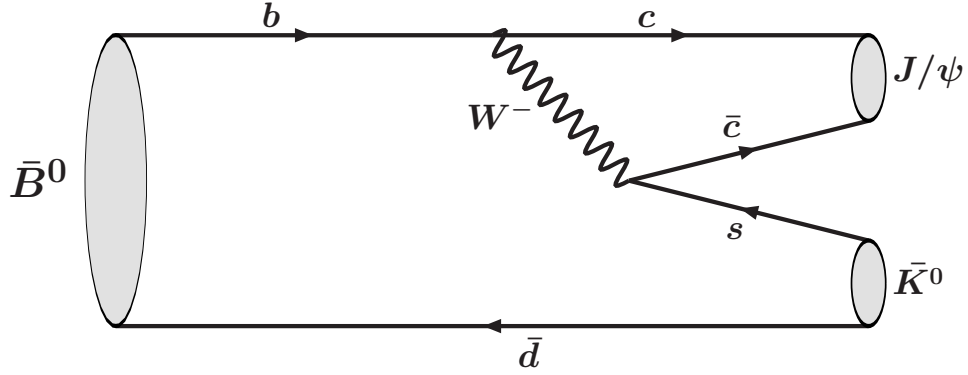
Figure 6.4: Tree diagram for the decay $\bar{B}^0 \to J/\psi \bar{K}^0$.

difference Δm_d [63], together with $\Delta m_d = M_- - M_+ = 2|M_{12}|$, imply that

$$M_{12} = a(V_{tb}V_{td}^*)^2 e^{-2i\theta_{CP}},$$

$$M_{12}^* = a(V_{tb}^*V_{td})^2 e^{2i\theta_{CP}} \tag{6.39}$$

where a is a real constant. Taking the results of Equation 6.36, we obtain

$$\frac{q}{p} = \sqrt{\frac{M_{12}^*}{M_{12}}} = \frac{V_{tb}^*V_{td}}{V_{tb}V_{td}^*}e^{2i\theta_{CP}}. \tag{6.40}$$

This yields

$$\begin{aligned}
\lambda &= \left(\frac{q}{p}\right) \cdot \frac{\langle f_{CP}|H|\bar{B}^0\rangle}{\langle f_{CP}|H|B^0\rangle} \\
&= \eta_{CP}(f_{CP})\frac{V_{tb}^*V_{td}}{V_{tb}V_{td}^*}e^{-2i\phi_W}
\end{aligned} \tag{6.41}$$

so that $|\lambda| = 1$. This simplifies Equation 6.37 considerably, as the term proportional to $\cos(\Delta m_d t)$ drops out of the calculation:

$$\mathcal{A}_{CP} = \operatorname{Im}\lambda \cdot \sin\left(\Delta m_d t\right). \tag{6.42}$$

157

If we consider the decay $B^0 \to J/\psi \; K_L$, the $b \to c\bar{c}s$ transition produces the weak phase

$$e^{-2i\phi_W} = \frac{V_{cb}V_{cs}^*}{V_{cb}^*V_{cs}}, \tag{6.43}$$

and an additional factor is introduced from K mixing in order to produce the K_L:

$$\gamma_K = \frac{V_{cs}V_{cd}^*}{V_{cs}^*V_{cd}}. \tag{6.44}$$

The K_L is a very nearly a CP eigenstate, with eigenvalue $\eta_{CP} = -1$. As a result, $\eta_{CP}(f_{CP} = J/\psi K_L) = +1$. This yields

$$\lambda = (+1) \cdot \frac{V_{tb}^*V_{td}}{V_{tb}V_{td}^*} \cdot \frac{V_{cb}V_{cs}^*}{V_{cb}^*V_{cs}} \cdot \frac{V_{cs}V_{cd}^*}{V_{cs}^*V_{cd}}. \tag{6.45}$$

In the Wolfenstein parameterization, all the CKM elements are real, with the exception of

$$V_{ub} = |V_{ub}|e^{i\gamma} \quad \text{and} \quad V_{td} = |V_{td}|e^{-i\beta},$$

where we have taken the angles from Figure 6.2. Consequently, the time-dependent asymmetry for $B^0 \to J/\psi \; K_L$ decay reduces to

$$
\begin{aligned}
\mathcal{A}_{CP}(B^0 \to J/\psi \; K_L) &= (\text{Im } e^{-2i\beta}) \cdot \sin(\Delta m_d t) \\
&= \sin 2\beta \cdot \sin(\Delta m_d t) \, . \tag{6.46}
\end{aligned}
$$

The simplicity of this result can be seen as a stroke of luck for both experiment and theory. Experimentally, we can examine $B^0 \to J/\psi \; K_L$ decay with good

precision provided we have a large sample of B decays. As penguin contributions to the direct decay to the $J/\psi K_L$ final state is small, and the dominant penguin decay has the same weak phase as the tree diagram, the end result is essentially free of complications due to the strong interaction. This means that if we observe an asymmetry in the decay $B^0 \to J/\psi \ K_L$, the extraction of the quantity $\sin 2\beta$ is relatively free of theoretical uncertainties. Consequently, this decay mode provides an excellent laboratory for a direct test of the Standard Model explanation for CP violation.

6.5   Physics at the $\Upsilon(4S)$ resonance

In order to provide a large sample of B mesons, the BABAR experiment spends a majority of its running time at the $\Upsilon(4S)$ resonance, which has a mass just above the $B\bar{B}$ production threshold. Consequently, half of all $\Upsilon(4S)$ mesons decay into a $B^0\bar{B}^0$ pair.

The $\Upsilon(4S)$ is in a $C = -1$ state [8]. The strong decay $\Upsilon(4S) \to B\bar{B}$ conserves C, so the resulting $B^0\bar{B}^0$ system must also have $C = -1$. This implies that, in the $\Upsilon(4S)$ rest frame, the $B^0\bar{B}^0$ system behaves as follows:

$$|\psi_{B\bar{B}}(t_1, t_2)\rangle = \frac{1}{\sqrt{2}}\left(|B^0(t_1), \vec{p}\rangle|\bar{B}^0(t_2), -\vec{p}\rangle - |B^0(t_2), \vec{p}\rangle|\bar{B}^0(t_1), -\vec{p}\rangle\right), \quad (6.47)$$

where t_1, t_2 describe time evolution for the forward and backward moving B mesons, respectively. If we substitute the results for the time evolution of $|B^0(t)\rangle$ and $|\bar{B}^0(t)\rangle$ (Equation 6.28) and for $f_\pm(t)$ (Equation 6.30), we obtain

$$
\begin{aligned}
|\psi_{B\bar{B}}(t_1, t_2)\rangle \;=\;\; & e^{-iM(t_1+t_2)}e^{-\Gamma(t_1+t_2)} \times \\[4pt]
& [\cos\frac{\Delta m_d(t_1 - t_2)}{2} \left(|B^0, \vec{p}\rangle|\bar{B}^0, -\vec{p}\rangle - |\bar{B}^0, \vec{p}\rangle|B^0, -\vec{p}\rangle\right) \\[4pt]
& -i\sin\frac{\Delta m_d(t_1 - t_2)}{2} \left(|B^0, \vec{p}\rangle|B^0, -\vec{p}\rangle - |\bar{B}^0, \vec{p}\rangle|\bar{B}^0, -\vec{p}\rangle\right)]
\end{aligned}
$$

As the sine term vanishes at $t_1 = t_2$, we conclude that for $B^0\bar{B}^0$ mesons produced in $\Upsilon(4S)$ decay, until one or the other B decays, one meson must be a B^0 and the other a $\bar{B}^0$. If we are able to determine (tag) the flavor of one meson the instant it decays (say it decays as a B^0 at time t_0), then we know that at time t_0 the other meson is a pure $\bar{B}^0$, and from that moment it evolves as $|\bar{B}^0(t - t_0)\rangle$.

In order to measure a CP asymmetry, we must therefore be able to reconstruct the final state $B^0/\bar{B}^0 \to J/\psi K_L$ and somehow manage to tag the flavor of the other B as shown in Figure 6.5. If we are unable to resolve the time difference between the decay of the B_{CP} and B_{tag} mesons, then the CP asymmetry

$$
\mathcal{A}_{CP}(B^0 \to J/\psi\ K_L) = \sin 2\beta \cdot \sin\left(\Delta m_d(t_1 - t_2)\right) \tag{6.48}
$$

will vanish, as the asymmetry for $t_1 - t_2 < 0$ will cancel the asymmetry for $t_1 - t_2 > 0$. For this reason, the $\Upsilon(4S)$ rest (CM) frame is boosted relative to the lab frame ($\beta\gamma = 0.56$) so that the B mesons are moving relative to the detector.
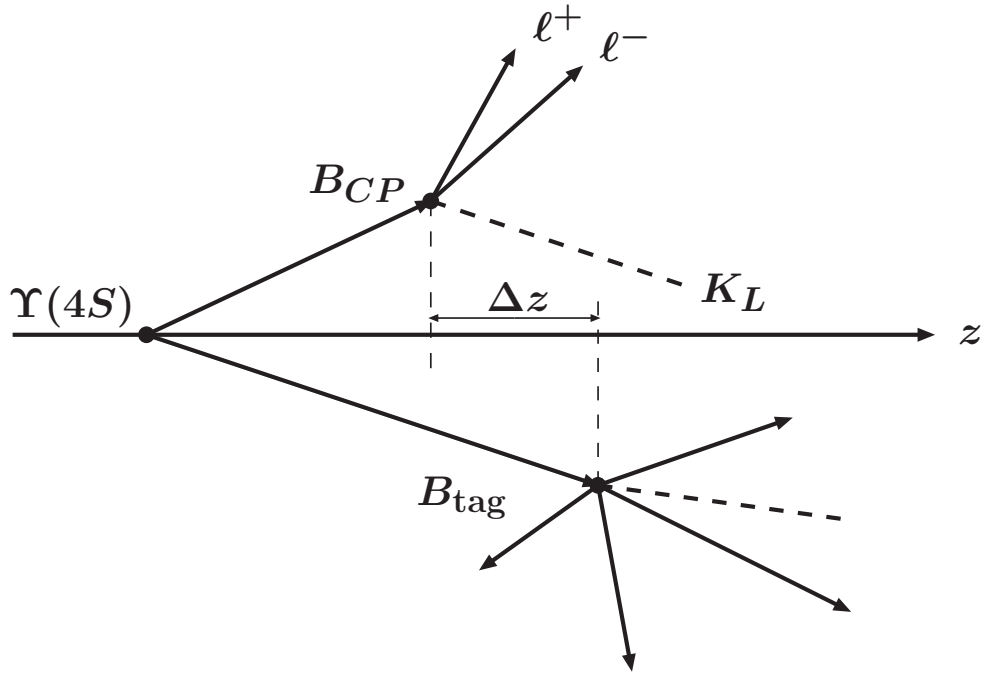
Figure 6.5: Diagram depicting the decay $\Upsilon(4S) \to B^0 \bar{B}^0$, with the B_{CP} meson decaying to the final state $J/\psi K_L$ (where $J/\psi \to \ell^+ \ell^-$), and the other B (B_{tag}) decaying in a way that allows us to determine its flavor. The time difference between B decays can be extracted from the spatial separation along the beam axis (Δz).

As a final note, we mention that it is also very important to be able to effectively tag the flavor of the B mesons at time t_0 (when one B decays). If we are unable to determine the flavor of the decaying B mesons, the asymmetry again vanishes. Great care needs to be taken to ensure that, whenever possible, we are able to determine the flavor of the B mesons produced in $\Upsilon(4S)$ decays. If we are successful, then the measurement of the CP asymmetry can give us very useful

information about the Standard Model. This allows us to determine the time difference Δt in terms of the distance between the two B decay vertices.

6.6 Historical Context

The primary physics goal of the BABAR experiment is the systematic study of CP-violating asymmetries in the decay of neutral B mesons to CP eigenstates [35]. Of all the possible decays, from our earlier discussions we see that $B^0 \to J/\psi K^0$ is a very attractive mode to study. Due to the clear $J/\psi \to \ell^+\ell^-$ signal and the ability to fully reconstruct $K_S \to \pi^+\pi^-, \pi^0\pi^0$ decay, the large high-purity event sample obtained from reconstructing $B^0 \to J/\psi K_S$ decays is the ideal environment for a study of $\sin 2\beta$ at an asymmetric B factory.

The $B^0 \to J/\psi K_L$ decay mode is nearly as valuable as $B^0 \to J/\psi K_S$. For every $B^0 \to J/\psi K^0$ decay at BABAR, the K^0 mesons are equally split between the K_S and K_L weak eigenstates. However, although the K_S may be reconstructed with high purity from its decay products, the long-lived K_L tends to interact hadronically with the detector before decaying. As a result, there is a significant amount of background in the $B^0 \to J/\psi K_L$ event sample relative to $J/\psi K_S$, which reduces its effectiveness for analysis.

As the CP eigenvalue switches sign for the $J/\psi K_S$ ($\eta_{CP} = -1$) and $J/\psi K_L$ ($\eta_{CP} = +1$) final states, an analysis of $B^0 \to J/\psi\ K_L$ events, provided the impact of background events could be understood, would be very beneficial for a CP-asymmetry measurement. Unfortunately, before the BABAR and Belle experiments began taking data, there were no published accounts of $B^0 \to J/\psi K_L$ decay.

Consequently, we first needed to demonstrate that it is possible to reconstruct $B^0 \to J/\psi\ K_L$ events at BABAR. We accomplished this feat using the first 23 million $B\bar{B}$ events recorded at BABAR from 1999 to 2000 (see Chapter 7). We then proceeded to measure $\sin 2\beta$ using reconstructed $B^0 \to J/\psi\ K_L$ events. In this thesis, I will document the $\sin 2\beta$ analysis using the first 88 million $B\bar{B}$ decays recorded at BABAR from 1999 through 2002. This analysis was published in the summer of 2002 [64]. After this analysis was complete, others took over the task of measuring $\sin 2\beta$ using $B^0 \to J/\psi\ K_L$ decays. I will briefly discuss these measurements at the conclusion of Chapter 8, as this portion of my thesis focuses on my involvement in the $\sin 2\beta$ analysis.

Chapter 7

Measuring the $B^0 \rightarrow J/\psi K^0$ Branching Fraction

The $B^0 \rightarrow J/\psi K^0$ branching fraction analysis was performed using 22.7 million $\Upsilon(4S) \rightarrow B\bar{B}$ decays accumulated between October 1999 and October 2000 with the BABAR detector located at SLAC. Before the B factories began taking data, the world average branching fraction for $B^0 \rightarrow J/\psi K^0$ decay [65],

$$BF(B^0 \rightarrow J/\psi K^0) = (8.9 \pm 1.2) \times 10^{-4}$$

was dominated by a measurement by the CLEO collaboration in 1997 using 3.4 million $\Upsilon(4S) \rightarrow B\bar{B}$ decays [66]. The data available at BABAR, after only one year of operation, is enough to substantially improve on this result.

The documentation for this portion of the $B^0 \rightarrow J/\psi\ K_L$ analysis will proceed as follows:

1. I will present the event selection criteria in Section 7.1.

2. The event yield, the reconstruction efficiency, and the systematic uncertainties associated with this measurement are included in Section 7.2.

3. Our results appear in Section 7.3.

7.1 $B^0 \to J/\psi \; K_L$ Event Selection

We reconstruct J/ψ mesons from pairs of oppositely charged leptons, and combine our results with a signature in the EMC or IFR that is consistent with a K_L meson. A B^0 candidate is then formed from the candidate J/ψ and K_L mesons. We document this selection below.

7.1.1 J/ψ reconstruction

We reconstruct $J/\psi \to e^+e^-, \mu^+\mu^-$ candidates from pairs of oppositely charged particle tracks that are required to originate from a common point in space. The J/ψ candidates are required to have momentum between 1.4 and 2.0 GeV, as this requirement safely eliminates J/ψ candidates that are kinematically incompatible with $B^0 \to J/\psi \; K_L$ decay, as shown in Figure 7.1.

In order to reduce the number of J/ψ candidates formed from random combinations of charged tracks, we apply particle identification criteria on the electron
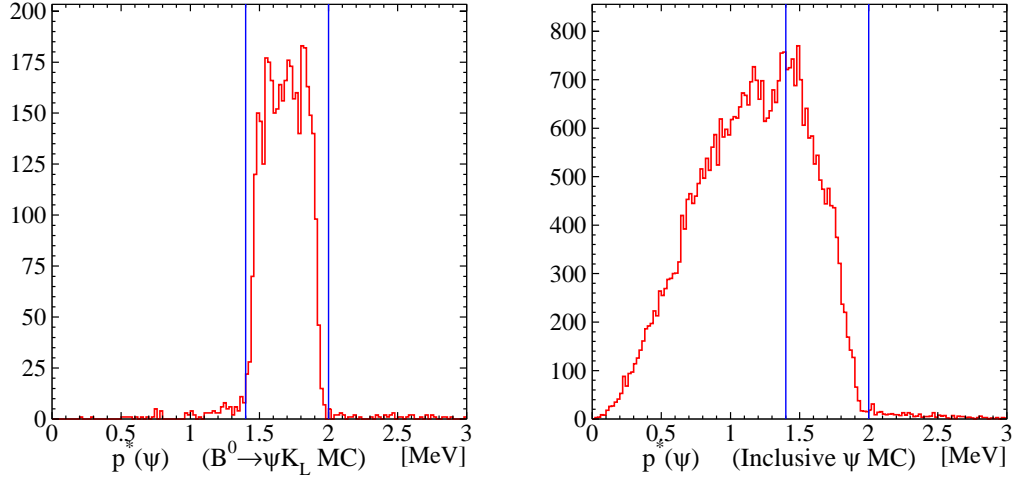
Figure 7.1: The J/ψ CM momentum (p^*) distributions for Monte Carlo events: $B^0 \rightarrow J/\psi\, K_L$ decays (left), and inclusive $B \rightarrow J/\psi X$ Monte Carlo (right). The lines indicate the applied cuts.

and muon candidate tracks. This criteria is described elsewhere [67], but we give a basic summary below.

Electron candidates are primarily identified by the ratio of the energy measured in the EMC to the track momentum, E/p. They must also have a measured mean $\mathrm{d}E/\mathrm{d}x$ in the DCH that is consistent with expectations for an electron. In addition, the shape of the EMC shower and the Cherenkov angles observed in the DIRC are expected to be consistent with expectations for an electron. We require one of the electrons to pass `Loose` requirements, and the other electron must pass the `Very Tight` selection. The requirements for each category are shown in Table 7.1. The electron identification efficiencies vary between 88% and 98% for

candidates with lab momentum between 0.5 and 3.0 GeV, with a pion rejection factor of order 1000 for the `Very Tight` selection.

	Loose	Very Tight
dE/dx (measured-expected)	-3 to $+7$ σ_{meas}	-2 to $+4$ σ_{meas}
E/p	$0.65 - 5.0$	$0.89 - 1.2$
N_{crys}	at least 3	at least 3
LAT	-	$0.1 - 0.6$
A_{42}	-	< 0.11
θ_C (measured-expected)	-	-3 to $+3$ σ_{meas}
Efficiency (%)	97.2	88.2
π mis-ID (%)	4.8	0.1

Table 7.1: Summary of electron identification criteria. Variables used: The energy loss measured in the DCH (dE/dx); The ratio of EMC cluster energy to measured momentum (E/p); The number of EMC crystals used to form the cluster (N_{crys}); The lateral energy distribution [68] of the EMC cluster (LAT); One of the Zernike moments [69] of the EMC cluster (A_{42}); The Cherenkov angle measured in the DIRC (θ_C). In some cases, the requirements are made relative to the measured resolution of the given quantity. In addition, the fraction of electrons in inclusive J/ψ events that pass each set of requirements is shown, along with the fraction of pions with momentum above 1 GeV that pass the selection requirements.

Muon candidates are primarily identified by the number of interaction lengths of material traversed from the outside radius of the DCH through the IFR iron. This value is compared to expectations for a muon of the same momentum traveling along the same path. The properties of the candidate muon signature within the IFR, such as the average number of hits per RPC layer, are also compared to predictions. As all muon candidates in the $B^0 \to J/\psi \; K_L$ analysis intersect with the EMC detector volume, the measured calorimeter energy is expected to be

consistent with a minimum ionizing particle. The muon identification efficiency varies between 60% and 92% for candidates in the momentum range $1.1 < p < 3.0$ GeV, with a pion rejection factor of order 30.

The mass distribution for $J/\psi \to ee, \mu\mu$ candidates is shown in Figure 7.2. We require $3.0 < m_{ee} < 3.13$ GeV, and $3.06 < m_{\mu\mu} < 3.13$ GeV. As the electron daughters of the J/ψ may radiate Bremsstrahlung photons, we attempt to recover missing energy by identifying neutral clusters with energy above 30 MeV near the electron direction (within 35 mrad in polar angle, and 50 mrad in azimuth) projected into the EMC. The asymmetric J/ψ mass window is chosen in order to accept candidates where we fail to recover some (or all) of the Bremsstrahlung photons emitted by the electrons.

In this analysis, we will make use of the mass sidebands of the $J/\psi \to \ell^+\ell^-$ distribution in order to estimate the background component due to combinatoric J/ψ candidates. For the $J/\psi \to ee$ mass distribution, the sideband region is defined as $3.175 < m_{ee} < 3.5$ GeV. The $J/\psi \to \mu\mu$ sidebands are defined as $2.9 < m_{\mu\mu} < 3.0$ GeV and $3.175 < m_{\mu\mu} < 3.5$ GeV.

7.1.2 K_L reconstruction

Identifying K_L mesons is a bit of a challenge at BABAR, as the particles are neutral and long-lived ($c\tau > 15$ m). Consequently, a K_L meson tends to interact
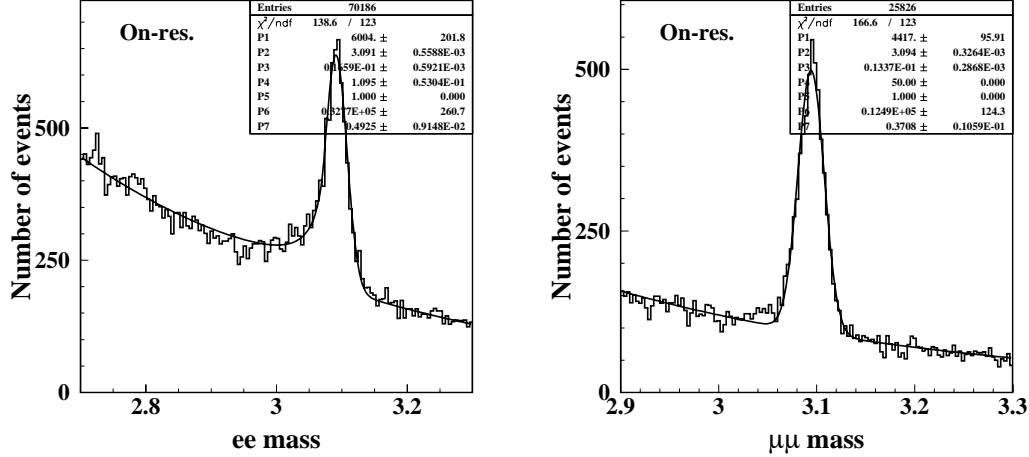
Figure 7.2: m_{ee} and $m_{\mu\mu}$ distributions (in GeV) for J/ψ candidates with $1.0 < p^* < 2.0$ GeV that pass the electron and muon requirements described in the text. A fit to the 'Crystal Ball' function [70], consisting of a Gaussian signal peak matched with a power law tail, is superimposed on the histograms.

hadronically with the detector before decaying. These hadronic interactions often leave a detectable signal in either the EMC or the IFR, but the kinetic energy is poorly measured.

As a result, the K_L selection criteria are rather minimal. A K_L candidate is identified as a reconstructed cluster in the EMC or IFR that cannot be associated with any charged track in the event. There are additional detector-specific criteria that we enumerate below:

- Approximately half of all K_L mesons from $B^0 \to J/\psi \; K_L$ decay deposit at least 200 MeV in the EMC. In Figure 7.3 we present the deposited energy

169

distribution for K_L mesons from $B^0 \to J/\psi\ K_L$ Monte Carlo. We require K_L candidates detected within the EMC to have a cluster energy between 200 MeV and 2 GeV. The clusters are also required to have a lab polar angle such that $\cos\theta < 0.935$ in order to reduce effects caused by reconstruction irregularities in the very forward region of the detector. This reduces the angular acceptance by about 4% in the CM frame.

- About 60% of K_L mesons from $B^0 \to J/\psi\ K_L$ leave a detectable signal in the IFR. K_L candidates in the IFR are defined as clusters with hits in two or more RPC layers. In order to reduce beam-related backgrounds, and to avoid regions where the charged tracking efficiency is low, we require the polar angle of the IFR cluster to satisfy $-0.75 < \cos\theta < 0.93$ and eliminate clusters that begin in the outer 25% of the forward IFR endcap.

Photons are the primary background for K_L mesons reconstructed in the EMC. We apply a requirement designed to reject photons from π^0 decay: if a K_L candidate that is found to be consistent with the photon hypothesis and can be paired with another neutral cluster (with EMC energy above 30 MeV) such that $100 < m(\gamma\gamma) < 150$ MeV, it is rejected. The remaining background in the EMC consists primarily of photons and overlapping EMC showers. Isolated clusters pro-
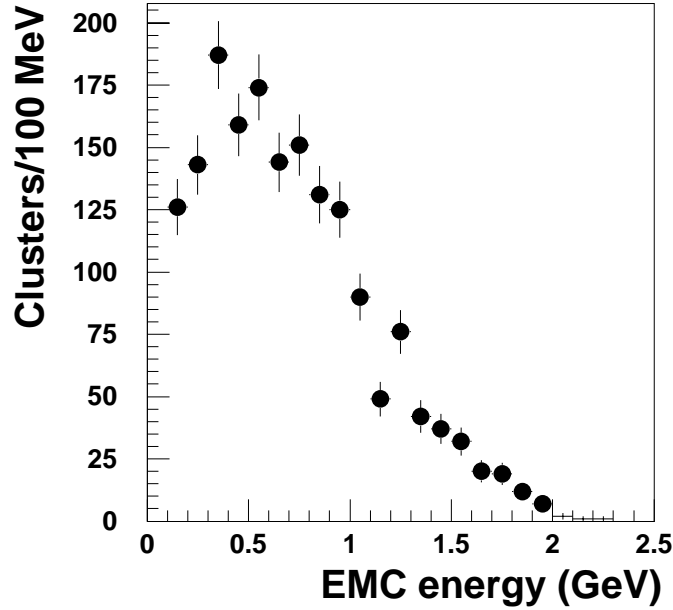
Figure 7.3: Energy deposited in the EMC for K_L candidates from Monte Carlo $B^0 \to J/\psi \ K_L$ events.

duced from charged particles are removed by a basic clustering algorithm which requires a minimum separation of 20 cm between clusters.

On occasion, IFR K_L candidates are contaminated by charged particle tracks where the IFR cluster was missed by the track association algorithm. We suppress these charged clusters by rejecting K_L candidates that lie within 350 mrad in polar angle and between -750(-300) to 300(750) mrad in azimuth of the EMC intersection point of any positively (negatively) charged particle track in the event.

171

7.1.3 $B^0 \to J/\psi \; K_L$ reconstruction

We form $B^0 \to J/\psi \; K_L$ candidates from pairs of K_L and $J/\psi \to \ell^+\ell^-$ candidates that pass our selection requirements. In order to improve the resolution of our measurement, we refit the momenta of the lepton tracks so that the mass of the $J/\psi \to \ell^+\ell^-$ candidate is constrained to the world average value of 3.097 GeV [65].

Using the result of the mass-constrained fit for the J/ψ candidate, we calculate the momentum of the K_L in the lab frame by using the measured K_L direction and constraining the invariant mass of the $J/\psi + K_L$ to the world average value for the B^0 meson [65]. Boosting to the $\Upsilon(4S)$ rest frame, we then calculate the difference between the calculated $J/\psi K_L$ candidate energy, assuming they were produced from B^0 decay, and the beam energy (recall Equation 5.3):

$$\Delta E \equiv |E_\psi^* + E_{K_L}^*| - \frac{1}{2}\sqrt{s}, \qquad (7.1)$$

where $\sqrt{s}/2$ is the beam energy in the $\Upsilon(4S)$ frame. For $B^0 \to J/\psi \; K_L$ signal events, ΔE will be equal to zero within experimental resolution. This quantity provides a powerful kinematic criterion to reject background.

The expected momentum of the K_L can also be used to reduce background originating from random combinations of J/ψ and K_L candidates. As K_L energy, and hence its momentum, is poorly measured by the BABAR detector, any event

that contains a real K_L meson will appear to violate momentum conservation. In the plane perpendicular to the beam axis, where the total momentum is expected to be zero, events containing a real K_L may be preferentially selected by measuring the missing transverse momentum in the event.

We require the missing transverse momentum for the event to be consistent with the expected K_L momentum for the $B^0 \rightarrow J/\psi \; K_L$ candidate. The missing momentum is calculated from all tracks and EMC clusters (not including the K_L candidate) and projected along the direction of the K_L candidate in the plane perpendicular to the beam axis. IFR clusters, which do not provide any momentum information, are not used in the missing momentum calculation. The expected transverse momentum of the K_L is then subtracted from the projection.

Figure 7.4 demonstrates the potential of a cut on the projected missing momentum by comparing distributions for signal and inclusive $B \rightarrow J/\psi X$ Monte Carlo. The discriminating power of this cut is lower for the IFR as there is significantly less background in this sample than for the EMC.

By considering only the transverse component of the missing momentum, we minimize the impact of charged particles which escape down the beampipe, as well as energy leakage in the EMC endcap. The effect of semileptonic decays, which also include missing momentum due to the neutrino, is reduced by projecting onto the direction of the K_L candidate. As the missing momentum originating
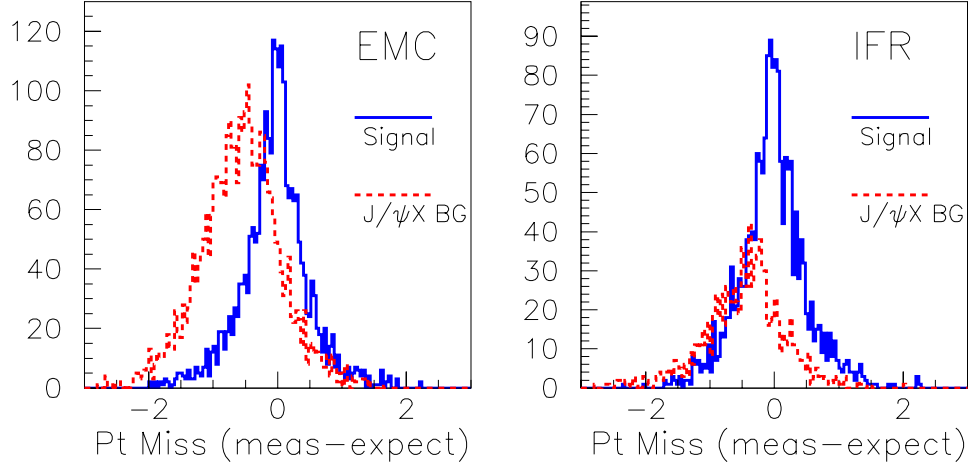
Figure 7.4: The projected missing transverse momentum (in GeV) minus the expected value for K_L mesons from $B^0 \to J/\psi\ K_L$ decay reconstructed in the EMC or IFR. Results are shown for $J/\psi K_L$ signal and inclusive $J/\psi X$ background Monte Carlo.

from semileptonic decays is uncorrelated with the K_L direction, these decays will decrease the resolution of the measurement without introducing a bias to the result.

We tested our ability to correctly model the missing momentum in Monte Carlo with a study of $B^\pm \to J/\psi K^\pm$ decay, as a relatively large and pure sample of these events can be extracted from data. In this study, we treat the $K^\pm$ as a K_L: we ignore the momentum from tracking measurements and only consider the energy of the calorimeter cluster and the initial direction of the track at the origin. Figure 7.5 compares the projected missing transverse momentum obtained from

data and $B^{\pm} \to J/\psi K^{\pm}$ Monte Carlo. We see that the Monte Carlo correctly

models the missing momentum as seen in data.
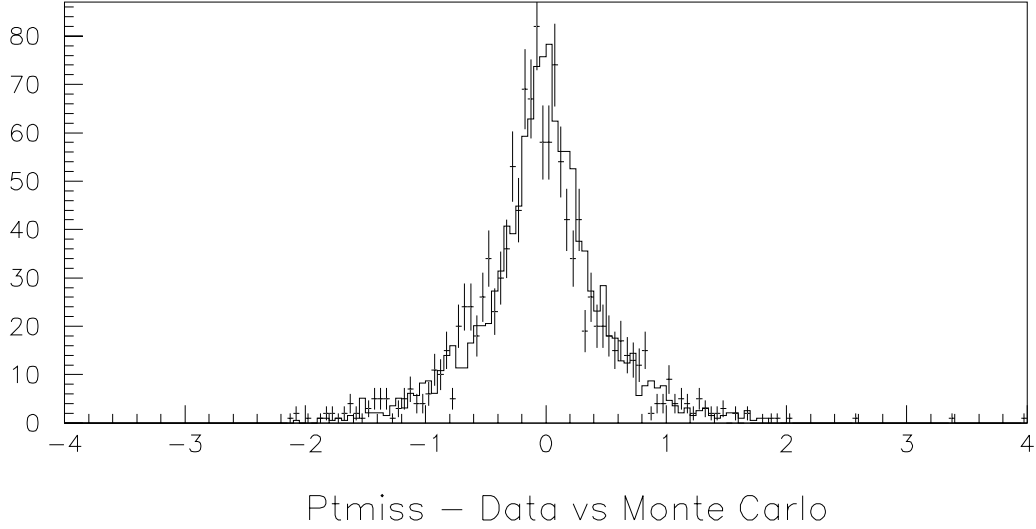
Figure 7.5: Missing transverse momentum measured (in GeV) in data and Monte Carlo from $B^{\pm} \to J/\psi K^{\pm}$ events. For this measurement we treat the $K^{\pm}$ as a K_L, i.e. we only use the 3-direction.

A final concern is that a missing momentum requirement could bias a CP

violation measurement using $B^0 \to J/\psi \; K_L$ decays. Semileptonic B decays are

used to tag the flavor of the other B when it decays, and the neutrino produced will

result in additional missing momentum in the event. If we require large missing

momentum in the event, the probability that this event contains a semileptonic

decay would increase. Monte Carlo studies show that setting the minimum missing

transverse momentum up to -300 MeV does not bias the efficiency of the lepton

flavor tag.

The optimal value of the missing momentum cut should maximize $S/\sqrt{S+B}$, where S represents the number of reconstructed signal $B^0 \to J/\psi \, K_L$ events, and B describes the number of expected background events (see Figure 7.6). For EMC K_L candidates, a rather broad optimum is found between -0.8 and -0.4 GeV. We choose a cut at -0.65 GeV in order to keep signal efficiency high. We also find that no cut value improves the selection for IFR K_L candidates, and therefore this cut is not applied to the IFR event sample.
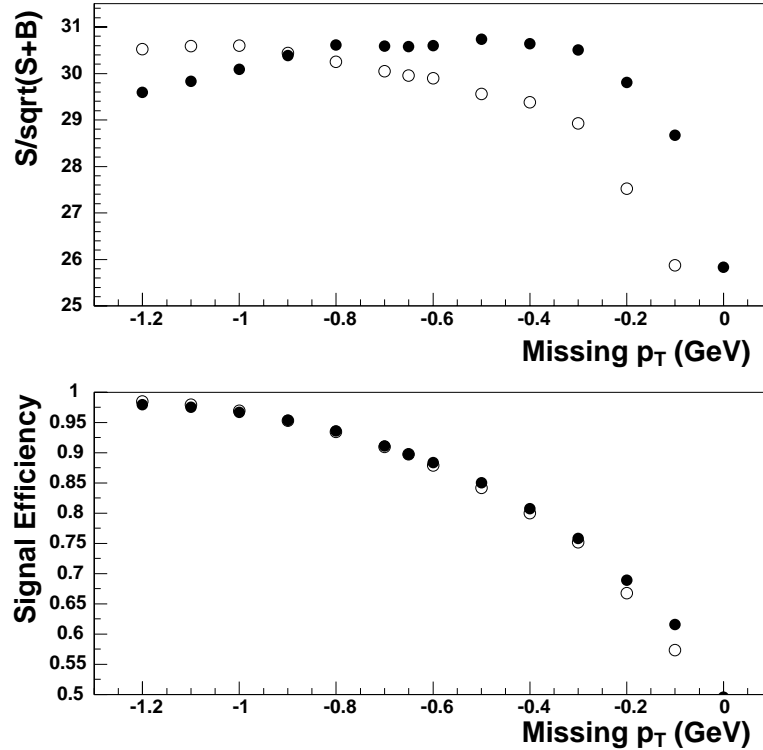
Figure 7.6: Performance of the missing transverse momentum (p_T) cut measured on a Monte Carlo sample of $B^0 \to J/\psi \, K_L$ events with inclusive $B \to J/\psi X$ background for EMC (filled circles) and IFR (open circles) K_L candidates.

In order to further reduce background, we examine the following decay angles, which are illustrated in Figure 7.7:

- The angle (θ_B) formed by the $J/\psi K_L$ candidate with respect to the e^- beam direction in the $\Upsilon(4S)$ rest frame. This angle has a $1 - \cos^2\theta_B$ distribution for B meson decays, while the background distribution is featureless. We require $|\cos\theta_B| < 0.9$.

- The angle (θ_{hel}), measured in the J/ψ rest frame, between one of the leptons from the $J/\psi \to \ell^+\ell^-$ candidate and the direction opposite the flight of the K_L. This angle has a $1 - \cos^2\theta_{\text{hel}}$ distribution for $B^0 \to J/\psi \; K_L$. We require that $|\cos\theta_{\text{hel}}| < 0.9$.

- We found that background rejection is improved if we cut on each of these variables simultaneously, such that $|\cos\theta_B| + |\cos\theta_{\text{hel}}| < 1.3$.

Finally, we reject events in which we can reconstruct one of the following decays:

- $B^0 \to J/\psi K_S$, with $K_S \to \pi^+\pi^-$ or $\pi^0\pi^0$;

- $B^0 \to J/\psi K^{*0}$, with $K^{*0} \to K^\pm\pi^\mp$ or $K_S\pi^0$;

- $B^\pm \to J/\psi K^\pm$;

- $B^\pm \to J/\psi K^{*\pm}$, with $K^{*\pm} \to K_S\pi^\pm$ or $K^\pm\pi^0$.
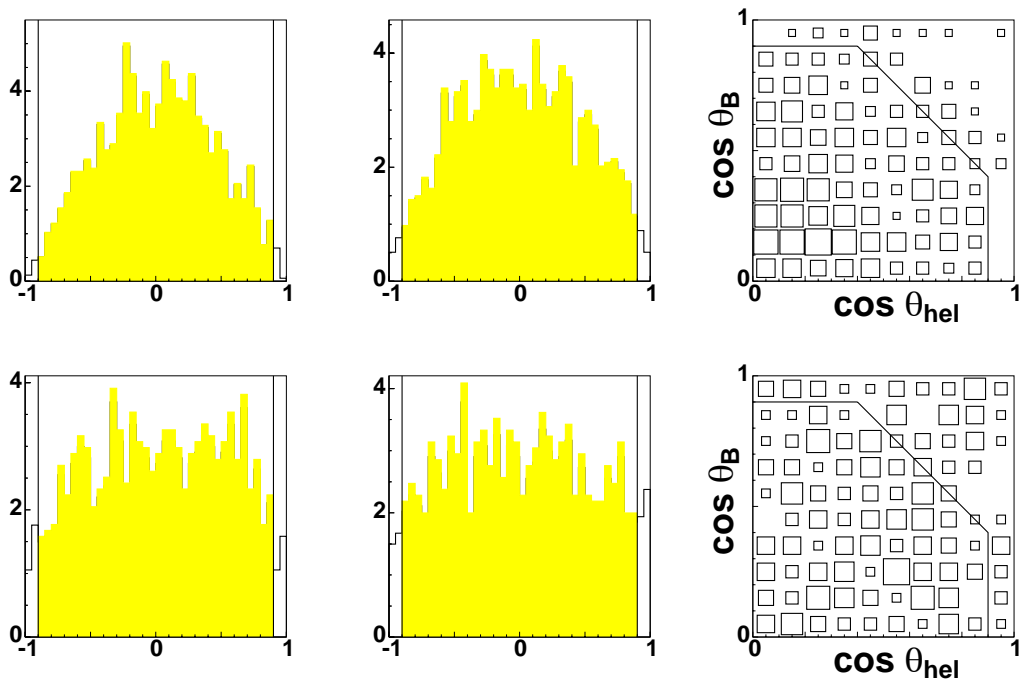
Figure 7.7: Distributions of $\cos\theta_{\text{hel}}$ (left) and $\cos\theta_B$ (middle) for signal (top) and inclusive $B \to J/\psi X$ background (bottom) Monte Carlo samples. Both quantities are plotted together at right. The lines denote the analysis requirements. For the single variable plots, the vertical scale is arbitrary.

The J/ψ momentum for these decays will likely fall within the accepted range for $B^0 \to J/\psi\ K_L$ decays, which makes it more likely that a false signal candidate may be formed from a real J/ψ and a random EMC/IFR cluster. We reject events if the energy-substituted mass (m_{ES}, see Equation 5.2) and ΔE (Equation 5.3) are consistent with a B^0 meson decaying according to any of the above modes. This specific-mode rejection is nearly 100% efficient for real $B^0 \to J/\psi\ K_L$ events, and it reduces backgrounds that contain a real J/ψ meson.

In a small fraction of events, more than one $B^0 \to J/\psi\ K_L$ candidate passes the above requirements. We select the best candidate based on the following algorithm:

- All candidates with $\Delta E > 80$ MeV are discarded.

- If multiple B candidates are formed using EMC K_L candidates, we select the candidate with the highest cluster energy.

- If multiple IFR candidates are present, we select the one with the largest number of layers hit.

- If an EMC and an IFR candidate pass all the selection criteria, we select the EMC candidate. This takes advantage of the better angular resolution in the EMC. We pay special attention to events where it appears that a single K_L was detected by both the EMC and the IFR. If we find an EMC and

an IFR K_L candidate such that $\cos\theta > 0.9$, where θ is the opening angle between the candidates, we use the EMC information to obtain a better resolution. The event is included along with other IFR candidates to take advantage of higher signal purity in the IFR sample.

7.2 Extraction of the $B^0 \to J/\psi \ K_L$ Branching Fraction

The $B^0 \to J/\psi \ K_L$ branching fraction is determined as follows:

$$BF(B^0 \to J/\psi \ K_L) = \frac{N_{RECO}}{N_{B\bar{B}} \times \epsilon \times BF(J/\psi \to \ell\ell)}, \qquad (7.2)$$

where:

- N_{RECO} is the number of signal $B^0 \to J/\psi \ K_L$ events reconstructed in data;

- The Monte Carlo acceptance is described by ϵ;

- $N_{B\bar{B}}$ represents the 22.72 ± 0.36 million $\Upsilon(4S) \to B\bar{B}$ decays recorded at BABAR between 1999 and 2000;

- We take the world average value for the branching fraction $BF(J/\psi \to \ell\ell) = (11.81 \pm 0.14)\%$ [65].

In the following sections we will discuss the various inputs to the $B^0 \to J/\psi \ K_L$ branching fraction measurement.

7.2.1 Event yield

We extract the number of reconstructed $B^0 \to J/\psi \ K_L$ decays that pass our event selection using a fit to the ΔE distribution, which is shown in Figure 7.8.
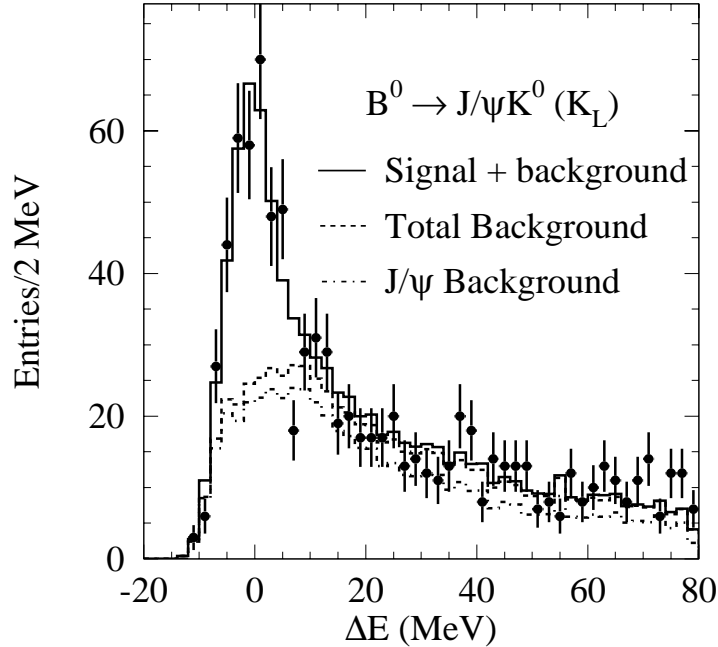
Figure 7.8: ΔE distribution for events from data (points) and Monte Carlo (histograms) which pass event selection criteria. We combine EMC and IFR candidates, as well as $J/\psi \to ee(\mu\mu)$ decays. The normalization of the Monte Carlo samples is taken from the results of the likelihood fit.

We extract the $B^0 \rightarrow J/\psi \ K_L$ event yield from data using a binned maximum

likelihood fit. We define the likelihood function as follows:

$$\mathcal{L}(N_{\psi K_L}, N_{\psi X}, N_{\text{non}-\psi}) = \prod_{i=1}^{n_{\text{bin}}} \frac{\mu_i^{d_i} e^{-\mu_i}}{d_i!} \times \frac{e^{-\frac{(N_{\text{non}-\psi}-M)^2}{2(\sigma^2 + N_{\text{non}-\psi})}}}{\sqrt{2\pi(\sigma^2 + N_{\text{non}-\psi})}}, \qquad (7.3)$$

where:

- $N_{\psi K_L}$, $N_{\psi X}$, and $N_{\text{non}-\psi}$ describe the number of reconstructed $B^0 \rightarrow J/\psi \ K_L$

  events, inclusive $B \rightarrow J/\psi X$ background, and events without a real J/ψ,

  respectively, extracted from the likelihood;

- μ_i is the expected number of events in the ith bin of the ΔE distribution,

$$\mu_i \equiv N_{\psi K_L} a_i + N_{\psi X} b_i + N_{\text{non}-\psi} c_i, \qquad (7.4)$$

  where a_i, b_i, and c_i are the fractions of $B^0 \rightarrow J/\psi \ K_L$, $B \rightarrow J/\psi X$ back-

  ground, and non-J/ψ events in the ith bin, respectively;

- d_i represents the number of data events reconstructed in the ith bin;

- M is the expected number of non-J/ψ background events determined from

  the mass sidebands of the J/ψ;

- σ is the uncertainty on the fitted value for M.

The ΔE distributions for $B^0 \rightarrow J/\psi \ K_L$ signal and inclusive $B \rightarrow J/\psi X$ back-

ground events are determined from Monte Carlo, and we obtain the shape of the

ΔE distribution for the non-J/ψ background by fitting the J/ψ mass sidebands to a threshold background function [47]. The $B^0 \to J/\psi\ K_L$ event yield will be used to determine the branching fraction, and the parameters $N_{\psi X}$ and $N_{\mathrm{non}-\psi}$ will be needed later to extract $\sin 2\beta$.

The signal region is defined as $|\Delta E| < 10$ MeV. There are 408 data events in this region that pass our selection requirements. Using the output of the maximum likelihood fit, we find 194 ± 23 $B^0 \to J/\psi\ K_L$ signal events, in addition to 200 ± 14 $B \to J/\psi X$ and 25 ± 3 non-J/ψ background events in the ΔE signal region.

7.2.2 Monte Carlo acceptance

We correct the observed signal yield to account for the reconstruction efficiency, determined from $B^0 \to J/\psi\ K_L$ Monte Carlo events, in order to extract the branching fraction. We apply small corrections to the Monte Carlo output in order to minimize observed discrepancies with respect to data. We list these corrections below, and summarize our work in Table 7.2:

- Studies of charged particle reconstruction at BABAR imply that the Monte Carlo slightly overestimates charged particle reconstruction efficiency, and studies of $J/\psi \to \ell\ell$ decays indicate that the Monte Carlo overestimates lepton identification efficiency. We adjust the Monte Carlo to account for these effects.

- Fitting the $J/\psi \to e^+e^-, \mu^+\mu^-$ distributions in Monte Carlo and data to the sum of a Crystal Ball [70] function and an exponential background, we determine that the J/ψ mass windows accept a slight excess of J/ψ events in Monte Carlo when compared to data. We correct the J/ψ reconstruction efficiency in Monte Carlo to account for this discrepancy.

- We study the intrinsic K_L selection efficiency using a sample $e^+e^- \to \phi\gamma, \phi \to K_S K_L$ decays. The ratio of Monte Carlo K_L efficiency in the EMC and IFR relative to data was found to be 0.94 ± 0.09 and 1.11 ± 0.09, respectively. We introduce a correction factor to account for this discrepancy.

- The efficiency of the π^0 veto in Monte Carlo and data is tested by measuring the neutral cluster multiplicity for $B^\pm \to J/\psi K^\pm$ events. We find that the Monte Carlo sample underestimates the number of EMC clusters with energy below 100 MeV in data by 19%. This implies that Monte Carlo simulations underestimate the number of K_L candidates rejected due to the π^0 veto. We degrade the efficiency loss of the Monte Carlo for this veto (16%) by 19% of its value ($0.19 \times 0.16 = 0.03$) in order to better reproduce the data environment.

- Studies of $B^\pm \to J/\psi K^\pm$ events indicate that the Monte Carlo slightly over-estimates the efficiency of the missing transverse momentum requirement. We degrade the Monte Carlo efficiency for EMC K_L candidates accordingly.

- Studies of $B^\pm \to J/\psi K^\pm$ events also indicate that the central value of the ΔE distribution in Monte Carlo is shifted by 0.5 MeV relative to data. Furthermore, the Gaussian width of the ΔE, which is dominated by the spread in the energy of the $e^\pm$ beams, is underestimated by the Monte Carlo. We introduce an additional Gaussian resolution term (with 1.4 MeV width) to the ΔE distribution, and we adjust ΔE values in $B^0 \to J/\psi\ K_L$ Monte Carlo by 0.5 MeV, to account for the observed differences.

- The position of the K_L candidate in the detector influences the ΔE measurement. Poor K_L angular resolution for some signal events is responsible for the small tail in the signal ΔE distribution which extends to large values, as seen in Figure 7.8. We use $e^+ e^- \to \phi\gamma$ events to test the modeling of K_L angular resolution in Monte Carlo simulation. We adjust $B^0 \to J/\psi\ K_L$ decays in Monte Carlo to reproduce the lower K_L angular resolution that is seen in data.

Correction	EMC	IFR	Combined
Tracking efficiency	0.98	0.98	0.98
Lepton efficiency	0.98	0.98	0.98
J/ψ mass cut	0.99	0.99	0.99
Intrinsic K_L efficiency	0.94	1.11	$\pm$ 9%
π^0 veto	0.97	-	$\pm$ 0.7%
Missing momentum	0.98	-	$\pm$ 0.5%
ΔE shift (MeV)	-0.5	-0.5	-0.5
Additional ΔE spread (MeV)	1.4	1.4	1.4
K_L angular resolution	re-weight ΔE templates		

Table 7.2: Summary of corrections made to $B^0 \to J/\psi\ K_L$ reconstruction efficiency in Monte Carlo. In each case we give the numerical value of the correction factor, with the exception of the K_L angular resolution, where the shape of the ΔE templates are redetermined. The additional ΔE spread introduced to account for beam energy spread differences in Monte Carlo and data is indicated by the width of the added Gaussian resolution term, which we give in MeV. In cases where the correction factors differ for EMC and IFR events, we quote the uncertainty on the combined correction, as the numerical value of the combined correction factor is never used explicitly in our analysis.

7.2.3 Systematic uncertainties

There is a systematic uncertainty associated with each of the corrections discussed above that are applied in order to correct the Monte Carlo acceptance. These uncertainties are summarized in Table 7.3, along with the following additional systematic uncertainties:

- The uncertainty associated with the parametrization of the non-J/ψ background shape is obtained by varying the parameters taken from the fit to the J/ψ mass sidebands by one standard deviation and recalculating the signal ΔE yield.

- The uncertainty associated with the content of the inclusive $B \to J/\psi X$ background is obtained by varying the relative content of the background according to the measured uncertainties on the known branching fractions [65]. For lesser known branching fractions, we vary their rate by conservative estimates. The systematic uncertainty due to this effect is dominated by the non-resonant decay $B \to J/\psi K\pi$, which is poorly measured. We vary this branching fraction from -50 to 400% of its measured value.

- The uncertainty on the number of $B\bar{B}$ pairs in data, as discussed in References [49, 67].

Source	Uncertainty (%)
Tracking efficiency	2.4
Lepton efficiency	1.2
J/ψ mass requirement efficiency	1.3
Intrinsic K_L efficiency	9
π^0 veto efficiency	0.7
Efficiency of missing p_T requirement	0.5
ΔE shift	1.0
Beam energy spread	3.0
K_L angular resolution	4
$B \to J/\psi X$ branching fractions	3.8
non-J/ψ background shape	2
Number of $B\bar{B}$ events	1.6
Monte Carlo statistics	2.2
$BF(J/\psi \to \ell\ell)$	1.2
Total systematic uncertainty	12.0
Statistical uncertainty	12.0

Table 7.3: Summary of uncertainties for the $B^0 \to J/\psi \; K_L$ branching fraction measurement.

- The uncertainty due to fitting the ΔE distribution with templates obtained from a finite number of Monte Carlo events. We vary the bin contents according to Poisson statistics and observe the change in the event yield extracted from the likelihood. Repeating this procedure 5000 times, we take the width of the event yield distribution as the systematic uncertainty.

7.3 Results

We obtain the following branching fraction for $B^0 \to J/\psi \ K_L$ decay:

$$BF(B^0 \to J/\psi \ K_L) = (3.4 \pm 0.4(\text{stat.}) \pm 0.4(\text{syst.})) \times 10^{-4}. \qquad (7.5)$$

This result is based on 408 events reconstructed using 22.7 million $B\bar{B}$ events collected between October 1999 and October 2000 at the BABAR detector at SLAC. This result was consistent with the 1998 world average value with a total uncertainty (16%) that is comparable to the 13% uncertainty on the world average value [65].

This work was originally published in Reference [67], where the $B^0 \to J/\psi K^0$ branching fraction was determined by combining our results with those obtained from $B^0 \to J/\psi K_S$ decay, where the K_S was reconstructed as a $\pi^+\pi^-$ or $\pi^0\pi^0$ pair:

$$BF(B^0 \to J/\psi K_S)(K_S \to \pi^+\pi^-) = (4.3 \pm 0.3(\text{stat.}) \pm 0.3(\text{syst.})) \times 10^{-4}$$

$$BF(B^0 \to J/\psi K_S)(K_S \to \pi^0\pi^0) = (4.8 \pm 0.8(\text{stat.}) \pm 0.4(\text{syst.})) \times 10^{-4},$$

Combining all BABAR results, we find

$$BF(B^0 \to J/\psi K^0) = (8.3 \pm 0.4(\text{stat.}) \pm 0.5(\text{syst.})) \times 10^{-4}, \qquad (7.6)$$

which is twice the branching fraction for $B^0 \to J/\psi K_S$ or $B^0 \to J/\psi\ K_L$. This result improved on the precision of the 1998 world average value by a factor of two.

Today, the world average value of $(8.5 \pm 0.5) \times 10^{-4}$ [8] is dominated by the results reported here, along with results from Belle (using 31.9 million $B\bar{B}$ events and reconstructing only $B^0 \to J/\psi K_S$, with $K_S \to \pi^+\pi^-$) in 2003 [71]:

$$BF(B^0 \to J/\psi K^0) = (7.9 \pm 0.4(\text{stat.}) \pm 0.9(\text{syst.})) \times 10^{-4},$$

and CLEO (using 9.7 million $B\bar{B}$ events, reconstructing $B^0 \to J/\psi K_S$ with $K_S \to \pi^+\pi^-, \pi^0\pi^0$) in 2000 [72]:

$$BF(B^0 \to J/\psi K^0) = (9.5 \pm 0.8(\text{stat.}) \pm 0.6(\text{syst.})) \times 10^{-4}.$$

Currently, the results reported here are the only instance of reconstructed $B^0 \to J/\psi\ K_L$ decays used to compute the world average value for the $B^0 \to J/\psi K^0$ branching fraction. Our result is comparable to those obtained using $B^0 \to J/\psi K_S$ decays, and therefore it plays a significant role in the determination of the $B^0 \to J/\psi K^0$ branching fraction.

Chapter 8

Measuring $\sin 2\beta$ with $B^0 \to J/\psi \; K_L$

The measurement of the CP-violating quantity $\sin 2\beta$ using the $B^0 \to J/\psi \; K_L$ decay mode was performed using roughly 88 million $\Upsilon(4S) \to B\bar{B}$ decays accumulated between 1999 and 2002 with the BABAR detector at the PEP-II asymmetric energy B Factory located at SLAC. The results reported here were published in Reference [64]. These results update an earlier BABAR measurement that first observed CP violation in the B^0 meson system using a sample of 32 million $\Upsilon(4S) \to B\bar{B}$ decays [73].

The procedure used to extract the quantity $\sin 2\beta$ from a sample of neutral B decays has been documented extensively in Reference [74], which expands on the results first reported in Reference [73]. I will focus on the aspects of the CP violation analysis that is specific to $B^0 \to J/\psi \; K_L$ decay, which was my contribution

191

to the analysis in 2002, and I will include changes that have been made relative to the procedure found in Reference [74]. The documentation proceeds as follows:

1. There are some differences in the $B^0 \to J/\psi\ K_L$ event selection when compared to the branching fraction analysis. I will discuss the changes, relative to the selection documented Section 7.1, in Section 8.1.

2. I discuss the details involved in extracting the CP asymmetry from B decays in Section 8.2. Particular attention will be paid to the specifics of the $B^0 \to J/\psi\ K_L$ event sample.

3. Our results, including a discussion of systematic uncertainties, appear in Section 8.3, and concluding thoughts can be found in Section 8.4.

8.1 CP Sample Selection

In Section 7.1 we presented the selection criteria for $B^0 \to J/\psi\ K_L$ events used to extract the $B^0 \to J/\psi\ K_L$ branching fraction. This selection was designed to optimize the quantity $S^2/(S+B)$, where S represents the number of reconstructed signal $B^0 \to J/\psi\ K_L$ events, and B describes the expected number of background events. Emphasis was placed on signal efficiency, in the sense that we would avoid tighter event selection if a large signal inefficiency for a given requirement resulted in only minimal improvement in $S^2/(S+B)$. Using this event selection,

we measured the $B^0 \to J/\psi\ K_L$ branching fraction from a dataset containing roughly 23 million $\Upsilon(4S)$ decays [67].

For the $\sin 2\beta$ measurement, we choose to optimize our event selection in order to minimize the uncertainty on $\sin 2\beta$, which is approximately given by [37, 75]:

$$
\begin{aligned}
\sigma_{\sin 2\beta} &= \frac{\sigma_0}{\sqrt{\epsilon \mathcal{D}^2\ N_S}}\ \frac{\sqrt{1 + N_B/N_S}}{1 + (A_B/A_S)(N_B/N_S)} \\
&= \frac{\sigma_0}{\sqrt{\epsilon \mathcal{D}^2\ N_S}}\ \frac{\sqrt{1 - F_B}}{1 - F_B(1 - A_B/A_S)}
\end{aligned}
\tag{8.1}
$$

where

- $\epsilon \mathcal{D}^2$ describes our ability to properly determine (tag) the flavor of event: The tagging efficiency is given by ϵ, and the dilution $\mathcal{D}$ is derived from the mistag probability w, $\mathcal{D} = 1 - 2w$;

- N_S (N_B) is the number of signal (background) events reconstructed before attempting to tag the flavor of the other B meson;

- F_B is the background fraction in the event sample;

- A_B/A_S is the ratio of the CP asymmetry in background compared to signal events;

- $\sigma_0 \approx 1.89$ is a constant that depends on δt resolution and the value $\sin 2\beta$, although the dependence on $\sin 2\beta$ is weak.

This new optimization is not far removed from our initial aim to maximize $S^2/(S+B)$. The two are actually equivalent if $(A_B/A_S) = 0$. In the first measurement of $\sin 2\beta$ using $B^0 \to J/\psi\ K_L$ decays [76], we discovered $A_B/A_S \approx -0.15$. With this information, and by nearly tripling our data sample, we see that our analysis could benefit from stricter requirements on our event selection. We enumerate the changes below.

8.1.1 Missing transverse momentum

We raised the minimum missing transverse momentum requirement ("missing p_T") for K_L candidates in the EMC and the IFR. Other than ΔE, the missing p_T requirement is the most effective variable for separating signal $B^0 \to J/\psi\ K_L$ decays from background. In the branching fraction analysis, we found that $S^2/(S+B)$ was maximized if we required missing p_T above -0.65 MeV in the EMC, with no requirement placed on IFR K_L candidates. As the $\sin 2\beta$ analysis benefits from increased signal purity, we now require missing p_T to exceed -0.25 MeV in the EMC, and -0.40 MeV in the IFR. The increase in signal purity in our event sample is shown in Figure 8.1.
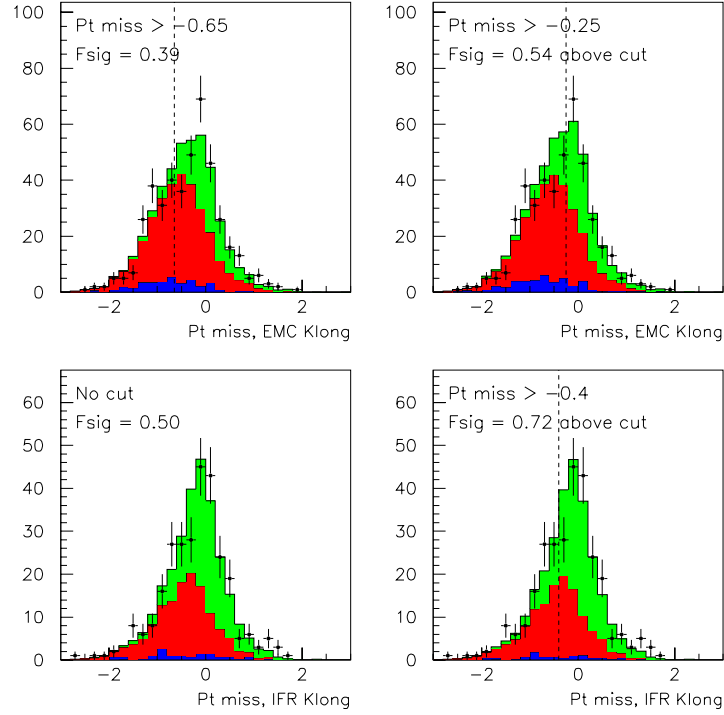
Figure 8.1: Missing transverse momentum (labeled "Pt miss" and given in GeV in the Figures) distributions for EMC and IFR K_L events, in data (points) and Monte Carlo (histograms), with $|\Delta E| < 10$ MeV. The signal $B^0 \rightarrow J/\psi\ K_L$ (green/light), inclusive $B \rightarrow J/\psi X$ background (red/medium), and non-J/ψ background (blue/dark) contributions were normalized above the missing transverse momentum cut value based on the results of the ΔE fit using the old (new) selection requirements. The signal purity ("Fsig") is indicated on each Figure.

8.1.2 EMC π^0 veto

Recall that in cases where the K_L candidate detected in the EMC is consistent with a photon, we veto the candidate if we also find another neutral cluster that combines with the K_L candidate to form an invariant mass compatible with a π^0. In the $\sin 2\beta$ analysis, we raise the minimum energy requirement for the neutral partner cluster from 30 MeV to 100 MeV. As EMC cluster multiplicity increases at low energy, this change reduces the number of real K_L mesons that are rejected due to unfortunate invariant mass combinations with random neutral clusters. We demonstrate the improvement due to this selection change in Figure 8.2.

8.1.3 Fitting the ΔE distribution

Recall from Section 7.2.1 that we extract the $B^0 \to J/\psi \ K_L$ event yield using a binned maximum likelihood fit to the ΔE distribution. The signal and inclusive $B \to J/\psi X$ background distributions are obtained from Monte Carlo, and the shape of the non-J/ψ distribution is obtained from a fit to the mass sidebands of the J/ψ dilepton distributions.

As expected, our event yield is strongly influenced by the ability of the Monte Carlo to reproduce what we see in data. In Section 7.2, we discussed corrections to signal Monte Carlo that affect the fitted $B^0 \to J/\psi \ K_L$ yield:
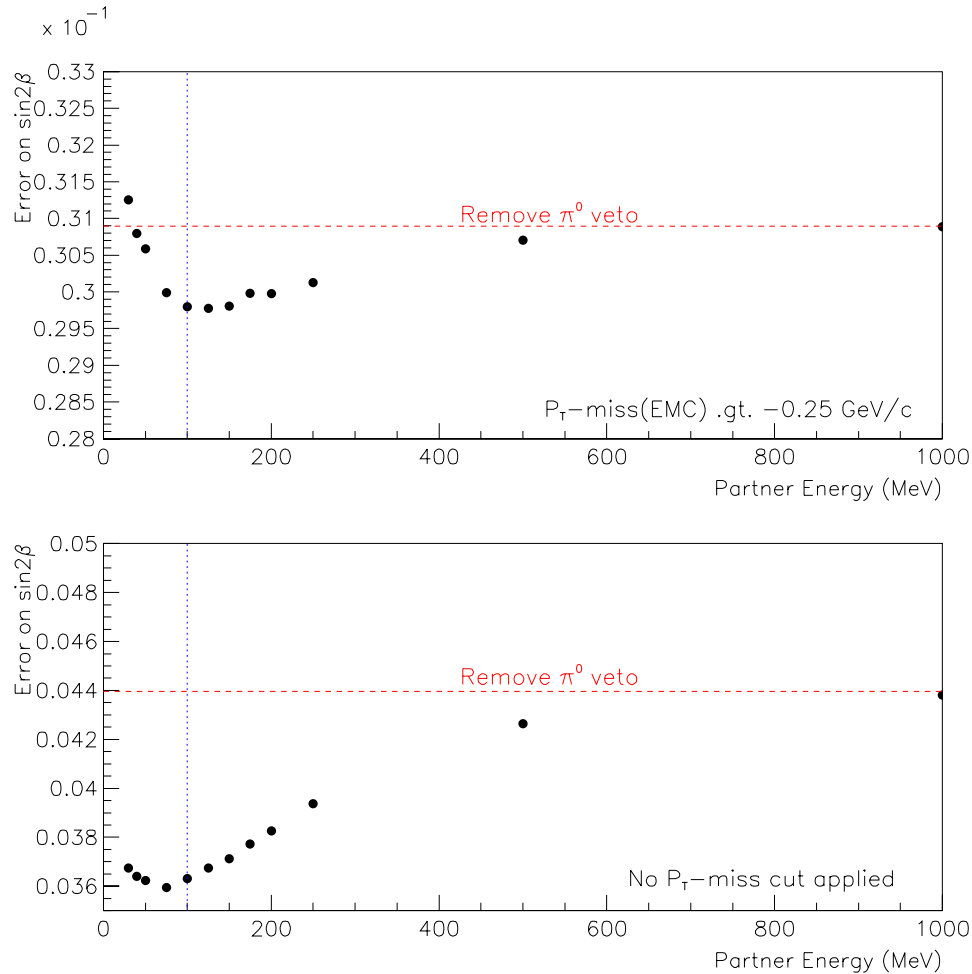
Figure 8.2: The error on $\sin 2\beta$ (not including constant factors or flavor tagging performance) as a function of the π^0 veto for varying minimum partner energies. The dashed red line describes the effects of removing the veto entirely, and the blue vertical line at 100 MeV indicates the current minimum allowed energy for the partner cluster. The previous minimum energy is the leftmost point on the plot. In the top plot, we show the effects of the π^0 veto when we require the missing p_T to exceed -0.25 GeV for EMC candidates. The missing p_T cuts have been removed in the bottom plot in order to accentuate the effects of the π^0 veto (and also demonstrate the usefulness of the missing p_T requirement).

197

1. We correct for the beam energy scale, and spread, based on a sample of $B^{\pm} \to J/\psi K^{\pm}$ decays, where the charged kaon is reconstructed as a K_L. This shifts the central value, and increases the width, of the ΔE distribution in Monte Carlo. With increased data available, we found that the shift in ΔE is unchanged (-0.5 MeV), but the additional Gaussian resolution included in order to "smear" the ΔE peak was reduced from $\sigma = 1.4$ MeV to $\sigma = 0.85$ MeV, where σ describes the width of the smearing Gaussian distribution.

2. We adjust the K_L resolution in the IFR to account for the overly optimistic expectations in the Monte Carlo. Based on a study of $e^+e^- \to \phi\gamma$, $\phi \to K_S K_L$ decays, we recompute the K_L flight direction to account for measurement differences between Monte Carlo and data. We then redetermine the value of ΔE for the new K_L direction. This tends to increase the signal population in the high ΔE tail. Improvements in Monte Carlo simulation made since the $B^0 \to J/\psi \ K_L$ branching fraction measurement allow us to safely drop this correction for $B^0 \to J/\psi \ K_L$ candidates reconstructed in the calorimeter, as we now see good agreement between Monte Carlo and data for the EMC.

Other corrections mentioned in Section 7.2 do not change the shape of the ΔE distributions, and as a result they do not influence the fitted yield.

We found that by lowering the muon identification requirements, we we able to increase the $J/\psi \to \mu^+\mu^-$ yield without significantly sacrificing purity. This change increases the relative amount of non-J/ψ background in the muon sample relative to electrons, and motivates us to split our sample according to lepton type. To take advantage of the higher signal purity in the IFR sample, we also split our results according to the detector used (*i.e.*, EMC or IFR) to reconstruct the K_L candidate.

In order to minimize the loss of statistical precision introduced by subdividing our dataset, the ΔE fits for the $J/\psi \to ee, \mu\mu$ decays are done simultaneously. For a given detector subsample, we expect that $\gamma(\ell^+\ell^-)$, which describes the fraction of $B^0 \to J/\psi \; K_L$ events relative to inclusive $B \to J/\psi X$ background for $J/\psi \to \ell^+\ell^-$ events, should not depend on lepton type. Therefore, we impose the following requirement on the ΔE fit:

$$\frac{\gamma(e^+e^-)}{\gamma(\mu^+\mu^-)} = 1.00 \pm 0.05 \tag{8.2}$$

where the value (and the uncertainty) is determined from studies of Monte Carlo events. We present the results of the ΔE fits to the data in Figures 8.3 and 8.4. The signal purity, as well as the background fraction with or without a J/ψ meson, will be used as inputs to the fit to determine $\sin 2\beta$.
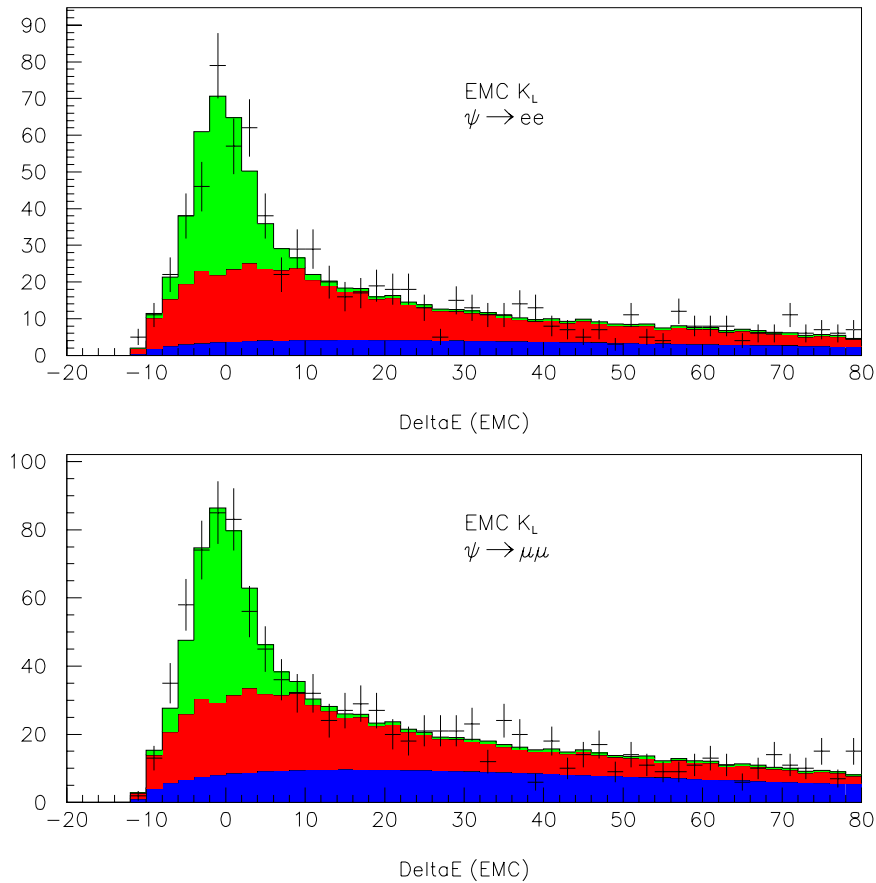
Figure 8.3: Fit of the ΔE spectrum (in MeV) for EMC K_L events in data. The blue (dark) distribution is the non-J/ψ component, which was fit to a threshold function. The red (medium) component is inclusive $B \to J/\psi X$ background from Monte Carlo and the green (light) component shows signal $B^0 \to J/\psi \ K_L$ events, also from Monte Carlo.
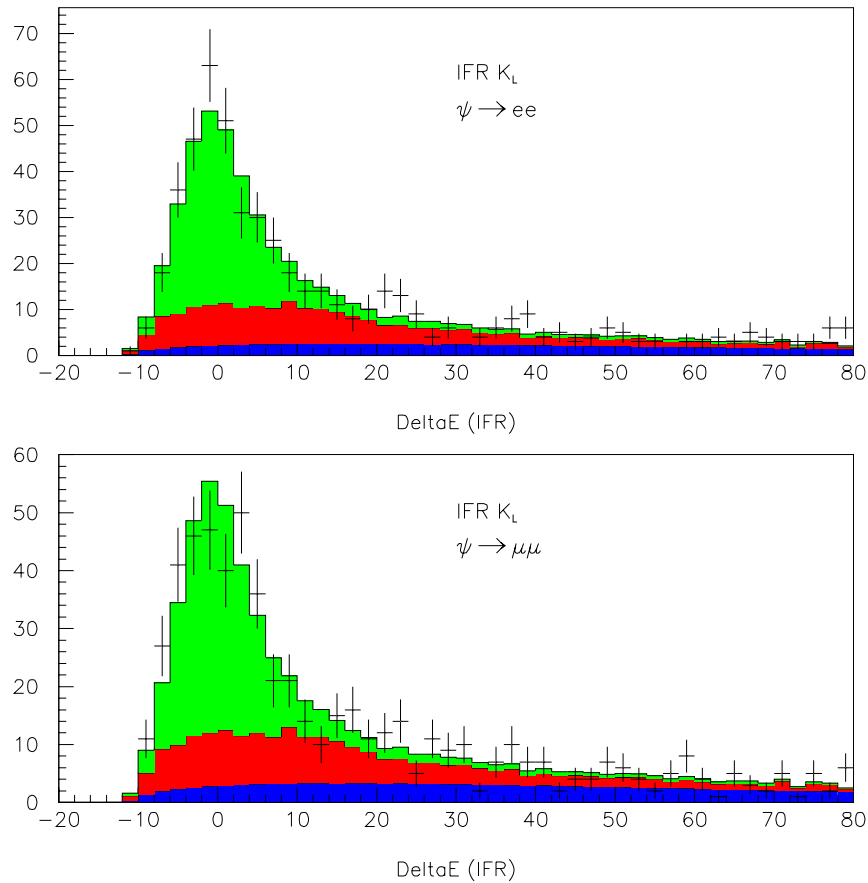
Figure 8.4: Fit of the ΔE spectrum (in MeV) for IFR K_L events in data, allowing for K_L angular resolution smearing. The blue (dark) distribution is the non-J/ψ component, which was fit to a threshold function. The red (medium) component is inclusive $B \rightarrow J/\psi X$ background from Monte Carlo and the green (light) component shows signal $B^0 \rightarrow J/\psi\ K_L$ events, also from Monte Carlo.

8.2 Determining $\sin 2\beta$

The $\Upsilon(4S)$ is an ideal environment to measure CP violation in the B meson system, as the $B^0\bar{B}^0$ system evolves in a coherent state until one of the B mesons decays. If we can successfully tag the flavor of one of the B^0 mesons (B_{tag}) from its decay products, then at moment of the B_{tag} decay, we know the other B meson (which we require to decay to $J/\psi K_L$) has the opposite flavor. Due to precise vertexing measurements provided by the BABAR SVT, we can measure the proper time interval between the decay of the B_{tag} meson and the $B^0 \rightarrow J/\psi K_L$ decay, $\Delta t = t_{\psi K_L} - t_{\text{tag}}$. Recall Equations 6.34 and 6.35, which describe the probability for a B^0 or $\bar{B}^0$ to decay to a common final state f_{CP} (such as $J/\psi K_L$). If we require that the $B^0\bar{B}^0$ system must be produced by $\Upsilon(4S)$ decay (see Section 6.5), and that the B mesons decay as $B_{\psi K_L}$ and B_{tag}, then the expression

$$
\begin{aligned}
\Phi(t_{\psi K_L}, t_{\text{tag}}) \quad &\propto \quad e^{-\Gamma(t_{\psi K_L} + t_{\text{tag}})} \times \\
&\left(1 \pm \left[\frac{2\ \text{Im}\ \lambda}{1 + |\lambda|^2}\sin(\Delta m_d \Delta t) - \frac{1 - |\lambda|^2}{1 + |\lambda|^2}\cos(\Delta m_d \Delta t)\right]\right)
\end{aligned}
\tag{8.3}
$$

describes the probability for a B^0 or $\bar{B}^0$ to decay to the final state $J/\psi K_L$ while the other decays to a flavor-defining state. The $\pm$ sign in Equation 8.3 depends on whether the B_{tag} meson is identified as a B^0 (+) or a $\bar{B}^0$ (−).

There are some steps that we can take to express $\Phi(t_{\psi K_L}, t_{\text{tag}})$ in a more manageable form:

- In order to obtain an expression that depends only on Δt, we can integrate Equation 8.3 with respect to $t_{\psi K_L} + t_{\text{tag}}$;

- We need to account for the fact that our ability to determine the flavor of the B_{tag} meson is not perfect. This will affect our ability to measure any CP asymmetry in the decay;

- We can take advantage of the Standard Model expectation that $|\lambda| = 1$ in B decays (see Equation 6.41) to simplify Equation 8.3. This assumption is equivalent to saying that CP violation in $B^0 \rightarrow J/\psi \ K_L$ decay is the result of interference between mixing and decay, or that any CP asymmetry is not the result of direct decay amplitudes only (see Section 6.4). This requires the tree diagram for $B^0 \rightarrow J/\psi \ K_L$ decay (Figure 6.4) to dominate over penguin contributions.

We may therefore describe the decay to the $J/\psi K_L$ final state as follows:

$$\phi_\pm(\Delta t; w, \sin 2\beta) \propto e^{-\Gamma|\Delta t|}[1 \mp \mathcal{D}\sin 2\beta \times \sin(\Delta m_d \Delta t)] \tag{8.4}$$

where the fraction of mistagged B decays (w) dampens the amplitude of the oscillation by a dilution factor $\mathcal{D} = (1 - 2w)$.

The results of Equation 8.4 still assume that the measured value of Δt is known precisely. In order to account for the finite resolution of the detector, we must

convolve the time-dependent distributions $\phi_\pm$ with a time resolution function, such that

$$\mathcal{F}_\pm(\Delta t; w, \sin 2\beta, \hat{a}) = \phi_\pm(\Delta t_{true}; w, \sin 2\beta) \otimes \mathcal{R}(\delta_t; \hat{a}), \qquad (8.5)$$

where $\delta_t \equiv \Delta t - \Delta t_{\text{true}}$ describes the difference between the measured and true proper time intervals, and $\hat{a}$ represents the set of parameters that describe the time resolution function $\mathcal{R}$. Figure 8.5 illustrates the impact of typical mistag and Δt resolution effects on the Δt distributions for flavor-tagged B decays.
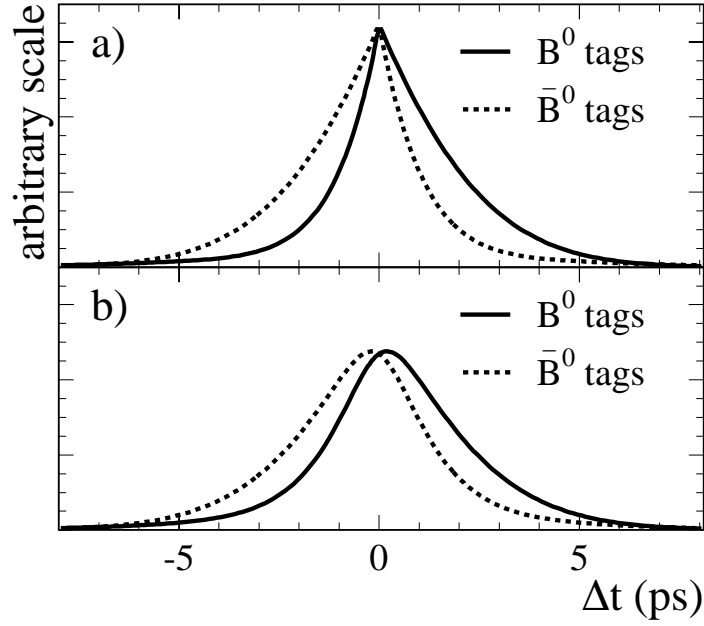
Figure 8.5: Expected Δt distributions for events tagged as a B^0 or a $\bar{B}^0$ with (a) perfect tagging and Δt resolution, and (b) typical mistag rates and Δt resolution. Nonzero mistag rates decrease the amplitude, and less than perfect time resolution smears out the peaks of the Δt distributions.

With this information, we may construct the CP-violating observable using Equation 6.37:

$$\mathcal{A}_{CP} = \frac{\mathcal{F}_+(\Delta t) - \mathcal{F}_-(\Delta t)}{\mathcal{F}_+(\Delta t) + \mathcal{F}_-(\Delta t)}. \tag{8.6}$$

If we assume that the penguin contribution to the decay amplitude is negligible and neglect resolution effects, this quantity is proportional to $\sin 2\beta$,

$$\mathcal{A}_{CP} \propto -\eta_{CP}\mathcal{D} \cdot \sin 2\beta \; \sin(\Delta m_d \Delta t), \tag{8.7}$$

where $\eta_{CP} = +1$ for $B^0 \to J/\psi \; K_L$ decays. Due to common B_{tag} notation, the sign of the asymmetry in Equation 8.7 is flipped with respect to Equation 6.37.

If we neglect background events, the value of $\sin 2\beta$ can be extracted from a sample of flavor-tagged decays by maximizing the likelihood function

$$\ln \mathcal{L}_{CP} = \sum_{\text{Tag.Cat.}} \left(\sum_{B^0 \text{tag}} \ln \mathcal{F}_+ + \sum_{\bar{B}^0 \text{tag}} \ln \mathcal{F}_- \right), \tag{8.8}$$

where the outer summation is over each of the different tagging categories, which we will discuss in Section 8.2.1, and the inner summations are over the $B^0/\bar{B}^0$ tagged events within a given tagging category. In reality, we must also include terms in the likelihood to account for the considerable backgrounds that are present in our reconstructed $B^0 \to J/\psi \; K_L$ event sample.

In addition to Equation 8.8, there is another likelihood function that is used to determine the $B^0 - \bar{B}^0$ oscillation frequency Δm_d. For this measurement, one of the neutral B mesons (B_{flav}) produced in $\Upsilon(4S)$ decay is fully reconstructed into

a decay mode such that the flavor of the B can be determined without ambiguity from its decay products:

$$\Upsilon(4S) \to B_{\text{tag}} B_{\text{flav}}, \quad B_{\text{flav}} \to D^{(*)-}(\pi/\rho/a_1)^+, J/\psi K^{*0}(K^{*0} \to K^+\pi^-).$$

We then tag the flavor of the B_{tag} using its decay products (see Section 8.2.1).

The probability for $B^0 - \bar{B}^0$ mixing can then be determined from Equations 6.28 and 6.30:

$$\text{Prob}(B^0\bar{B}^0 \to (B^0B^0 \text{ or } \bar{B}^0\bar{B}^0), B^0\bar{B}^0) \propto e^{-\Gamma\Delta t}\left(1 \mp \cos(\Delta m_d \Delta t)\right), \qquad (8.9)$$

where $\tau_{B^0} = 1/\Gamma$ is the B^0 lifetime. The $-(+)$ sign corresponds to mixed (unmixed) events, where we say mixing has occurred if the flavor of the B_{flav} and B_{tag} mesons are equal.

In the limit of perfect Δt resolution and flavor tagging, the mixing asymmetry as a function of Δt,

$$\mathcal{A}_{\text{mixing}} = \frac{N_{\text{unmix}}(\Delta t) - N_{\text{mix}}(\Delta t)}{N_{\text{unmix}}(\Delta t) - N_{\text{mix}}(\Delta t)}, \qquad (8.10)$$

would describe a cosine function with unit amplitude. Similar to our results in Equation 8.7, imperfect Δt resolution and flavor tagging reduces the observed mixing asymmetry as a function of Δt. Neglecting contributions from background events, the probability density functions (PDFs) for mixed and unmixed events can be written as

$$\mathcal{M}_\pm(\Delta t; w, \hat{a}) = e^{-\Gamma|\Delta t|}(1 \pm \mathcal{D} \cdot \cos(\Delta m_d \Delta t)) \otimes \mathcal{R}(\delta_t; \hat{a}), \qquad (8.11)$$

where $\mathcal{R}$ is the same resolution function that was introduced in Equation 8.5.

The full B mixing likelihood function, ignoring background contributions, can be written as

$$\ln \mathcal{L}_{\text{mix}} = \sum_{\text{Tag.Cat.}} \left(\sum_{\text{unmixed}} \ln \mathcal{M}_+ + \sum_{\text{mixed}} \ln \mathcal{M}_- \right), \tag{8.12}$$

which parallels our treatment of $\mathcal{L}_{CP}$. This likelihood term is combined with $\mathcal{L}_{CP}$ in order to simultaneously extract the value of $\sin 2\beta$ and Δm_d, in addition to the mistag parameters (w) and the Δt resolution function parameters ($\hat{a}$). We must also include additional terms in the likelihood in order to account for backgrounds and their time dependence.

It should be clear at this point that the $\sin 2\beta$ analysis is the product of many complicated ingredients. In the following sections, I will describe the various inputs to the likelihood function used to determine $\sin 2\beta$.

8.2.1 B flavor tagging

After we reconstruct a $B \rightarrow f_{CP}$ or B_{flav} decay in the BABAR detector, we examine the remaining tracks with the hope that we can identify the flavor of the recoiling B_{tag} meson. We use four different tagging categories in this analysis in order to determine the B_{tag} flavor:

1. For the `Lepton` category, a B^0 ($\bar{b}d$) meson is tagged according to the charge of the lepton produced in semileptonic decay, $\bar{b} \rightarrow \bar{c}\ell^+\nu$.

2. In a similar fashion, the charge of the kaon produced from the $b \rightarrow c \rightarrow s$ transition tags the flavor of the initial b quark. For the two `Kaon` tag categories, we exploit the charge correlation between the b quark and the kaon(s) produced in B decay. When available, we also utilize the charge of the low-momentum charged pion produced from $D^{*\pm}$ decay. If the soft pion is found traveling in roughly the same direction as the kaon, and has the opposite charge of the kaon, we can use the soft pion information to reduce the mistag rate for the `Kaon` tag. These event are placed in the `Kaon I` tag category, which is set aside for kaon-tagged events with lower mistag rates. If no soft pion is found, events with a kaon tag may be placed in the `Kaon I` or `Kaon II` category, depending on the estimated mistag probability. Events with a soft pion that have no identified kaon are placed in the `Kaon II` category. In the event that the kaon from the decay of the charm meson is found for an event that already has a lepton tag, the charge of the kaon is used as additional tagging information for the `Lepton` tag category. This information reduces the probability that the flavor of the b quark will be misidentified.

	Lepton	Kaon I	Kaon II	Inclusive
N_{sig}	2979 ± 57	5450 ± 83	6489 ± 92	6535 ± 94
N_{BG}	491 ± 28	4745 ± 78	7677 ± 99	7599 ± 99
Purity (%)	0.956 ± 0.005	0.862 ± 0.005	0.826 ± 0.005	0.823 ± 0.005

Table 8.1: Results of the m_{ES} fits shown in Figure 8.6, where N_{sig} and N_{BG} represents the number of signal and background events reconstructed with $m_{ES} > 5.2$ GeV. The purity is computed for events in the signal region ($m_{ES} > 5.27$ GeV) only.

3. The final tagging category contains all remaining events that have some available tagging information, but for whatever reason they do not belong in any of the other three tagging categories. These include events with a high-momentum particle that has not been identified as a lepton (such as $B^0 \to D^{*-}\pi^+$) as well as semileptonic decays where the electron/muon did not meet the lepton identification criteria. In this case, the charge of the high-momentum particle can be correlated to the flavor of the b quark. As might be expected, the power of this inclusive category is small relative to the other three.

Each of the above categories are mutually exclusive, and they accumulate events based on the output of a neural network which combines the outputs of the various physics-based criteria for each category. The estimates of the tagging efficiencies and the mistag probabilities are obtained from the B_{flav} sample, in which neutral B mesons are reconstructed with high purity (see Figure 8.6 and Table 8.1). As
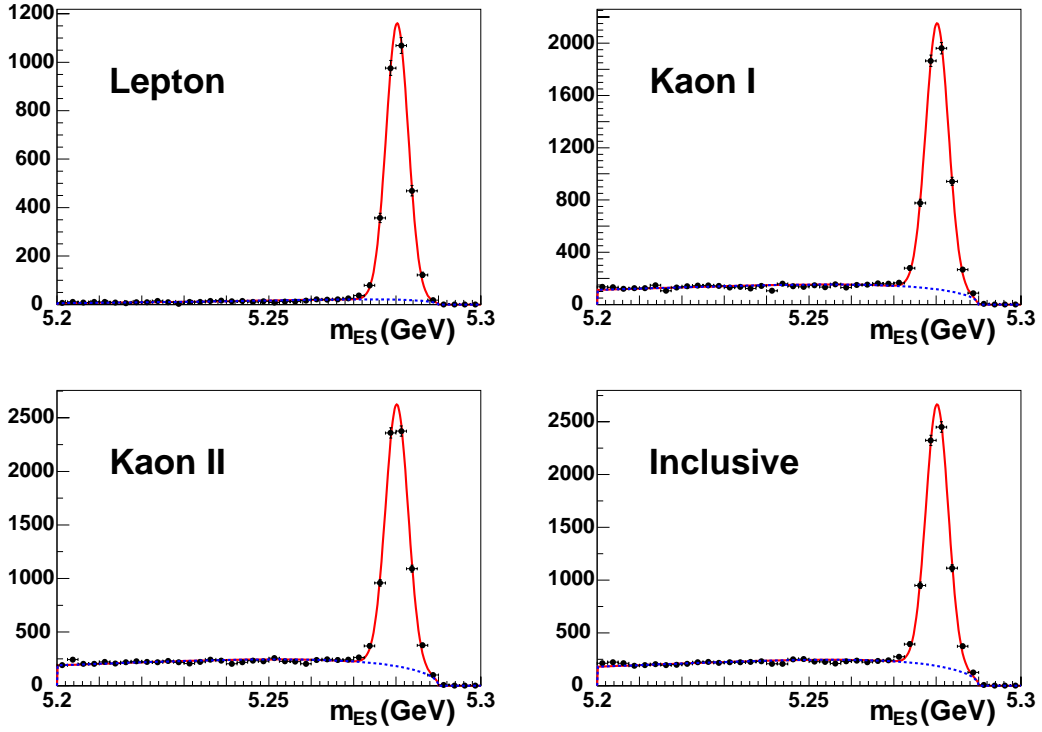
Figure 8.6: Fits to the m_{ES} distribution for events in the B_{flav} sample in data for each tagging category. (Recall from Equation 5.2 that $m_{ES} = \sqrt{E^*_{\text{beam}} - \vec{p}^{\,*}_B}$.) Events are fit to the sum of a Gaussian function and a threshold background function, and the signal region is defined as $m_{ES} > 5.27$ GeV, and the bin width in each plot is set to 2.5 GeV.

the B_{flav} can be uniquely determined from its decay products, we may attempt to determine the flavor of the B_{flav} using the recoiling B_{tag} meson in order to estimate the mistag probability for each tagging category.

We summarize the performance of each tagging category in Table 8.2. The figure of merit for tagging power is the effective tagging efficiency $Q_i \equiv \sum_i \epsilon_i \mathcal{D}_i^2$, where ϵ_i describes the tagging efficiency for a given tagging category i. The average mistag fractions w and the differences $\Delta w \equiv w(B^0) - w(\bar{B}^0)$ for each tagging category are used as inputs to the maximum likelihood fit used to determine $\sin 2\beta$.

Category	ϵ (%)	w (%)	Δw (%)	Q (%)
Lepton	9.1 ± 0.2	3.3 ± 0.6	-1.5 ± 1.1	7.9 ± 0.3
Kaon I	16.7 ± 0.2	10.0 ± 0.7	-1.3 ± 1.1	10.7 ± 0.4
Kaon II	19.8 ± 0.3	20.9 ± 0.8	-4.4 ± 1.2	6.7 ± 0.4
Inclusive	20.0 ± 0.3	31.5 ± 0.9	-2.4 ± 1.3	2.7 ± 0.3
All	65.6 ± 0.5			28.1 ± 0.7

Table 8.2: Efficiencies ϵ_i, average mistag fractions w_i, mistag fraction differences $\Delta w_i = w_i(B^0) - w_i(\bar{B}^0)$, and Q extracted for each tagging category i from the B samples used to extract $\sin 2\beta$ (see Reference [64]).

8.2.2 Time difference

From Equation 8.7 we see that measuring $\sin 2\beta$ depends on our ability to measure the proper time difference (Δt) between the $B^0 \rightarrow J/\psi \ K_L$ decay and the decay of the B_{tag} meson. Neglecting the momentum of the B mesons in the

$\Upsilon(4S)$ frame, we may express Δt in terms of the separation along the beam axis between the reconstructed B (in our case, either a $B^0 \rightarrow J/\psi \ K_L$ or a B_{flav} meson) and the B_{tag} meson:

$$\Delta z = \beta\gamma c\Delta t, \tag{8.13}$$

where $\beta\gamma = 0.56$ is the average $\Upsilon(4S)$ boost factor. When we account for the 340 MeV momentum of the B mesons in the $\Upsilon(4S)$ frame, the resulting corrections improve the resolution on Δt by about 5%.

From Figure 8.5 we see that our measurement of the asymmetry $\mathcal{A}_{CP}$ depends on the Δt resolution. As we have already reconstructed one decay vertex as a B_{flav} meson or $B^0 \rightarrow J/\psi \ K_L$, the remaining tracks in the event are used to determine the B_{tag} vertex. These tracks are required to originate from a single point, where we include information from the fully-reconstructed B candidate (its three-momentum and decay vertex), the average position of the interaction point, and the average $\Upsilon(4S)$ boost factor in order to improve the result of the geometric fit. In order to reduce the bias introduced from long-lived particles, we form the B_{tag} candidate using K_S and Λ^0 candidates in place of their daughters.

The Δt resolution function is expressed in terms of $\delta_t \equiv \Delta t - \Delta t_{true}$ as the sum of three Gaussian distributions:

$$
\begin{aligned}
\mathcal{R}(\delta_t, \hat{a}) \;=\; & \frac{f_{\text{core}}}{S_{\text{core}}\sigma_{\Delta t}\sqrt{2\pi}} \cdot \exp(-\frac{(\delta_t - b_{\text{core}}\sigma_{\Delta t})^2}{2(S_{\text{core}}\sigma_{\Delta t})^2}) + \\
& \frac{f_{\text{tail}}}{S_{\text{tail}}\sigma_{\Delta t}\sqrt{2\pi}} \cdot \exp(-\frac{(\delta_t - b_{\text{tail}}\sigma_{\Delta t})^2}{2(S_{\text{tail}}\sigma_{\Delta t})^2}) + \\
& \frac{f_{\text{out}}}{\sigma_{\text{out}}\sqrt{2\pi}} \cdot \exp(-\frac{\delta_t^2}{2\sigma_{\text{out}}^2}),
\end{aligned}
\tag{8.14}
$$

where the majority of the data is described by the narrowest (core) Gaussian. The width of the the core and tail Gaussians is equal to the the measurement uncertainty of the vertex fit ($\sigma_{\Delta t}$) multiplied by scale factors S_{core} and S_{tail}, respectively. We also allow the core and tail Gaussian distributions to have a nonzero mean in order to account for the lifetimes of charmed mesons used to form the B_{tag} vertex. The final Gaussian distribution describes the small fraction of events that have poor Δt resolution (outliers).

For the CP measurement, the we require $|\Delta t| < 20$ psec, with an uncertainty on Δt below 2.4 psec. About 95% of the events satisfy this requirement, and the RMS resolution on Δt for 99.7% of these events is 1.1 psec. The Δt resolution function parameters are input to the maximum likelihood fit used to determine $\sin 2\beta$, although only eight parameters are free in the fit: the scale factor of the core Gaussian (S_{core}), four individual core bias scale factors (b_{core}^i) for each of the

tagging categories, a common tail bias b_{tail}, and the tail (f_{tail}) and outlier (f_{out}) fractions. We fix $S_{\text{tail}} = 3.0$ and $\sigma_{\text{out}} = 8$ psec in the fit.

8.2.3 Sample composition

It is difficult to forget that a significant fraction of the $B^0 \rightarrow J/\psi \; K_L$ event sample contains background. Our current definition of the likelihood $\mathcal{L}_{CP}$ (Equation 8.8) ignores any contributions from background events. We must carefully determine the properties of the $B^0 \rightarrow J/\psi \; K_L$ event sample, and include the effects of background events in the $\mathcal{F}_\pm$ PDFs (Equation 8.5), in order to be able to extract any CP asymmetry from our data sample. In this Section, and Section 8.2.4, we will focus on the important features of the $B^0 \rightarrow J/\psi \; K_L$ event sample, and in Section 8.2.5 we will discuss our modifications to $\mathcal{F}_\pm$ and $\mathcal{L}_{CP}$.

Figures 8.3 and 8.4 demonstrate that more than 90% of the events that pass our selection requirements contain a real J/ψ. In Table 8.3 we list the fraction of $B \rightarrow J/\psi X$ Monte Carlo events with $|\Delta E| < 10$ MeV that pass our selection, separated according to tagging category. In Section 7.1.3 we discussed our concern that the missing p_T requirement would bias our results for events with a lepton tag, as the neutrino from semileptonic B decay degrades the resolution of the missing p_T measurement. This effect degrades signal efficiency for lepton-tagged events, but it does not significantly alter the background efficiency (see Table 8.4). We

EMC K_L	All events	No flavor tag	Lepton	Kaon1	Kaon2	Inclusive
$J/\psi \, K_L^0$ (signal)	61.5 ± 0.6	61.3 ± 1.1	56.8 ± 1.7	63.2 ± 1.0	62.7 ± 2.2	61.1 ± 1.6
$J/\psi \, K^{*0}$	6.9 ± 0.3	7.9 ± 0.6	6.7 ± 0.8	5.6 ± 0.5	7.2 ± 1.2	7.7 ± 0.9
$J/\psi \, K_L^0 \, \pi^0$	0.4 ± 0.1	0.5 ± 0.2	0.6 ± 0.3	0.4 ± 0.1	0.2 ± 0.2	0.3 ± 0.2
$J/\psi \, K^{*+}$	10.0 ± 0.4	9.9 ± 0.6	10.7 ± 1.0	10.1 ± 0.6	8.7 ± 1.3	9.9 ± 1.0
$J/\psi \, K_L^0 \, \pi^+$	0.5 ± 0.1	0.4 ± 0.1	0.3 ± 0.2	0.7 ± 0.2	0.2 ± 0.2	0.5 ± 0.2
$J/\psi \, K_S^0, \, K_S^0 \to \pi^0 \, \pi^0$	4.9 ± 0.3	4.9 ± 0.5	5.8 ± 0.8	4.2 ± 0.4	5.8 ± 1.1	5.1 ± 0.7
$\chi_c(1) \, K_L^0$	1.4 ± 0.1	1.3 ± 0.2	2.2 ± 0.5	1.2 ± 0.2	1.4 ± 0.5	1.1 ± 0.3
Other $J/\psi \, X$ modes	14.5 ± 0.4	13.8 ± 0.7	16.8 ± 1.3	14.7 ± 0.7	13.7 ± 1.6	14.2 ± 1.1

IFR K_L	All events	No flavor tag	Lepton	Kaon1	Kaon2	Inclusive
$J/\psi \, K_L^0$ (signal)	75.8 ± 0.6	77.0 ± 1.1	71.6 ± 2.0	76.6 ± 1.1	77.7 ± 2.4	73.9 ± 1.7
$J/\psi \, K^{*0}$	5.8 ± 0.4	6.1 ± 0.6	6.4 ± 1.1	5.1 ± 0.6	5.9 ± 1.3	6.5 ± 1.0
$J/\psi \, K_L^0 \, \pi^0$	0.2 ± 0.1	0.1 ± 0.1	0.2 ± 0.2	0.3 ± 0.1	0.0 ± 0.0	0.2 ± 0.2
$J/\psi \, K^{*+}$	11.1 ± 0.5	9.3 ± 0.8	13.7 ± 1.5	11.6 ± 0.8	10.2 ± 1.7	12.3 ± 1.3
$J/\psi \, K_L^0 \, \pi^+$	0.4 ± 0.1	0.3 ± 0.1	1.0 ± 0.4	0.4 ± 0.2	0.0 ± 0.0	0.3 ± 0.2
$J/\psi \, K_S^0, \, K_S^0 \to \pi^0 \, \pi^0$	0.7 ± 0.1	1.1 ± 0.3	1.0 ± 0.4	0.3 ± 0.1	0.7 ± 0.5	0.6 ± 0.3
$\chi_c(1) \, K_L^0$	1.5 ± 0.2	1.6 ± 0.3	1.4 ± 0.5	1.5 ± 0.3	1.6 ± 0.7	1.3 ± 0.4
Other $J/\psi \, X$ modes	4.5 ± 0.3	4.6 ± 0.6	4.8 ± 0.9	4.2 ± 0.5	3.9 ± 1.1	5.0 ± 0.9

Table 8.3: The sample composition (in %) in inclusive J/ψ Monte Carlo as a function of flavor tag. We specifically list the top six background modes in each detector sample (EMC/IFR) in addition to signal $B^0 \to J/\psi \; K_L$ decays. Each of the major background modes, with the exception of $B \to J/\psi K_S$, contain a real K_L in the decay.

Category	Efficiency (%)
Signal, Lepton, EMC	60.2 ± 1.3
Signal, Non-lepton, EMC	71.3 ± 0.6
Signal, Lepton, IFR	70.1 ± 1.6
Signal, Non-lepton, IFR	81.4 ± 0.6
$B \rightarrow J/\psi X$ BG, Lepton, EMC	23 ± 5
$B \rightarrow J/\psi X$ BG, Non-lepton, EMC	22 ± 2
$B \rightarrow J/\psi X$ BG, Lepton, IFR	46 ± 13
$B \rightarrow J/\psi X$ BG, Non-lepton, IFR	45 ± 6

Table 8.4: Efficiency of the missing p_T requirement for signal and $B \rightarrow J/\psi X$ background for lepton and non-lepton tagged events in Monte Carlo.

see this effect in Table 8.3, as the fraction of signal events is lower in lepton-tagged events with respect to the other tagging categories.

Background events that pass our event selection requirements, but do not contain a real $J/\psi \rightarrow \ell^+\ell^-$ decay, are modelled using a sample of events taken from the sidebands of the J/ψ dilepton mass distribution:

- For $J/\psi \rightarrow e^+e^-$, $3.175 < m_{ee} < 3.50$ GeV;

- For $J/\psi \rightarrow \mu^+\mu^-$, $3.175 < m_{\mu\mu} < 3.50$ and $2.90 < m_{\mu\mu} < 3.00$ GeV.

The Δt distribution for J/ψ-sideband events are fit to the sum of three Gaussians (see Equation 8.15), as shown in Figure 8.7. The Δt resolution function parameters obtained from the fit are presented in Table 8.5. The resolution function parameters (with the exception of σ_{out}) and the lifetime were free in the fit. The

values in Table 8.5 are fixed inputs to the maximum likelihood function used to extract $\sin 2\beta$.
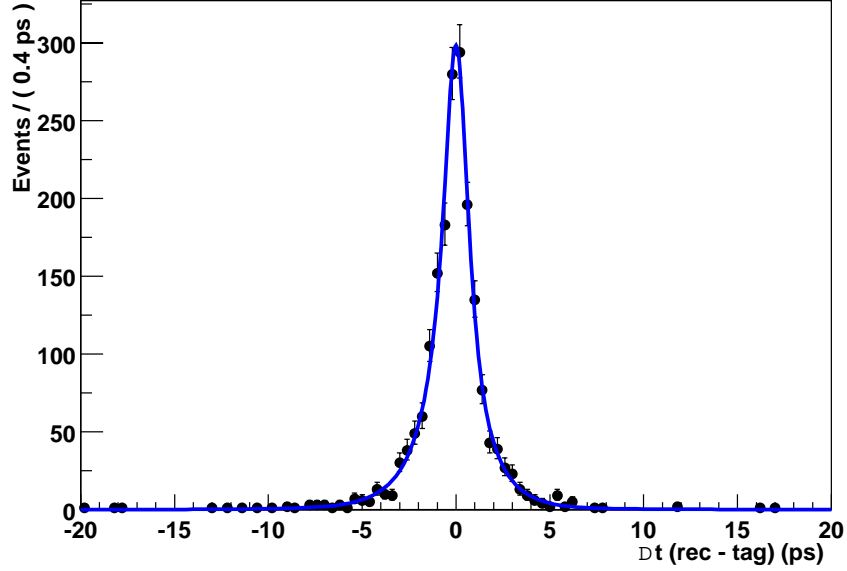
Figure 8.7: Fit of the Δt distribution for data events in the J/ψ mass sidebands.

Parameter	value
Core Gaussian σ scale factor	1.16 ± 0.07
Core Gaussian bias	-0.04 ± 0.05
Tail Gaussian σ scale factor	2.65 ± 0.40
Tail Gaussian bias	-0.91 ± 0.39
Fraction in tail	0.18 ± 0.06
Fraction in $\sigma = 8$ psec Gaussian (outlier)	0.02 ± 0.006
Fraction with no lifetime	0.61 ± 0.07
Lifetime (Γ_{non})	(1.13 ± 0.13) psec

Table 8.5: Results of an unbinned likelihood fit to the Δt distribution in Figure 8.7 for data events in the J/ψ mass sidebands.

217

We again find that the lepton tag efficiency is significantly lower for data events in the J/ψ mass sidebands than for events in the B_{flav} sample. In this case, the results reflect the small chance of finding three high momentum leptons, two to reconstruct the J/ψ and one to tag the event, in B decays involving charmonium.

In our analysis of the $B^0 \rightarrow J/\psi \ K_L$ branching fraction, we determined that a minimum missing transverse momentum requirement above -300 MeV could bias lepton-tagged events; we exceed this value in the CP analysis. In order to account for the drop in the lepton tag efficiency for signal and non-J/ψ background events, we separate our results for the `Lepton` tag category from the results for the other tagging categories.

8.2.4 Input parameters from ΔE distributions

Figures 8.3 and 8.4 present the fits to the ΔE distributions for all reconstructed $B^0 \rightarrow J/\psi \ K_L$ events. We use a subset of these events, where we are able to tag the flavor of the B, to determine $\sin 2\beta$. As a result, we take the signal and background fractions extracted from our fit to the ΔE distribution for all flavor-tagged $B^0 \rightarrow J/\psi \ K_L$ events as inputs to the maximum likelihood function $\mathcal{L}_{CP}$, which we will discuss in Section 8.2.5.

We present the results of the fit for all flavor-tagged events in Tables 8.6 and 8.7. Recall from Section 8.1.3 that we fit $J/\psi \rightarrow e^+ e^-$ and $J/\psi \rightarrow \mu^+ \mu^-$

events simultaneously, and we fit the EMC and IFR samples separately. The various $B \to J/\psi X$ backgrounds (see Table 8.3) are normalized to the inclusive J/ψ fraction extracted from the ΔE fit. We adjust all fractions to account for the lepton flavor tag efficiency differences discussed in Section 8.2.3.

	ΔE Fit $J/\psi \to ee$		ΔE Fit $J/\psi \to \mu\mu$	
	Events	Fraction	Events	Fraction
Signal	122 ± 13	$49.8 \pm 3.6\%$	164 ± 17	$47.4 \pm 3.4\%$
$J/\psi X$	101 ± 10	$41.4 \pm 3.7\%$	135 ± 12	$39.1 \pm 3.4\%$
non-J/ψ	22 ± 3	$8.8 \pm 1.2\%$	47 ± 3	$13.5 \pm 1.2\%$

Table 8.6: Results of binned maximum likelihood ΔE fit for all flavor tagged $B^0 \to J/\psi \ K_L$ events where the K_L is reconstructed in the EMC. The fractions and yields are given for events with $|\Delta E| < 10$ MeV.

	ΔE Fit $J/\psi \to ee$		ΔE Fit $J/\psi \to \mu\mu$	
	Events	Fraction	Events	Fraction
Signal	134 ± 16	$65.2 \pm 5.1\%$	142 ± 17	$64.2 \pm 5.1\%$
$J/\psi X$	60 ± 10	$29.3 \pm 5.2\%$	64 ± 11	$28.9 \pm 5.1\%$
non-J/ψ	11 ± 2	$5.5 \pm 1.0\%$	15 ± 2	$6.9 \pm 1.0\%$

Table 8.7: Results of binned maximum likelihood ΔE fit for all flavor tagged $B^0 \to J/\psi \ K_L$ events where the K_L is reconstructed in the IFR. The fractions and yields are given for events with $|\Delta E| < 10$ MeV.

In order to distinguish between signal and background on an event-by-event basis in the maximum likelihood fit to extract $\sin 2\beta$, we model the EMC and IFR ΔE distributions for the $B^0 \to J/\psi \ K_L$ event sample using a series of probability density functions:

- $B^0 \to J/\psi\ K_L$ signal events are fit to the sum of two Gaussian distributions and a threshold function in the region $-20 < \Delta E < 80$ MeV.

- $B \to J/\psi K_S$ events, which have opposite CP relative to signal events, are fit to the sum of a Gaussian distribution and a threshold function in the region $-20 < \Delta E < 80$ MeV.

- The remaining inclusive $B \to J/\psi X$ background is fit to a 4th order polynomial for $|\Delta E| < 20$ MeV.

- The shape of the non-J/ψ background is determined using a threshold function in the range $-20 < \Delta E < 80$ MeV.

In each case, the form of the PDFs are chosen in order to successfully model the event behavior in the signal region ($|\Delta E| < 10$ MeV). We extract the PDF parameters from fits to ΔE distributions for Monte Carlo and J/ψ sideband events, which are shown in Figures 8.8 and 8.9. A total of eight PDFs are used as inputs to the $\sin 2\beta$ fit, four for events with the K_L reconstructed in the EMC, and four for IFR K_L reconstruction, although the parameters of the threshold function used for the non-J/ψ events are common to both the EMC and IFR PDFs. The relative fractions of signal and inclusive J/ψ background are fixed to the results from the binned maximum likelihood fit to the ΔE distribution, given in Tables 8.6 and 8.7.
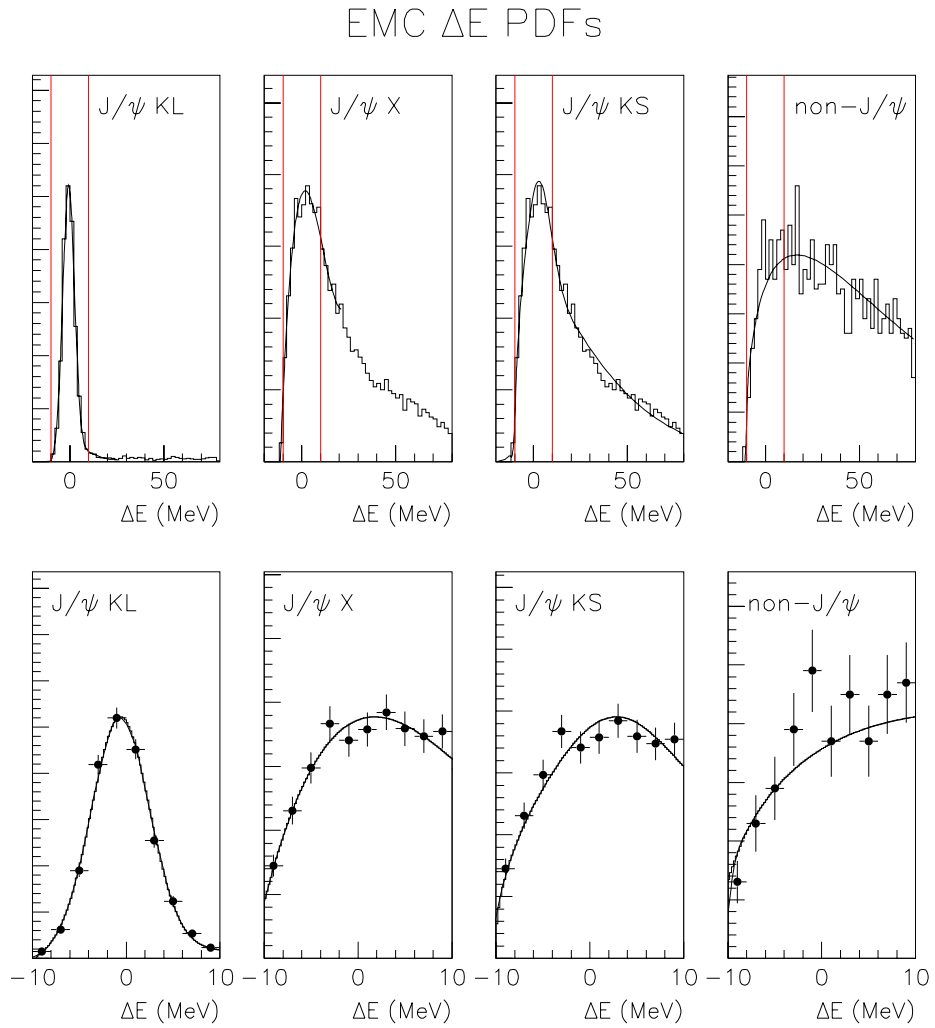
Figure 8.8: Fits of the EMC-K_L ΔE distributions for the probability density functions used in the $\sin 2\beta$ fit. The fit functions are described in the text.

IFR ΔE PDFs
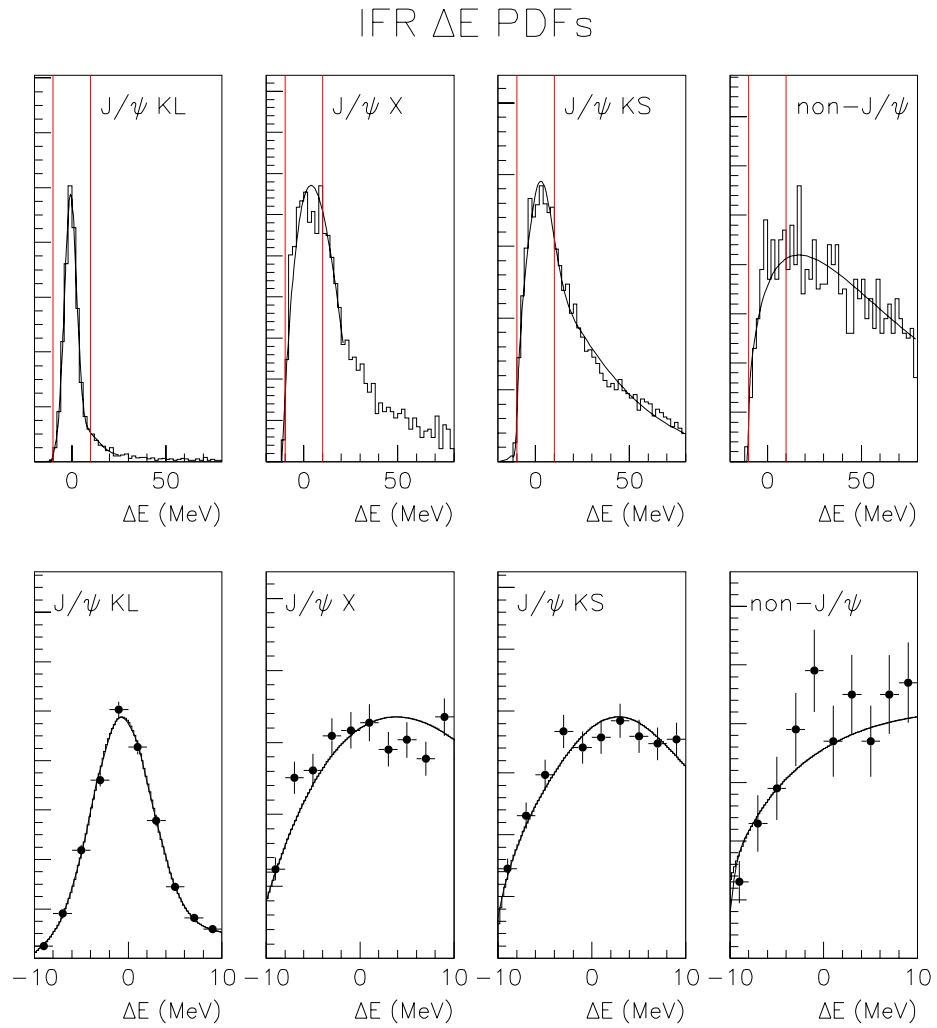
Figure 8.9: Fits of the IFR-K_L ΔE distributions for the probability density functions used in the $\sin 2\beta$ fit. The fit functions are described in the text.

8.2.5 The likelihood function $\mathcal{L}_{CP}$

We extract $\sin 2\beta$ from a flavor-tagged sample of reconstructed $B^0 \rightarrow J/\psi\ K_L$ decays using an unbinned maximum-likelihood technique (Equation 8.8) based on the probability density functions $\mathcal{F}_\pm$ described in Equation 8.5. Up to this point, our definition of the likelihood has neglected to include the effects of background events. In reality, a sizable fraction of our event sample consists of background from $B \rightarrow J/\psi X$ decays as well as events with a misreconstructed $J/\psi \rightarrow \ell\ell$ candidate. Some of these backgrounds, such as $B \rightarrow J/\psi K_S$ and $B \rightarrow J/\psi K^{*0}$, have non-zero CP asymmetry, which we summarize in Table 8.8. In Sections 8.2.3 and 8.2.4 we discussed the properties of events reconstructed as $B^0 \rightarrow J/\psi\ K_L$. In this Section, we will put our discussion in the proper context, as we will modify the likelihood function to include the effects of background.

In order to address the complications introduced by background events, we need to modify the $\mathcal{F}_\pm$ PDFs in the following way:

$$
\begin{aligned}
\mathcal{F}_{\pm,i} \;=\; & f_{i,k}^{\text{signal}}(\Delta E)\mathcal{F}_\pm(\Delta t; w, \sin 2\beta, \hat{a}) \\
& + \sum_{\alpha\,=\,J/\psi X} f_{i,k}^\alpha(\Delta E)\mathcal{F}_\pm(\Delta t; w, \sin 2\beta, \hat{a}) \qquad (8.15) \\
& + f_{i,k}^{\text{non}-J/\psi}(\Delta E)\mathcal{F}_\pm^{\text{non}}(\Delta t; \hat{b}).
\end{aligned}
$$

Each event is classified according to its tagging category (i), its flavor tag value ($\pm$), and the K_L reconstruction category (k, either EMC or IFR). The major con-

223

tributors to the $B \rightarrow J/\psi X$ background (see Table 8.3), as well as the unitemized $B \rightarrow J/\psi X$ events, are included in the sum over α. The relative fractions of signal, $B \rightarrow J/\psi X$, and non-J/ψ events ($f_{i,k}^{\text{signal}}$, $f_{i,k}^{\alpha}$, and $f_{i,k}^{\text{non}-J/\psi}$, respectively) are determined from the binned maximum likelihood fits to the ΔE distributions discussed in Section 8.1.3 and are different for lepton versus non-lepton tagging categories. Based on studies of Monte Carlo events, we use the same resolution function parameters ($\hat{a}$) to describe both signal and $B \rightarrow J/\psi X$ background events. The non-J/ψ background PDF $\mathcal{F}_{\pm}^{\text{non}}$ is computed as the sum of prompt (f_0) and lifetime continuum background components,

$$\mathcal{F}_{\pm}^{\text{non}} = f_0 \cdot \frac{1}{2}\delta(\Delta t) \otimes \mathcal{R}(\delta_t; \hat{b}) + (1 - f_0) \cdot \frac{\Gamma_{\text{non}}}{4}e^{-|\Delta t|/\tau} \otimes \mathcal{R}(\delta_t; \hat{b}), \qquad (8.16)$$

where the resolution function parameters $\hat{b}$ and the effective decay width Γ_{non} are fixed to the values from Table 8.5, and τ is taken as the B^0 lifetime.

Event type	Effective CP
$B^0 \rightarrow J/\psi K^{*0}, K^{*0} \rightarrow K_L\pi^0$	-0.68 ± 0.07
$B^0 \rightarrow J/\psi K_S$	-1
$B^0 \rightarrow \chi_{c1} K_L$	$+1$
Other $B \rightarrow J/\psi X$ (EMC)	$0.21^{+0.12}_{-0.06}$
Other $B \rightarrow J/\psi X$ (IFR)	$0.24^{+0.14}_{-0.06}$
non-J/ψ	0 ± 0.25

Table 8.8: Expected CP content for $B^0 \rightarrow J/\psi \ K_L$ background events. The CP content for $B^0 \rightarrow J/\psi K^{*0}$ was taken from Reference [77], and the CP content for the non-itemized $B \rightarrow J/\psi X$ were determined from Monte Carlo samples, where we require $|\Delta E| < 10$ MeV. The quoted errors are conservative estimates used to determine the systematic uncertainty on $\sin 2\beta$ due to backgrounds.

As we mentioned in Section 8.2, the nominal fit to extract $\sin 2\beta$ from re-constructed $B^0 \to J/\psi\ K_L$ events includes the likelihood term $\mathcal{L}_{\text{mix}}$ for the B_{flav} sample that describes $B^0 - \bar{B}^0$ mixing. This term is also modified to account for the effects of background events, as documented in Reference [74].

A total of 33 parameters are allowed to float in the maximum likelihood fit to the $B^0 \to J/\psi\ K_L$ and B_{flav} samples to determine the value of $\sin 2\beta$:

- The value of $\sin 2\beta$ itself.

- Eight parameters which describe the average mistag fraction w_i and the the differences $\Delta w_i = w_i(B^0) - w_i(\bar{B}^0)$ for each tagging category i. In addition, there are eight parameters that account for w_i and Δw_i in background.

- Eight parameters define the signal Δt resolution, discussed in Section 8.2.2. For background $B \to J/\psi X$ events, we allow the quantities S_{core}, f_{core}, and b_{core} to float in the fit. The remaining Δt resolution parameters for $B \to J/\psi X$ background are assumed to agree with signal values.

- Four parameters quantify the fraction of background events with zero life-time in each tagging category in the B_{flav} sample. One additional parameter is used to determine the lifetime of the non-prompt background events.

In addition, there are several parameters that are fixed in the fit:

- The relative fractions of $B^0 \rightarrow J/\psi \ K_L$ signal, and $B \rightarrow J/\psi X$ and non-J/ψ backgrounds in the ΔE signal region as a function of tagging category (lepton or non-lepton), K_L reconstruction mode (EMC/IFR), and the $J/\psi \rightarrow \ell^+\ell^-$ reconstruction type ($\ell = e, \mu$). These fractions were determined from the results of the fit given in Tables 8.6 and 8.7, and the relative amounts of the $B \rightarrow J/\psi X$ backgrounds are obtained from Monte Carlo studies (see Table 8.3). A total of 56 parameters, which specify the relative fractions of $B^0 \rightarrow J/\psi \ K_L$ signal and six background modes ($B \rightarrow \chi_c K_L$, $J/\psi K_S$, $J/\psi K^{*0}$, as well as prompt and non-prompt non-J/ψ background and the sum of the remaining $B \rightarrow J/\psi X$ modes) for the eight reconstruction categories, are used in the fit.

- The parameters that describe the shape of the signal and background ΔE PDFs (see Figures 8.8 and 8.9) are fixed in the $\sin 2\beta$ fit. In either the EMC or the IFR, eight parameters describe the $B^0 \rightarrow J/\psi \ K_L$ signal shape, five parameters describe the $B \rightarrow J/\psi K_S$ distribution, and four parameters model the $B \rightarrow J/\psi X$ distribution. The two parameters used to describe the non-J/ψ background are common to both EMC and IFR events. This yields a total of 36 unique shape parameters that are inputs to the fit.

- The Δt resolution function parameters ($\hat{b}$) for the non-J/ψ background events, given in Table 8.5.

- The CP content of the background is also included in the fit. We fix the effective CP of $B \to J/\psi K^{*0}$ events to -0.68 ± 0.07 from a recent BABAR study [77]. Studies of $B \to J/\psi X$ events in Monte Carlo estimates the CP content of the background at $0.21(0.24)$ in the EMC(IFR) sample. We assume the CP content of the non-J/ψ background is zero.

- We fix the lifetime of the B^0 and the mass difference Δm_d to the 2002 PDG values: $\tau_{B^0} = 1.542$ psec, $\Delta m_d = 0.489$ psec^{-1} [78].

8.3 $\sin 2\beta$ **Fit Results and Systematics**

The value of $\sin 2\beta$ obtained from the fit to the $B^0 \to J/\psi\ K_L$ and B_{flav} samples is

$$\sin 2\beta = 0.723 \pm 0.158, \tag{8.17}$$

where the quoted (statistical) uncertainty does not yet include systematic uncertainties. In Table 8.9 we include the results of the $\sin 2\beta$ fit in various subsets of the data.

Sample	Tagged Yields	Purity	$\sin 2\beta$
$J/\psi K_L$	561 ± 32	55.2	**0.723 ± 0.158**
Lepton	91 ± 11	63.9	0.233 ± 0.291
Kaon I	147 ± 15	54.7	0.959 ± 0.248
Kaon II	142 ± 15	48.4	0.643 ± 0.360
Inclusive	174 ± 17	56.0	1.593 ± 0.530
B^0-tagged events	296 ± 22	54.7	0.858 ± 0.224
$\bar{B}^0$-tagged events	258 ± 21	54.6	0.624 ± 0.224
EMC $J/\psi \rightarrow e^+e^-$	122 ± 13	49.8	1.121 ± 0.364
IFR $J/\psi \rightarrow e^+e^-$	134 ± 16	65.2	0.422 ± 0.299
EMC $J/\psi \rightarrow \mu^+\mu^-$	164 ± 17	47.4	0.742 ± 0.371
IFR $J/\psi \rightarrow \mu^+\mu^-$	142 ± 17	64.2	0.772 ± 0.270

Table 8.9: Result of fitting the $B^0 \rightarrow J/\psi \ K_L$ and B_{flav} samples for the *CP*-violating parameter $\sin 2\beta$ in the full $J/\psi K_L$ flavor-tagged sample and in various subsamples. The yields are given for tagged events, which are obtained by a likelihood fit and are therefore free of background. In the fits to only B^0- or $\bar{B}^0$-tagged events, each Δw_i parameter was its fitted value.

8.3.1 Systematic uncertainties

Most of the systematic uncertainties associated with the extraction of the *CP* asymmetry using $B^0 \rightarrow J/\psi \ K_L$ events are due to the unique properties associated with $B^0 \rightarrow J/\psi \ K_L$ decay. We enumerate these sources of systematic uncertainty below, where we also discuss the uncertainties associated with the B_{flav} sample. We summarize our findings in Table 8.10.

1. In order to determine the systematic uncertainty due to the sample composition extracted from the ΔE fit, we vary the signal and background fractions using a set of Gaussian random numbers, where the width of the Gaussian

distribution is taken from the measured uncertainty on the sample composition. The covariance matrix from the ΔE fit is used so that we may account for the correlations between the signal and background fractions. The width of the resultant $\sin 2\beta$ distribution is taken as the systematic uncertainty.

2. We vary the $B \rightarrow J/\psi K^*$, $J/\psi K_L \pi$, $B^0 \rightarrow J/\psi K^0$, $\chi_{c1} K_L$, and the non-itemized $B \rightarrow J/\psi X$ branching fractions in the inclusive $B \rightarrow J/\psi X$ Monte Carlo event sample by either their measured uncertainties or conservative estimates. In each case, we recompute the sample composition and determine the deviation from the nominal result for $\sin 2\beta$. The systematic uncertainty from this source is taken as the sum in quadrature of each deviation.

3. Referring to Table 8.8, we measured the CP content of the non-itemized $B \rightarrow J/\psi X$ background events in Monte Carlo to be $0.21^{+0.12}_{-0.06}$ in the EMC, and $0.24^{+0.14}_{-0.06}$ in the IFR. The asymmetric uncertainty is the result of conservatively varying the $B \rightarrow J/\psi X$ branching fractions. For $B^0 \rightarrow J/\psi K^{*0}$ events, we take the effective CP derived from Reference [77], and for non-J/ψ events we assume a net CP of zero and conservatively vary this value by ± 0.25. We take the deviation from the nominal $\sin 2\beta$ value as our systematic uncertainty.

4. In Section 8.1.3 we discussed various corrections to the Monte Carlo that alter the shape of the ΔE distributions. In order to gauge our sensitivity to the shape of the ΔE PDFs, we alternately introduced a Gaussian smear of 0.85 ± 0.45 MeV and a shift of -0.5 ± 0.25 MeV. We take the deviation in the value of $\sin 2\beta$ with respect to the nominal result as a systematic.

5. Comparing ΔE fits to $B^0 \to J/\psi\ K_L$ events reconstructed in Monte Carlo and data, we find the ratio of EMC events to IFR events is 1.29 ± 0.03 in Monte Carlo and 0.95 ± 0.07 in data. This implies that the Monte Carlo does not accurately model the K_L reconstruction efficiency in the detector. To correct for this effect, events in Monte Carlo with a real K_L are weighted by a factor of 0.74 in the EMC. This changes the shape of the $B \to J/\psi X$ background PDF, as a significant fraction of the EMC background is due to photons that mimic K_L mesons. We recompute the sample composition, and take the resulting deviation from the nominal $\sin 2\beta$ value as our systematic uncertainty.

6. As we mention in Section 8.1.3, based on studies of $e^+e^- \to \phi\gamma$ events, we randomly smear the K_L angular position in the IFR to correct for the overly optimistic resolution in Monte Carlo events. The nominal value of $\sin 2\beta$ extracted from the maximum likelihood fit includes this smearing.

We remove this correction, and take the deviation from the nominal $\sin 2\beta$ as the systematic uncertainty.

7. We examine the effects of our treatment of lepton-tagged events (recall that signal efficiency drops for these events) by using an average efficiency for all tagging categories. We take the deviation from the nominal value as the systematic uncertainty.

8. In order to test our sensitivity to signal Δt resolution function parameters, we compute $\sin 2\beta$ for different fixed values determined from various Monte Carlo samples. We take the average deviation in $\sin 2\beta$ from the nominal result as the systematic uncertainty for this effect.

9. For the non-J/ψ background, we vary the Δt resolution function parameters given in Table 8.5 and take the maximum change in $\sin 2\beta$ as the systematic uncertainty.

10. We also examine the impact the fixed resolution function parameters (the width and bias of the outlier Gaussian, as well as the scale factor of the tail Gaussian, see Section 8.2.2) have on the value of $\sin 2\beta$. We vary the width of the outlier Gaussian between 4 and 12 psec (nominally 8 psec), and the outlier bias between -2 and $+2$ psec (nominally, we assume no bias). We

also vary the tail scale factor (nominally 3) between 2 and 5. The change in

$\sin 2\beta$ relative to the nominal value is taken as the systematic uncertainty.

11. We also recompute $\sin 2\beta$, where we compute separate Δt resolution function

parameters for each tagging category. The overall change in $\sin 2\beta$ is taken

as the systematic uncertainty.

12. In the nominal fit, we assume that the Δt resolution is the same for correctly

and incorrectly tagged events. We test this assumption using signal Monte

Carlo, where we split the sample according to the quality of the tag and fit

each sample with it own resolution function. Although no significant differ-

ence is seen between the two fits, we take the uncertainty on the difference

as a systematic uncertainty.

13. To determine the influence the mistag parameters have on the value of $\sin 2\beta$,

we fix the Δt parameters and recompute $\sin 2\beta$ using mistag parameters

obtained from the B_{flav} and $B^0 \rightarrow f_{CP}$ Monte Carlo samples. We take the

uncertainty on our results as the systematic uncertainty.

14. The probability that an event found in B_{flav} sample is a real B is a function

of its m_{ES} value, as events in the m_{ES} signal region are modelled by the

sum of a Gaussian and a threshold background function. First, we vary

the B_{flav} signal probabilities by their measured uncertainties, and observe

the change in $\sin 2\beta$. After this test, we vary the endpoint of the threshold background function by ± 2 MeV and observe the effect on $\sin 2\beta$. The sum in quadrature of the deviations due to each effect is taken as the systematic uncertainty due to the uncertainty in the composition of the B_{flav} sample.

15. Nominally, we assume that the background in the B_{flav} sample has no mixing component, but as a systematic check we assume all non-prompt background mixes with frequency Δm_d.

16. For the B_{flav} sample, we ignore the possibility of doubly Cabibbo-suppressed $b \rightarrow u$ transitions. In other words, we assume decays such as $\bar{B}^0 \rightarrow D^+\pi^-$ only occur as a result of the favored $b \rightarrow c$ transition. As a systematic check, we include the effects of the $b \rightarrow u$ transitions and observe the variation in the value of $\sin 2\beta$ as a function of the strong phase difference between B^0 and $\bar{B}^0$ decays. The relative strong phases for the suppressed B_{flav} and B_{tag} decays cannot be determined experimentally, and so we take the maximum variation in $\sin 2\beta$ as our systematic uncertainty.

17. We allow the B^0 lifetime and mixing frequency to vary within measured errors according to the 2002 PDG [78]. We compare the results for $\sin 2\beta$ to the nominal value, and take this difference as the systematic uncertainty.

18. Various detector effects, such as the uncertainty on the boost, beam spot position, and the alignment of the SVT, contribute an addition ± 0.014 to the total systematic uncertainty.

19. Finally, studies of Monte Carlo event samples indicate that there is a small bias in the likelihood extraction of $\sin 2\beta$. The value for $\sin 2\beta$ quoted in Equation 8.17, as well as those in Table 8.9, have already been corrected by -0.014 in order to account for this bias. We assign a systematic uncertainty of ± 0.010 to this correction.

Source	$\delta(\sin 2\beta)$
1. ΔE sample composition	± 0.051
2. $B \rightarrow J/\psi X$ branching fractions	± 0.051
3. CP content of background	± 0.022
4. ΔE shift, smear	-0.016
5. K_L re-weighting in the EMC	$+0.006$
6. IFR K_L angular resolution	$+0.020$
7. `Lepton` tag correction	± 0.023
8. Signal Δt resolution	± 0.002
9. Non-J/ψ Δt resolution	± 0.003
10. Fixed Δt resolution parameters	± 0.009
11. Tag-dependent Δt resolution function	± 0.013
12. Δt resolution based on tag quality	± 0.001
13. Mistag parameters	± 0.012
14. B_{flav} sample PDF variation	± 0.004
15. B_{flav} background mixing	± 0.003
16. Doubly Cabibbo-suppressed decays	± 0.008
17. B^0 lifetime and mixing frequency	± 0.004
18. Detector effects	± 0.014
19. Monte Carlo correction (Bias)	-0.014 ± 0.010
Total systematic uncertainty	± 0.086
Total statistical uncertainty	± 0.158

Table 8.10: Summary of contributions to the systematic uncertainty on $\sin 2\beta$ for $B^0 \rightarrow J/\psi\ K_L$ decay. The number next to each source corresponds to the numbering in the text.

8.4 Conclusions

We measure the CP-violating quantity $\sin 2\beta$ using 88 million $\Upsilon(4S) \to B\bar{B}$ decays recorded at the BABAR detector at SLAC between 1999 and 2002. Reconstructing $B^0 \to J/\psi\ K_L$ events in this data sample, we obtain

$$\sin 2\beta = 0.723 \pm 0.158 \text{(stat.)} \pm 0.086 \text{(syst.)}, \tag{8.18}$$

which is consistent with Standard Model expectations.

This result was initially included in Reference [64], where the CP asymmetry in $B^0 \to J/\psi\ K_L$ events was combined with several decay modes with $\eta_{CP} = -1$: $B^0 \to J/\psi K_S$, $\psi(2S)K_S$, $\chi_{c1}K_S$, $\eta_c K_S$, and $J/\psi K^{*0}$, $K^{*0} \to K_S\pi^0$. The results are summarized in Table 8.11, where you can see that the statistical precision of the $B^0 \to J/\psi\ K_L$ measurement exceeds all but $J/\psi K_S$, $K_S \to \pi^+\pi^-$. The fit to

Sample	$\sin 2\beta$
$J/\psi K_L$ ($\eta_{CP} = +1$)	0.72 ± 0.16
$J/\psi K_S$ ($K_S \to \pi^+\pi^-$)	0.82 ± 0.08
$J/\psi K_S$ ($K_S \to \pi^0\pi^0$)	0.39 ± 0.24
$\psi(2S)K_S$ ($K_S \to \pi^+\pi^-$)	0.69 ± 0.24
$\chi_{c1}K_S$	1.01 ± 0.40
$\eta_c K_S$	0.59 ± 0.32
$J/\psi K^{*0}$ ($K^{*0} \to K_S\pi^0$)	0.22 ± 0.52
Full CP sample	0.74 ± 0.07

Table 8.11: Result of fitting for CP asymmetries in various BABAR data samples. The quoted uncertainty on the results is statistical only.
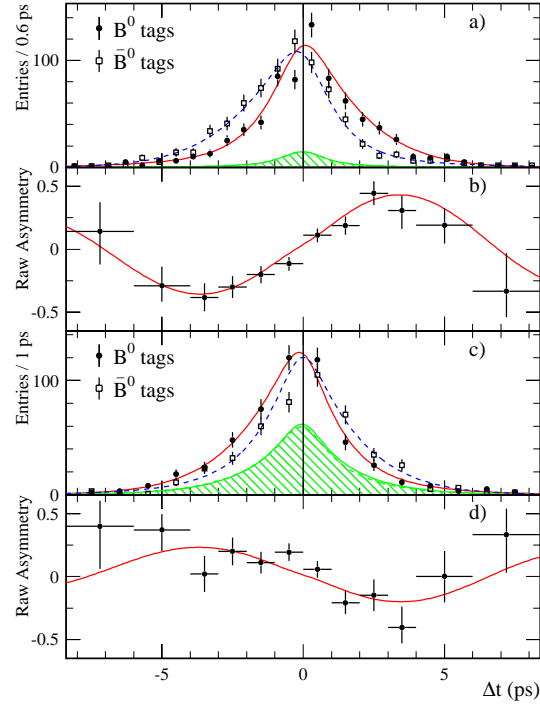
Figure 8.10: a) Number of $\eta_{CP} = -1$ candidates ($J/\psi K_S$, $\psi(2S)K_S$, $\chi_{c1}K_S$, and $\eta_c K_S$) in the signal region with a B^0 tag (N_{B^0}) and with a $\bar{B}^0$ tag ($N_{\bar{B}^0}$), and b) the raw asymmetry ($N_{B^0} - N_{\bar{B}^0}$)/($N_{B^0} + N_{\bar{B}^0}$) as functions of Δt. The solid (dashed) curves represent the fit projection in Δt for B^0 ($\bar{B}^0$) tags. The shaded regions represent the background contributions. Figures c) and d) contain the corresponding information for the $J/\psi K_L$ mode ($\eta_{CP} = +1$).

the full CP and B_{flav} samples yields

$$\sin 2\beta = 0.741 \pm 0.067(\text{stat.}) \pm 0.034(\text{syst.}), \qquad (8.19)$$

where the $B^0 \to J/\psi\ K_L$ results contribute ± 0.015 to the total systematic error.

In Figure 8.10 we present the flavor-tagged Δt distributions and the raw CP asymmetry for $B^0 \to J/\psi\ K_L$ and $\eta_{CP} = -1$ events in data.

8.4.1 Impact on the Unitarity Triangle

The results for $\sin 2\beta$ are used (along with other analysis results) to constrain the (ρ,η) vertex of the Unitarity Triangle (Figure 6.2). In the summer of 2002, the CKMfitter Group [79] compiled available results from BABAR and elsewhere in order to show the various experimental constraints on CP violation in the quark sector according to the Standard Model. The results are shown in Figure 8.11. In this case the vertex of the Unitarity Triangle, $(\bar{\rho}, \bar{\eta})$, incorporates higher order corrections to the Wolfenstein parameterization [80]:

$$\bar{\rho} = \rho \left(1 - \frac{\lambda^2}{2} \right) \quad \bar{\eta} = \eta \left(1 - \frac{\lambda^2}{2} \right),$$

so that $V_{td} = A\lambda^3(1 - \bar{\rho} - i\bar{\eta})$ is correct to $\mathcal{O}(\lambda^5)$. In 2002, experimental results implied that within $\pm 1\sigma$ errors,

$$\bar{\rho} = 0.125 \text{ to } 0.306, \quad \text{and} \quad \bar{\eta} = 0.287 \text{ to } 0.402.$$
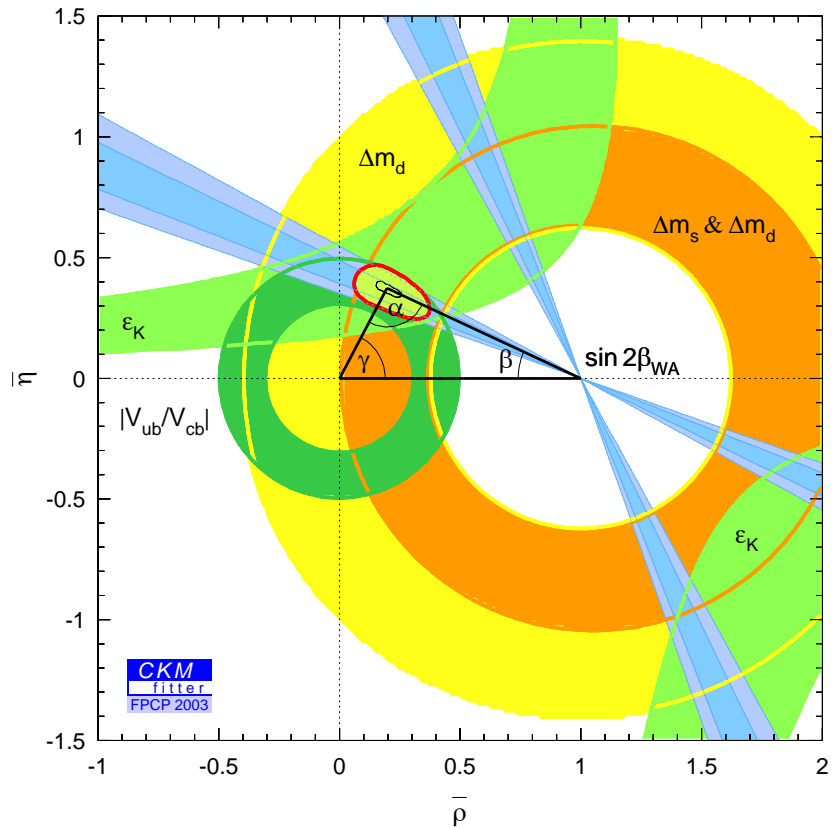
Figure 8.11: Unitarity Triangle results obtained from the CKMfitter Group using 2002 results. The constraint due to the world average value of $\sin 2\beta$, which includes the results obtained in this thesis along with those from Belle [81], CDF [82], and ALEPH [83], can be seen as the four conical regions originating from (1,0).
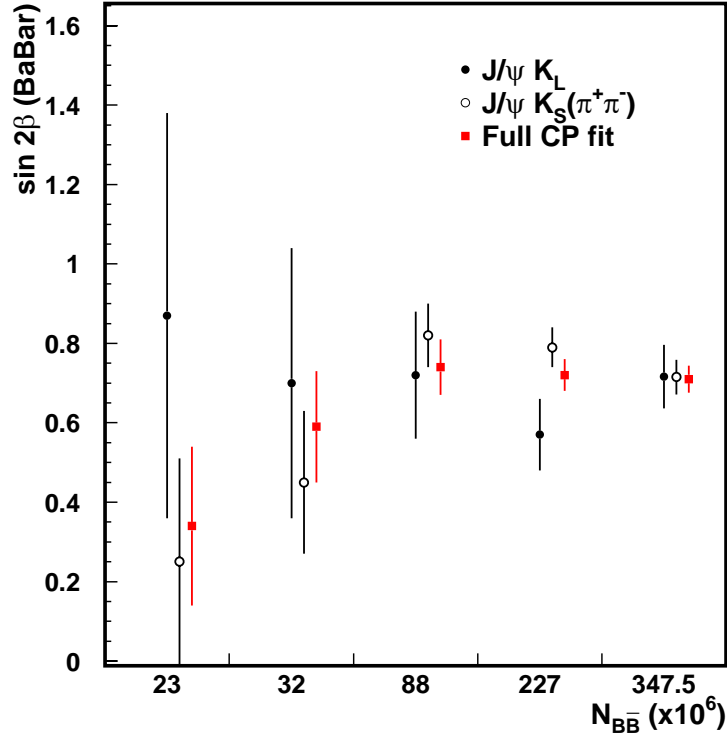
Figure 8.12: $\sin 2\beta$ results at *BaBar* as a function of the number of $B\bar{B}$ decays used. All results have been published [76, 73, 64, 84], with the exception of the preliminary results using 347.5 million $B\bar{B}$ decays [85].

8.4.2 Progress beyond the 2002 results

A summary of the *BaBar* $\sin 2\beta$ results is shown in Figure 8.12 as a function of the number of $B\bar{B}$ decays used in each analysis. In the years following the $\sin 2\beta$ analysis documented here, the B factories have accumulated a vast number of additional $B\bar{B}$ decays. The most recent (preliminary) results from *BaBar* [85] report the value of $\sin 2\beta$ obtained from a study of nearly 350 million $\Upsilon(4S) \to B\bar{B}$

decays:

$$\sin 2\beta = 0.710 \pm 0.034(\text{stat.}) \pm 0.019(\text{syst.}), \qquad (8.20)$$

with $|\lambda|$ deviating from unity by about 2σ (any deviation from unity would be an indication that CP Violation in these modes is not strictly the result of interference between mixing and decay).

The most recent results from the CKMfitter Group have been compiled using experimental results presented at the 2006 winter conferences, and are shown in Figure 8.13. They conclude

$$\bar{\rho} = 0.197^{+0.026}_{-0.030} \quad \text{and} \quad \bar{\eta} = 0.339^{+0.019}_{-0.018}$$

within $\pm 1\sigma$ errors.

The study of $\sin 2\beta$ in B decays to charmonium final states has been an excellent test of Standard Model predictions. Vast amounts of data have allowed us to measure this quantity to a precision of less than 5% in the past year. This already serves as an excellent constraint on the Standard Model, and further data will only increase our understanding of CP violation in the quark sector.
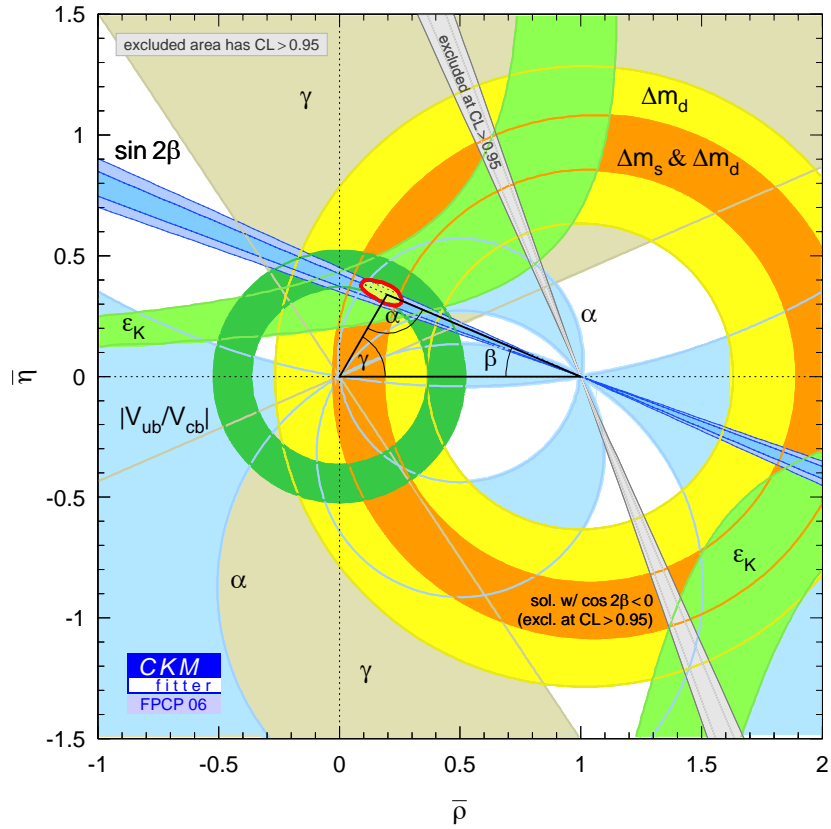
Figure 8.13: Unitarity Triangle results obtained from the CKMfitter Group using 2006 results. The constraint due to the world average value of $\sin 2\beta$ is obtained from Reference [86].

Bibliography

[1] S. L. Glashow, Nucl. Phys. **22**, 579 (1961); A. Salam, p. 367 of *Elementary Particle Theory*, edited by N. Svartholm (Almquist and Wiksells, Stockholm, 1969); S. Weinberg, Phys. Rev. Lett. **19**, 1264 (1967).

[2] P. W. Higgs, Phys. Rev. Lett. **12**, 132 (1964).

[3] Super-Kamiokande Collaboration, Y. Fukuda *et al.*, Phys. Rev. Lett. **81**, 1562 (1998).

[4] For a review, see *e.g.* A. Riotto, "Theories of baryogenesis", **arXiv:hep-ph/9807454**.

[5] K. G. Wilson, Phys. Rev. **D10**, 2445 (1974).

[6] M. Breidenbach *et al.*, Phys. Rev. Lett. **23** 935 (1969).

[7] D. H. Perkins, *Introduction to High Energy Physics* 3rd Ed., (Addison-Wesley, Reading), p. 202 (1987).

[8] Particle Data Group, S. Eidelman *et al.*, Phys. Lett. **B592**, 1 (2004).

[9] For reviews see, for example, A. S. Kronfeld and P. B. Mackenzie, Ann. Rev. Nucl. and Part. Sci. **43**, 793 (1993); H. Wittig, Int. J. Mod. Phys. **A12**, 4477 (1997).

[10] Y. S. Tsai, Phys. Rev. **D4**, 2821 (1971); **13**, 1771(E) (1976).

[11] CLEO Collaboration, F. Anderson *et al.*, Phys. Rev. **D61**, 112002 (2000).

[12] CLEO Collaboration, K. W. Edwards *et al.*, Phys. Rev. **D61**, 072003 (2000).

[13] N. Isgur and M. B. Wise, Phys. Lett. **B232**, 113 (1989), Phys. Lett. **B237**, 527 (1990)

[14] J. Richman, "Heavy-quark physics and CP violation," *Prepared for Les Houches Summer School in Theoretical Physics, Session 68: Probing the standard model of particle interactions, Les Houches, France, 28 Jul - 5 Sep 1997.*

[15] G. Alterelli and L. Maiani, Phys. Lett. **B52**, 351 (1974); M. K. Gaillard and B. W. Lee, Phys. Rev. Lett. **33**, 108 (1974).

[16] K. G. Wilson, Phys. Rev. **179**, 1499 (1969).

[17] F. G. Gilman and M. B. Wise, Phys. Rev. **D20**, 2392 (1979).

[18] J. D. Bjorken, Nucl. Phys. Proc. Suppl. **11**, 325 (1989).

[19] R. P. Feynman, in *Symmetries in Particle Physics*, edited by A. Zichichi, (Acad. Press), p. 167 (1965); O. Haan and B. Stech, Nucl. Phys. **B22**, 448 (1970).

[20] M. Bauer and B. Stech, Phys. Lett. **B152**, 380 (1985); M. Bauer, B. Stech, and M. Wirbel, Z. Phys. **C34**, 103 (1987).

[21] M. Neubert and V. Rieckert, Nucl. Phys. **B382**, 97 (1992).

[22] M. Neubert, V. Rieckert, B. Stech, and Q. P. Xu, in *Heavy Flavors*, edited by A. J. Buras and H. Linder (World Scientific, Singapore), p. 286 (1992).

[23] J. Körner and G. Goldstein, Phys. Lett. **B89**, 105 (1979).

[24] CLEO Collaboration, S. E. Csorna *et al.*, Phys. Rev. **D67**, 112002 (2003).

[25] CLEO collaboration, J.P. Alexander *et al.*, Phys. Rev. **D64** 092001 (2001)

[26] Belle Collaboration, H. Miyake *et al.*, Phys. Lett. **B618**, 34 (2005).

[27] *BABAR* Collaboration, B. Aubert *et al.*, Phys. Rev. **D67**, 092003 (2003).

[28] *BABAR* Collaboration, B. Aubert *et al.*, submitted to Phys. Rev. **D**, hep-ex/0602023.

[29] Z. Ligeti, M. Luke, and M. B. Wise, Phys. Lett. **B507**, 142 (2001); also, Reader and Isgur, Phys. Rev. **D 47**, 1007 (1993).

[30] G. 't Hooft, Nucl. Phys. **B72**, 461 (1974); Nucl. Phys. **B75**, 461 (1974).

[31] M. Neubert and B. Stech, Adv. Ser. Direct. High Energy Phys. **15**, 294 (1998).

[32] A. J. Buras, G. M. Gerard, and R. Rückl, Nucl. Phys. **B268**, 16 (1986).

[33] M. Beneke, G. Buchalla, M. Neubert, C. T. Sachrajda, Nucl. Phys. **B591**, 313 (2000).

[34] N. Isgur, D. Scora, B. Grinstein and M. B. Wise, Phys. Rev **D39**, 799 (1989); also, D. Scora and N. Isgur, Phys. Rev **D52**, 2783 (1995).

[35] *BaBar* Collaboration, B. Aubert *et al.*, Nucl. Inst. Methods **A479**, 1 (2002).

[36] *BaBar* Collaboration, D. Boutigny *et al.*, *BaBar Technical Design Report*, SLAC-R-0457 (1995).

[37] *BaBar* Collaboration, *The BaBar physics book: Physics at an asymmetric B factory*, edited by P. F. Harrison and H. R. Quinn, SLAC-R-0504 (1998).

[38] Belle Collaboration, *Belle Technical Design Report*, KEK Report 95-1, (1995).

[39] D. Lange, Nucl. Inst. Methods. **A462**, 152 (2001).

[40] T. Sjörstrand, Comp. Phys. Comm. **82**, 74 (1994).

[41] S. Agostinelli *et al.*, Nucl. Inst. Methods. **A506**, 250 (2003).

[42] BABAR Collaboration, B. Aubert *et al.*, Phys. Rev. **D74**, 012001 (2006).

[43] R. H. Dalitz, Phil. Mag. **44**, 1068 (1953).

[44] D. H. Perkins, *Introduction to High Energy Physics* 2nd Ed., (Addison-Wesley, Reading, 1982), p.136, 1982; B. C. Maglic *et al.*, Phys. Rev. Lett. **7**, 178 (1961).

[45] S. Kopp *et al.*, Phys. Rev **D63**, 092001 (2001).

[46] G. C. Fox and S. Wolfram, Phys. Rev. Lett. **41**, 1582 (1978).

[47] The ARGUS function is $A(m) \propto m\sqrt{1-x^2}\exp[-\zeta(1-x^2)]$, where $x \equiv 2m/\sqrt{s}$ and ζ is a free parameter in the fit; ARGUS Collaboration., H. Albrecht *et al.*, Z. Phys. **C48**, 543 (1990).

[48] For a review, see *e.g.* discussion by W. M. Dunwoodie, http://www.slac.stanford.edu/~wmd/omega_decay/isoscalar_vector_to_3pi.note.

[49] BABAR Collaboration, B. Aubert *et al.*, Phys. Rev. **D67**, 032002 (2003).

[50] Belle collaboration, K. Abe *et al.*, Phys. Rev. **D69** 112002 (2004).

[51] J. D. Richman CALT 68-1231 (1984), unpublished; G. Kramer and W. F. Palmer, Phys. Rev. **D45**, 193 (1992).

[52] J. H. Christenson, J. W. Cronin, V. L. Fitch, and R. Turlay, Phys. Rev. Lett **13**, 138 (1964).

[53] V. L. Fitch, Rev. Mod. Phys. **53**, 367 (1981).

[54] A. D. Sakharov, Pisma Zh. Eksp. Teor. Fiz. **5**, 32 (1967) [Sov. Phys. JETP Lett. **5**, 24 (1967)].

[55] M. E. Peskin and D. V. Schroeder, *An Introduction to Quantum Field Theory*, Addison-Wesley Publishing Company, 1995.

[56] C. S. Wu *et al.*, Phys. Rev. **105**, 1413 (1957).

[57] N. Cabibbo, Phys. Rev. Lett. **10**, 531 (1963);

[58] M. Kobayashi and T. Maskawa, Prog. Th. Phys. **49**, 652 (1973).

[59] C. Jarlskog, in *CP Violation, Advanced Series on Directions in High Energy Physics - Vol. 3*, edited by C. Jarlskog (World Scientific, Singapore, 1989), p. 3.

[60] L.-L. Chau and W.-Y. Keung, Phys. Rev. Lett. **53**, 1802 (1984).

[61] L. Wolfenstein, Phys. Rev. Lett **51**, 1945 (1983).

[62] E. Leader and E. Predazzi, *An Introduction to Gauge Theories and Modern Particle Physics, Vol. 2* (Cambridge University Press, Cambridge), p. 12 (1996).

[63] A. J. Buras and R. Fleischer, "Quark mixing, CP violation and rare decays after the top quark discovery," Adv. Ser. Direct. High Energy Phys. **15**, 65 (1998).

[64] *BaBar* Collaboration, B. Aubert *et al.*, Phys. Rev. Lett. **89**, 201802 (2002).

[65] Particle Data Group, C. Caso *et al.*, European Physics Journal **C3**, 1 (1998).

[66] CLEO Collaboration, C. P. Jessop *et al.*, Phys. Rev. Lett. **79**, 4533 (1997).

[67] *BaBar* Collaboration, B. Aubert *et al.*, Phys. Rev. **D65**, 032001 (2002).

[68] A. Drescher *et al.*, Nucl. Instrum. Methods Phys. Res. **A237**, 464 (1985).

[69] R. Sinkus and T. Voss, Nucl. Instrum. Methods Phys. Res. **A391**, 360 (1997).

[70] The Crystal Ball function is given by

$$
C(x) \propto
\begin{cases}
\left(\frac{n}{\alpha}\right)^n \frac{\exp(-\alpha^2/2)}{((\mu-x)/\sigma \, + \, n/\alpha \, - \, \alpha)^n} & x < \mu - \alpha\sigma \\
\exp\left[\frac{-1}{2}\left(\frac{x-\mu}{\sigma}\right)^2\right] & x > \mu - \alpha\sigma
\end{cases}
,
$$

where the parameters μ and σ are the mean and resolution of a Gaussian and the parameter n describes a power-law function. The Gaussian and the power-law functions are joined continuously at the point $\mu - \alpha\sigma$. The four parameters μ, σ, n, and α are free in the fit; D. Antreasyan, Crystal Ball Note 321 (1983).

[71] Belle Collaboration, K. Abe *et al.*, Phys. Rev. **D67** 032003 (2003).

[72] CLEO Collaboration, P. Avery *et al.*, Phys. Rev. **D62** 051101 (2000).

[73] BABAR Collaboration, B. Aubert *et al.*, Phys. Rev. Lett. **87**, 091801 (2001).

[74] BABAR Collaboration, B. Aubert *et al.*, Phys. Rev. **D66**, 032003 (2002).

[75] F. Le Diberder, "Precision on CP Violation Measurements and Requirement on the Vertex Resolution," BABAR Note **34** (1990).

[76] BABAR Collaboration, B. Aubert *et al.*, Phys. Rev. Lett. **86**, 2515 (2001).

[77] BABAR Collaboration, B. Aubert *et al.*, Phys. Rev. Lett. **87**, 241801 (2001).

[78] Particle Data Group, K. Hagiwara *et al.*, Phys. Rev. **D66**, 010001 (2002).

[79] CKMfitter Group, J. Charles *et al.*, Eur. Phys. J. **C41**, 1 (2005) [hep-ph/0406184], updated results and plots available at: http://ckmfitter.in2p3.fr.

[80] A. Buras *et al.*, Phys. Rev. **D50**, 3433 (1994); see also M. Schmidtler and K. Schubert, Z. Phys. **C53**, 347 (1992).

[81] Belle Collaboration, K. Abe *et al.*, Phys. Rev. **D66**, 071102 (2002).

[82] CDF Collaboration, A. Affolder *et al.*, Phys. Rev. **D61**, 072005 (2000).

[83] ALEPH Collaboration, R. Forty for the collaboration, ALEPH 99-099 (1999).

[84] *BABAR* Collaboration, B. Aubert *et al.*, Phys. Rev. Lett. **94**, 161803 (2005).

[85] *BABAR* Collaboration, B. Aubert *et al.*, BABAR-CONF-06/036 (2006).

[86] The Heavy Flavor Averaging Group (HFAG), Winter 2006 averages, http://www.slac.stanford.edu/xorg/hfag.